UNIVERSITY OF NAPLES "FEDERICO II"

DOCTORATE SCHOOL

IN

INDUSTRIAL ENGINEERING
(XXIII CYCLE)

PH.D. THESIS

IN

AEROSPACE ENGINEERING

A COOLING SYSTEM

FOR

S.M.A. (SHAPE MEMORY ALLOY) BASED ON THE USE OF PELTIER CELLS

by

Michele Granito

ADVISOR

Prof. Eng. Leonardo Lecce (DIAS)

Dept. Of Aerospace Engineering

Abstract

A COOLING SYSTEM

FOR

S.M.A. (SHAPE MEMORY ALLOY) BASED ON THE USE OF PELTIER CELLS

by

Michele Granito

Doctor of Philosophy in Aerospace Engineering

University of Naples "Federico II" - ITALY

Advisor – Prof. Eng. Leonardo Lecce (DIAS)

The aim of this thesis has been the study and the implementation of an innovative cooling system for S.M.A. (Shape Memory Alloy) material by using a Peltier cell.

This system has demonstrated a consistent cooling time reduction during the application and so that the solution adopted has confirmed that it can be used for a better operability of the S.M.A. material during the cooling phase.

After an accurate selection of possible cooling system to be adopted on these materials the better choice in terms of efficiency and energy consumption reduction has converged on Peltier cell design development.

In this context for our research three investigation have been conducted.

The first one has concerned an analytic investigation in order to understand the phenomenology and the terms involved during the heat exchange.

After this study a numerical investigation through a Finite Element approach by commercial software has been carried out. Also an experimental investigation has been conducted, at the CIRA Smart Structure Laboratory, in order to verify the results obtained by the numerical prediction. The set-up with the Peltier cell used as heater and cooler of the S.M.A. has confirmed the soundness of the solution adopted.

Finally, a correlation between numerical and experimental results have been presented

demonstrating the validity of the obtained results through the developed investigations.

This system, composed of Peltier cell has confirmed also an energy consumption reduction because the cell has been used for heating and cooling phase without additional system as resistive system (Joule effect).

This project shall be also industrial involvement in a new cost cut down point of view.

Napoli (ITALY), November 30, 2010

Acknowledgments

The Doctorate at the University of Naples is the last step for a student professional achievement after the degree. In particular the passion for the research field into aerospace applications has always been my purpose.

In this section I would like to provide my deep gratitude to all persons that have given a contribution to this PhD thesis work and that have supported me during this work period.

I express a thanks to my Professor Leonardo Lecce of DIAS (Department of Aerospace Engineering) at the University of Naples “Federico II” ITALY, my advisor who followed my activities carefully and with enormous patience.

I would like to thanks PhD. Antonio Concilio, responsible of the Smart Structure team at CIRA (Italian Aerospace Research Centre) and in particular I would like to express my deep gratitude to PhD Salvatore Ameduri who supervised my experimental activity in the laboratory and who always gave me his precious aid during this last activity.

Differently from the previous thesis during my degree study cycle, this research activity, for my doctorate, has been developed in different conditions because during these years I have worked too.

So that, in order to continue and to be over this research I have joined these two activities in parallel with some difficulties also because I have worked inside a different but interesting field.

I would like to thanks also my chief and my team colleagues and friends where I worked during these years because even if the job context is different from my research, I have always felt their support.

Finally, but certain not for order, I would like to express a special thanks to all my family, my mother, my father, my grandmother and my grandfather who have always known in my possibilities and capacities and without them I couldn't have achieved my goals. They have always supported my choice suffering and enjoying with me showing always their love during difficulties that have been presented all over my life.

This work is dedicated to all persons who are fond of me and who wherever and whenever have been near me.

Index

List of figures

List of tables

Index

Nomenclature

3A.S. Active Aeroelatic Aircraft Structures (EU project)

A.A.W. Active Aeroleasitic Wing (NASA project)

A.B.S. Acrylonitrile Butadiene Styrene

A.C. Alternate Current

A.D.I.F. Adaptive Wing Project (EADS-Airbus, DaimlerCrysler, DLR)

A.F.I.T. Air force Institute of Technology

A.F.R.L. Air Force Research Laboratory

A.F.T.I. Advanced Fighter Technology Integration (NASA program)

A.H.P.A. Active Hing Pin Actuator

A.L.I.C.E. Air launched Ingtegrated Counter-Measure Expendable

A.M.P. Aircraft Morphing Program

A.o.A. Angle of Attack

A.P.V.E. Adaptive Planform Vehicle Experiment

A.V.T. Actrive Vertical Tail

A.T.B. Active Twist Blade

B.I.G.B.L.U.E. Baseline Inflatable Wing Glider, Ballon-Launched Unmanned Experiment

B.V.I. Blade Vortex Interaction

C.F.R.P. Carbon Fibres Reinforced Plastics

C.I.R.A. Italian Aerospace Research Centre

C.R.G. Cornerstone Research Group

C.T.D. Composite Technology Development

D.A.R.P.A. Defense Advanced Research Project Agency

D.I.A.S. Dept. of Aerospace Engineering, Univ.of Naples “Federico II”

D.L.R. Deutschen Zentrum fur Luft-und Raumfahrt

D.o.D. Department of Defence

D.S.C. Differential Scanning Calorimetry

E Young elastic modulus

E.A.D.S. European Aeronautic Defence and Space

F.E.A. Finite Element Method

F.L.Y.R.T. Flying Radar Target

F.S.M.A. Ferromagnetic Shape Memory Alloy (known as magnetic S.M.A.)

H.A.L.E. High Altitude Long Endura

L.F.S.A. Lightweight Flexible Solar Array

M.A.R. Mission Adaptive Rotor

M.A.S. Morphing Aircraft Structures (D.A.R.P.A. Program)

M.A.V. Micro Air Vehicle

M.A.W. Mission Adaptive Wing

M.F.C. Macro Fiber Composite

M.I.T. Massachusetts Institute of Technology

M.P.U.A.V. Multi-Purpose Unmanned Aerial Vehicle

M.S.M.A. Magnetic Shape Memory Alloy (also known as Ferromagnetic S.M.A.)

N.A.S.A. National Aeronautics and Space Administration

N.I.A.C. NASA Institute for Advanced Concepts

NiTiNOL Commercial name for one of the most diffused Ni-Ti S.M.A.

N.R.L. Naval Research Laboratory

O.S.U. Oklahoma State University

P.D.E. Partial Differential Equation

P.M.N. Lead Magnesium Niobate (electro-strictive material)

P.V.D.F. Polyvinylidenefluoride (polymeric piezo-electric material)

P.Z.T. Lead Zirconate Titanate (piezo-ceramic material)

R.I. Rigidizable Inflatable

R.P.T. Rhombohedral Phase Transformation (also known as **R-Phase**)

R.R.B. Reconfigurable Rotor Blade

R.T.G. Radioisotope Thermoelectric Generator

S.A.M.P.S.O.N. Smart Aircraft and Marine Project System Demonstration

S.I.C.S.A. Sasakawa International Center for Space Architecture

S.I.M. Stress-Induced Martensite

S.M.A. Shape Memory Alloy

S.M.A.H.C. Shape Memory Alloy Hybrid Composite

S.M.E. Shape Memory Effect

S.M.P. Shape Memory Polymer

Terfenol-D Terbium-Iron-naval Ordinance Laboratory-Dysprosium (magneto-strictive material)

T.I.I.M.S. Texas Institute for Intelligent Bio-Nano Materials and Structures for Aerospace Vehicles

T.W.I.S.C.A. Twistable Section Closed by Actuation

U.A.V. Unmanned Aerial Vehicle

U.C.A.V. Unmanned Combat Aerial Vehicle

U.M.A.A.V. Unmanned Morphing Aerial Attack Vehicle

U.S.A.F. United States Air Force

V.A.F.N. Variable Area Fan Nozzle

V.G.C. Variable Geometry Chevrons

Z.I.F. Zero Injection Force

CHAPTER 1
INTRODUCTION TO PHD THESIS WORK

1.1 Introduction

Recently the development of new aeronautical structures and the implementation of innovative materials has been mandatory for succeeding in critical tasks in terms of weight, fuel consumption, aerodynamic efficiency, cost reduction and so on.

In fact, improvements in terms of aeroelastic behaviour, stability and manoeuvrability performance have been proved in the past, but now a new aircraft design concept is necessary and Shape Memory Alloy (S.M.A.) materials are taken into account for more and more aerospace applications.

S.M.A., are well doing for themselves for several engineering fields: from aeronautics to civils, from surgery to electronics and so on. Morphing wing field is benefiting of S.M.A.: some airfoil geometrical features (f.i. camber, chord) and some wing characteristics (twist angle, swept) are object of investigations aiming at producing suitable geometry variations achieving optimal configurations for different flight regimes.

In this work a S.M.A. tape, used as actuator system for a flap deflection by activation and de-activation through heating and cooling, by assuming complete Austenite and Martensite concentration, as initial and final states, has been considered.

In particular drawback of S.M.A. is the activation – deactivation time: even if the activation phase of S.M.A. tape, by heating through Joule effect, is reasonably fast, the de-activation phase by cooling the system is actually an open problem for this type of materials.

According to a real flap deflection on a civil aircraft actuation time has to be very fast in order to allow all manoeuvres during the flight.

In this PhD thesis a new concept of cooling time reduction of S.M.A. de-activation has been dealt with by means of a Peltier cell bonded on the S.M.A tape.

This is an innovative solution in terms of energy reduction because it is possible to shunt current from the system in order to supply the Peltier cell for the cooling effect on the tape.

The intent of the international scientific community is related to the reduction of energy consumption for the civil aviation in general and the adaptive wing is a choice as provided

by a lot of theoretical and experimental studies.

In order to assure improved performance in different flight regimes actuator systems especially active designed and realized according to the new concept of “smart structure”.

The possibility of improving aircraft performance, just changing the geometry of aerodynamic surfaces like wings, horizontal and vertical tails has been more and more taken into account in the last decades, as shown in the scheme of Figure 1.1.

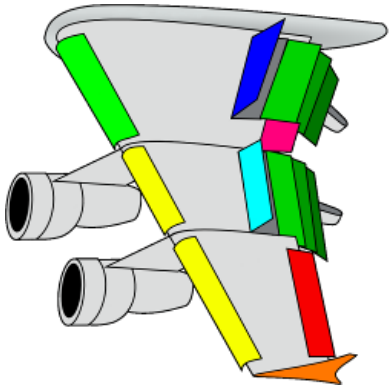

Figure 1.1: A morphing wing new arrangement.

1.2 "Smart Structure"concept

A structure or a material are defined "smart" if they are able to perceive external stimulus and to act on that a real time active control [1] [2].

A common and efficient way to demonstrate the behaviour of such structure or material is to have a parallel with a biological system. In fact in a biological system we can recognize:

- An apparatus able to have an external stimulus perception;
- An apparatus able to movement (muscles);
- A nervous system able to process the perceived stimulus and to generate others in order to have a muscles contraction.

According to such scheme in a smart structure we can define the following systems:

- A sensor system able to detect the environmental conditions and their variations;
- An actuation system able to modify the structure geometry;
- A control system able to manage signals from the sensor system and able to generate impulses for the actuator activation.

According to the following considerations a smart structure has to be able to "feel" and to "react" to external stimulus from the environment and to adapt to such conditions.

The structure control system has to consider his previous experience and, according to that, has to be able to act. In particular this system has to be able to have a 'memory' of all events further than to have a behaviour related to defined and predicted laws but in addition a smart structure can adapt own function according to each design configuration.

In terms of smart structures piezoceramics are more common materials used as actuators to transmit great level of excitation for several structural elements as beams with rectangular section (1D), plates (2D) or beams with thin walls (3D).

In this context Shape Memory Alloy (S.M.A.) are able to guarantee a good level of performance in terms of actuation.

A problem related to the S.M.A. is a restricted frequency application range: S.M.A. actuators are able to transmit displacements larger than piezoceramics but can act only at a low frequency range. Apart from piezoceramics in addition S.M.A. can have a sensor function too and this is the future application.

At the end, as stated before, the control system has to be able to learn the system behaviour and then, during the operation, to modify his function according to different situation from the design concept. In other words, a control system for a smart structure

has an adaptive function for every environmental condition even if different from design concept.

The smart structure application fields are several. In fact, a structure able simultaneously to perceive, learn and act can be a valid solution to a lot of problem.

In the previous paragraph in order to define a smart structure a biological comparison has been presented. The possibility of the substitution of human organs with artificial ones produced by means of smart structures is real: in literature a lot of works can be mentioned and in particular [3], [4], [5];

- The Tokyo Denki University program for an hand prosthesis has the target to develop a control architecture based on tactile information. The structural movement and the external stimulus perception are assured by an electrical engine and by tactile sensors. In order to reproduce hand movement 16 micro-engines located along the hand phalanx have been used;
- The program conducted by the Dept. Of Electronic Engineering of the University of Salford (UK), with the target to develop artificial muscles, able to match the conventional characteristics of the actuators with a modulated interaction between muscular system and limb.

The smart structure concept in terms of transmittable forces and deformations are well doing for themselves for several engineering applications. From aeronautics to civil field, from surgery to electronics or in order to solve nano-positioning problems or to the vibration control.

In the aeronautical fields a new tendency to develop this type of materials has been signed. Among the others, the morphing wing field is benefiting of S.M.A.: some airfoil geometrical features (f.i. camber, chord) and some wing characteristics (twist angle, swept, winglets) are, at the moment, object of investigations aiming at producing suitable, remarkable geometry variations thus achieving optimal configurations for different flight regimes in terms of efficiency improvement.

In the aerospace field some interesting program aiming at a performance improvement and cost reduction of civil and military aircraft are illustrated below:

- The ‘Smart Wing’ program with NASA-Langley, Mission Research Corporation and Lockheed Martin- Denver as partners for a new adaptive wing design by means of S.M.A. actuators for geometry modification. This solution foresees an improvement of

30% for the missiles and bombs loaded inside and a reduction from 20% to 40% of the aerodynamic drag;

- The 'Smart Aircraft and Marine Propulsion System Demonstration' (SAMPSON) program with Mc Donnell Douglas, Lockheed Martin- Denver, Georgia Institute of Technology, NASA-Langley, the Naval research laboratory, Electric Boat Corp. And Pennsylvania State University as partners. Targets for the aeronautical field are inherent to design, manufacturing and testing in the wind tunnel of an air intake real scale for a tactical aircraft. The coupled use of S.M.A. materials and piezoelectric materials has the intent to improve manoeuvrability to have a buffet control and a aircraft radar track reduction.

Other programs for a vibration control here are mentioned.

- A NASA-Langley program for a buffet control on the tail by means of piezoelectric materials. The test demonstrated a buffet reduction for all the angle of attack of the tail during flight. These results have been obtained by the use of piezoelectric actuators able to induce a bending momentum on the horizontal tail;
- The 'Active Vertical Tail' (AVT) with Mc Donnell Douglas Aerospace (MDA) and Parks College of St. Louis University as partners The AVT is a scale model (5%) of a tail with a vibration behaviour similar to a real tail. In order to control the two bending and twisting modes piezo actuators have been bonded along the horizontal tail span;
- The Smart Materials Actuated Rotor Technology (SMART) for noise active control from the helicopter rotor blade. Mc Donnell Douglas Helicopter and DARPA are partners for the program and foresee, by means of a blade trailing edge variation, a noise reduction of 10dB during the landing phase, a reduction of 80% of cell vibration, an improvement of 10% of the rotor performance an a better manoeuvrability.

1.3 Economic motivation for the research: future developments

In the last years aeronautic civil sector has signed a considerable economic growth due to an increase of 6% every year [6]. So that many companies like Boeing and Airbus have the intent to develop new aircraft concept and design for the development of cargo and passenger transport for the next 25 years.

By the way, because of this crisis period in several fields economic and social also aeronautical fields has a new mission for a sustainable economy aviation.

In this context even if there is an increase of transport all around the world in particular from Asiatic country like China or India there is a must for all aeronautical sector in terms of reduction of costs.

For these reasons during these years and for a great part of the next decades the research and the use of new materials and new design concept are necessary in comparison with the crisis time; new program are going to develop materials and technical solutions for an environmental use of energy.

In particular aeronautical industry, from a competitive point of view, has to increase the efficiency of next aircraft generation. New engine with a fuel consumption reduction and a reduced level of emission in terms of CO_2 or also a new concept for weight reduction and cost cut down.

A possible evaluation for new technological solution to adopt evidences that improvement in aerodynamic fields can allow a fuel consumption reduction above 36% during next 20 years for civil aircraft in transonic flight regime. A better propeller technology, a optimization of structural solution and an aerodynamic efficiency shall be a smart solution for the fuel consumption cut down of 50%.

On the other hand there is also, in military context, a necessity to develop aircraft with better performance in terms of reduction radar track, increase military cargo (bombs or missiles), great manoeuvrability by means of a new conceptual design devices [7] [8].

In next 20 years, according to new aeronautical transport requirements a new concept for aircraft shall be developed also for new UAV design (figure 1.3).

A study commissioned by Fundamental Aeronautic Program started 1.5 years ago by NASA Langley Research Centre (Hampton, Virginia U.S.A.) in order to define a roadmap for new civil transport aircraft design no later than 2030, a lot of industries, universities and research centres joined in but

In particular purpose of the program is an improvement in terms of operative capacities, environment impact and energy efficiency.

In fact, awareness of this economic crisis and consequently difficulties to come back from it, has influenced the targets to be achieved for next generation liner.

Typical innovation concerns some aspects as:

- Improved energetic efficiency through a consumption reduction of 70% within

2030: this is related to emissions and direct operative costs cut down.

- Nitrogen dioxide reduction (as fundamental pollution cause) of 755 near airports.
- Engine and aerodynamic noise reduction (about 71 dB lower than today value). This is translated into a 125 db perceived at a distance of 50 m.
- Airports concept design for a traffic clearing thanks top secondary tracks installed.

So, many projects have been presented and a lot of solutions have been adopted.
In 2020 a new bi-jets with on wing nozzles could be developed. This intermediate hybrid aircraft (230 passengers) as substitute of B757 category could have 'virtual windows' for passengers.
Another project named SUGAR (Subsonic Ultra Green Aircraft Research) Volt is a new aircraft, in place of B737 category, with a wind bracing and open rotor engines. Actuators should be electric supplied and engines shall be supplied by advanced batteries in an energetic reduction optic (figure 1.2).
Other solutions are in a prototypical phase: in fact, a new version of Bwb (Blended wing body) has a 'double bubble' solution 'drowned' in the wings with two turbofan inside the tail having a morphing and geometry nozzle (figure 1.4).

Figure 1.2: "SUGAR Volt" NextGen Aeronautics' aircraft design with electric power supply [17]

Figure 1.3: NASA solution for future morphing UAV design [18].

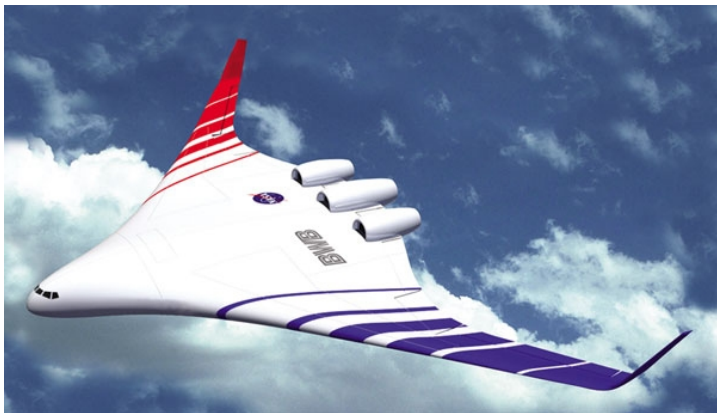

Figure 1.4: NASA new Bwb (Blended wing body) aircraft [19].

In this context a new approach and new materials have to be introduced into an innovative aircraft design and S.M.A. could be play a rule in this.

Other imporatnt project for future airplanes are the Green Supersonic Machine (figure 1.5)

This future aircraft design concept for supersonic flight over land comes from the team led by the Lockheed Martin Corporation.

The team used simulation tools to show it was possible to achieve over-land flight by dramatically lowering the level of sonic booms through the use of an "inverted-V" engine-under wing configuration. Other revolutionary technologies help achieve range, payload and environmental goals. This concept is one of two designs presented in April 2010 to the NASA Aeronautics Research Mission Directorate for its NASA Research Announcement-funded studies into advanced supersonic cruise aircraft that could enter service in the 2030-2035 timeframe.

Figure 1.5: NASA Green Supersonic Machine.

The "double bubble" D8 Series (figure 1.6) future aircraft design concept comes from the research team led by the Massachusetts Institute of Technology.

Based on a modified tube and wing with a very wide fuselage to provide extra lift, its low sweep wing reduces drag and weight; the embedded engines sit aft of the wings. The D8 series aircraft would be used for domestic flights and is designed to fly at Mach 0.74 carrying 180 passengers 3,000 nautical miles in a coach cabin roomier than that of a Boeing 737-800.

Figure 1.6: Boeing "double bubble" D8.

The "Icon-II" (figure 1.7) future aircraft design concept for supersonic flight over land comes from the team led by The Boeing Company.

A design that achieves fuel burn reduction and airport noise goals, it also achieves large reductions in sonic boom noise levels that will meet the target level required to make supersonic flight over land possible.

This concept is one of two designs presented in April 2010 to the NASA Aeronautics Research Mission Directorate for its NASA Research Announcement-funded studies into advanced supersonic cruise aircraft that could enter service in the 2030-2035 timeframe.

Figure 1.7: Boeing "Icon II" supersonic aircraft.

The Hybrid Wing Body H-Series (figure1.8) future aircraft design concept comes from the research team led by the Massachusetts Institute of Technology. This design is suitable for intercontinental flights and larger passenger loads similar to a Boeing 777. It features embedded engines using variable area nozzles with thrust vectoring, noise shielding thanks to the fuselage and other technologies, and advanced onboard vehicle health monitoring systems. This aircraft is designed to fly at Mach 0.83 carrying 354 passengers 7,600 nautical miles. The H Series is among the designs presented in April 2010 to the NASA Aeronautics Research Mission Directorate for its NASA Research Announcement-funded studies into advanced aircraft that could enter service in the 2030-2035 timeframe.

Figure 1.8: Boeing-Hybrid wing body H series aircraft.

In fact, the possibility of controlling the geometry of aerodynamic surfaces (ailerons, flaps, horizontal and vertical tails, etc.) represents a challenging target that justifies the more and more research activities carried out on the morphing concept.

The aerodynamic surfaces of a typical aircraft are characterized by a fixed geometry and this design approach leads a non complete exploitation of the aerodynamic performance, being the geometry not optimized for all flight condition [9]. The wing shape control, as proved by several numerical and experimental investigations [10-11], improves aerodynamic efficiency of a wing by assuring an optimal adaptive behaviour with respect to the external free stream conditions. Geometry modifications affect different parameters as local or global chamber [12-13], the wing span [14-15], the twist angle [16].

Within the Smart Materials family, due to their promising performance in terms of transmittable forces and deformations, Shape Memory Alloys (S.M.A.) play a more and more fundamental role. Several S.M.A. applications may be found in different engineering fields: aerospace, surgery, civil buildings and so on.

1.4 PhD thesis description

As stated before, the smart structure in aerospace field is justified by the need of improving performances and comfort in general.

In this context all aerodynamics studies, aimed at an improvement of all aircraft components, are addressed.

By the way, if a wing optimised geometry definition for a better operation in a assigned trim condition is possible, it is very difficult that all aircraft performances for each mission profile do not have a strong decrease.

A solution could be to foresee during the design phase the introduction of devices or new material as S.M.A. able to modify their shape and able to adapt the geometry for each flight condition.

The possibility of improving aircraft performance, just changing the geometry of aerodynamic surfaces like wings, horizontal and vertical tails has been more and more taken into account in the last decades.

A considerable incentive towards this direction has been given by the advent of above mentioned smart materials, generally guaranteeing compactness, cost and weight reduction, high integration level.

Among the others, a morphing application focusing on flap zone chamber control, based on S.M.A. ribbon integrated within the structure, has been carried out and a lab technology demonstrator has been built and tested. However, the intrinsic limit of S.M.A., that is the necessity of a heating and cooling for activation and deactivation, strongly penalized the frequency working range of the prototype, thus restricting tests to steady state.

While the activation time can be remarkably reduced by increasing the power supply, the deactivation cannot be made faster unless introducing a dedicated cooling system.

In the work at hand, the cooling effects due to a Peltier cell working at several regimes [5-6], bonded on a face of a S.M.A. ribbon in natural convection, has been considered.

In this thesis a new approach for the S.M.A. tape cooling by means of Peltier cell system has been presented.

This work has been developed at the University of Naples “Federico II” at the Dept. Of Aerospace Engineering (DIAS) in order to develop a control system for a cooling time reduction of the deactivation time of the S.M.A. actuator.

In chapter 1 an introduction has been presented.

In chapter 2 a general description of S.M.A. materials shall be provided in order to describe theri relevant properties and features and their wide applicability.

In chapter 3 an overview of state of the art of wing morphing shall be presented with particular reference to aerospace applications developed during international collaboration all around the world.

In chapter 4 Peltier cell characteristics and their operability shall be provided with particular attention to physical aspects.

In chapter 5 a theoretical model of the S.M.A. tape –Peltier cell system shall be presented explaining the phenomenology of the cooling effect of the solution adopted according to thermodynamic equations.

In chapter 6 a FEM model of S.M.A. –Peltier cell system shall be provided correlating main results each others and focusing on real advantage in terms of cooling time reduction by using this solution.

In chapter 7 an experimental investigation aiming at validating numerical results shall be presented confirming the soundness of the numerical predictions.

In chapter 8 conlcusion on the developed work shall be provided.

Finally, in the appendix developed tools and publications for these activities shall be illustrated.

1.5 References

[1] Concilio A., 1995 "Controllo attivo del rumore in cabina mediante attuatori piezoelettrici distribuiti sulla struttura", *PhD. thesis Univ. 'Federico II' Naples, Italy.*

[2] Srisavan A. V., McFarland D. M., 2001 "Smart Structures – Analysis and Design", *Cambridge University Press*.

[3] Matsuzaki Y., Wada B. K., "Second Joint Japan/U.S. Conference an Adaptive Structures", *Technomic Publishing Co., Inc.: Lancaster, PA, 1992, 885 pages*.

[4] Moses, R. W., "Vertical Tail Buffeting Alleviation using Piezoelectric Actuators", *Industrial and Commercial Applications of Smart Structures and technologies, SPIE Volume 3044, paper 07, 1997.*

[5] Varadan V. K. Varadan V. V., "Smart Structures, MEMS and Smart Electronics for Aircraft", *AGARD Lecture Series 205 Smart Structures and Materials. Implications for Military Aircraft of new Generation.*

[6] Bencke M., "Boeing International Cooperative Programs", *International Conference Aerospace technologies of the 21st Century, New Technologies Research and Simulation, Session II, 8-9 June, 2000, Berlin, Germany, pp.89-92.*

[7] Dmitriev V. G., "Advanced Technologies of TsAGI Experimental Research for Development of Modern Aircraft", *International Conference Aerospace Technologies New Technologies Research and Simulation, Session I, 8-9 June, 2000, Berlin, Germany, pp.7-18.*

[8] gal-Or B., "The New Era of Flight Control & Safety" *International Conference Aerospace Technologies New Technologies Research and Simulation, Session I, 8-9 June, 2000, Berlin, Germany, pp.59-66.*

[9] A.L. Martins and F.M. Catalano, "*Viscous Drag Optimization for a Transport Aircraft Mission Adaptive Wing*", 21st ICAS Congress, Melbourne, Australia Paper A98-31499 (1998).

[10] E. Stanewsky, "*Adaptive Wing and Flow Control Technology*", Progress in Aerospace Sciences, Elsevier Science Ltd., 37,583-667 (2001).

[11] J. Browman, B. Sanders, T. Weisshaar, "*Evaluating the Impact of Morphing Technologies on Aircraft Performance*", AIAA J. 2002-1631 (2002)

[12] J. Spillman, "*The Use of Variable Chamber to Reduce Drag, Weight and Costs of Transport Aircraft* ", Aeronaut. J. 96,1-8 (1992).

[13] H.P. Monner, T. Bein, H. hanselka, E. Breitbach, "*Design Aspects of the Adaptive Wing – The Elastic Trailing Edge and Local Spoiler Bump*", Royal Aeronautical Society, Multidisciplinary Design and optimization, London, 1998.

[14] Gevers Aircraft Inc., "Multi-Purpose Aircraft", U.S. Patents No. 5,645,250 (1997).

[15] J. Blondeau and D. Pines, "*Pneumatic Morphing Aspect Ratio Wing*", 45th AIAA/ASME/ASCE/AHS/ASC Structures, Structural Dynamics and Materials Conference, Palm Springs, California, AIAA J. 2004-1888 (2004).

[16] J. R. Wilson, "*Active Aeroelastic Wing: A New/Old Twist On Flight*", Aerospace America 40(99), 34-37 (2002).

[17] Boeing Sugar phase Boeing Research and technology (on line Presentation)

[18] Aerospace /American on line journal.

[19] NASA Conference Computational Engineering and Science in the NASA Fundamental Aeronautics Program AIAA 46th Aerospace Sciences Meeting Grand Sierra Resort Reno, NV January 9, 2008

CHAPTER 2

S.M.A.(SHAPE MEMORY ALLOY) FEATURES AND APPLICATIONS

2.1 Introduction

In this section thanks to a great bibliography research work, an overview about Shape Memory Alloy (S.M.A) technology is presented, in order to provide indications on the state of art and fields of investigations still open for additional studies.

In the following a brief historical description aiming at describing the S.M.A. discovery process shall be provided, starting from initial research led to *shape memory effect* comprehension to an involvement of these materials in the industrial application field, general characteristics and peculiar S.M.A. thermo - mechanic behaviour shall be presented.

However, typical behaviour and intrinsic S.M.A. thermo - mechanic properties is not apart from an accurate microscopic analysis of these ones.

During the description a more detailed analysis shall be included for the mathematic models presentations still now greatly used for the experimental phase on this materials.

The mathematical models comprehension is not completely enough if there is not a deep bibliographic literature research as reference ands basis for the future application as done in the present work.

So, during the material description all aspects strictly related to this type of materials in all fields from surgery, to civil or aeronautical applications, starting from the state of art of structural solutions with composite materials integrated with S.M.A., until methodology and bonding limitations with other materials.

This chapter stops with a comparison among S.M.A. and other smart materials typology, this comparison not only provides information about main S.M.A. advantages in several fields of applications, but also includes technological limits linked to their use in particular applications or related to adopted solutions to overcome these limitations.

2.2 S.M.A. history

Shape Memory Alloys (S.M.A.) have an interesting properties thanks to metal "remembers" his shape or original dimension, and is able to come back if subjected to determinate characteristic temperatures: this kind of property is well known as *shape memory effect (S.M.E.)*.

Firstly Chang & Read in 1932 provided documented observation of the shape memory transformations; they pointed out the reversibility of the Cadmium-Gold (Cd-Au) alloy transformation on the basis of metallurgic observations and resistivity changes; in addition in 1951 they noted the shape memory effect too.

In 1938 such transformations in the brass (Cu-Zn) were observed.

Only in 1962, however, a strong impulse in the applied research on shape memory alloys took place, after that William J. Buehler & al. [1] discovered that equi-atomic alloys Nickel-Titanium (Ni-Ti) had the shape memory property.

As for a lot of important discoveries this was due by chance and to deductive abilities of the two researchers , as by Kauffman & Mayo [2] [3] reported.

In fact, Buehler was doing research activities at the Naval Ordnance laboratory (NOL) of White Oak (Maryland) of the U.S. Navy about inter metallic compounds: his purpose was aiming at finding a metal with a higher melting temperature and properties with higher impact resistance for the SUBROC missile cap.

Among sixty compounds, Buehler choose twelve to be tested: among these ones there was the Nickel-Titanium alloy that showed wanted properties., then in this way he decided to named that **NiTiNOL**, including also the laboratory name where he worked.

In the table 2.1 and 2.2 some characteristics of this alloy are reported:

NiTiNOL properties		
Density	6.45 gm/cm^3	(0.23 lb/in^3)
Thermal Conductivity	10 W/mK	(5.78 Btu/hrft°F)
Specific heat	322J/kgK	(0.08 Btu/lboF)
Latent heat	24,200 J/kg	(10.4 Btu/lb)
Ultimate Tensile Strength	750-960 MPa	(110-140 ksi)
Elongation to failure	15.5%	(15.5 %)
Yield Strength (Austenite)	560 MPa	(80 ksi)
Young's Modulus (Austenite)	75 GPa	(11 mpsi)
Yield Strength (Martensite)	100 MPa	(15 ksi)
Young's Modulus (Martensite)	28 GPa	(4 Mpsi)

Table 2.1: some material with shape memory effect [4]

Alloy	Composition	Transormation range (°C)	Hysteresis (°C)
Ag-Cd	44-49% Cd	-190 to -50	15
Au-Cd	46,5-50% Cd	30 to 100	15
Cu-Al-Ni	14-41.5% Al; 3-4.5% Ni	-140 to 100	35
Cu-Sn	15 at.% Sn	-120 to 30	/
Cu-Zn	38.5-41.5% Zn	-180 to -10	10
Cu-Zn-X (X=Si,Sn,Al)	5-10% X	-180 to 200	10
In-Ti	18-23% Ti	60 to 100	4
Ni-Al	36-38% Al	-180 to 100	10
Ni-Ti	49-51% Ni	-50 to 110	30
Fe-Pt	25% Pt	-130	4
Mn-Cu	5-35% Cu	-250 to 180	25
Fe-Mn-Si	32% Mn; 6% Si	-200 to 150	100

Table 2.2: Alloys with Shape Memory Effect [5]

One day in 1959, while he was going on his studies about NiTi alloy variation percentage of the two components in order to verify the material properties, Buehler observed a new phenomenon that was the basis of an important property discovery: the small bars of NiTi alloy used for the experimental tests, if were free to fall down, they produced different sounds according to their temperature, as indication about different damping properties and, in from a microscpopic point of view, they had different atomic arrangements, in addition, it was possible to induce a variation in this behaviour simply heating or cooling the small bars.

But only in 1960, when Buehler was helped by Raymond Wiley for the experimental tests about fatigue resistance, the shape memory effect was discovered: in fact, during a meeting between Wiley and the management, in order to show the obtained results about fatigue resistance, one of the technical director, David Muzzey, decided to evaluate the behaviour of one of NiTiNOL tape, that were brought as sample, to subsequent bending and then to heating; with a great surprise of all people, when Muzzey heated the deformed

tape with his pipe, it came back to his original state.

Immediately, enormous functionality of these alloys and their study has gone on very fast, and a lot of researchers and producers have dedicated their efforts in the experimental, modelling phase for a better comprehension of S.M.A. behaviour and for other alloys investigations.

In table 2.1 and 2.2 some properties are shown about shape memory effect.

The most interesting and useful from an application point of view were the nickel-Titanium alloys and some alloys of Copper (Cu).

Today the most studied shape memory alloys are Nickel-Titanium, Copper-Zinc-Alluminium and Copper-Alluminium-Nickel.

Properties	Ni-Ti	Cu-Zn-Al	Cu-Al-Ni
Max Temp. shape recovery	100 °C	120 °C	200 °C
Max recoverable deformation	8 %	6%	5%
hysteresis	12-50 °C	10-25 °C	15-20 °C
Austenitic yield stress	415 Mpa (41.5 Kg/mm^2)	350 Mpa (35 Kg/mm^2)	400 Mpa (40 Kg/ mm^2)
Martensitic yield stress	70 Mpa (7 Kg/ mm^2)	80 Mpa (8 Kg/ mm^2)	130 Mpa (13 Kg/ mm^2)
Stress rupture	700 Mpa (70 Kg/mm^2)	600 Mpa (60 Kg/mm^2)	500-800 Mpa (50-80 Kg/mm^2)
Density (g/cm^3)	6.5	7.6-8.0	7.2
Resistivity (microohm-cm)	80-90	8.5-9.7	11-13
Thermal capacity (J/Kg °K)	837	400	373-574
Thermal conductivity (J/m*sec*°K)	18	120	30-43

Table 2.3: some S.M.A. property [6]

The great complexity of the metallurgic system of S.M.A. has been a stop to their diffusion in the industrial sector for several years.

During the middle of eighties and since 1991 a progressive penetration of these materials in a lot of high level technology fields as aerospace, biomedical and so on traditionally able to accept innovative materials, because can sustain relatively higher costs, has been developed.

In the last years in particular, availability of materials with high quality features and in a constant improvement and more and more reduced production costs, allowed development of several products, determining preliminary conditions for material diffusion in different technological fields; new and numerous commercial solution has determined a stimulus for the research growth, going on a synergic process for a strong evolution of this sector.

2.3 S.M.A. materials main properties

At present shape memory alloys (S.M.A.) can be found in a more increasing number of applications in aerospace, civil, mechanic, medical and other fields.

They represents a class of metallic materials with uncommon mechanical properties, in particular their main characteristic is related to their ability to recover (from this the special characteristic of 'remember') a macroscopic shape pre-impressed (extended or compressed) by means of simple temperature exchange or by the applied load.

An example of shape memory effect is illustrated in the following images in the Figure 2.1 [6]. To a thread of Ni-Ti, by means of adequate thermal treatment the shape of a Christmas tree with the write CNR has been impressed.

When it is cooled, the small gadget has been deformed in such a way the initial shape is no more recognizable.

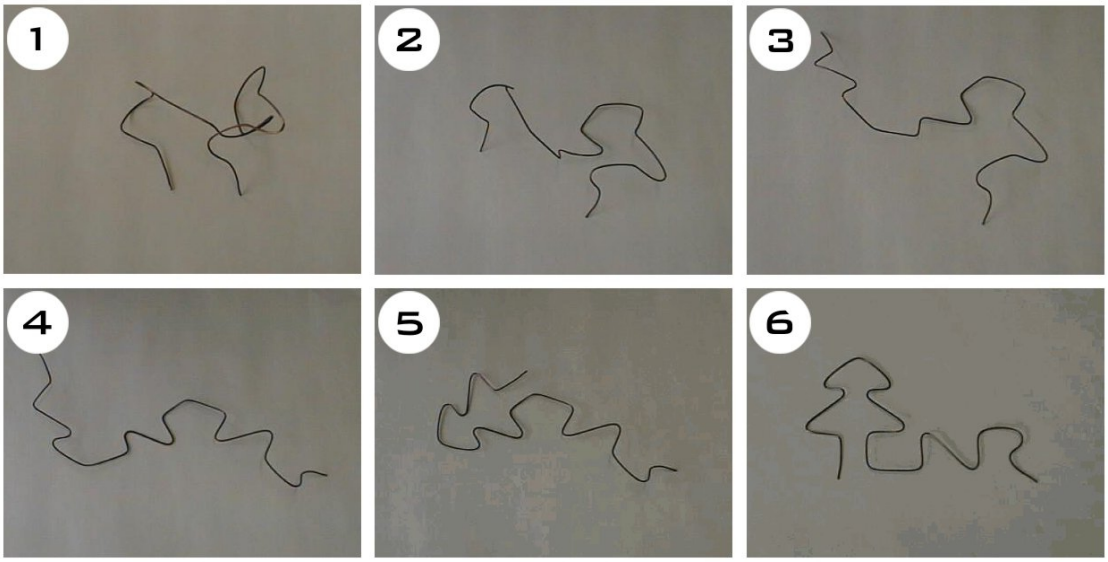

Figure 2.1: Example of shape memory effect. In a NiTi thread a small gadget shape has been remembered. After the deformation at a room temperature it recovers its remembered shape by means of simple heating at about 60°C [6]

Nevertheless, initial atomic arrangement have not been damaged and simply heating the tape (by means of an hair-drier with hot air) a progressive recovery of preimpressed shape is obtained.

As stated before, Buehler & al. [7] in 1962 discovered a Nickel Titanium alloy called NiTiNOL, that had an improved capacity with respect to other alloys before studied, 'to remember' the original shape.

This alloy, in fact, shows a stretching recovery property of 100%, as the impressed deformation doesn't exceed 8 % of extensional pre-deformation; this property is very attractive as actuator use at low frequency range (<1Hz). This shape recovery property is linked to the possibility of the alloy to be in two different phases (high and low temperature): the temperature when alloy 'remembers' shape, if heated, by means of small changes in the material composition and by thermal treatments can be modified; for the equi-atomic alloy NiTi phase transition temperature is 100°C, but adding extra quantity of Nickel, phase transition happens at a temperature of 0°C.

So, according to required applications alloy behaviour can be modified.

Another interesting characteristic is the Young's modulus (E) increase from 2 to 4 times when the alloy is subjected to a phase change, this increase is linked to a relevant resistivity variation and to latent heat emission or absorption.

The most important property that makes S.M.A. very interesting also as actuators is related to the possibility, during the pre-deformation recovery phase, of producing a relevant stress recovery (many times higher than starting required stress for the pre-stretching or pre-stress at low temperature).

S.M.A. can remember a shape that can be assigned or re-assigned through annealing (as for Ni-Ti alloy) >500°C.

Several methods exist for S.M.A. manufacturing, generally melting techniques are involved (through electric arc melting, electron stream etc.) in vacuum [8] [9].

The melted alloy (at a temperature between 700°C to 900°C) is forged by rotation and / or press-fusion by small bars and finally by wires.

A cold manufacturing alloy process exists too, this procedure is similar to the Titanium yarn production. Cold work determines physical and mechanical properties different for the alloy produced by hot work. Jackson & al. [10] dealt with very well this theme.

2.4 S.M.A. mechanical behavior

S.M.A. have a peculiar characteristic because during a solid state transformation where the start phase (original phase called Austenite by the name of the English scientist William C. Austen) and the finish one (or produced phase called Martensite, by the name of the German scientist Adolf Martens who first observed that) are solid structures, even if with different crystallographic arrangements [2] (see figure 2.2): this transformation **Martensitic Thermoplastic Transformation** is called.

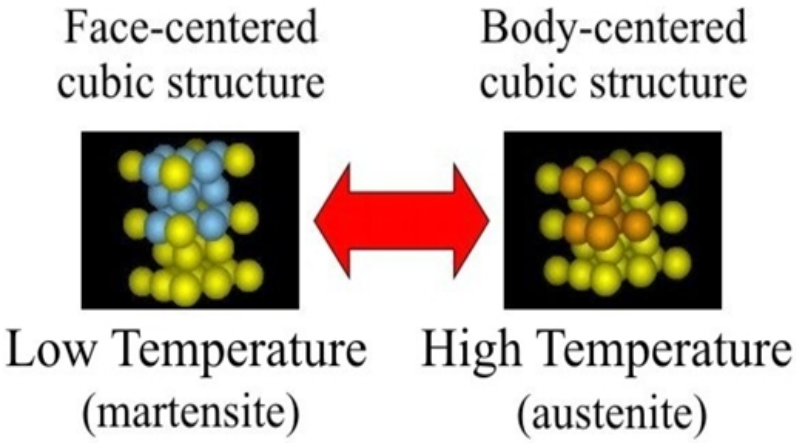

Figure 2.2: Martensitic Thermoplastic Transformation

The different crystallographic structure makes the Austenite as several metals, while Martensite is more or less as an elastomer, where a stress *plateau* is in: figure 3 helps the comprehension of this different behaviour by means of the stress-strain curves in the two cases of investigation.

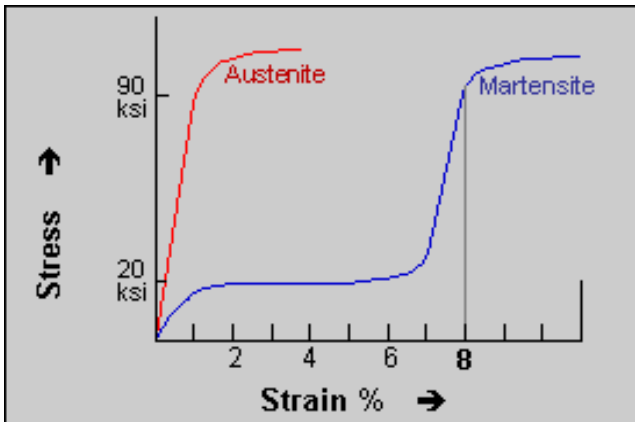

Figure 2.3: Stress-Strain curves for the two different phases.

S.M.A. thermo-mechanical behaviour is due to this typical transformation between the two different solid phases. It depends on the temperature, loads and material history.

Martensitic crystal structure, from Austenite, through a mechanical load application or temperature decrease, is obtained, by heating or applied load decrease, Austenitic phase is recovered [3] [12].

With no applied loads, start and finish transformation material temperature from a phase to another one are indicated as M_s, M_f, A_s, A_f (M = Martensite, A = Austenite, s = start, f = finish) adn , for a lot of material, $M_f < M_s < A_s < A_f$.

Figure 4 shows the material composition variation according to temperature.

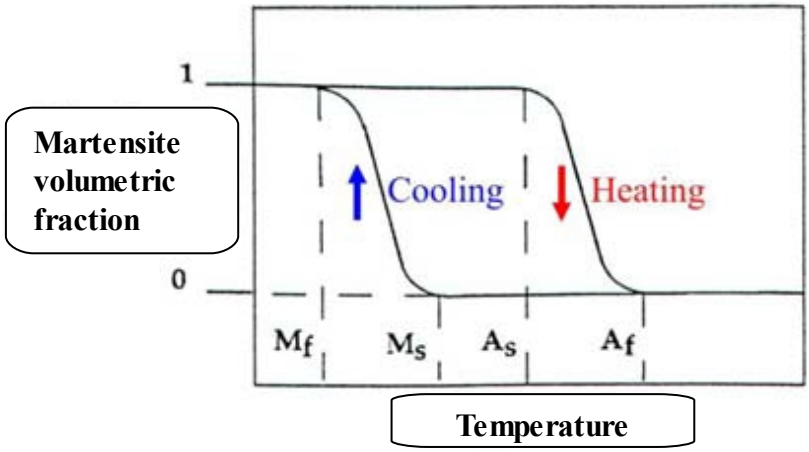

Figure 2.4: Phase transformation in S.M.A. materials

So, through a temperature variation, without applied loads, S.M.A. state will change, and its composition defined by a Martensite volumetric fraction (ξ) in it; in particular a transformation from a 100% Austenite phase (temperature is the same or higher than A_f and $\xi = 0$) to a phase where shall be together Austenite and Martensite, in different percentage, until a 100% Martensite phase (temperature the same or lower than M_f and $\xi = 1$) shall occur. All the process shall be valid even if an alloy heating rather than a cooling happens.

These transition temperature, also called *critical temperature*, are variable according to the applied load, and in particular they grows with the load (because an higher energy for a crystal structure deformation occurs) as explained in the paragraph 4.1.

As result of this transformation, it is possible to make a distinction for the macroscopic mechanical behaviour in the S.M.A. and to define 2 categories as in the figure 5 is

illustrated.

In the following the two behaviour shall be presented.

1) *Shape Memory Effect (S.M.E.)*

In figure 2.5 (a) S.M.A. sample exhibits a large residual strain (apparently plastic) after that it has been loaded and then unloaded; such strain can be completely recovered by increasing material temperature.

2) Pseudo-elastic Effect

In figure 2.5 (b) S.M.A. sample exhibits a very large strain (apparently plastic) after that it has been loaded; such strain can be completely recovered through an hysteresis cycle, after that the sample has been unloaded.

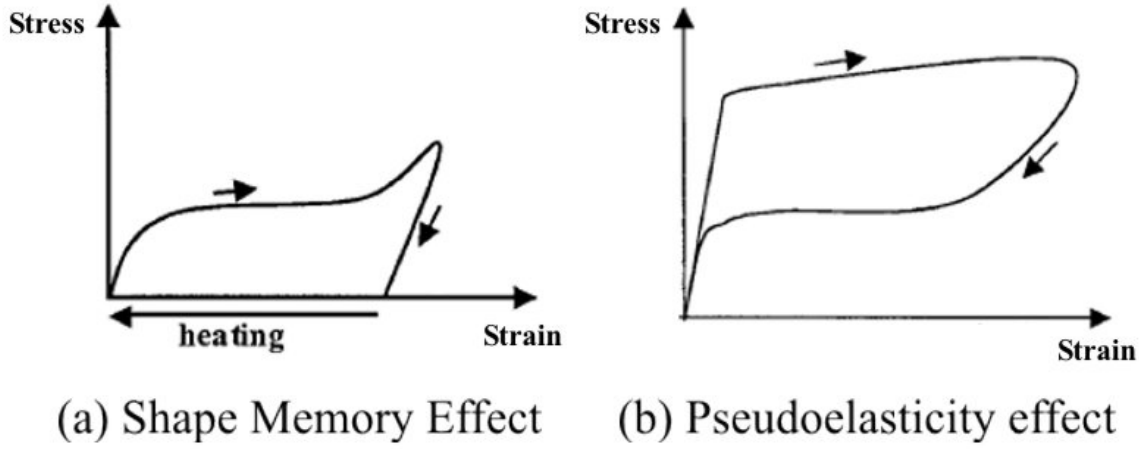

Figure 2.5: S.M.A. Stress-Strain behaviour [11]

In the following a more detailed phenomenon description shall be presented [6].

First property *(S.M.E.)* is particularly useful, and it is related to a specific Martensite crystallographic structure when generally a S.M.A. alloy at an ambient temperature (or low temperature) exists.

It consists of a dense crystallographic plane disposition specularly arranged each other and with a very high relative motion (for this reason there is a low Young's modulus and low damping in this phase).

These planes play a very important rule and it is the following: when the material is deformed (in Martensitic phase) by an external stress (for example extensional), higher than yielding stress one, crystallographic bonds and internal structure are not damaged but

a progressive reticular planes deployment occurs (this phenomenon is known as detwinning), arranging the total deformation without relevant atomic displacements.
Figure 6 summarizes all this focusing on microscopic plane [11].

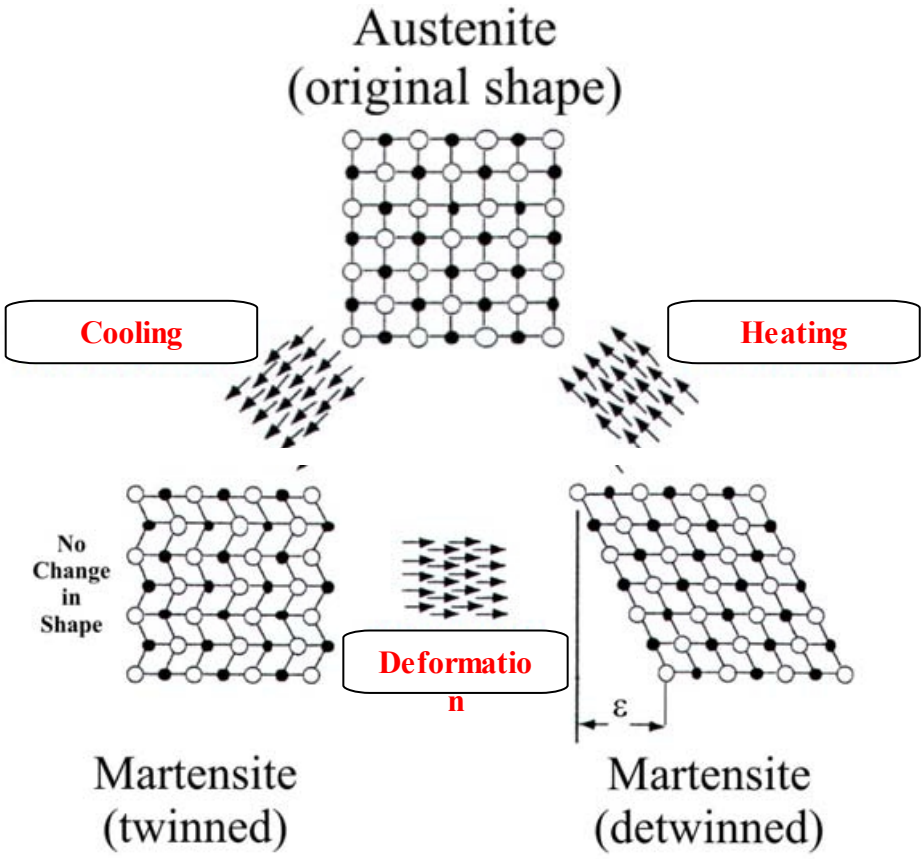

Figure 2.6: S.M.A. Stress-Strain behaviour for Shape Memory Effect [11]

For a more complete comprehension, we can consider bellows of a an accordion: consider that during the elongation phase of an accordion where, even if single bellow pleat moves a little bit, whole structure deploys much more.
Since during this situation single atoms move only a little bit from their original positions, when they, by an imposed heating effect, have to move in order to rearrange the original crystal structure (Austenite, high temperature phase), can easily recover their original configuration and go on to the initial macroscopic shape (this determines the deformation recovery too), that normally it is defined by a low movable crystallographic structure (this is the reason of a high Young's modulus and high damping).
In the following macroscopic effects in details, considering S.M.A. small bars, shall be

explained [13].

If the S.M.A. during the heating activation cannot recover the original shape (for example because strain is limited by constrains), then in it a great recovering stress happens; vice versa, if the alloy in no way is constrained, no recovering stress happens and then free recovery occurs.

Second property *(Pseudoelasticity)* of martensitic thermoplastic transformations is related to the possibility of making a transformation not only by a temperature variation but also through application of an appropriate stress state in adequate temperature conditions ($T > A_f$, starting from the Austenite phase).

So, it is possible that the *accordion* structure can occur in the material during the external load application, directly passing from the austenite phase to the deformed martensite phase. During the transformation imposed by and external force, material progressively create the martensitic structure and this instantaneously is deformed allowing again to 'repair' large deformations without damages permanently to the material crystallographic structure: with respect to the previous case there is no twinned martensite phase.

As for the shape memory effect the pseudolesticity effect is summerized in figure 2.7.

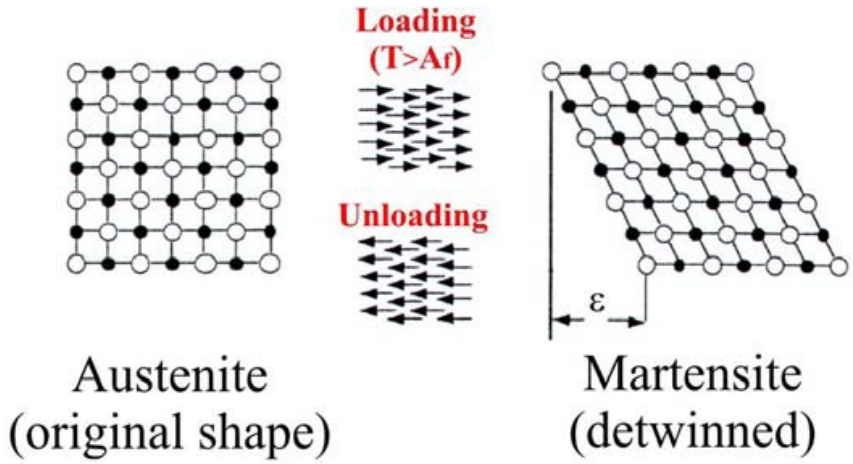

Figure 2.7: S.M.A. Stress-Strain behaviour for pseudoelasticity effect

However, this procedure is obtained between a temperature range where martensite created could not exist (because at that temperature the stable phase should be austenite phase at high temperature), when the external force is removed the alloy is in an unstable thermodynamic condition and instantaneously come back again, immediately recovering

the original shape (not following heating phase). The phenomenological reason of this is related to the material property of recovering immediately the original shape, showing a relevant elasticity, and it is able to support relevant deformations and instantaneously recover the original shape.

This second S.M.A. property have found several applications also thanks to a better utility apart from the material heating and/or cooling necessity. An example is presented in figure 8. Glasses with metallic parts composed of pseudolastic material can be closed in one hand and then it is able to recover again its original shape simply opening the hand.

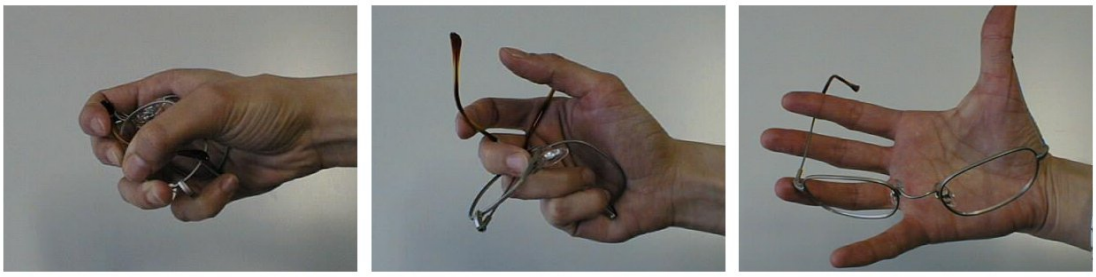

Figure 2.8: Pseudolasticity example of a NiTi alloy. Glasses composed od S.M.A. is strongly deformed and it is able to recover the original shape when the load is removed.

Both effect (S.M.E. and Pseudoelasticity) can be summarized in one plot called stress-strain (figure 9), in order to better understand the behaviour.

In the diagram with a continue line is represented the S.M.A. behaviour tested at a temperature $T > A_f$; in other words continue line represents the *pseudolestic* effect.

The alloy is loaded by a stress load starting from the initial condition with no stress.

The linear trend in the initial part is associated to a S.M.A. pseudolestic behaviour with 100% austenite phase (Young's modulus E_A) until the initial martensitic stress (σ_{Ms}), after that the transition phase from austenite into martensite happens; still a linear trend is observed until the finish martensitic stress (σ_{Mf}).

Successively, going to increase the load, linear trend is still observed, this time associated to an elastic S.M.A. behaviour with 100% martensitic phase (Young's modulus E_M), until the yielding stress (σ_y). After σ_y, the 100% martensitic phase has a plastic deformation.

During the load application generally a point between σ_y and σ_{Mf} , and then the unloading phase starts.

During this phase, still considering a constant temperature ($T > A_f$) there is a linear trend

associated to the elastic unloading phase, until the initial austenite stress (σ_{As}). Still with an applied load decreasing, the transition phase starts leading to the transformation of martensiote into austenite, according to a linear trend until the finish austenite stress (σ_{Af}), when the S.M.A. alloy is 100% austenite.

The additional load decreasing come back to the initial condition.

The cycle plotted by the continue line is associated to the pseudolastic behaviour (also called superelastic) of the S.M.A. alloy.

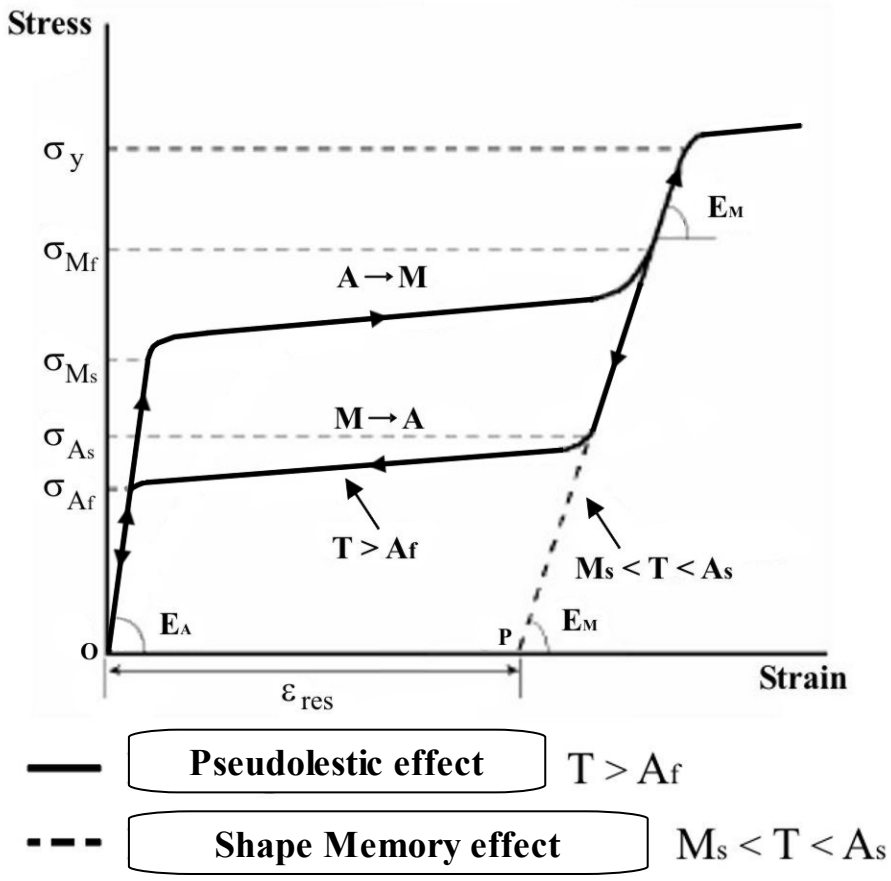

Figure 2.9: Stress – Strain diagram for S.M.A. material

If the loading –unloading process is conducted at a constant temperature $M_s < T < A_s$ so referring to the shape memory effect S.M.E. then the trend followed by the S.M.A. shall be laid to the precedent in the stress application phase, while it shall follow the dotted line during the unloading phase.

Now the obtained condition shall be with a null stress, leaving then in the material a residual deformation (ε_{res}). If the alloy with this type of residual strain is heated until a

temperature $T > A_f$, then the material shall recover its initial shape reaching newly the original condition (zero stress and strain); it is necessary again for the shape memory effect to increase the temperature in order to recover the austenitic phase (and then the initial shape), vice versa this is not necessary for the pseudolestic effect.

The shape memory effect for S.M.A. can be divided into the categories.

1) One – Way Shape Memory (figure 2.10)
2) Two – Way Shape Memory (figure 2.11)

Figure 2.10 and 2.11 [14] show the differences between the two categories.

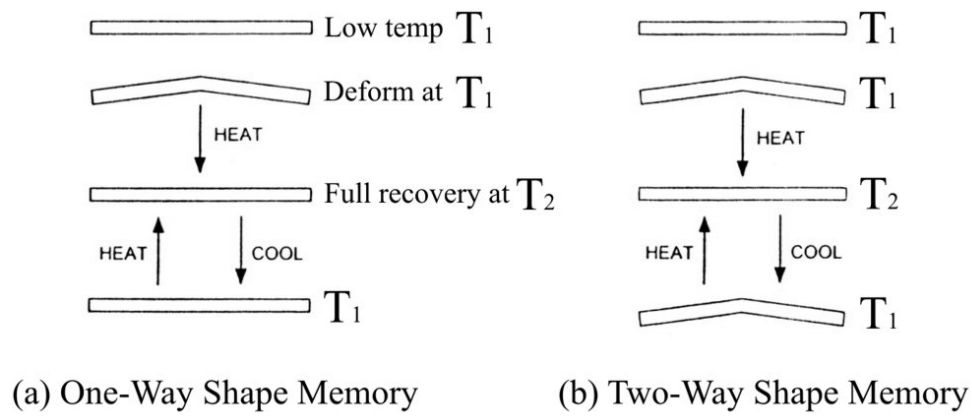

Figure 2.10: Shape Memory (a) One Way, (b) Two Way

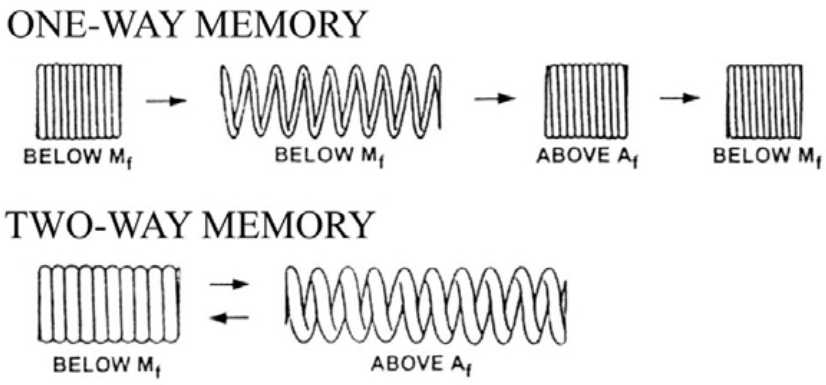

Figure 2.11: Shape Memory example (a) One Way, (b) Two Way

First category is referred to S.M.A. material until here exposed, where an assigned shape is recovered after a martensitic phase deformation and heating; on the other hand, second category concerns materials that 'remember' two shape, each other can be recovered at different temperature, without preventive deformations.

2.5 S.M.A. mechanical behavior

In order to define the S.M.A. thermo-mechanical behaviour, a lot of constitutive models have been developed. Some of these are primarily base on a micro-mechanical approach, other ones are based on a combination of micro and macro mechanic (S.M.A. phenomenology) or on statistic techniques and kinetic methods.

The development of numerical models as F.E.M., has conducted to constitutive models based on a continuum description (macro-scale, related to phenomenology); in addition these models allow to use material engineering constants as modelling parameters rather than difficult quantity to be measured.

Most of these macro-scale models only for quasi-static loads have been developed. One of the well known models is the Tanaka monodimensional model [15], based on thermo-mechanics. In this model the Second Law of Thermodynamic written as Helmholtz free energy has a variation formulation.

Mono-axyal deformation is assumed and temperature and martensitic volumetric fraction (ξ) are the only state variables, for (ξ) an exponential expression in terms of stress and temperature has been developed.

Liang & Rogers [16] also a model, based on constitutive equation developed by Tanaka, have presented; in this model for the martensitic volumetric fraction (ξ) a cosine function has been introduced.

One of the most important limitations of these two models is the only description of (ξ) induced by stress (pseudolestic effect) and they don't consider the induced transformation by strain (S.M.E.); then, these models cannot be applied to model the martensitic detwinning responsible for the S.M.E. at low temperature.

In order to overcome this problem, Brinson [17] has developed a new model through a distinction of (ξ) in two contribution: the first one induced by stress (in literature known as S.I.M. stress-induced martensite) and the second one induced by temperature.

In detail the first one defines the detwinned martensite quantity (induced by stress), while the second one concerns the martensitic volumetric fraction (ξ) induced by a reversible transformation phase coming from austenite (twinned).

So, in order to describe the S.M.E. and pseudoelastic effect constitutive equation with non constant coefficient have been considered.

Another constitutive model is the Boyd & lagoudas [18] [19] thermodynamic model

based on the free energy and dissipation potential.

This model derives by Gibbs free energy rather than by Helmholtz free energy as for the Tanaka model. This model can deal with 3D states and non proportional loads.

A thermodynamic formulation is used also in the Ivshin & Pence [20] model.

There are also models not based on this type of approach. For example, Grasser & Cozzarelli [21] have developed a 3D model based on evolutive plasticity approach. Similarly Juhasz & al. [22] have proposed evolutive equations based on the viscous-plasticity analogy, assuming that the phase transformation by a defined finite velocity takes place, so that the relaxation process happens: these evolutive equations assure the time dependent effect calculation: this model is able to predict the S.M.A. behaviour under combined thermal and mechanical loading.

Sun & Hwang [23] have obtained a micro-mechanical model taking into account the thermodynamics, micro-structure, micro-mechanics and dealing with the shape memory effect and pseudoelastic effect. Matsuzakiet & al. [24] a general 1D thermo-mechanic model have developed taking into account the dissipation energy effects, latent heat and heat transmission during the phase transformation. They a general energy function, with phase interaction found through experimental data for different stress conditions, have introduced. Barrett [25] a 1D S.M.A. constitutive model have developed, all changing phase effects including, hysteresis due to a partial transformation and stress-compression transformation; the model distinguishes stress-induced and temperature-induced martensitic volumetric fraction.

In the following some of these model in details shall be analyzed.

Tanaka [15] assumes that strain **ε,** temperature **T**, and martensitic volumetric fraction **ξ** are state variables that define the 1D S.M.A. behaviour (for example S.M.A. wires).

The constitutive equation is the following:

$$(\sigma - \sigma_0) = E(\xi)(\varepsilon - \varepsilon_0) + \Theta(\xi)(T - T_0) + \Omega(\xi)(\xi - \xi_0) \tag{2.1}$$

where the 0 represents the initial condition. This equation shows that stress consists of three parts:

- mechanic stress,
- thermoplastic stress
- stress induced by phase transformation

It is evident that Young's modulus E and the phase transformation coefficient Ω are function of martensitic volumetric fraction ξ, these functions are normally expressed as:

$$E(\xi) = E_A + \xi(E_M - E_A) \quad ; \quad \Omega(\xi) = -\varepsilon_L E(\xi) \tag{2.2}$$

where ε_L is the maximum recoverable strain, while E_A and E_M represent, respectively, austenite and martensite phases Young's moduli.

Tanaka for the martensitic volumetric fraction develops an evolutive equation determined by the dissipation potential, as in the following:

$$\xi = \Xi(\sigma, T) \tag{2.3}$$

This equation implies that martensitic volumetric fraction is a function of stress and temperature. in particular, in the Tanaka's model it is an exponential function with the following formulation:

Transformation A $\longrightarrow$ M (Cooling)

$$\xi = 1 - \exp\left[a_M (M_S - T) + b_M \sigma\right]$$

Transformation M $\longrightarrow$ A (Heating)

$$\xi = 1 - \exp\left[a_A (A_S - T) + b_A \sigma\right]$$

With material constants defined as:

$$a_A = \frac{\ln(0.01)}{(A_S - A_F)} \quad ; \quad b_A = \frac{a_A}{C_A}$$

$$a_M = \frac{\ln(0.01)}{(M_S - M_F)} \quad ; \quad b_M = \frac{a_M}{C_M}$$

In this formulation σ represents applied stress, T is the temperature.

Used coefficients in previous relations E, Θ, and Ω, and parameters M_S, M_F, A_S, A_F, C_A, C_M, are obviously determined through experimental tests on S.M.A. wires [11]: for typical

values see table 2.4.

For the martensite transformation phase critical stress start σ_{cr}^{S} and finish σ_{cr}^{F} and for stress influence, inclination (tangent) of critical stress-temperature diagram curves respectively for austenite C_A and martensite C_M transformations margin regions.

It is evident that transformation temperatures M_S, M_F, A_S, A_F are determined without applied stress, in particular, note that M_S, M_F temperatures according to the chosen model are different.

In the table some relevant value for characteristic S.M.A.temperature

Coefficient	Unity of meas.	Value
Critic stress start mart.transform.σ_{cr}^{S} (Brinson's model)	Pa	1.38e+6
Critic stressfinish mart.transform.σ_{cr}^{F} (Brinson's model)	Pa	1.72e+6
Derivative critic stress-temperature curve austenite phase C_A	Pa/°C	8+e6
Derivative critic stress-temperature curve austenite phase C_M	Pa/°C	12e+6
Austenite Young's modulus E_A	Pa	45e+9
MartensiteYoung's modulus E_M	Pa	20.3e+9
Austenite start temperature A_S	°C	52
Austenite finish temperature A_F	°C	65
Martensite start temperature M_S (Tanaka's model)	°C	43.5
Martesite finish temperature M_F (Tanaka's model)	°C	40.7
Martensite start temperature M_S (Brinson's model)	°C	55
Martesite finish temperature M_F (Brinson's model)	°C	42

Table 2.4: Thermo-mechanical properties of S.M.A. wires (Dynalloy 15 mil Ni-Ti [25])

Liang & Rogers [16] use the same Tanaka's model constitutive relation, but for the evolutive equation of martensite volumetric fraction a cosine function has been adopted.

This choice by a simply graphical observation can be found.

In fact, if again a S.M.A. material transformation phase diagram is considered (figure 2.14), it is evident that appropriately defining its coefficient a cosine function well describe the phenomenology.

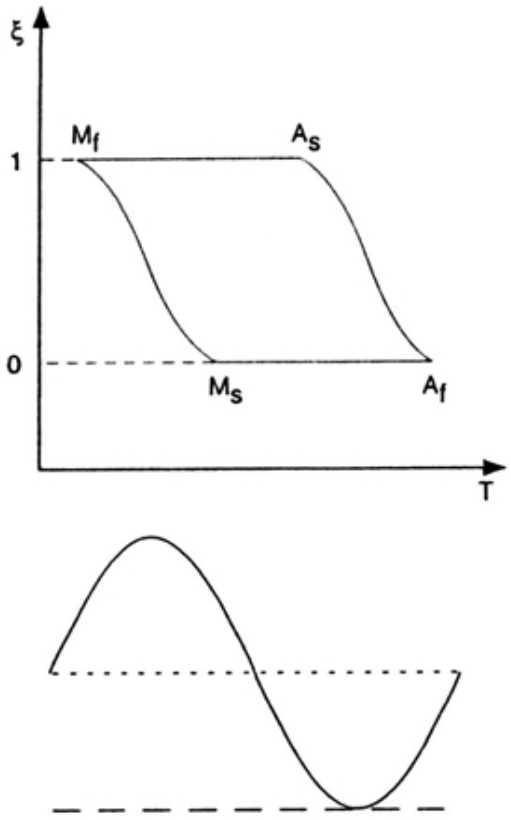

Figure 2.12: Martensite volumetric phase transformation cycle [4]

From this formulation ξ is:

Transformation A ⟶ M (Cooling)

$$\xi = \frac{1-\xi_0}{2}\cos\left[\alpha_M\left(T - M_F\right) + b_M\sigma\right] + \frac{1+\xi_0}{2} \tag{2.4}$$

Transformation M ⟶ A (Heating)

$$\xi = \frac{\xi_0}{2}\cos\left[\alpha_A\left(T - A_S\right) + b_A\sigma\right] + \frac{\xi_0}{2} \tag{2.5}$$

Where these relations are

$$\alpha_A = \frac{\pi}{A_F - A_S} \quad ; \quad \alpha_M = \frac{\pi}{M_S - M_F} \tag{2.6}$$

$$b_A = -\frac{\alpha_A}{C_A} \quad ; \quad b_M = -\frac{\alpha_M}{C_M} \tag{2.7}$$

ξ_0 is the initial quantity present.

The argument of the cosine function should be a value between 0 and π : this implies that the transformation occurs only if the temperature is within an adequate range (or within a defined stress range):

Transformation A ⟶ M (Cooling)

$$M_F \le T \le M_S \quad ; \quad C_M(T - M_F) - \frac{\pi}{|b_M|} \le \sigma \le C_M(T - M_F) \tag{2.8}$$

Transformation M ⟶ A (Heating)

$$A_S \le T \le A_F \quad ; \quad C_A(T - A_S) - \frac{\pi}{|b_A|} \le \sigma \le C_A(T - A_S) \tag{2.9}$$

In the figure 2.13 a constitutive law description is shown.

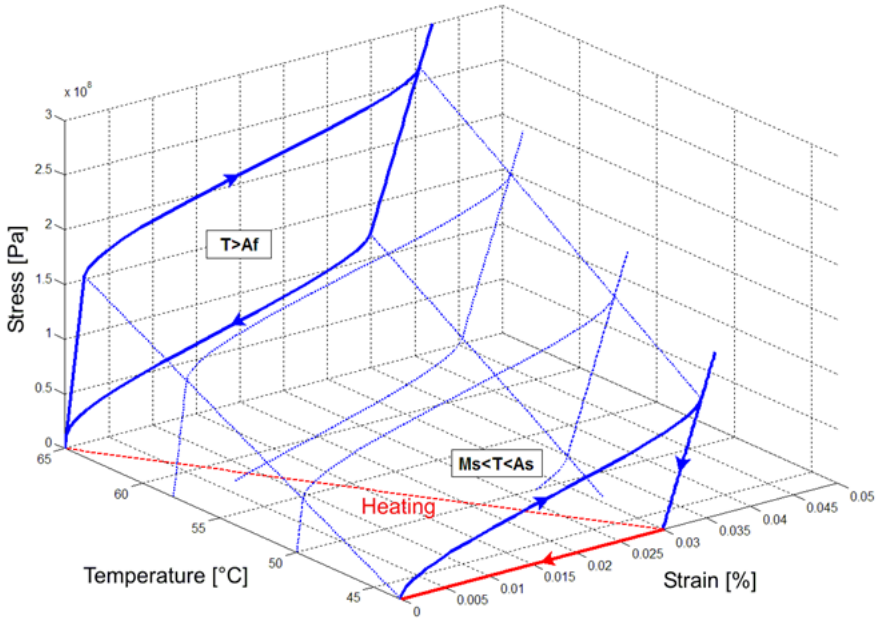

Figure 2.13: S.M.A. behaviour during heating and cooling phase.

Every case both models haven't a S.M.E. (detwinning at low temperature) representation; they describe martensite into austenite transformation and vice versa, they are valid only whenm martensite is completely determined, so, only one variable exists.

Differently from two previous models, **Brinson** model [17] represents the detwinned maertensite transformation due to tensile stress induced, so describing S.M.E. under A_S temperature.

This model a similar Tanaka's constitutive equation representation uses, introducing 0 as initial condition:

$$(\sigma - \sigma_0) = E(\xi)\varepsilon - E(\xi_0)\varepsilon_0 + +\Omega(\xi)\xi_S - \Omega(\xi_0)\xi_{S0} + \Theta(T - T_0) \tag{2.10}$$

Where martensite volumentric fraction is now didived into two parts:

$$\xi = \xi_S + \xi_T \tag{2.11}$$

with ξ_S detwinned martensite stress induced at low temperature and ξ_T twinned martensite (randomly oriented) due to reversible thermal phase transformation coming from austenite.

in addition, a cosine formulation modified for the martensite volumetric fraction, is used:

- Transformation into detwinned martensite

$$T > M_S \begin{cases} \xi_S = \dfrac{1-\xi_0}{2}\cos\left\{\dfrac{\pi}{\sigma_{cr}^S - \sigma_{cr}^F}\left[\sigma - \sigma_{cr}^F - C_M\left(T - M_S\right)\right]\right\} + \dfrac{1+\xi_{S0}}{2} \\ \xi_T = \xi_{T0} - \dfrac{\xi_{T0}}{1-\xi_{S0}}\left(\xi_S - \xi_{S0}\right) \end{cases} \tag{2.12}$$

$$T < M_S \begin{cases} \xi_S = \dfrac{1-\xi_{S0}}{2}\cos\left\{\dfrac{\pi}{\sigma_{cr}^S - \sigma_{cr}^F}\left[\sigma - \sigma_{cr}^F\right]\right\} + \dfrac{1+\xi_{S0}}{2} \\ \xi_T = \xi_{T0} - \dfrac{\xi_{T0}}{1-\xi_{S0}}\left(\xi_S - \xi_{S0}\right) + \Delta_{T\xi} \end{cases} \tag{2.13}$$

with $\Delta_{T\xi} = \dfrac{1-\xi_{T0}}{2}\left\{\cos\left[\alpha_M\left(T - M_F\right)\right] + 1\right\}$ if $M_F \le T \le M_S$ and $T < T_0$

otherwise $\Delta_{T\xi} = 0$.

Transformation into austenite

$$T > A_S \begin{cases} \xi = \dfrac{\xi_0}{2}\left\{\cos\left[\alpha_A\left(T - A_S\right) - \dfrac{\sigma}{C_A}\right] + 1\right\} \\ \xi_S = \xi_{S0} - \dfrac{\xi_{S0}}{\xi_0}\left(\xi_0 - \xi\right) \\ \xi_T = \xi_{T0} - \dfrac{\xi_{T0}}{\xi_0}\left(\xi_0 - \xi\right) \end{cases} \tag{2.14}$$

The forth model due to **Boyd & Logoudas** [18][19] is more general and it is a 3D model. in it Gibbs total specific free energy is determined by summing free energy of each S.M.A. phase and the mixture free energy.

So, a constitutive formulation according to the Second Thermodynamic Law is developed. Total strain consists of two parts: mechanical strain ε_{ij} anjd transformation strain ε_{ij}^{tr} , as function of martensite volumetric fraction:

$$\sigma_{ij} = C_{ij}\left[\varepsilon_{kl} - \varepsilon_{kl}^{tr} - \alpha_{kl}\left(T - T_0\right)\right] \tag{2.15}$$

For martensite volumetric fraction, evolutive equation is derived by dissipation potential:

$$\sigma_{ij}^{eff} + d^1T - \rho b\xi = Y^{**} + d^3_{ijkl}\sigma_{ij}\sigma_{kl} + d^4_{ij}\sigma_{ij}\Delta T \qquad (2.16)$$

where Y^{**} is the limit stress value, d^1T is related to entropy reference state, d^3_{ijkl} and d^4_{ij} are parameters linked to Young's moduli variation, ρ is density, b_1 is material constant, ΔT temperature difference.

Brinson & Huang [27] have shown that this model, at 1D level, is identical to Tanaka's model. This model is different from the Tnaka's one because it can represent the martensite transformation from twinned into detwinned at low temperature.

Another model, developed by **Ivshin & Pence** [20] is derived by thermodynamic considerations about kinetic relations for phase fraction hysteresis.

Instead of ξ as primarily variables they use α as $\alpha = 1 - \xi$.

So, total strain is: $\varepsilon = (1-\alpha)\varepsilon_M + \alpha\varepsilon_A$ where ε_M and ε_A are strain in martensite and austenite region.

After Tanaka's model formulation genesis [15] is has been updated to cover also S.M.E. influence [28] [29] [30] [31] [32] [33].First model updating called rhombohedric phase transformation (R.P.T.) or R-phase transformation has been developed.

R.P.T. is a reversible thermal transformation producing low strain and temperature as for detwinning martensite; a very low hysteresis and cyclic stability make that very interesting, so that stress-strain curve during unloading with the loading phase can be approximated. Disadvantage is the reduced strain to be obtained.

At low temperature (lower than A_S) R.P.T. takes place followed by typical martensite transformation. For repeated stress-strain cycles (strain < 1%) at ambient temperature, R.P.T. only in the first cycle can be observed and then it goes away.

This is related to a two-way shape memory effect by heating ad cooling the sample.

At higher temperature (between A_S and A_F) in small non linear region in the linear pseudoelastic curve R.P.T. can be obtained.

R.P.T. (or phase R effect) by a volumetric fraction coefficient η can be represented.

By assuming that first cycle has null strain (η=0, ξ=0), a strain less than 1% is within R phase transformation (η=1, ξ=1).

By an heating activation, R phase is recovered. In all other cases, R phase is not recoverable. By using this concept authors previews with experimental data can link, in particular at low temperature. Naito & al.[33] and Sittner & al. [32] R.P.T. and martensite

transformation have unified, by applying an energy relation with appropriate switching functions in order to manage different transformations.

Constitutive models in combination with ξ models allow to obtain stress-strain curves. Since ξ is a stress function for all models; in order to solve the mathematical problem an iterative approach as Newton-Raphson method has to be used.

In this context it is relevant to point out that Tanaka's model for ξ an exponential approach uses, so, during the iteration process, convergence problems can be presented.

Recent works have evidenced limitations in the phenomenological models. In fact, **Elahinia & Ahmadian** [34] have pointed out that in some circumstances, combining contemporary applied tension and temperature variation (that can be consequent to the physical problem) of S.M.A., model predictions are not linked to experimental tests: this happens because critical temperatures depend on applied stress and because, as assumption, the transformation only within adequate critical temperature, towards thermal cycle direction, can happen.

2.6 Transformation critical regions

In order to have a correct S.M.A: modelling, appropriate constitutive models are necessary.

These models require knowledge of some material constant obtained through diagram describing relationship between temperature and critical stress phase transformation inducing.

Even if experimental results for critic stress values during start and finish transformation in several cases provide non perfectly linear results, trend for critic stress transformations adequately as linear function of temperature can be represented.

Figure 15 shows a plot defining transformation area of interest [11].

By analyzing Tanaka's model [15] diagram, critic temperature when phase transitions occur are M_S, M_F, A_S, A_F, when null stress are assumed; vice versa considering non null stress, in order to have the phase transition, with a linear increasing, higher critic temperature need.

This is evident even if we have temperature higher than M_S : stress able to induce martensite formation, coming from austenite, according temperature grows.

By analyzing critic stress-temperature for Brinson's model [17] (containing twinned

martensite into detwinned martensite transformation), an addition area, non being in the Tanaka's model, appears. This one allows at low temperature S.M.E. modelling.

Critic stress σ^{S}_{cr} is stress of starting transformation from twinned into detwinned martensite, while σ^{f}_{cr} is critic stress when almost complete transformation happens: these stresses are determined at temperature lower than M_S and they are temperature independent. Strain when a complete martensite detwinning happens is indicated as ε_L (limit strain).

It is evident that, during the material phase transformation, it absorbs (or emits) great heat quantity with relatively small temperature variation: appropriate instrument as Perkin-Elmer D.S.C. (differential scan calorimeter) able to record such change needs.

This instrument is able to determine start and finish transformation by means of material thermal capacity measurement.

In the figure 2.14, areas signed by arrows are that where material in a pure shape (martensite or austenite) exists; in all other areas a mixture of phases take place, and exact shape depends on thermo-mechanical material history.

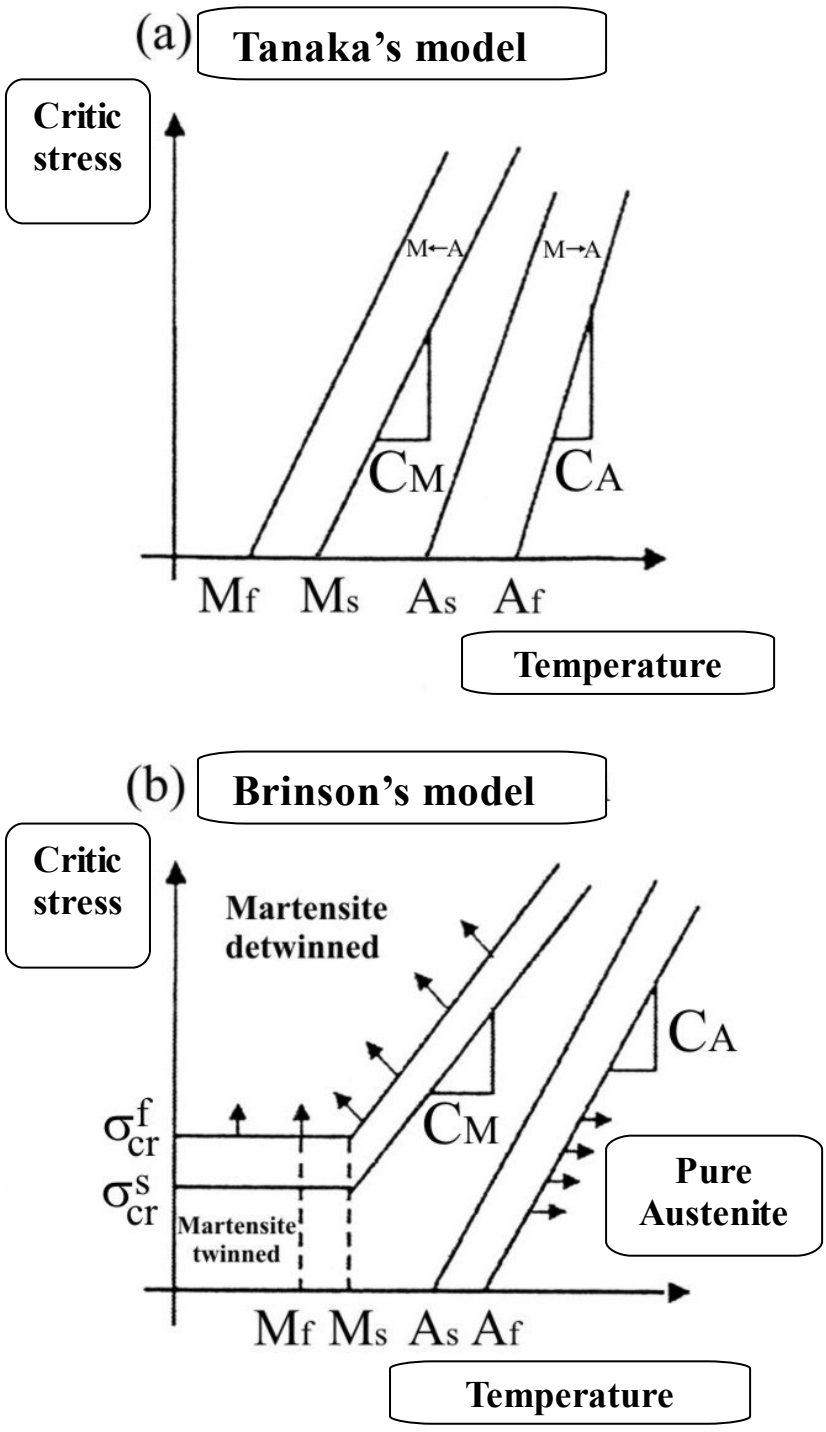

Figure 2.14: Critic stress-temperature plots in the constitutive models (a) Tanaka's model (b) Brinson's model [11].

As it is noticeable, for material constants definition (C_A and C_M as curve inclination) in various models there are some differences.

Both Tanaka's and Liang & Rogers' models [16] a linear relationship, between stress and

temperature, assume and M_S and M_F correspond without stress condition; in addition generally $C_A = C_M$, with a constant value for all temperature range.

This critic stress-temperature relationship is different in the Brinson's model because critic stress distinguishes transformation regions: now M_S and M_F are defined temperature as limit value after that no applied stress determines pure transformation from twinned martensite into detwinned one. Because of this interpretation transformation temperature are different in the two models.

In the Brinson's model M_S and M_F parameters are defined as temperature behind that martensite transformation stresses are a temperature linear function as shown in figure 2.14b. In Tanaka's and Liang & Rogers' models these parameters in null stress condition are defined and those one are start and finish martensite temperature from austenite cooling, with no stress applied (figure 14a).

So, when these constants by critic point in the diagram are experimentally calculated, numerical values used by Tanaka and Liang & Rogers for M_S and M_F through extrapolation approach of start and finish martensite temperature, with no stress applied, are obtained; on the other hand values used by Brinson are found in critic stress σ^S_{cr} and σ^f_{cr} condition.

In order to compare different models a necessary reference to calculated parameters for different conditions, so that an experimental comparison is achieved.

Prahlad & Chopra [35] have presented experimental data for stress-strain diagrams found through different tests on the same curve (figure 2.15) and they have demonstrated a linear critic stress variation with temperature as assumption in all previous models.

Data correspond to 3 different tests, all conducted with low heating velocities, so that, quasi-static conditions have been assumed.

Recovering stress points are within transformation region between austenite start and austenite finish during heating phase and between marteniste start and finish during cooling phase.

So, two straight lines are martensite and austenite start phase and they allow M_S and A_S determination; martensite and austenite finish phase have almost same inclinations and they allow M_F and A_F determination.

It is evident that if model coefficients are correctly identified coming from experimental data, all constitutive models can well predict stress-straijn behaviour at high temperature (behind A_S) [26].

Tanaka's and Liang & Rogers' models are invalid for $T<A_S$.

In fact two different methods for temperature control have been developed: the first one concerns a thermal chamber use (environmental heating), while the second one is related to internal heating (resistive heating) .

Even if similar trends exist through both methods, transformation stresses are different as result of small temperature variations (diagram moves through lower temperature for resistive heating, but inclinations are the same).

During phase transformation in the martensite a great internal resistance variation occurs [36] related to a different crystallographic arrangement of the two phases, a constant temperature value, by resistive heating technique, is quite different.

In particular, during transition if heating is very slow a control of 2°C -3°C is possible.

In order to make stable S.M.A. behaviour (so that it is constant and repeatable), material has mechanical cycles to undergone (20 - 30 cycles [37] [38]).

These cycles may be based on strain (behind A_F) at a constant temperature and may be relaxed with null stress, or they may be based on mechanical strain (martensite phase) an at ambient temperature followed by a thermal cycle with small stress, by heating martensite before A_F and then under M_F it is cooled.

Both methods have a good efficacy for material stabilization and in addition the first procedure no thermal cycles needs.

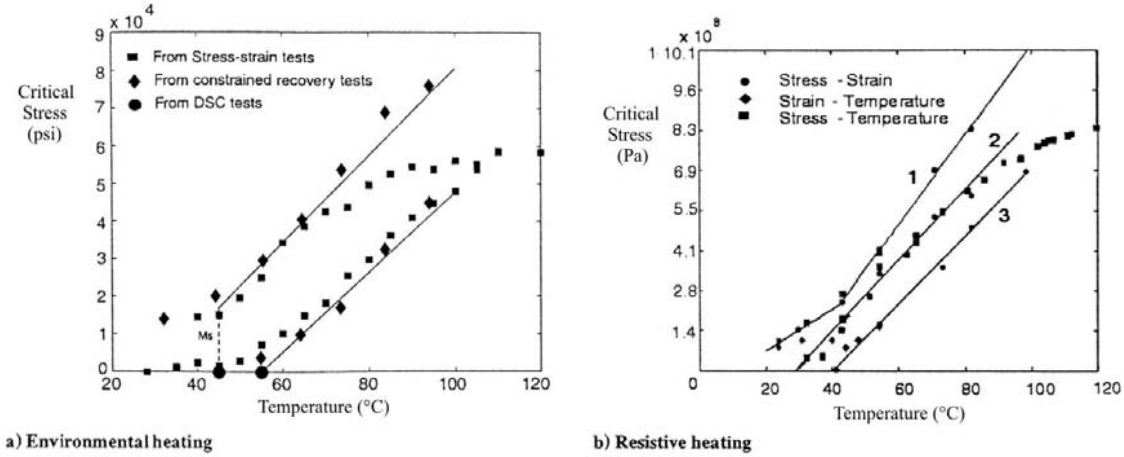

Figure 2.15: Experimental critic stress-temperature plots.

2.7 Constrained recovering behaviour

During an heating phase, when S.M.A. wires is constrained, it cannot freely recover

detwinned martensite strain in order to achieve austenite phase: in this context, large recovering stresses in the material are developed.

Figure 2.16 shows recovering stresses developed at different temperatures and at different pre-strain conditions.

Final recovering stress is independent from pre-strain only if pre-strain is higher than 2%, under this value final stresses, as the trend in the plot, depend on pre-stress.

great part of models sufficiently well predict recovering stress ion constrained cases since values are low (they have to be under plastic yield stress).

lower pre-strains provide a lower permanent plastic strain and fatigue followed by repeated cycles[36] [39].

Generally, by S.M.A. tape testing with repeatable cucles, after three cycles a behaviour stabilization is observed. Clearly this shows that S.M.A. as force actuator in repeatable loading condition can be used.

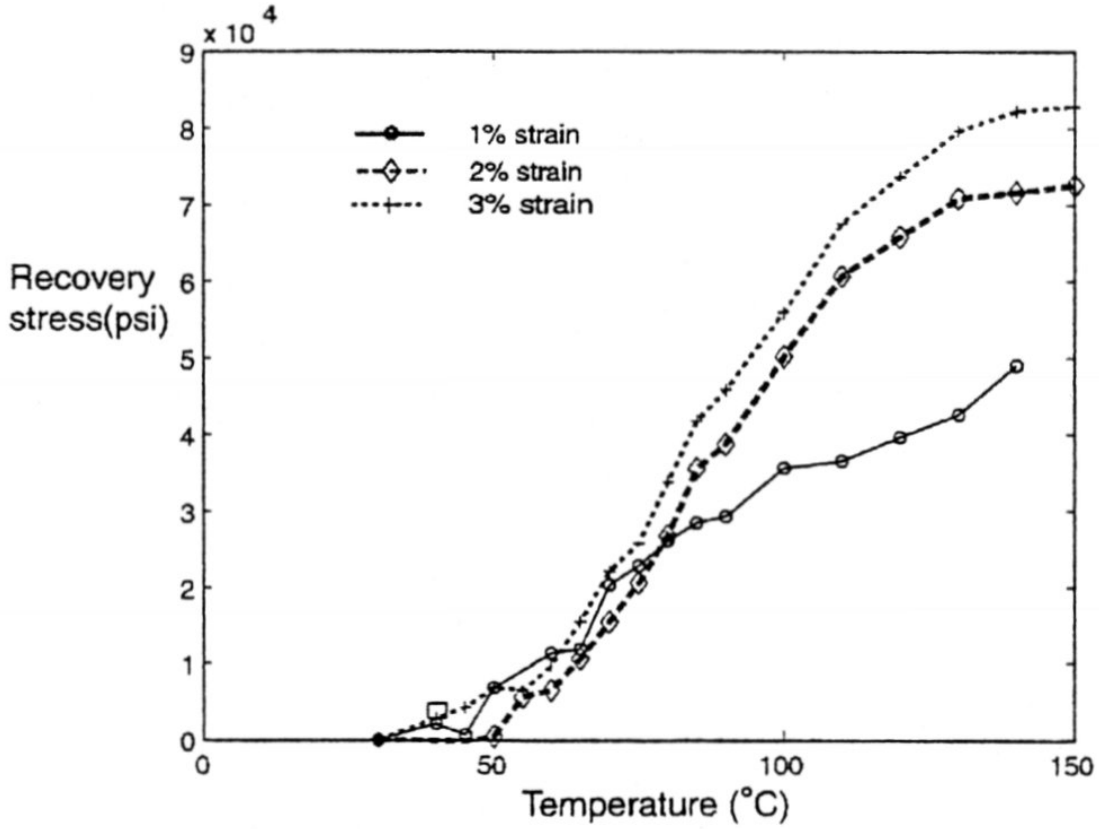

Figure 2.16:Controlled recovering behaviour with pre-strain [35].

2.8 Non quasi-static loading application

Since now a quasi-static loading application has been considered: if material at higher

temperature is deformed, it have no time to relax and as result a greater stress level can be obtained.

Stress increase could happen as result of local temperature change immediately if tape is under a non quasi-static loading. In any case, after a fast deformation if material has no time to relax, in it stresses to typical quasi static loading value come back (local temperatures can stable e come back to equilibrium values).

This phenomenon is called stress relaxation [36] [39] [40] [41].

Shaw [42] has underlined that some auto-heating effects through a local nucleation, with temperature differences along the tape, take place. It has been demonstrated that transformation stresses greatly increase as a strain velocity function as in figure 2.17.

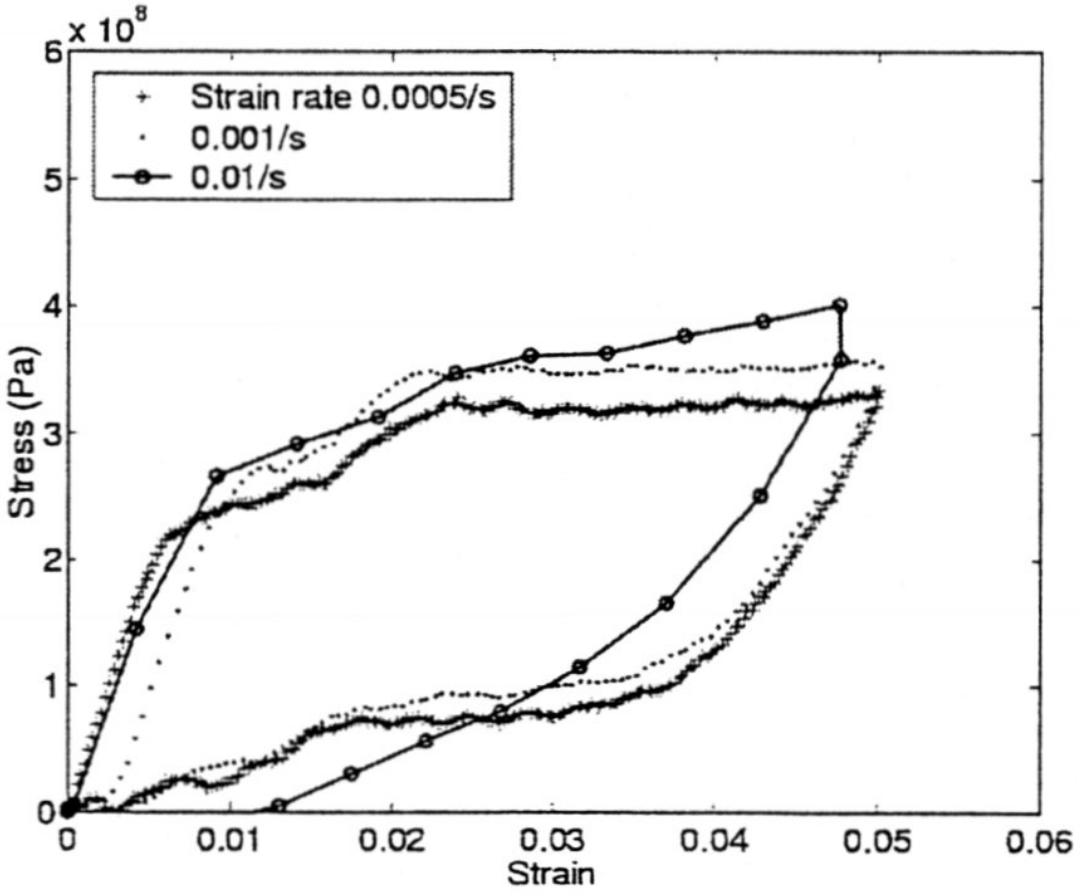

Figure 2.17:Loading velocity effect on stress-strain behaviour [35].

If loading is not continuous, S.M.A. material seems to come back to thermodynamic equilibrium (stress relaxation). This phenomenon takes place as material behaviour

dependent according to loading application method (figure 2.18).

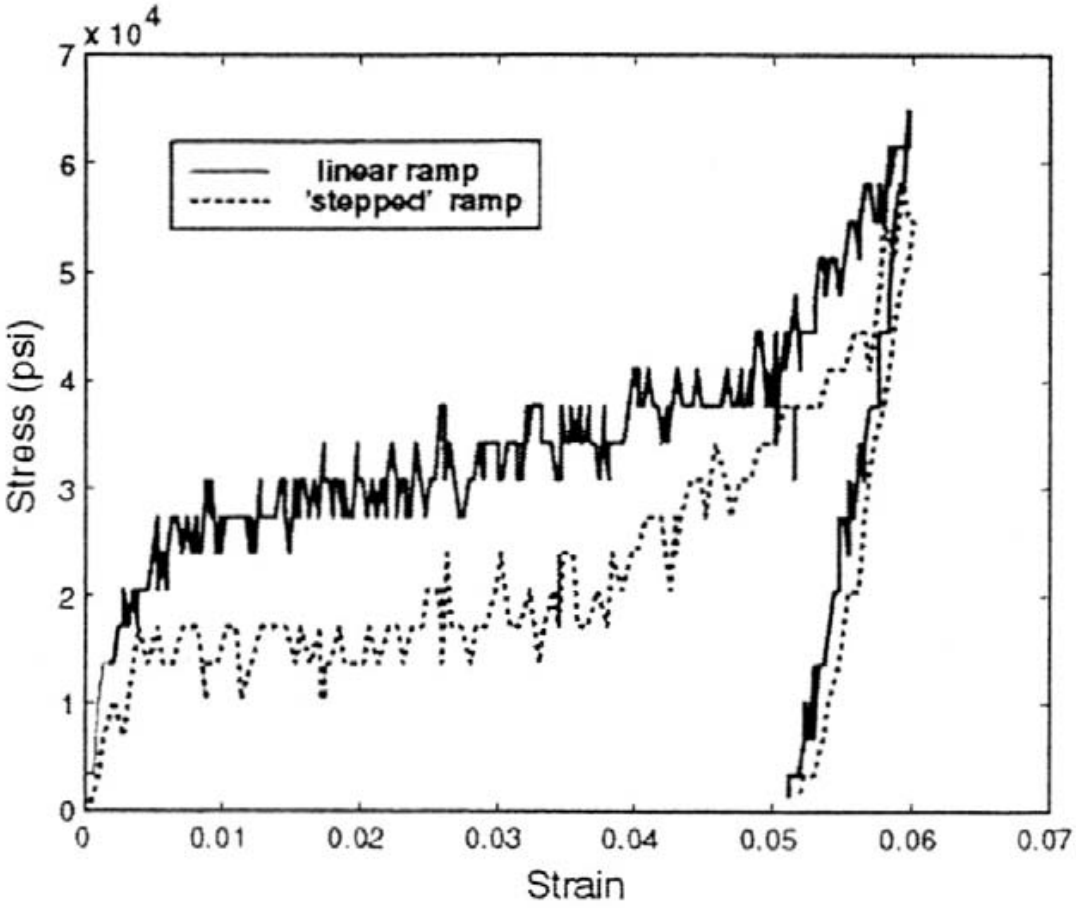

Figure 2.18:Loading application method effect on stress-strain behaviour [35].

For dynamic loading adapted constitutive models have to be developed.

Lexcellent & Rejzner [43] have determined temperature variation caused by strain velocity through the heat equation integration. Predicted results quite well to experiment data can be adapted.

Prahlad & Chopra [41] have used a variation formulation for Brinson equation coupled with analysis of energy equilibrium in order to obtain simultaneously temperature and stress as a strain function for assigned strain velocity. Predictions have shown good qualitative adaptation for temperature and stress evolution under loading condition, involving also instantaneous strain velocity change during loading cycle (figure 2.19).

In any case, additional more detailed experimental measurement about temperature for a model validation are necessary.

Potapov & Silva [44] have developed a simple model for time response for NiTi alloys

considering latent heat and thermal hysteresis of transformation during free and forced convection. It is clear that S.M.A. activation frequency is primarily controlled by necessary cooling time, while an electric power increase may reduce heating time: time response, found by model, a good adaptation to experimental data has shown.

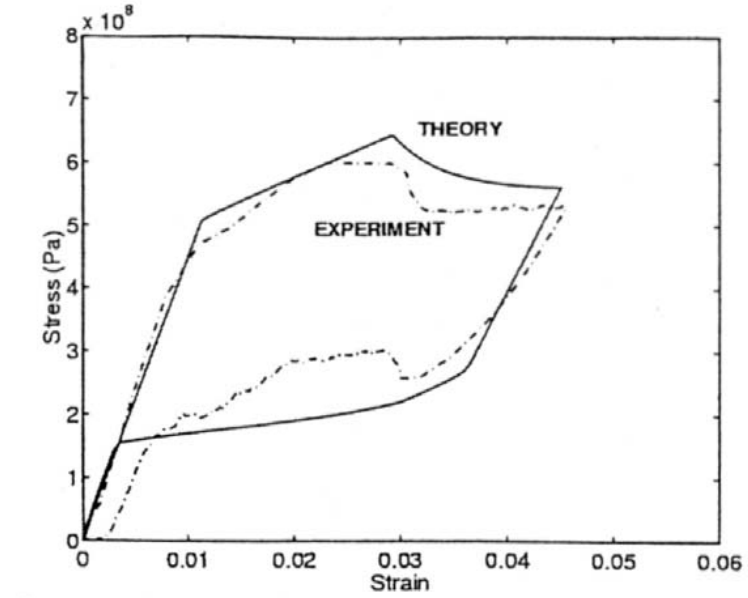

Figure 2.19:Non quasi-steady model prediction comparison with experimental data (strain applied step by step from 0.01/s to 0.0005/s until 3%) [41].

2.9 S.M.A. tubes and bars torsional features

In addition to S.M.A. tapes as actuators in 1D conditions, also S:M.A. tubes and bars as torsional actuators have been experimented.

Operation principle is the same for S.M.A. tapes; bars or tubes initially is deformed by torsional and then it leads to recover its original state with no torsional application through heating.

One of the first model was proposed by **Davidson & al.** [45]: it uses the Liang & Rogers' constitutive model [16] in combination with standard relationships for pure shear strains.

Model parameters are obtained by an accurate adaptation of required parameters of Liang & Rogers's model to experimental torsional curves.

Keefe & Carman [46] have proposed a torsional model based on Brinson's model for S.M.A. constitutive behavior description. Model parameters are found through experimental extensional tests and then to torsional case applied.

Generally, a good correlation with experimental data at constant temperature (figure 2.20a) and for torsional springs activation has been obtained (figure 2.20b).

Contrarily to these models, only concerning S.M.A. shear strain modeling, there are a lot of models completely 3D and then in theory able to include a loading application towards every arbitrary directions (also combined loads stress-twist).

An example of these models is **Boyd & Lagoudas** one [18][19].

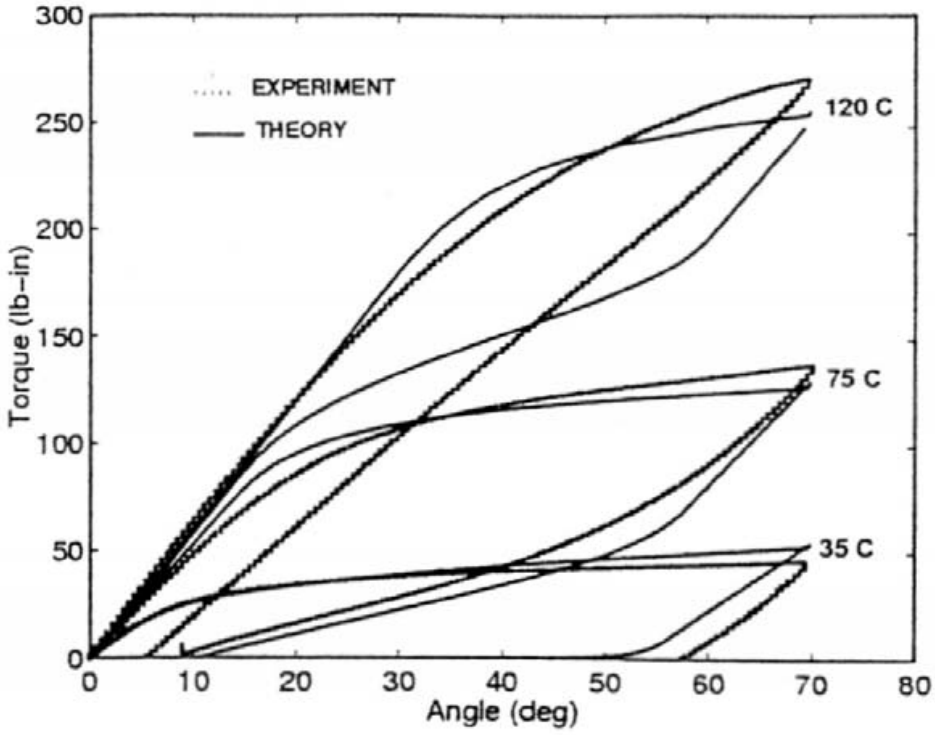

a) Constant temperature predictions

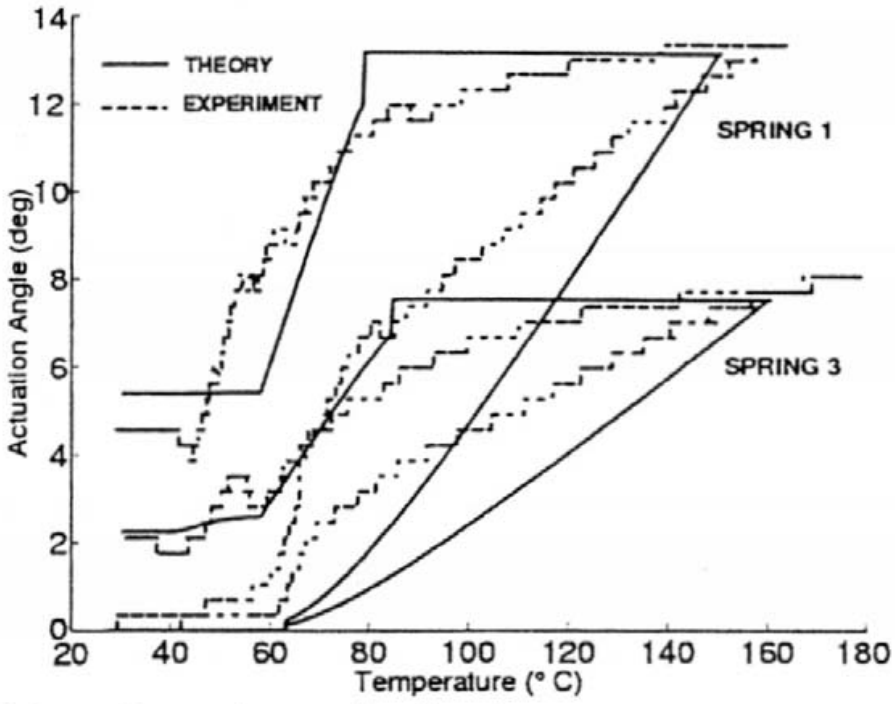

b) Actuation against torsional springs

Figure 2.20:Torsional model and experimental data comparison prediction [41].

2.10 Damping features

Until now it has been shown that S.M.A. produce pseudoelastic hysteresis on a large strain range (6-8%). Cyclic variation in stress and strain can determine a great strain energy dissipation, and this fact is translated into a damping growth [48].

Wolons & al. [49] in order to determine damping characteristics of Ni-Ti alloy tape for 1D loading an experimental investigation have conducted and systematically they have studied damping effects induced by cycles, oscillating frequency, strain amplitude, temperature static displacement due to strain.

It has been demonstrated that hysteresis cycle shape significantly changes according to frequency, energy dissipation decreases with frequency and reaches saturation value about at 10Hz; in addition, energy dissipation decreases at higher temperature and increases in accordance with static displacement due to strain [50].

Lammering & Schmidt [51] Ni-Ti alloys damping capacities into pseudoelastic range have studied too. They have demonstrated that hysteresis cycle area is reduced according to a strain velocity rise.

Ju & Shimamoto [52] in order to rise damping a composite beam with integrated S.M.A. fibres have developed; damping is a temperature and electric current function.

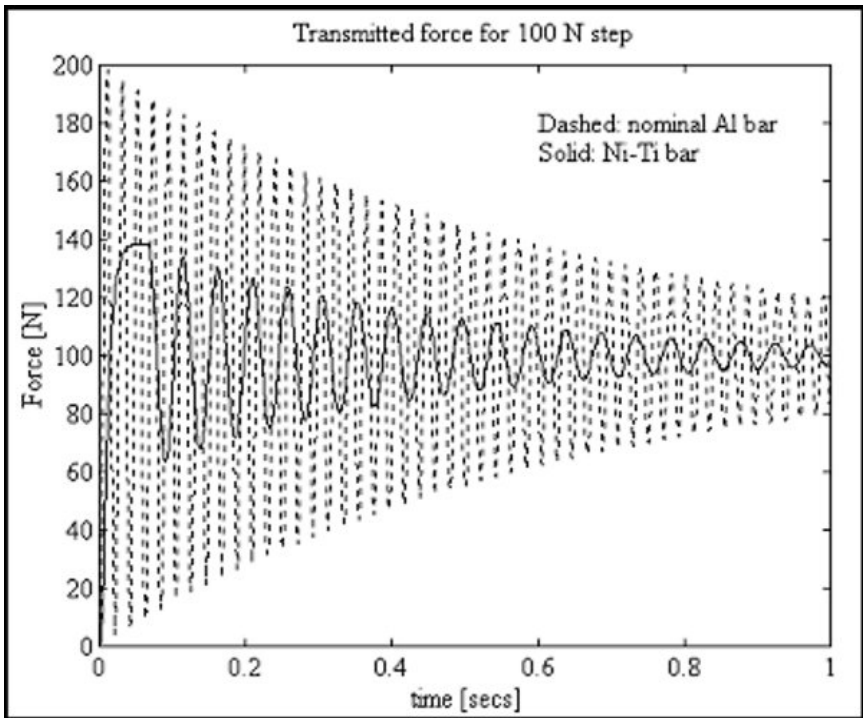

Figure 2.21: NiTiNOL bar simulated response compared to Aluminium bar of similar geometry [53].

2.11 Composite panels with integrated S.M.A. yarn

The innovative idea of an S.M.A. wires integration inside a composite laminate as active structural control at fist was introduced by **Rogers & Robertshaw** [54]: such structure S.M.A.H.C. was named, as hybrid composite with S.M.A. material.

A realization of composite structure with S.M.A. wires integrated is a hard work.

In fact, yarn surface has to be opportunely treated in order to obtain a good bonding property with composite; in addition, yarn pre-strain loss has to be prevented during the composite manufacturing procedure (generally at high temperature).

In order to solve this problem three possible approaches exist.

The fist one concerns a special composite use able to be wrapped at ambient temperature, keeping away from S.M.A. critic temperatures.

The second one consists of separately fastening each S.M.A. yarn during the manufacturing process in the autoclave.

The third one, during the manufacturing process and instead of S.M.A. wires, opportune silicon small tubes filled with temporary steel wires. When the process is over steel wires are substituted with pre-strained S.M.A. wires: in order to assure a sufficient seal between silicon tubes and epoxy resin-graphite composite an adhesive film can be used.

S.M.A. wires have been used to have a natural frequency alteration in composite beams, in order to achieve that the natural frequency goes away from resonance due to an harmonic or periodic excitation and/or to have a frequency range without resonance (without natural frequencies).

Rogers & Barker [55] have demonstrated a composite beam natural frequencies increase through the activation of S.M.A. wires directly integrated inside the structure: during wires heating beam was subjected to axial force caused by shape memory effect. They have shown a natural frequency increase of 200% in graphite-epoxy resin beam, by using a volumetric fraction of 15% for S.M.A. wires.

Baz & al. [56] have conducted a study about active control on flexible beams vibrations through S.M.A. wires mechanically constrained outside the structure, taking advantage of recovering force at high temperature provided by pre-strained wires.

Obviously, in such applications, extremely important is the outside structure accessibility and then on it to fasten the wires, for several use in aerospace field or on aerodynamic exposed surfaces this approach is not applicable.

In another study, **Baz & al.** [57] have inserted S.M.A. wires inside flexible beams by

using sleeves in order to control vibration and buckling behavior.

They have used a Finite Element Method (F.E.M.) to correlate experimental results: they have demonstrated that in a flexible composite (glass fiber) beam buckling load can be increased three times in a controlled case with respect to a non controlled one.

Brinson & al. [58] have investigated active control for beam deflection by means of a single S.M.A. yarn bonded on the surface, activated by temperature. Potential control of shape through S.M.A. wires has been evidenced.

Lagoudas & al. [59] have used a layered shear strain theory in order to demonstrate shape control for plate structures always by means of S.M.A. wires.

Turner [60] has developed a F.E.M. formulation in order to predict thermo-mechanical response for hybrid composite and S.M.A. structures with free and constrained boundary conditions. The model is able to reproduce material non linearity with temperature.

Epps & Chandra [61] have tested solid beams in graphite-epoxy resin with S.M.A. wires integrated inside small ducts in order to verify vibration frequencies with constrained boundary conditions.

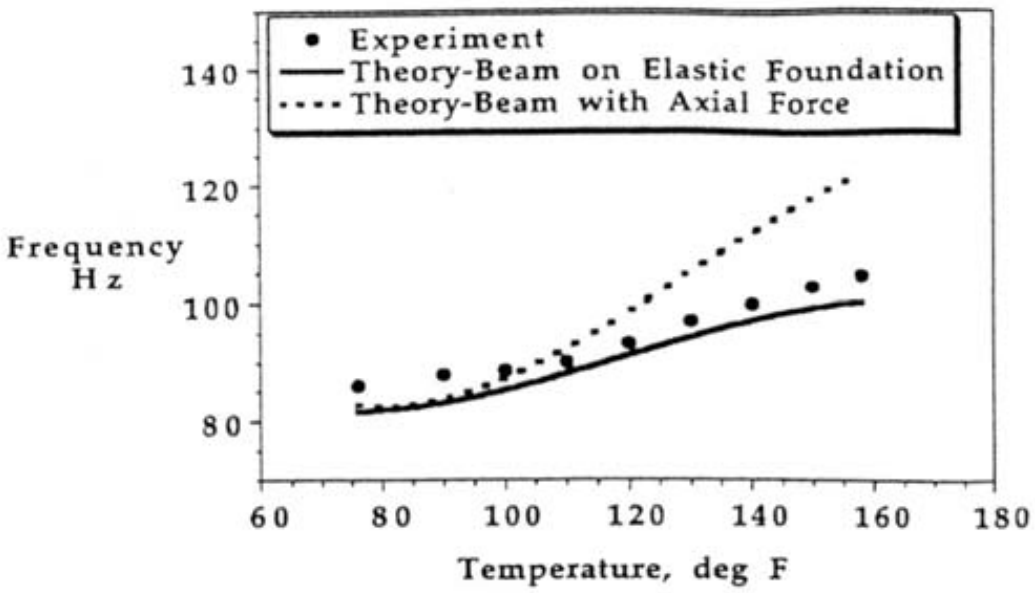

Figure 2.22: Fundamental frequency for constrained –constrained beam in graphite epoxy resin activated by S.M.A. yarn with 20mm diameter. Beam dimensions. Length=18in (45.72cm), width00.25in (6.35cm) thick=0.068in (0.173cm) [61].

They have proved that natural frequencies not only depend on beam characteristics, but

also on S.M.A. properties (stress carried out during constrained strain recovering phase depending on pre-strain, on alloy mechanical properties and temperature).

Figure 2.22 shows the first vibration frequency in a composite beam activated by a S.M.A. yarn of 20mm diameter.

This plot shows a rise of 22% for the beam deflection fundamental frequency, with a S.M.A. volumetric fraction of 2%: a good correlation between theory and experimental data has been achieved.

A similar work has been developed at C.I.R.A. by **Diodati & al.** [62], developing a numerical model for the behavior simulation of a composite $[\pm 45^{G}_{3}]_{S}$ with glass fiber laminates and epoxydic matrices, with S.M.A. wires integrated through small ducts inside the medium laminate.

So, natural frequency variation in the composite panel, according to change of S.M.A. wires number and their temperature fluctuations (figure 2.23), has been verified.

Furuya [63] has studied design and material choice for development of composite with S.M.A. integration. He has proposed two concepts. The first one is related to development of a composite with aluminum matrix and Ti-Ni fibers, the second one concerns the use of a composite with plastic matrix and Ti-Ni fibers.

The first one a tension resistance (yield stress) and a fatigue resistance has shown, the second one a fracture resistance e vibration damping increase has shown.

Birman [64] a micro-mechanical analysis of composite with integrated S.M.A. wires structure has presented.

Bisagni & Sala [65] by microscope and through thermal analysis S.M.A. wires presence inside the composite (in terms of thermal damage due to wires activation, reduced stress transfer capacity between fiber and matrix) have evaluated. In particular they have investigated laminates with epoxydic matrix and carbon or aramidic fibers. Results haven't shown negative effects or alterations in composite mechanical behavior.

In addition, they have evaluated also composite panel behavior activated by S.M.A. wires in free and buckling compression conditions, showing, in this last case, only little variations with respect to panel behavior with no activation.

Gao & al. [66] instead of that have proposed to use S.M.A. wires integrated inside a composite panel with metallic matrix in order to repair eventual crack inside the matrix followed by tension load (figure 2.24).

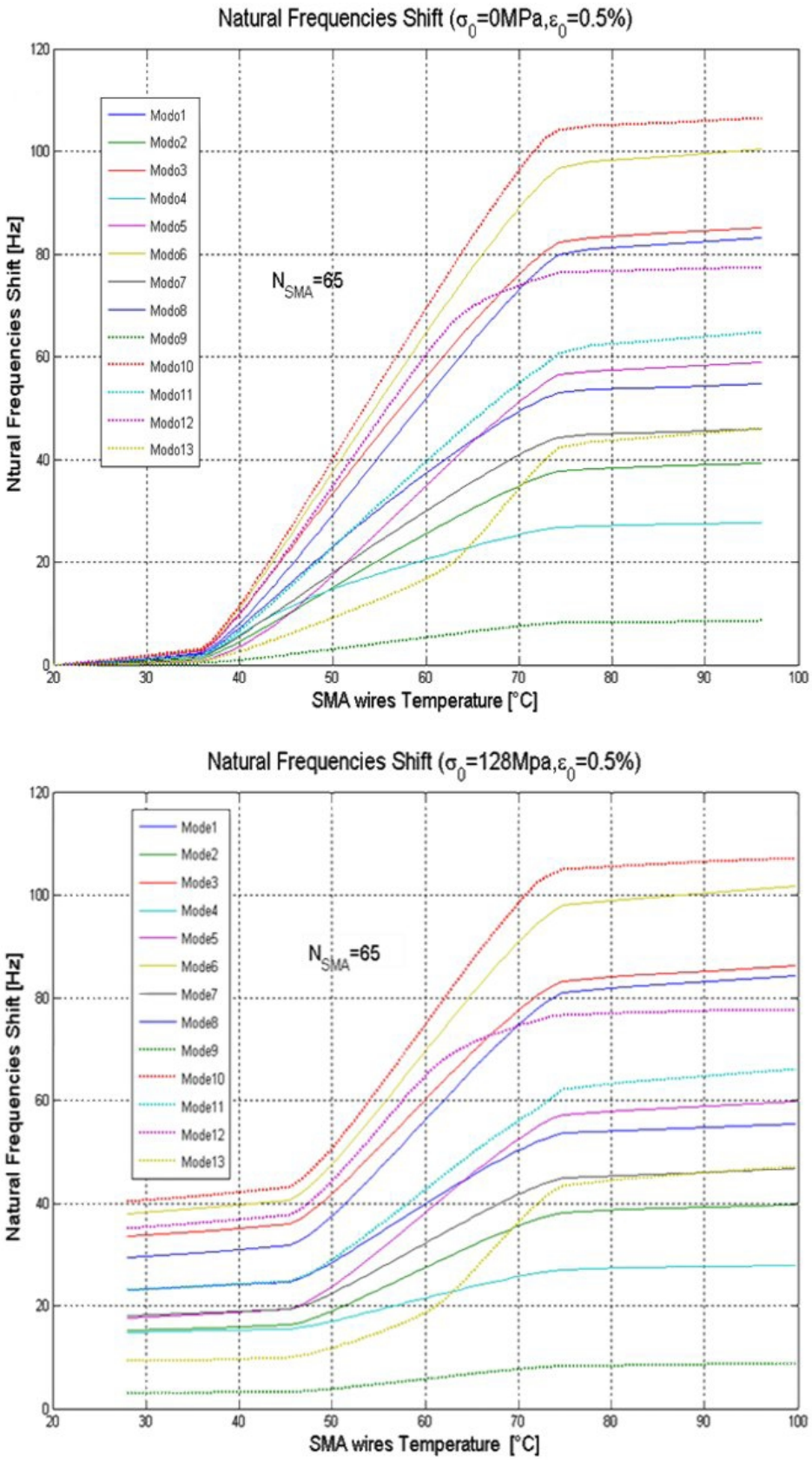

Figure 2.23:Natural frequencies variations with S.M.A. wires temperature [62].

By this approach a panel able to “auto-repair” through S.M.A. activation may be realized. In addition, they have evaluated different behavior if wires are subjected to a pre-existing strain or to a tension load-induced strain.

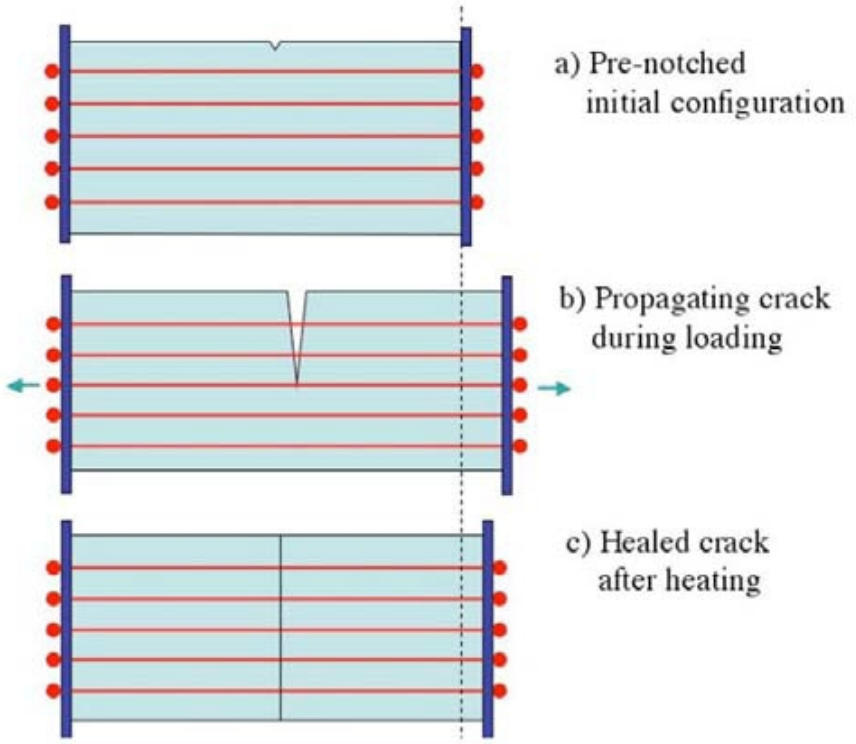

Figure 2.24: Metallic matrix composite panel reinforced with S.M.A. wires [66].

2.12 S.M.A. junction techniques

A lot of applications using S.M.A. require that S.M.A. elements are bonded to other S.M.A. elements or to composed parts of different materials.

Possibility of such aggregation is not always so simple and then, the junction technique to be used has to be chosen too.

There are four fundamental methods for Ni-Ti alloy bonding.

- *Fusion welding without binding metal*

In order to bond a Ni-Ti alloy with itself one of the well known methods for fusion welding can be used: by means of laser [67], plasma, electron stream, electric arc, etc.; welding can simply happen by contact or by a compression of elements to be bound during cooling, so that eventual cracks due to impurity (typical for commercial alloys) are eliminated.

However, such techniques are no acceptable during a Ni-Ti alloy conjunction with other materials, for example steel, because local inter-metallic alloys should be as TiFe very fragile where the welding has taken place [68].

In order to obtain welding without oxide or other substances able to damage the alloy, in fact, because of high reactivity of titanium an inert atmosphere, clean or under vacuum is necessary.

In several cases, after the junction, Ni-Ti alloys can require a thermal treatment for reducing stresses in the bonding zone. It is important to highlight that area affected by thermal treatment (T.A.Z.) in a lot of cases is not able to exhibit pseuelastic effect expected by S.M.A. materials.

Another techniques is based on a **diffusion junction** of metals at solid state, without fusion. In such case, in order to avoid inter-metallic alloys, an intermediate layer, composed of appropriate metal, is used [69].

Junction techniques between titanium alloy and steel have been experimented based on the use of **explosive** [70], so to generate a shock wave and bind interface materials (explosive choice and quantity determine detonation and collision velocity, by varying in consistent way binding quality obtained), or by **rubbing** [71], heat generating and determining a plastic flux of material towards interface.

- *Soldering with binding metal*

Soldering can be efficacy during the Ni-Ti alloy junction with steels and other materials.
This junction method is preferred because it prevent thermal degradation of pseudoelasticity. In fact, when Ni-Ti alloys are heated until 500°C (as during direct welding), they have no more their pseuelasticity, requiring thermal treatment for recovering [70]; welding happens at about 426°C it doesn't present particular problems.
However, surface oxide formation (impacting on anti-corrosive alloy capacities and it makes that also extremely difficult to welded) has to be prevented.
Some producers have found extremely effective using welding techniques similar to aluminium welding, based on **halogen substances**: however, in 1993 this method has been patented by Cook Industries [72].
After this an always growing market demand for an effective solution for Ni-Ti alloy welding, S.M.A. Inc. Has developed a proprietary blend (purchasable on licence), known as Nitinol Flux 400 (tm).
A method able to solve the low weldability for Ni-Ti alloys can be to proceed by **plating** of the alloys through other metals more easily weldable: experiences in this way has been positive for covering Ni-Ti alloys with Nickel through electrolytic process, in order to rise further on welding possibility, a second layer of noble metal can be arranged, for example silver. Primarily problem connected to this technique is its difficult of application: in fact, it is necessary to proceed with an appropriate preparation for the alloy to be covered, in particular in order to eliminate surface oxide; often covering happens step by step, and this makes this process very expensive.
In addition, other problems are associated to stowage and utilization of chemical substances involved in the work.
In order to avoid oxide also **ultrasounds welding** has been experimented, obtaining excellent results [73]. Ultrasounds welding concept has not focused a great attention until it has been successfully used for heat exchangers in aluminium alloy realization.
It is based on the same principle of ultrasounds clean. In the melted metal used for welding is introduced a high frequency vibration (about 20kHz) that induce the cavitation phenomenon with consequent strong erosion of surface to be welded (figure 2.25), so that surface oxides are dispersed.
Junction resistance so realized is comparable to traditional welding, deleting cleaning of

welding residuals.

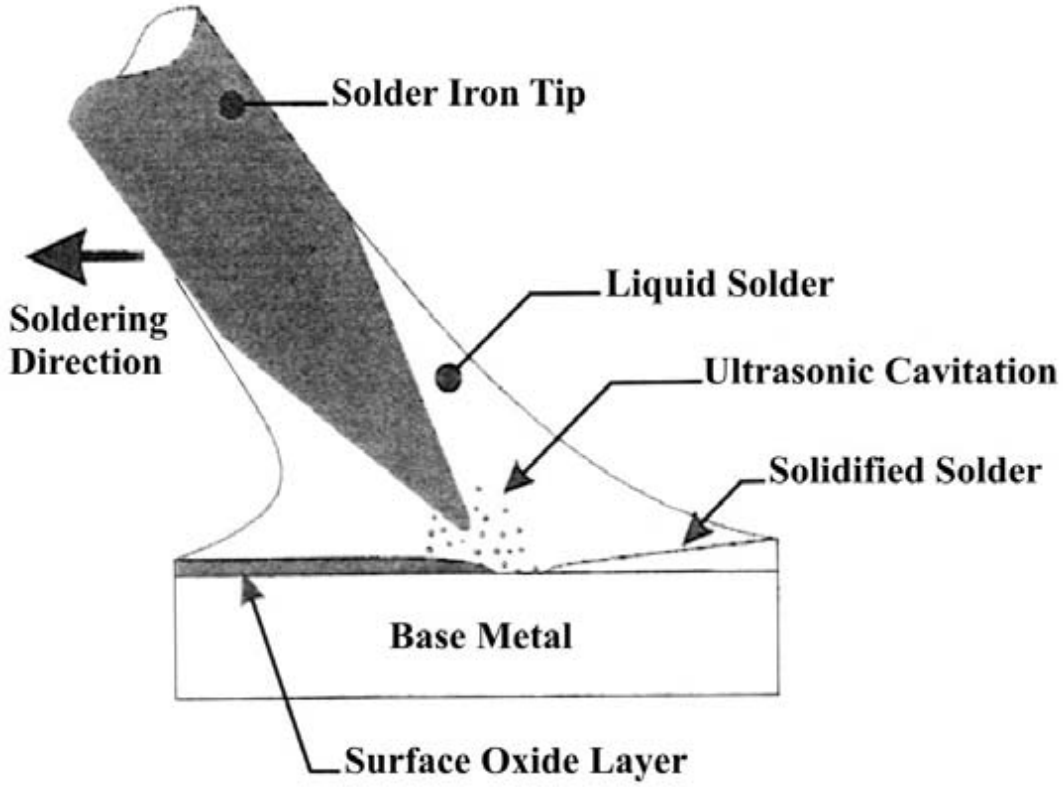

Figure 2.25: Ultrasounds welding [73].

- *Adhesive and epoxy resin*

A lot of epoxy resins and adhesives have been positively used in several applications in order to bond Ni-Ti alloys with themselves and with other materials.

The choice has to take into account compatibility with manufacturing techniques of the system and with the environment it will be in.

- *Mechanical joining*

Crimping is maybe one of the most usable techniques, however Ni-Ti alloys have a very limited ductility, so that it is necessary to point out for a non excessive deformation of material or to induce cracks in it.

Another method is based on the mechanical interference or on fastening among components. Also in this situation a great attention has to be pointed out for the deformation level of the alloy and for dimensional tolerances.

Because of manipulating difficulties for the alloys, with great attention the possibility to work Ni-Ti materials, through spinning and beating, has to be considered.

2.13 S.M.A. properties and other 'smart' materials

In this paragraph shall be summarized some of the fundamental properties of engineering interest about S.M.A. materials: following tables represent an additional examination of that already presented in para.2.1.

It has to be considered that S.M.A. properties can have a great variability caused by different possible chemical compositions and by different thermal treatments an alloy is subjected to.

In table 2.5 there is a comparison among different alloy typology included S.M.A. related to some fundamental characteristics.

Metal	Specific Damping Capacity (%)	Yield Strength (10^3 psi)	Density (g/cm^3)
Magnesium (wrought)	49	26	1,74
Cu-Mn alloys (Incramute, Sonoston)	40	45	7,5
Ni-Ti alloy (NiTiNOL)	40	25	6,45
Fe-Cr-Al alloy (Silentalloy)	40	40	7,4
High-C gray iron	19	25	7,7
Nickel (pure)	18	9	8,9
Iron (pure)	16	10	7,86
Martensitic strainless steel	8	85	7,7
Gray cast iron	6	25	7,8
SAP (aluminum powder)	5	20	2,55
Low-carbon steel	4	50	7,86
Ferritic stainless steel	3	45	7,75
Malleable, nodular cast irons	2	50	7,8
Medium-carbon steel	1	60	7,86
Austenitic stainless steel	1	35	7,8
1100 Aluminum	0,3	5	2,71
Aluminum alloy 2024-T4	< 0,2	47	2,77
Nickel-base superalloys	< 0,2	Range	8,5
Titanium alloys	< 0,2	Range	4,5
Brasses, bronzes	< 0,2	Range	8,5

Table 2.5: Comparison among various alloy properties [3].

In table 2.6 some S.M.A. properties are presented (Ni-Ti, Cu-Zn-Al, Cu-Al-Ni).

Physical Properties	Ni-Ti	Cu-Zn-Al	Cu-Al-Ni
Density (g/ m³)	6,4	6,45	7,64
Resistivity (μΩ cm)	80 ÷ 100	8,5 ÷ 9,7	11 ÷ 13
Thermal Conductivity (W/m K)	10	120	30 ÷ 43
Heat Capacity (J/kg K)	390	400	373 ÷ 574
Mechanical Properties	**Ni-Ti**	**Cu-Zn-Al**	**Cu-Al-Ni**
Young's modulus (GPa) (parent phase)	83	72	85
Young's modulus (GPa) (martensite)	34	70	80
Yield Strength (MPa) (parent phase)	690	350	400
Yield Strength (MPa) (martensite)	70 ÷ 150	80	130
Ultimate Tensile Strength (MPa)	900	600	500 ÷ 800
Transformation Properties	**Ni-Ti**	**Cu-Zn-Al**	**Cu-Al-Ni**
Heat of Transformation (J/mole) (martensite)	295	160 ÷ 440	310 ÷ 470
Hysteresis (K) (martensite)	30 ÷ 40	10 ÷ 25	15 ÷ 20
Recoverable Strain (%) (One-Way martensite)	8	4	4
Recoverable Strain (%) (Two-Way martensite)	3	2	2

Table 2.6: S.M.A. properties [3].

Among all S.M.A. a particular attention is towards Ni-Ti alloys until their discovery these materials have caught interest for better thermo-mechanical properties, lower manufacturing costs (with respect to original Ag-Cu alloys)and, today they are the most widespread in commercial field.

In table 2.7 typical properties of engineering interest for a Ni-TiNOL alloy have been reported: these properties are as a guideline because they can be affected by variations due to single producers according to motivations before stated.

Transformation temperatures and strains	
Transformation temperature range	-200* ÷ +110 °C
Transformation enthalpy	0,47 ÷ 0,62 kJ/Kg K
Transformation strains: up to 1 cycle	up to 8 %
" up to 100 cycles	up to 5 %
" up to 100.000 cycles	up to 3 %
" above 100.000 cycles	ca. 2 %
Thermal hysteresis**	30 ÷ 80 °C
Latent Heat of Transformation	5,78 cal/g

Physical properties	
Melting point	ca. 1310 °C
Density	6,45 kg/dm^3
Thermal conductivity of the Martensite	ca. 9 W/m K
Thermal conductivity of the Austensite	ca. 18 W/m K
Electrical resistivity	50 ÷ 110 μΩ cm
Linear thermal expansion factor α of the Martensite	ca. 6,7 e-6 1/K
Linear thermal expansion factor α of the Austenite	10 ÷ 11 e-6 1/K
Corrosion properties and biocompatibility	excellent
Specific Heat	0,20 cal/g °C
Magnetic permeability	< 1,002
Magnetic susceptibility	3,0 e+6 emu/g

Mechanical Properties	
Young's modulus of the Austenite	ca. 70 ÷ 80 GPa
Young's modulus of the Martensite	ca. 23 ÷ 41 GPa
Ultimate tensile strength (cold worked condition)	up to 1.900 MPa
Ultimate tensile strength (fully annealed condition)	ca. 900 MPa
Elongation to fracture	15,5 %
Plateau stress Martensite	70 ÷ 200 MPa
Plateau stress Austenite	200 ÷ 650 MPa
Yield stress Austenite	550 ÷ 700 MPa
Yield stress Martensite	~100 Mpa
Transversal contraction factor (Poisson's ratio)	0,33
Tensile strain (fully annealed)	20 ÷ 60 %
Tensile strain (cold worked)	5 ÷ 20 %
Hot workability	reasonable
Cold workability	difficult (work hardening)
Machinability	very poor

Table 2.7: Typical Ni-Ti alloy properties [74].

* Too low transformation temperature can be easily achieved by increasing Nickel percentage: this makes material very fragile.

** Hysteresis evaluated on complete loading –unloading cycles. For partial cycles hysteresis decreases.

S.M.A. are included in the 'smart' materials family, as all materials able to modify their mechanical behavior in response to appropriate external excitations.

Apart from S.M.A. in the following ferromagnetic or magnetic S.M.A. (indicated as **F.S.M.A**. or **M.S.M.A.**) shall be discussed.

They are characterized by the presence of perromagnetic metals, allowing activation by means of alloy magnetic fields: main advantages with respect to S.M.A. is higher activation frequency for these alloys, however, first practical application are still in an experimental phase.

Also well known and used in commercial field are **piezoelectrics**.

They are materials subjected to strain when an electric field around them is applied and, vice versa, they produce electric voltage is a strain is applied too; so they as actuators or sensors may be used.

However, there is a distinction from S.M.A.: they have a large activation frequency range that they are able to generate, even if strain are very limited.

Piezoelectric materials are relatively linear (for low electric field values) and bipolar, bt they exhibit hysteresis. The most widespread piezoceramic is P.Z.T. (lead zirconate titanate) and it is commercially available as thin plates able to be bonded or integrated in the structure to be controlled or assembled to create discrete actuators (able to apply higher forces but small displacements).

These thin plates produce isotropic strains: however it is possible to produce induced directional strains by using particular techniques (piezoceramics with special shapes, appropriate piezoceramic dispositions, etc.)

Piezoelectric polymeric film as P.V.D.F. (Polyvinylidenefluoride) is widespread.

Electro-strictive materials exist similar to piezoelectrics with almost same properties to produce strains. They are activated through an electric field, but they are very sensitive with temperature. They exhibit negligible hysteresis and they are a non linear relationship between applied field and induced strain.

A common ceramic electrostrictive material is P.M.N. (lead magnesium niobate).

Magneto-strictive materials are subjected to deformation if they are exposed to a magnetic field. They are monopolar materials non linear and they exhibit hysteresis; they allow forces and moderate strain generation within a wide frequency range.

The most widespread material is TerFeNOL-D. the name has in it the element constituting the material as terbium, iron and dysprosium and the name of the laboratory that

discovered it (Naval Ordnance Laboratory NOL).

In table 2.8 main differences between 'smart' materials discussed are summarized. Different properties of each material allow preferred use of each one for various application fields.

Actuator	PZT-5H	PVDF	PMN	TerFeNOL-D	Ni-TiNOL	NiMnGa
Type	Piezoceramic	Piezofilm	electrostrictive	magnetostrictive	S.M.A.	S.M.A.
Free strain (μ strain)	1.000	700	1.000	2.000	60.000	40.000
Young's modulus (10^6 psi)	10	0.3	17	7	4 ÷ 13	4
Band width	High	High	High	Moderate	Low	Moderate
ε_{max} for aluminum beam (t_{beam}/t_{act}=10)	350	10	500	580	8.500	/
Behaviour	Linear	Linear	Non-linear	Non-linear	Non-linear	Non-linear

Table 2.8: 'Smart' material comparison [11].

Figure 2.26 presents analogous data from Midè Technology Corporation [53]

	PZT 5H	PVDF	PMN	Terfenol D	Nitinol	PowerAct™
Actuation Mechanism	Piezo-ceramic (31)	piezo film	electro-strictive	magneto-strictive	shape mem. alloy	Conformable piezo-electric composite
Max Strain	0.13%	0.07%	0.1%	0.2%	2%-8%	Call
Modulus, GPA	60.6%	2	64.5	29.7	28 m, 90 a	Call
Density, kg/m3	7500	1780	7800	9250	7100	Call
Actuation Energy Dens	6.83	0.275	4.13	6.42	252-4032	Call
Hysteresis	10%	>10%	<1%	2%	High	Call
Temp Range	-20 to 200C	-70 to 70C	0 to 40C	-20 to 180C	-100 to 200C	0 to 200C
Bandwidth	100 kHz	100 kHz	100 kHz	<10 kHz	<5 Hz	>10 kHz

Figure 2.26: 'Smart' material comparison [53].

2.14 S.M.A. applications

In this paragraph a brief description of some applications today available or in an experimental phase, involving S.M.A. use, shall be provided.

Application and use of these metallic alloys are rapidly spreading even if manufacturing costs are quite high. They are commercially available in different typology, generally wires, sheets with reduced dimensions (wires of 30 μm and sheets of 50 μm thick).

S.M.A. materials have different behaviors, related to shape memory effect and pseudoelasticity, so that applications may be divided into two categories.

- *Applications with pseudoelastic effect*

In this context are included all applications requiring high flexibility: Ni-Ti alloys, with a pseudoelasticity 10 times higher than steel one, are the best.

In para. 2.3 an example of a frame for a glass has been proposed. In practice, a lot of antennas for mobile phone are composed of wires of this type of material.

But in particular a field where S.M.A. have determined a real revolution is the biomedical field. In fact, applications include simple wires in orthodontic field, aortic stent as permanent system after surgery, or angioplasty and system for connection of cervical column.

In all cases these systems take advantages of the particular mechanic response of S.M.A. wires, because during loading phase (as seen in para.2.3) a region (due to phase transformation) appears, where by a strain increasing there is no stress growth; during unloading phase a similar situation happens.

These pseudolestic “plateaux” makes possible a very large material deformation (6-8%) without a perception of material resistance increase.

By this the possibility to apply *orthodontic wires* for recovering large tooth deformations with no pain for the patient and by the application of a low an progressive force, clinically more efficient with respect to the great response provided by old steel wires (figure 2.27).

Figure 2.27: S.M.A. application in orthodontic field [74].

In the same case, in a very large surgery instrumentations (for example endoscopies, cateteries [75]) in particular in the mini-invasive surgery field it is possible to apply elements that, even if are subjected to great deformations, as those ones required for coming through small vases or for rotating into body cavities, don't develop high forces and don't maintain permanent deformations (figure 2.28).

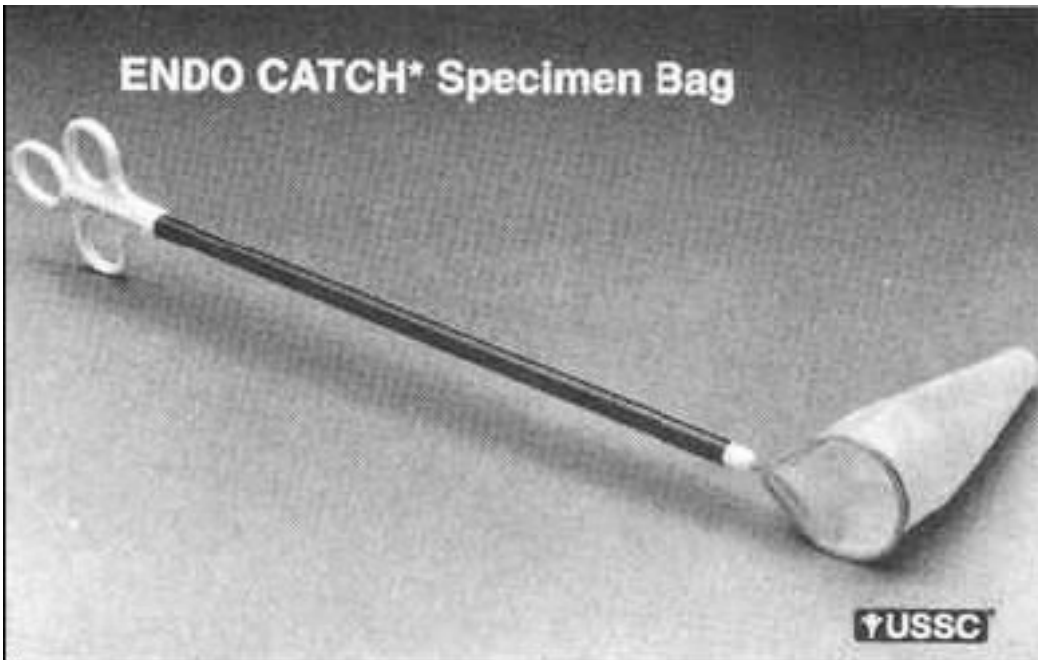

Figure 2.28: S.M.A. surgery instrument [74].

For aortic stents (as cylindrical nets aiming at preventing arteries restrictions), in order to locate them, they are reduced to a smaller diameter than the one that the vase; when positioned, shape memory allows to dilate artery walls (figure 2.29).

Figure 2.29: S.M.A. aortic stents[76].

- *Applications with shape memory effect*

In this case, different typology of shape recovery has to be taken into account.

Free recovering : no constrains.

Fundamental applications are in the "gadgets" field and in developing of logo or small devices remembering the preordered shape, generally through simply heating at temperature a little bit higher than ambient one.

Another typical application is thermostats.

Free recovering of S.M.A: also in aerospace field has been used in order to design "zippers" for solar arrays deployment (figure 2.30) in the L.F.S.A. (Lightweight Flexible Solar Array) project, of AFRL (Air Force Research Laboratory) flying on the NASA EO-1 (Earth Observing-1) satellite [77].

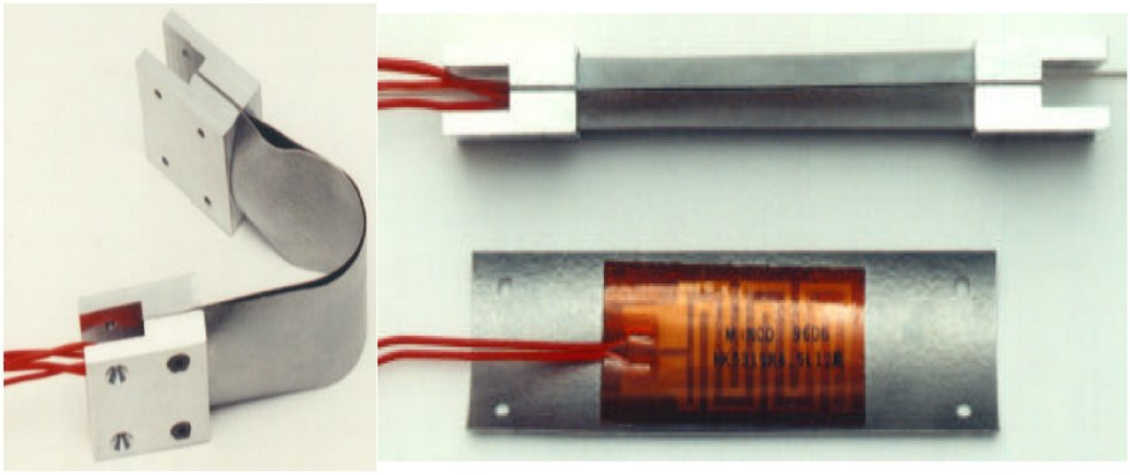

Figure 2.30: S.M.A. zipper for solar array deployment on EO-1 satellite [77].

Constrained recovering: recovering prevented by a non-yielding constrain

This has been one of the first field where S.M.A. have been successfully used technically and commercially. Metallic rings have been used in order to realize connections well substituting braising and mechanical locks when these ones are difficult to design (heterogeneous materials, limited spaces, small dimension objects) [78].

Using techniques is very simple: at first S.M.A. element is "formed" with a smaller geometry than the system to be locked; then at a low temperature it is widened in such way to be easily installed when mounted.

After installed S.M.A. element is simply heated to recover the original shape (presence of element to be locked shall prevent complete initial geometry recovering, so allowing a stress generation) (figure 2.31).

Figure 2.31: Hydraulic lines mechanical locking by S.M.A. [76].

This methodology has found practical application in particular during hydraulic lines locking on aircraft as F-14 since 1960 [79].
Other implementations regard electronic cards locking as Connectors ZIF (Zero Insertion Force) (figure 2.32) or electric connections by wires.

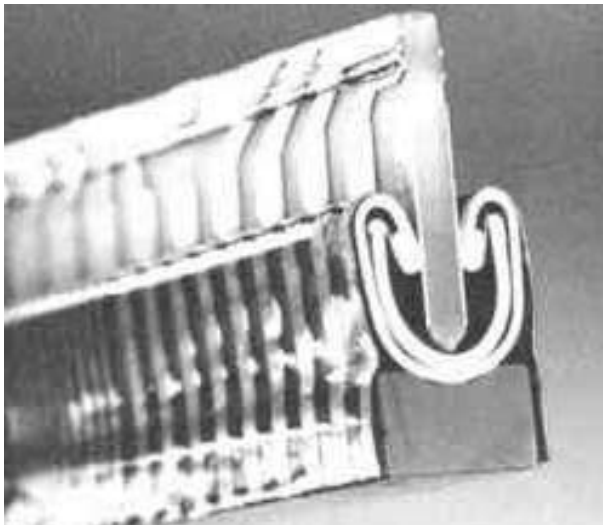

Figure 2.32: Connectors for electronic cards at high performances locking by S.M.A. [76].

Partial recovering: recovering limited by a constrain surrendering according to a law related to stress produced by the material during the recovering phase, law able to restore

initial conditions, making repeatable system (actuators) applications: in such case work may be developed.

A very known scheme is that represented in figure 2.33 where a S.M.A. spring works as antagonist of a common steel spring.

Different Young's modulus is exploited that at high and low temperature S.M.A. shows: at low temperature material has a such modulus that steel spring is simply able to win the force keeping in compressed position S.M.A. spring.

By increasing temperature until transformation point, spring shall compress the antagonist steel spring, so determining a sliding-block displacement towards opposite side. When spring is cooled, original condition shall come back ready to repeat this activation procedure.

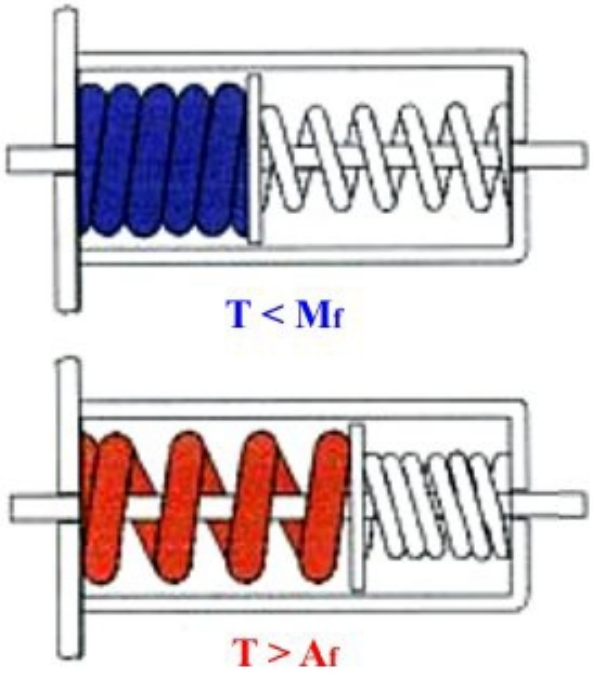

Figure 2.33: S.M.A. actuators scheme.

On the basis of this simple constructive scheme for different solutions able to provide automatic small, compact, silent and without engine for controlling parameters depending on temperature, have been developed.

A direct application of this scheme is a common water mixer able to automatically control outflow temperature, with an better improved efficiency (in terms of time response) with respect to common wax system.

Other applications concern robotic field where human muscle movement simulation is

possible only controlling forces developed by S.M.A. during heating (figure 2.34) [80] [85];

In the same case snake, fishes, etc. movement can be reproduced.

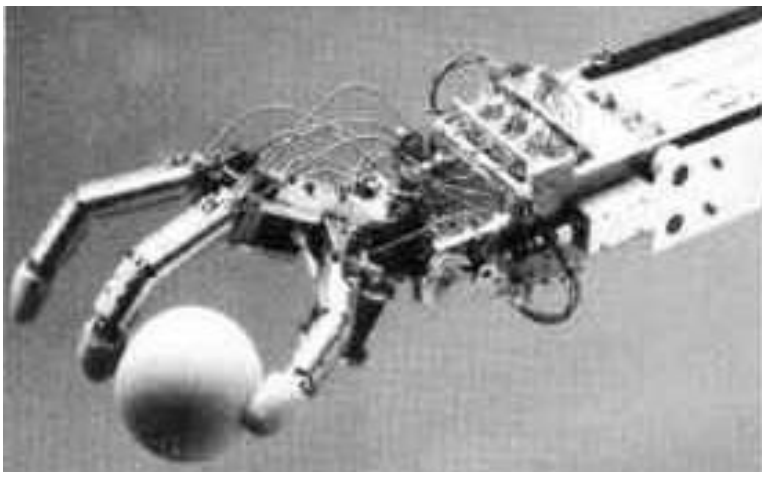

Figure 2.34: S.M.A. robotic application [85].

Also in civil field S.M.A. start to be successfully adopted, in particular for safety and anti-fire systems: in fact, it is possible to have thermal actuators aiming at producing smoke and heat evacuator automation (figure 2.35) [81], or fire-block doors, able to assure functionality, activation reversibility and reliability.

Figure 2.35: S.M.A. smoke evacuator [81].

In space field first of all S.M.A. actuators have been used in substitution to traditional pyrotechnic actuator for unhoohing satellite parts and/or deployment of solar arrays, radiators etc.

Main advantages of this system is reusability in addition to lower stress involved and transmitted to element actuated, during the activation phase.

An example is given by actuator developed by NASA Lewis Research Center (figure 2.36) [82].

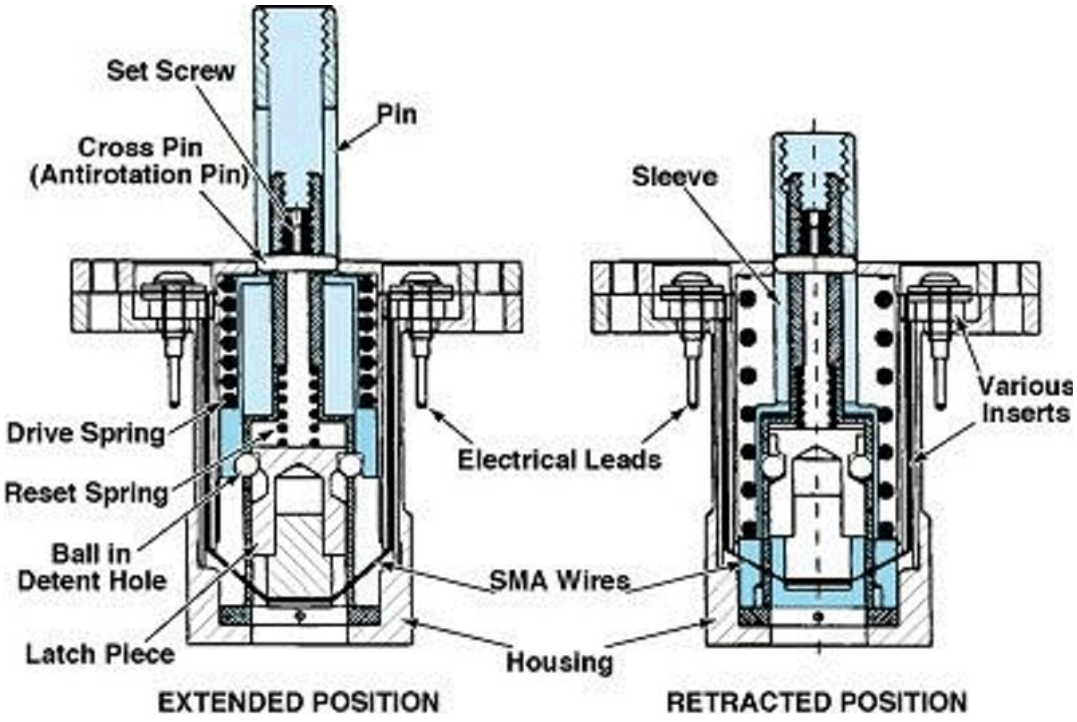

Figure 2.36: Actuator for space use activated by S.M.A. [82].

Recent applications have seen S.M.A., always in space field, also as *active control of telescope mirrors* (in order to increase aim accuracy) [83][84] and for the actuation of *robotic arms* [4]; there are interest also in the vibration control field for great dimension space systems.

There are a lot of studies for S.M.A. actuators in other fields as naval, in particular for submarine *rudder activation* [86] or for the realization of propeller inside *directional conduct* deformable by means of S.M.A. materials, so that improving manoeuvre capability [87].

Generally in the aeronautical helicopter field, S.M.A. has application first of all in the

active control vibration (exploiting different damping characteristics for the two S.M.A. phases or to stiffen materials constituting structural elements), for aerodynamic characteristics improvement in aircraft with fixed or rotating wing (through flutter control [88] [89] [90] [91] [92], shape and inclination changing for lift surfaces or their parts, with lift distribution variation, optimization of transonic regime [93] or aeroelastic problem control [94] [95]), manoeuvrability improvement, etc.

Due to high helicopter complexity, they seem to provide today a better power of performance development and improvement by means of S.M.A. and generally through 'smart' materials: in this optical many studies focus on optimization of main rotor blades in different operation conditions, because it generates relevant vibrations [96], noise [97] and low aerodynamic performances [98] [99] [100] [101] [102] [103].

2.15 S.M.A. evolution: F.S.M.A. / M.S.M.A.

Until now, in this section S.M.A. materials have dealt with.

Their 'activation' is obtained by thermal heating so that, thermoplastic martensite transformation takes place: this induces a limitation on activation frequency for these alloys, low than 1 Hz, related to necessary cooling time, because of natural convection.

S.M.A. exist with a composition of ferromagnetic metals and then their activation may be provided by an external magnetic field, making these alloys able to faster and more efficient transformation, and in addition, large strain recovering possibility.

These materials, known as F.S.M.A. (Ferromagnetic S.M.A.) or (Magnetic S.M.A.) match typical ferromagnetic properties with those ones coming from martensite transformation (reversible and with no diffusion).

Since their discovery, ferromagnetic S.M.A. have focused attention due to high deformations induced by magnetic field in the Ni-Mn-Ga [104] [105] [106]: this deformation is due to martensite phase property to change itself (as explained for S.M.A.) and it differs from magnetization phenomenon observed in 1842 by Joule in ferromagnetic materials.

In fact, traditional ferromagnetic fo instance Fe or Ni (with an omogeneous crystallographic structure), strains in association with magneto-striction are about 10^{-4}% while in materials with relevant magneto-striction as Tb-Dy-Fe (TerFeNOL-D) alloy, 0.1% value achieved [107].

On the other hand F.S.M.A. materials show induced strain of 10% [108] because magnetic activation, during martensite phase, with a highly deformable micro-structure, happens.

In fact, if we consider Ni_2mnGa alloy it has in austenite phase (high temperature) an ordered crystallographic structure $L2_1$ (also know as Heusler structure), that, according to martensite transformation into a tetragonal structure (low temperature, martensite phase) may be modified (figure 2.37).

As for S.M.A. description, because of crystal reticular deformation (twinning) from high symmetry austenite structure into various equivalent ways shall may happen; so, different reticular deformation 'directions' in different material areas shall occur (for Ni_2Mnga alloys three different martensite arrangement exist).

So, well defined domains shall appears, each ones with its martesite variation (particular mobility of these domains responsible for extreme martesnite strinability); a typical

martensite micro-structure by a mixture of different variables shall be characterized.

The fact that distinguishes F.S.M.A. from S.M.A., here dealt with, is the particular spontaneous magnetic momentum, differently oriented and each one shall have own magnetization direction.

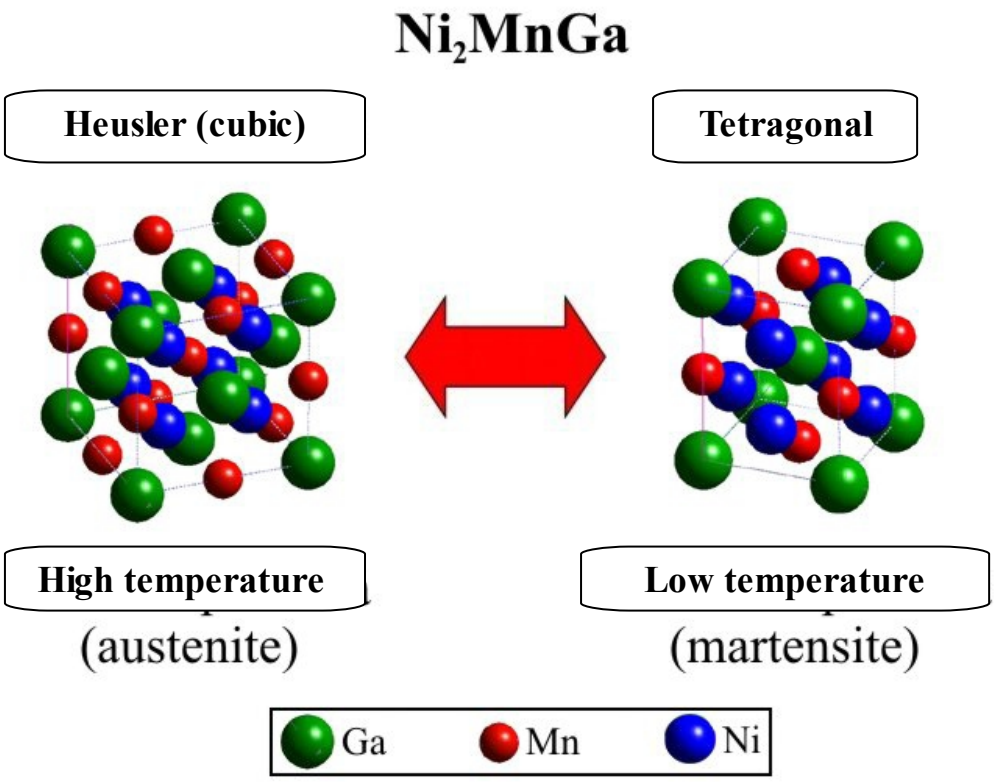

Figure 2.37: Crystallographic structure transformation into F.S.M.A. [82].

Because of an external magnetic field application, magnetic momentum try to align with the field: if necessary energy, for each domains magnetization 'rotation', is quite high, then from an energetic point of view shall be favorable to re-orient whole domain (due to externally each other mobility).

According to magnetization field direction domain number shall increase: this induces only one martensite arrangement with consequent high shape variation.

So, in order to achieve F.S.M.A. magnetic activation, it has to be at a low temperature (martensite phase) and external magnetic field intensity should be high (magneticd anisotropy energy should be higher than energy for domain rotation) [111].

At moment, shape memory effect through magnetic activation has been observed in the Fe-Pd alloys [106] (also with additive as Co and Pt [110]), Co-Ni-Ga [112], La-Sr-CuO_4

[113] and Ni-Mn-Ga [105] [108] [114] [115]: on the other hand, these alloys are expensive an fragile for required applications. La-Sr-CuO_4 is interesting because it is not a ferromagnetic material but anti-ferromagnetic. This confirms that magnetic anisotropy is more important than macroscopic magnetic momentum in these alloys.

For practical applications the most promising alloy is Ni-Mn-Ga.

This alloy has a relatively high Curie temperature (about 90°C) and martensite transformation temperature may be controlled, as for S.M.A., by changing percentage composition of different metals inside the alloy (Guo & al. [116] have experimentally verified varitions due to small quantity of Fe, Co, Tb addition).

Some of this alloy features are included in table 2.9 [109].

Ni-Mn-Ga alloy properties	
Composition	Ni : 51.3 Mn : 24.0 Ga : 24.7
Trnsformaion temperature M_S	≈ -10 °C
Transforamtion hysteresis M_S-M_F	< 3 °C
Curie temperature T_C	≈ 85 °C
Austenite saturation Magnetization a_S (at 20°C)	485 emu/cm^3
Martensite saturation Magnetization m_S (at -17°C) Density ρ	602 emu/cm^3 8.02 g/cm^3

Table 2.9: Ni-Mn-Ga alloy properties [109]

In any case, F.S.M.A. materials are very promising: in fact, they combine S.M.A. advantages (high strain percentage until 10%) also the possibility of a faster activation frequency (about milliseconds).

However, thei behaviour is still under numerical and experimental investigation, in order to evaluate external megnatic field and temperature influence on transition phase [117] [118]. There are some applications still now in prototype phase [119] as, for instance, two actuators experimented by Tellinen & al. [120].

A lot of experimental works are very promising able to adopt F.S.M.A. materials for evolved helicopter rotor development, aiming at improving performances and modifying typical activation [121].

2.16 A look at the future: Shape Memory Polymers (S.M.P.)

Shape Memory Polymers (SMPs) are a class of polymers which can undergo deformation at high temperatures, retain the deformed shape when cooled and return to its original unaltered configuration upon heating above the glass transition temperature.

Advanced polymers could have two or more different shapes that would be reached at different target temperatures.

Materials capable of undergoing thermal shape-recovery are a division of smart or intelligent materials. In contrast to SMAs, SMPs possess a much lower density, have a lower cost and recover strains up to a reported 400%, an order of magnitude greater than their metal counterparts [122-124].

Conversely, SMPs present as design challenge due to their material weakness.

First introduced in Japan and then the United States in 1984, SMP are polymers whiose qualities whose qualities have been altered to give them dynamic shape "memory" properties. Using thermal stimuli, SMPs can exhibit a radical change from a rigid polymer to a very elastic state, then return back to a rigid state again. In the elastic state a shape memory polymer will recover its "memory" shape if left unrestrained. However, while in this pliable state it can be stretched, folded or otherwise conformed to other shapes, tolerating up to 500% elongation. While manipulated, the SMP can be cooled and therefore returned to a rigid state, maintaining its manipulated shape indefinitely. This manipulation process can be repeated many times without degradation.

Unlike SMA, a SMP exhibits a radical change from a normal rigid polymer to a very stretchy elastic and back on command, a change which can be repeated without degradation of material. The "memory" (or recovery) quality comes from the stored mechanical energy attained during the reconfiguration and material cooling.

The secret behind these clever materials lies in their molecular network structure, which contains meltable "switching segments".

SMP, like all polymers, have show two materials phases. The two phases – the glass and the rubber phases - are separated by the glass-transition temperature T_g. In the glass phase, the material is rigid and cannot be easily deformed.

On the other hand, when the temperature is greater than T_g the material enters the soft6 rubber phase and becomes easily deformable. In this phase, the SMP can be strained to large values, which can be recovered through a specific cooling and heating procedure to

be discussed later.

Modern variations on the classic turn-of-the millennium Shape Memory Polymers react to other stimuli than heat – one of the most important is a photonic reaction [125, 126] which allowed the creation of quick and affordable optic fiber switching units. Other developments include exposure (or lack of exposure) to oxygen – these polymers are now in use in many orbital applications where they can instantly seal small breaches in vehicle and station hulls as well as personal protective equipment.

Finally, piezo-stimulus SMP react to different electrical currents by taking on different shapes. Some become pliable under a specific current, others remain pliable until a current is established, and the more elaborate designs have multiple states and can switch from one hardened state to another through the intermediary pliable state simply by changing the current applied to the plastic [127].

Some other varieties include magnetic field-triggered polymers [128] and acid-base reaction polymers used in some scientific applications.

The most common usage for SMP is the production of other plastics. SMP moulds can be made of a hard and high temperature material for high precision injection moulding, and then with the application of electrical current, the moulds seem to melt away from the final product, then reform into the mould format again when the current is turned off.

In addition, modern SMP foamed polystyrene allows convenient shipping of products in large polystyrene shipping units to protect against jostling and abuse, then the polystyrene packing containers can be compressed releasing the air within the structure and reducing the container down to a plastic block less than 3% of the normal volume of the polystyrene. These are shipped back to the original sender where they are heated and "fluffed" to be returned to their normal size and shape.

However, a lot of industries are already underway for the adoption of a SMP, such as CRG Inc. which produces the Veriflex (Figure 2.38) [129].

The ability of SMPs to recover large strains combined with its low weight and low cost advantages has produced much interest in design applications. For instance, Lockheed Martin and Hypercomp/NextGen are developing and testing morphing wings, with portions of the testing set to occur at NASA Langley Research Centre. These wings are expected to adjust the surface area based on the flying conditions with possible surface area increases of 300%. In this project funded by the Defense Advanced Research project Agency (DARPA), Toensmeir [130] reports that SMPs are being considered as a possible

choice for the skin of the wing.

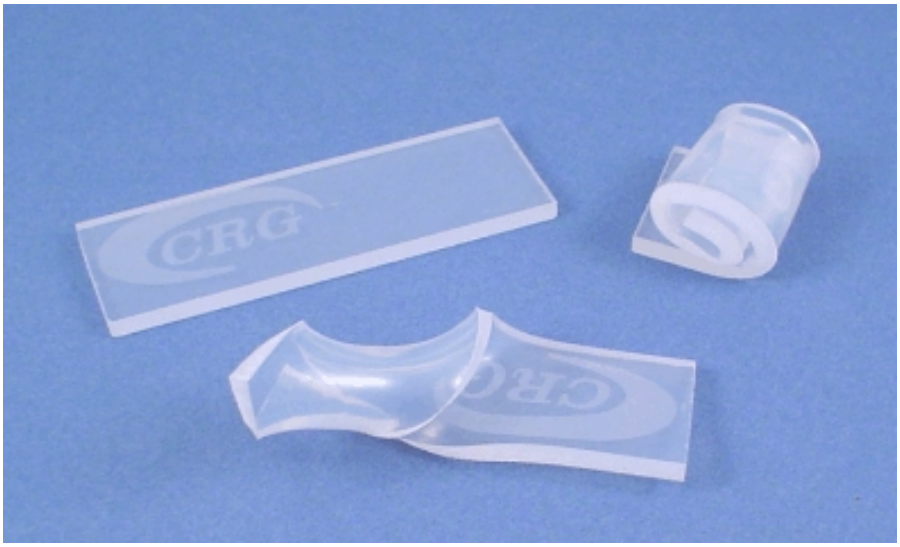

Figure 2.38: Veriflex sample: it is elastic when heated over transition temperatures and keeps the imposed shape when cooled down [129].

Other possible applications for shape memory polymers are biodegradable sutures and other biomedical applications [131-133], repairable automobile skins, satellites and other space vehicles. In order to better and more efficiently investigate application possibilities, it is necessary to accurately model the SMP thermo-mechanical behavior.

Consequently, to develop the necessary constitutive model, a thorough set of experiments must be performed to fully characterize the material: today, many avenues exist for such investigation [134-136].

By the late 2020's, it is expected that SMP characteristics can be engineered into almost all polymers, allowing automobile fenders to be bent back into shape with the application of the right amount of heat, the creation of multiform solid-state furniture that shifts to accommodate different users with the press of a button and a million other household uses. Some low rent apartment buildings could even use piezo-activated SMPs for the doors on their units so the door can be quickly "melted" with the application of a simple stun-gun like device.

2.17 Conclusions

S.M.A. as NiTiNOL are able to expound large forces and to recover large deformations and then they have an enormous capability in low frequency (quasi-steady) applications.

Actually these alloys are commercially available as wires, wires, tapes, small bars or plates and in different chemical arrangement exist, even if Ni-Ti alloys are absolutely the most employed material.

So defined all chemical element constituting the alloy, properties strongly depend on metal percentage and typical workmanship.

In the last time three components alloys are widely diffused. Their properties for a specific application may be better adopted; the last alloy typology shows a behaviour strictly depend on temperature (as non linear function), stress, and on strain history and then it requires an accurate tuning in order to have the appropriate configuration for expected applications.

Actually this represents an obstacle for their rapid exploitation in various application fields.

Most of constitutive models developed for S.M.A. thermo-mechanical behaviour comprehension are validated for quasi-steady loads and they should be extended also for dynamic field at low frequency.

Generally, particular success in the validation process of constitutive models for NiTiNOL wires under extensional load condition has been found.

Validation process should be extended also to different loading condition as for instance torsion load.

An additional investigation field, still open, concerns predictive models validation for composite beams and plates integrated with S.M.A. wires (wires).

For all these structural elements local (high order)shear stress/strain distribution could not be only used for structure integrity verification under assigned load condition but further they could provide relevant information about activation mechanism.

In a wide part of commercial applications, S.M.A: are not directly used but they are exploited as activation elements for actuators able to expound mechanic work followed to S.M.A. phase transformation during heating: in such way, S.M.A. activation in terms of force and displacement, according to geometry and actuator design, can be distributed.

Enormous S.M.A. capabilities of loading and unloading cycle repeatability makes them

particularly proper to various actuators.

S.M.A. limitations are related to low activation frequency: but in this context F.S.M.A. materials show to be a valid alternative, joining relevant recoverable strains (until 10%) with an increased activation velocity (about milliseconds) .

2.17 References

[1] Buehler W.J., Gilfrich J.V., Wiley R.C., 1963, "*Effect of low-temperature phase changes on the mechanical properties of alloys near composition TiNi*" – Journal of Applied Physics, vol.34, pp.1475

[2] Kauffman G.B., Mayo I., 1993, "*The metal with a memory*" – Invention & Tecnology, vol.9, no.2, pp.18-23

[3] Srinivasan A.V., McFarland D.M., 1995, "*Smart Structures: Analysis and Design*" – Cambridge University Press, ISBN 0-521-65977-9

[4] TiNi Aerospace Inc., sito web: http://www.tiniaerospace.com/

[5] Shimizu K., Tadaki T., 1987, "*Shape Memory Alloys*" – Funakubo H. Ed., Gordon and Breach Science Publishers, New York, pp.1-60

[6] Stefano Besseghini, 2000, CNR – TEMPE –Lecco section , sito web: http://www.tempe.mi.cnr.it/tempelc/index.htm

[7] Buehler W.J., Wiley R.C., Wang F.E., 1965, "*Nickel-based Alloys*" – U.S. Patent 3,174,851,23

[8] Stoeckel D., Yu W., "*Superelastic Nickel- Titanium Wires*" –Raychem Corporation, Menlo Park, CA

[9] Lin R., 1996, "*Shape Memory Alloys and Their Applications*" – Sito web: http://www.stanford.edu/~richlin1/sma/sma.html

[10] Jackson C.M., Wagner H.J., Wasilewski R.J., 1972, "*55-Nitinol-The Alloy With a Memory: Its Physical Metallurgy, Properties, and Applications: A Report*" – NASA, Washington.

[11] Chopra I., 2002, "*Review of State of Art of Smart Structures and Integrated Systems*" – 42nd AIAA/ASME/ASCE/AHS/ASC Structures, Structural Dynamics, and Materials Conference, Seattle, WA, AIAA Journal, vol.40, no.11

[12] Brocca M., Brinson L.C., Bazant Z.P., 2002, "*Three Dimensional Constitutive Model for Shape Memory Alloys Based on Microplane Model*" – Journal of the Mechanics and Physics of Solids, vol.50, pp.1051-1077

[13] Brinson L.C., 1993, "*One-Dimensional Constitutive Behaviour of Shape Memory Alloys: Thermomechanical Derivation with Non-Constant Material Functions and Redefined Martensite Internal Variable*" – Journal of Intelligent Material Systems and Structures, vol.4, no.2, pp.229-242

[14] Wayman C.M., 1992, "*Shape Memory and related phenomena*" – Progress in Materials Science, vol.36, pp.203-204

[15] Tanaka K., 1986, "*A Thermomechanical Sketch of Shape Memory Effect: One-Dimensional Tensile Behaviour*" – Res. Mechanica, vol.18, no.3, pp.251-263

[16] Liang C., Rogers C.A., 1990, "*One-Dimensional Thermomechanical Constitutive Relations for Shape Memory Material*" – Journal of Intelligent Material Systems and Structures, vol.1, no.2, pp.207-234

[17] Brinson L.C., 1990, "*One-Dimensional Constitutive Behaviour of Shape Memory Alloy Constitutive Models*" – Journal of Intelligent Material Systems and Structures, vol.1, no.2, pp.207-234

[18] Boyd J.G., Lagoudas D.C., 1996, "*A Thermodynamical Constitutive Model for Shape Memory Materials. Part. I. The Monolithic Shape Memory Alloys*" – International Journal of Plasticity, vol.12, no.6, pp.805-842

[19] Boyd J.G., Lagoudas D.C., 1996, "*A Thermodynamical Constitutive Model for Shape Memory Materials. Part. II. The Monolithic Shape Memory Alloys*" – International Journal of Plasticity, vol.12, no.7, pp.843-873

[20] Ivshin Y., Pence T.J., 1994, "*A Thermo Mechanical Model for One variant Shape Memory Material*" – Journal of Intelligent Material Systems and Structures, vol.5, no.4, pp.455-473

[21] Graesser E.J., Cozzarelli F.A., 1994, "*A Proposed Three-Dimensional Model Constitutive Model for Shape Memory Material*" – Journal of Intelligent Material Systems and Structures, vol.5, no.1, pp.78-89

[22] Juhàsz L., Andrä H., Hesebeck O., 2000, "*A Constitutive Model of Shape Memory Alloys Based on Viscoplastic Like Evolution Equations*" – Periodica Polytechnica Ser. Mech. Eng., vol.44, no.1, pp.59-69

[23] Sun Q.P., Hwang K.C., 1993, "*Micromechanics Modeling for the Constitutive Behaviour of Polycrystalline Shape Memory Alloys-1. Derivation of General Relations*" – Journal of Mechanical Physics Solids, vol.41, no.1, pp.1-17

[24] Matsuzaki Y., Naito H., Ikeda T., Funami K., 2001, "*Thermo-Mechanical Behaviour Associated with Pseudoelastic Transformation of Shape Memory Alloys*" – Smart Materials and Structures, vol.10, no.5, pp.884-892

[25] Barrett D.J., 1995, "*A One-Dimensional Constitutive Model for Shape Memory Alloys*" – Journal of intelligent Material Systems and Structures, vol.6, no.3, *pp*.329-337

[26] Prahlad H., Chopra I., 2001, "*Comparative Evaluation of Shape Memory Alloy Constitutive Models with Experimental Data*" – Journal of Intelligent Material Systems and Structures, vol.12, no.6, pp.386-396

[27] Brinson L.C., Huang M., 1996, "*Simplification and Comparisons of Shape Memory Alloy Constitutive Models*" – Journal of Intelligent Material Systems and Structures, vol.7, no.1, pp.108-114

[28] Tobushi H., Lin P.H., Tanaka K., Lexcellent C., Ikai A., 1995, "*Deformation Properties of TiNi Shape Memory Alloy*" – Journal of Physique IV, vol.5, C2, pp.409-410

[29] Lin P.H., Tobushi H., Ikai A., Tanaka K., 1995, "*Deformation Properties Associated with the Martensitic and R-Phase Transformations in TiNi Shape Memory Alloy*" Journal of Applied Biomechanics, vol.10, no.2, pp.1-11

[30] Tanaka K., Nishimura F., Matsui H., Tobushi H., Lin P.H., 1996, "*Phenomenological Analysis of Plateaus on Stress-Strain Hysteresis in TiNi Shape Memory Alloy Wires*" – Mechanics of Materials, An International Journal, vol.24, no.1, pp.19-30

[31] Tobushi H., Yamada S., Hachisuka T., Ikai A., Tanaka K., 1996, "*Thermomechanical Properties due Martensitic and R-Phase Transformations of TiNi Shape Memory Alloy Subjected to Cyclic Loadings*" – Smart Materials and Structures, vol.5, no.6, pp.788-795

[32] Sittner P., Stalmans R., Tokuda M., 2000, "*An Algorithm for Prediction of the Hysteresis Responses of Shape Memory Alloys*" – Smart Materials and Structures, vol.9, no.4, pp.452-465

[33] Naito H., Matsuzaki Y., Ikeda T., 2001, "*A Unified Model of Thermo-mechanical Behaviour of Shape Memory Alloys*" – Society of Photo-Optical Instrumentation Engineers, vol.4333, Society of Photo-Optical Instrumentation Engineers (International Society for Optical Engineering), Bellingham, WA, pp.291-313

[34] Elahinia M.H., Ahmadian M., 2005, "*An Enhanced SMA phenomenological model: I. The Shortcomings of the existing models*" – Smart Materials and Structures, vol.14, pp.1297-1308

[35] Prahlad H., Chopra I., 2000, "*Experimental Characterization of NiTi Shape Memory Alloy Wires Under Uniaxial Loading Conditions*" – Journal of Intelligent Material Systems and Structures, vol.11, no.4, pp.272-282

[36] Faulkner M.G., Amairaj J.J., Battaacharyya A., 2000, "*Experimental Determination of Thermal and Electrical Properties of Ni-Ti Shape Memory Wires*" – Smart Materials and Structures, vol.9, no.5, pp.632-639

[37] Epps J., Chopra I., 1997, "*Comparative Evaluation of Shape Memory Alloy Constitutive Models with Experimental Test Data*" – 38th AIAA/ASME/ASCE/AHS/ASC Structures, Structural Dynamics, and Materials Conference and Adaptive Structures Forum, Reston, VA, AIAA 1997-1194

[38] Bo Z., Lagoudas D.C., 1994, "*Comparison of Different Thermo Mechanical Models for Shape Memory Alloys*" – Adaptive Structures and Composite Materials: Analysis and Applications: American Society of Mechanical Engineers Symposium, vol.54, pp.9-19

[39] Mikuriya S., Nakahara T., Tobushi H., Watanabe H., 2000, "*The Estimation of Temperature Rise in Low-Cycle Fatigue of TiNi Shape-Memory Alloy*" – JSME International Journal, Series A, vol.43, no.2, pp.166-172

[40] Tobushi H., Nakahara T., Shimeno Y., Hashimoto T., 2000, "*Low-Cycle Fatigue of TiNi Shape Memory Alloy and Formulation of Fatigue Life*" – Journal of Engineering Materials and Technology, vol.122, no.2, pp.186-191

[41] Prahlad H., Chopra I., 2001, "*Development of a Strain-Rate Dependant Model for Uniaxial Loading of SMA Wires*" – 12th International Conference on Adaptive Structures and Technologies, CRC Press, Boca Raton, FL

[42] Shaw J.A., 2002, "*Thermo-Mechanical Model for 1-D Shape Memory Alloys Wire with Propagating Instabilities*" – International Journal of Solids and Structures, vol.139, no.5, pp.1275-1305

[43] Lexcellent C., Rejzner J., 2000, "*Modeling of the Strain Rate Effect, Creep and Relaxation of a Ni-Ti Shape Memory Alloy Under Tension (Compression)- Torsional Proportional Loading in the Pseudoelastic Range*" – Smart Materials and Structures, vol.9, no.5, pp.613-621

[44] Potapov P.L., Silva P.D., 2000, "*Time Response of Shape Memory Alloy Actuators*" – Journal of Intelligent Material Systems and Structures, vol.11, no.2, pp.125-134

[45] Davidson F.M., Liang C., Lobitz D., 1996, "*Investigation of Torsional Shape Memory Alloy Actuators*" – Society of Photo-Optical Instrumentation Engineers' Symposium on Smart Structures and Materials, Smart Structures and Integrated Systems, vol.2717, Society of Photo-Optical Instrumentation Engineers (International Society for Optical Engineering), Bellingham, WA, pp.672-682

[46] Keefe A.C., Carman G.P., 2000, "*Thermo-Mechanical Characterization of Shape Memory Alloy Torque Tube Actuators*" – Smart Materials and Structures, vol.9, no.5, pp.665-672

[47] Prahlad H., Chopra I., 2002, "*Characterization of SMA Torsional Actuators for Variable Twist Tilt Rotor (VTTR) Blades*" – 43rd AIAA/ASME/ASCE/AHS/ASC Structures, Structural Dynamics, and Materials Conference and 10th Adaptive Structures Forum, Reston, VA, AIAA 2002-1445

[48] Thomson P., Balas G.J., Leo P.H., 1993, "*Pseudoelastic Hysteresis of Shape Memory Wires for Passive Structural Damping: Theory and Experiments*" – Society of Photo-Optical Instrumentation Engineers, vol.1917, Society of Photo- Optical Instrumentation Engineers (International Society for Optical Engineering), Bellingham, WA

[49] Wolons D., Gandhi F., Malovrh B., 1998, "*Experimental Investigation of the Pseudoelastic Hysteresis Damping Characteristics of Shape Memory Alloy Wires*" – Journal of Intelligent Material Systems and Structures, vol.9, no.2, pp.116-126

[50] Malovrh B., Gandhi F., 2001, "*Mechanism-Based Phenomenological Models for the Pseudoelastic Hysteresis Behaviour of Shape Memory Alloys*" – Journal of Intelligent Material Systems and structures, vol.12, no.1, pp.21-30

[51] Lammering R., Schmidt I., 2001, "*Experimental Investigations on the Damping Capacity of NiTi Components*" – Smart Materials and Structures, vol.10, no.5, pp.853-859

[52] Ju D.Y., Shimamoto A., 1999, "*Damping Property of Epoxy Matrix Composite Beams with Embedded Shape Memory Alloy Fibers*" – Journal of Intelligent Material Systems and Structures, vol.10, no.7, pp.514-520

[53] Midè Technology Corporation, Smart Materials, sito web: http:// www.mide.com/expertise_sm_pdf.html

[54] Rogers C.A., Robertshaw H.H., 1988, "*Shape Memory Alloy Reinforced Composite*" – Engineering Science Preprints 25, Society of Engineering Science Inc., ESP25.8027

[55] Rogers C.A., Barker D.K., 1990, "*Experimental Studies of Active Strain Energy Tuning of Adaptive Composites*" – 31st AIAA/ASME/ASCE/AHS/ASC Structures, Structural Dynamics, and Materials Conference, Washington, DC, AIAA 1990-1086

[56] Baz A., Imam K., McCoy J., 1990, "*Active Vibration Control of Flexible Beams Using Shape Memory Actuators*" – Journal of Sound and Vibration, vol.140, no.3, pp.437-456

[57] Baz A., Ro J., Mutua M., Gilheany J., 1991, "*Active Buckling Control of Nitinol-Reinforced Composite Beams*" – Conference on Active Material and Adaptive Structures, Society of Photo-Optical Instrumentation Engineers (International Society for Optical Engineering), Bellingham, WA, pp.167-176

[58] Brinson L.C., Bekker A., Huang M., 1996, "*Deformation of Shape Memory Alloys due to Thermo-Induced Transformation*" – Journal of Intelligent Material Systems and Structures, vol.7, no.1, pp.97-107

[59] Lagoudas D., Moorthy D., Quidwai M.A., Reddy J.N., 1997, "*Modeling of Thermomechanical Response of Active Laminates with SMA Strips Using Layerwise Finite Element Method*" – Journal of Intelligent Material Systems and Structures, vol.8, no.6, pp.476-488

[60] Turner T.L., 2000, "*A New Thermoelastic Model for Analysis of Shape Memory Alloy Hybrid Composites*" – Journal of Intelligent Material Systems and Structures, vol.11, no.5, pp.382-394

[61] Epps J., Chandra R., 1995, "*Shape Memory Actuation for Active Tuning of Composite Beams*" – Society of Photo-Optical Instrumentation Engineers (International Society for Optical Engineering), Bellingham, WA

[62] Diodati G., Ameduri S., Concilio A., 2005, "*A SMA Embedded Anisotropic Panel Aimed at Controlling Vibration due to Variable Regimes Sources*" – 8th Conference on Dynamical Systems Theory and Applications, Lódź, Polonia

[63] Furuya Y., 1996, "*Design and Material Evaluation of Shape Memory Composites*" – Journal of Intelligent Material Systems and Structures, vol.7, no.2, pp.321-330

[64] Birman V., 1996, "*Micromechanics of Composites with Shape memory Alloy Fibers in Uniform Thermal Fields*" – AIAA Journal, vol.34, no.9, pp.1905-1912

[65] Bisagni C., Sala G., 2004, "*Buckling and Shape Control of Composite Laminates Using Embedded Shape Memory Alloys Wires*" – 45th AIAA/ASME/ASCE/ AHS/ASC Structures, Structural Dynamics, and Materials Conference, Palm Springs, California, AIAA 2004-1648 Gao X., Burton D.S., Brinson L.C., 2004, "*Finite Element Simulation of a Self-Healing Shape Memory Alloy Composite*" – Mechanics of Materials, An International Journal

[67] Schloßmacher P., Haas T., Schüßler A., 1997, "*Laser Welding of a Ni-Rich TiNi Shape Memory Alloy: Pseudoelastic Properties*" – 2nd International Conference on Shape Memory and Superelastic Technologies, ed. da Pelton A. & al., SMST- 97, pp. 137-142

[68] Wang G., 1995, "*Weldability of Nitinol to Stainless Steel*" – 2nd International Conference on Shape Memory and Superelastic Technologies, ed. da Pelton A. & al., SMST-97, pp.131-136

[69] Wisbey A., Ward-Close C.M., 1994, Materials Letters, vol.21, pp.47-53

[70] Nishida M., Chiba A., Honda Y., Hirazumi J., Horikiri K., 1995, ISIJ International, vol.35, pp.217-219

[71] Fuji A., North T.H., Ameyama K., Futamata M., 1992, Materials Sci. Technol., vol.3, p.219

[72] Hall T.A., 1993, "*Joint, a Laminate and a Method of Preparing a Nickel-Titanium Alloy Member Surface for Bonding to Another Layer of Metal*", U.S. Patent 5,242,759

[73] Hall P.C., 1997, "*Methods of Promoting Solder Wetting on Nitinol*" – 2nd International Conference on Shape Memory and Superelastic Technologies, ed. Da Pelton A. & al., SMST-97, pp.125-130

[74] Johnson Matthey Inc., sito web: http://www.jmmedical.com/

[75] Langelaar M., Van Keulen F., 2004, "*Modeling of a Shape Memory Alloy Active Catheter*" – 45th AIAA/ASME/ASCE/AHS/ASC Structures, Structural Dynamics, and Materials Conference, Palm Springs, California, AIAA 2004-1653

[76] Memory-Metalle GmbH, sito web: http://www.memory-metalle.de/

[77] Fosness E., Maji A., Guerrero J., Carpenter B., Tupper M., 2003, "*Development of Low Shock Deployment Devices for Aerospace Applications Using Shape Memory and Elastic Memory Materials*" – AIAA Journal 2003-6246

[78] Raychem Corporation, Tyco Electronics, sito web: http://www.raychem.com/

[79] Kauffman G.B., Mayo I., 1993, "*Memory Metal*" – Chem Matters, vol.11, no.3, pp.4-7

[80] Rogers C., 1995, "*Intelligent Materials*" – Scientific American, Settembre 1995, pp.154-157

[81] Gambardella V., Cavanna G., Bravin E., 2003, "*I materiali a memoria di forma - Una nuova applicazione nel campo della previsione incendi*" – L'Edilizia- Speciale ITC, Istituto per le Tecnologie delle Costruzione, C.N.R., sito web: http://www.itc.cnr.it/default.asp

[82] Bokaie M. of TiNi Alloy Co. for NASA Lewis Research Center, Febbraio 1998, LEW-16511, sito web: http://www.nasatech.com/Briefs/Feb98/LEW16511.html

[83] Wada B.K., Fanson J.L., Crawley E.F., 1990, "*Adaptive Structures*" – Journal of Intelligent Material Systems and Structures, vol.1, no.2, pp.157-174

[84] Pollard E.L., Jenkins C., 2005, "*Shape Memory Alloy Deployment of Membrane Mirrors for Spaceborne Telescopes*" – 46th AIAA/ASME/ASCE/AHS/ASC Structures, Structural Dynamics, and Materials Conference, Austin, Texas, AIAA 2005-

2196

[85] Università di Alberta, Canada, sito web: http://www.cs.ualberta.ca/~database/MEMS/sma_mems/muscle.html

[86] Gowing S., Carpenter B., Lee Y., Atsavapranee P., Hess D., 2004, "*Flextac: An Advanced Submarine Control Surface and Actuation System*" – 42nd AIAA Aerospace Sciences Meeting and Exhibit, Reno, Nevada, AIAA 2004-902

[87] Quackenbush T.R., Carpenter B.F., Gowing S., 2005, "*Design and Testing of a Variable Geometry Ducted Propulsor Using Shape Memory Alloy Actuation*" – 43rd AIAA Aerospace Sciences Meeting and Exhibit, Reno, Nevada, AIAA 2005- 1077

[88] Lin C.Y., Crawley E.F., Heeg J., 1996, "*Open- and Closed-Loop Results of a Strain-Actuated Active Aeroelastic Wing*" – Journal of Aircraft, vol.33, no.5, pp.987-994

[89] Kudva J., Appa K., Martin C., Jardine P., Sendeckji G., 1997, "*Design, Fabricatio and Testing of the DARPA/WL 'Smart Wing' Wind Tunnel Model*" – AIAA Paper 97-1198

[90] Kudva J., Martin C.A., Scherer L.B., Jardine A.P., McGovan A.R., Lake R.C., Sendeckji G., Sanders B., 1999, "*Overview of the DARPA/AFRL/NASA Smart Wing Program*" – Society of Photo-Optical Instrumentation Engineers' North American Symposium on Smart Structures and Materials, vol.3674, Society of Photo-Optica Instrumentation Engineers (International Society for Optical Engineering), Bellingham, WA, pp.230-248

[91] Becker J., Schroeder W., 1999, "*Advanced Aircraft Structures Program: An Overview*" – Society of Photo-Optical Instrumentation Engineers' North American Symposium on Smart Structures and Materials, vol.3674, Society of Photo-Optical Instrumentation Engineers (International Society for Optical Engineering), Bellingham, WA, pp.2-12

[92] Duan B., Abdel-Motagaly K., Guo X., Mei C., 2003, "*Suppression of Supersonic Panel Flutter and Thermal Deflection Using Shape Memory Alloy*" – 44th AIAA/ASME/ASCE/AHS Structures, Structural Dynamics, and Materials Conference, Norfolk, Virginia, AIAA 2003-1513

[93] Bein T., Hanselka H., Breitbach E., 2000, "*An Adaptive Spoiler to Control the Transonic Shock*" – Smart Materials and Structures, vol.9, no.2, pp.141-148

[94] Ehlers S.M., Weisshaar T.A., 1993, "*Static Aeroelastic Control of an Adaptive Lifting Surface*" – Journal of Aircraft, vol.30, no.4, pp.534-540

[95] Lazarus K.B., Crawley E.F., Bohlmann J.D., 1991, "*Static Aeroelastic Control Using*

Strain Actuated Adaptive Structures" – Journal of Intelligent Material Systems and Structures, vol.12, no.3, pp.386-410

[96] Konstanzer P., Grohmann B., Kroplin B., 2001, "*Decentralized Vibration Control and Coupled Aeroservoelastic Simulation of Helicopter Rotor Blades with Adaptive Airfoils*" – Journal of Intelligent Material Systems and Structures, vol.12, no.4, pp.209-214

[97] Chen P.C., Baeder J.D., Evans R.A.D., Niemczuk J., 2001, "*Blade-Vortex Interaction Noise Reduction with Active Twist Smart Rotor Technology*" – Smart Materials and Structures, vol.10, no.1, pp.77-85

[98] Koratkar N.A., Chopra I., 2001, "*Wind Tunnel Testing of a Mach-Scaled Rotor Model with Trailing-Edge Flaps*" – Smart Materials and Structures, vol.10, no.1, pp.1-14

[99] Bernhard A.P.F., Chopra I., 2001, "*Analysis of a Bending-Torsion Coupled Actuator for a Smart Rotor with Active Blade Tips*" – Smart Materials and Structures, vol.10, no.1, pp.35-52

[100] Cesnik C.E.S., Shin S.J., Wilbur M.L., 2001, "*Dynamic Response of Active Twist Rotor Blades*" – Smart Materials and Structures, vol.35, no.1, pp.6-16

[101] Shin S.J., Cesnik C.E.S., Hall S.R., 2002, "*Control of Integral Twist-Actuated Helicopter Blades for Vibration Reduction*" – 58th American Helicopter Society Annual Forum, American Helicopter Society, Alexandria, VA, vol.2, pp.328-343

[102] Epps J.J., Chopra I., 2000, "*In-Flight Tracking of Helicopter Rotor Blades Using Shape Memory Alloy Actuators*" – Smart Materials and Structures, vol.10, no.1, pp.104-111

[103] Singh K., Chopra I., 2002, "*Design of an Improved Shape Memory Alloy Actuator for Rotor Blade Tracking*" – Society of Photo-Optical Instrumentation Engineers' North American Symposium on Smart Structures and Materials, vol.4701, Society of Photo-Optical Instrumentation Engineers (International Society for Optical Engineering), Bellingham, WA, pp.244-266

[104] Ullakko K., Huang J.K., Kantner C., O'Handley C., Kokorin V.V., 1996, "*Large Magnetic-Field-Induced Strains in Ni2MnGa single Crystals*" – Journal of Applied Physics Letters, vol.69, pp.1966-1968

[105] James R.D., Tickles R., Wuttig M., 1999, "*Large Field-Induced Strains in Ferromagetic Shape Memory Materials*" – Materials Science and Engineering, A273-275, pp.320-325

[106] James R.D., Wuttig M., 1998, "*Magnetostriction of Martensite*" – Philosophical Magazine, vol.77A, pp.1273-1299

[107] Clark A.E., 1980, "*Ferromagnetic Materials*" – Wohlfarth E.P., North Holland, Amsterdam, vol.1, p.531

[108] Sozinov A., Likhachev A.A., Lanska N., Ullakko K., 2002, – Journal of Applied Physics Letters, vol.80, p.1746

[109] Tickle R., Aerospace Engineering and Mechanics, University of Minnesota, sito web: http://www.aem.umn.edu/people/others/tickle/

[110] Vokoun D., Wang Y.W., Goryczka T., Hu C.T., 2005, "*Magnetostrictive and Shape Memory Properties of Fe-Pd alloys with Co e Pt additions*" – Smart Materials and Structures, vol.14, pp.261-265

[111] Enkovaara J., 2003, "*Atomistic Simulations of Magnetic Shape Memory Alloys*" – Dissertations of Laboratory of Physics, Helsinki University of Technology, Espoo, Finlandia, ISBN 951-22-6313-0

[112] Wuttig M., Li J., Craciunescu C., 2001, "*A New Ferromagnetic Shape Memory Alloy System*" – Scripta Materialia, vol.44, pp.2393-2397

[113] Lavrov A.N., Komiya S., Ando Y., 2002 – Nature, vol.418, p.385

[114] Murray S.J., Marioni M., Allen S.M., O'Handley R.C., Lograsso T.A., 2000, "*6% magnetic-field-induced strain by twin-boundary motion in ferromagnetic Ni–Mn– Ga*" Journal of Applied Physics Letters, vol.77, p.886

[115] Söderberg O., Ge Y., Sozinov A., Hannula S.-P., Lindroos V.K., 2005, "*Recent Breakthrough Development of the Magnetic Shape Memory Effect in Ni-Mn-Ga Alloys*" – Smart Materials and Structures, vol.14, pp.223-235

[116] Guo S., Zhang Y., Quan B., Li J., Qi Y., Wang X., 2005, "*The Effect of Doped Elements on the Martensitic Transformation in Ni-Mn-Ga Magnetic Shape Memory Alloy*" – Smart Materials and Structures, vol.14, pp.236-238

[117] Vasil'ev N., Bozhko A.D., Khovailo V.V. et al., 1999, "*Structural and magnetic phase transitions in shape-memory alloys Ni2+xMn1-xGa*" – Phys. Rev., vol.59,*p*p.1113-1120

[118] Chu S.-Y., Cramb A., De Graef M., Laughlin D.E., McHenry M.E., 2000, "*The Effect of Field Cooling and Field Orientation on The Martensitic Phase Transformation in a Ni2MnGa Single Crystal*" – Journal of Applied Physics Letters, vol.87, p.5777

[119] Murray S., 2000, "*Ferromagnetic Shape Memory Alloys – Device Application*",

Midè Technology Corporation, sito web: http://www.darpa.mil/dso/thrust/matdev/chap/briefings/timchap2000day3/murray_mide.pdf

[120] Tellinen J., Suorsa I., Jääskeläinen A., Aaltio I., Ullakko K., 2002, "*Basic Properties of Magnetic Shape Memory Actuators*" – 8th International Conference ACTUATOR 2002, Bremen, Germania

[121] Couch R.N., 2005, "*Development of a Swashplateless Rotor Using Magnetic Shape Memory Alloys*" – Storming Media, Report no. A918234, sito web: http://www.stormingmedia.us/91/9182/A918234.html

[122] LiangC. , Rogers C.A., Melafeew E., 1997, "*Investigation of Shape Memory Polymers and Their Hybrid Composites*" – Journal of Intelligent Material Systems and Structures, vol.8, no.4, pp.380-386.

[123] Gall K., Mikulas M., Munshi N.A., Beavers F., Tupper ;M., 2000, "*Carbon Fiber Reinforced Shape Memory Polymer Composites*" – Journal of Intelligent Material Systems and Structures, vol.11, no.11, pp.877-886.

[124] Abrahamson E.R., Lake M.S., Munshi N.A., gall K., 2003, "*Shape Memory Mechanics of an Elastic Memory Composite Resin*" - Journal of Intelligent Material Systems and Structures, vol.14, no.10, pp.623-632.

[125] Erine H., Emily A.S., tat H.T., 2005, "*Light-Activated Shape Memory Polymers and Associated Applications*" – Proceedings of SPIE, Bellingham, WA., vol. 5762, pp. 48-52.

[126] Andreas L., Honyan J., OliverJ., Robert L., 2005, "*Light-Induced Shape Memory Polymers*" – Nature, vol. 434, pp.879-882.

[127] Leng J., Lu H., Du S., 2008, "*Conductive Shape Memory Polymer Composite Technology and Its Applications in Aerospace*" – 49th AIAA/ASME/ASCE/AHS/ASC Structures, Structural Dynamics and materials Conference, April 7-10, Schaumburg IL, AIAA Journal 2008-2203.

[128] Schmidt A.M., 2006, "electromagnetic Activation of Shape Memory Polymer Networks Containing Magnetic Nanoparticles" – macromol. Rapid Commun., vol.27, pp.1168-1172.

[129] Cornerstone research Group Inc., website. http://www.crgrp.net/veriflex.htm

[130] Toensmeir P.A., 2005, "*Radical Departure*" Aviation week 6 Space technology, May 23, pp.72-73.

[131] Wache H.M., Tartakowska D.J., Hentrich A., Wagner M.H., 2003, "*Development of a polymer stent with shape memory effect as a drug delivery system*" – J. mater. Sci.

Mater. Med., vol.14, pp.109-12.

[132] Small W., IV, Buchley P.R., Wilson T.S., Benett W.J., Hartman J., Saloner D., Maitland D.J., 2007, "*Shape Memory Polymer stent with expandable foam. A new concept for endovascular embolization of fusiform aneurysms*" – IEEE Trans. Biomed. Eng., vol.54, pp.1157-1160.

[133] Lendlein A., Langer R., 2002, "*Biodegradable, elastic shape memory polymers for potential biomedical applications*" – Science, vol.296, pp.1673-1676.

[134] Beblo R., Mauckweiland l., 2008, "*Strain Induced Anisotropic Properties of Shape Memory Polymer*" – Smart Materials and Structures, vol.17, 055021 (7pp).

[135] Huang W.M., Lee C.W., teo H.P., 2006, "*Thermomechanical Behaviour of Polyurethane Shape Memory Polymer Foam*" – Journal of Intelligent Material Systems and Structures, vol. 17, no.8-9, pp.753-760.

[136] Atli B., Gandhi F., Krast G., 2007, "*Thermomechanical Characterization of Shape Memory Polymers*" – Proceeding of 2007 SPIE Conference on Smart Structures and Materials, March 18-22, San Diego, California.

CHAPTER 3
WING MORPHING: STATE OF ART

3.1 Introduction

A collection of new technologies are being developed that may allow aircraft to readily change their shape during flight. The recent advances in adaptive structures and smart materials have created much interest in aircraft applications of these technologies.

In particular, one of the areas of high interest of these applications is a "morphing wing" aircraft, which would be able to change its wing shape over multiple, dissimilar flight segments.

The term "morphing" has Greek root (μορφη) and it indicates shape in general but in this context with another acceptation it may be considered. Allowing the wing to change its geometry and shape over different mission segments could maximize the efficiency and performance of that aircraft over the entire mission considered. Therefore, it is important to investigate the possible advantages that an aircraft with a morphing wing could gain over a conventional fixed wing aircraft. The main focus of this thesis work is to examine the benefits of allowing the geometry of an aircraft's wing to change during flight while taking into account other aircraft subsystem interactions. The term "Morphing wing" generally describes an aircraft wing or structure that can change size and shape during flight to enable the aircraft to drastically change its standard performance or characteristics. For aircraft, performance usually implies cost (energy or monetary), weight, and maneuverability.

Classic aircraft wings have a fixed geometry and are designed to suit all mission segments, but do not achieve a favorable airframe configuration for any of the individual mission segments. With morphing wing technology it may be possible to overcome this less than optimal design by allowing the wing to "morph" from one configuration to another during a mission to achieve the best overall configurations for each flight segment. Of course, wing morphing comes with penalties that must be taken into account. There will be added weight and energy consumption by the overall aircraft system due to the addition of actuators that are used to physically morph the wing.

3.2 Brief History of Morphing

From an historical point of view morphing concept is connected to physic consideration and since aeronautic origins it has been exploited.

The concept of a morphing aircraft design has been around since 1903 when the Wright brothers made their first flight. Morphing, from Webster's dictionary, can be defined as "to cause a change in shape" and has been attempted in the aircraft industry several times with ideas such as the AFTI/F-111 MAW and the F-14. True aircraft morphing could be described as a smooth change in physical shape that produces beneficial and desirable differences in the flight characteristics of an aircraft.

Throughout the history of the aircraft, airplanes have been designed for particular tasks. An aircraft's assignment is based on its performance and physical shape. Take for example a World War II bombing aircraft; although good at carrying large payloads great distances, they were unable to defend themselves adequately and required escorts of smaller, more agile fighters for protection. Today we have thousands of aircraft, each one being the best for its given assignment. What morphing can enable us to do is provide a mission adaptable aircraft suitable for many tasks, instead of being limited to a select few. It can also be used to enhance the characteristics of an aircraft that is already in use (such as the F-18A with its active aeroelastic wing) and make it better at what it already does.

By changing the shape of the wing, the camber of the airfoil, or even the roughness of an aircraft's skin, the aircraft of the future will not be mission specific, but instead be able to adapt to many different situations and requirements. One can look at several designs and see how morphing is in use today and also see how far research has come and where it is looking to go in the future.

When on December 17th 1903 at Kitty Hawk (North Carolina) On December 17, 1903 the first aircraft flew in Kitty Hawk, North Carolina for twelve seconds and covered a distance of 120 feet [2] The first vehicle heavier than air, the Wright Flyer, took fly in order to have manoeuvrability it had wings that were controlled by means of connecting rods was able to be deformed (through torsion): that control techniques can be considered with reason an adaptive system with a morphing wing.

This aircraft, called the Wright Flyer, used morphing to control its flight. To do this the Wright Brothers utilized a concept of morphing called wing warping. They used a variety of pulleys and cables to physically twist the wing to change the direction of the plane.

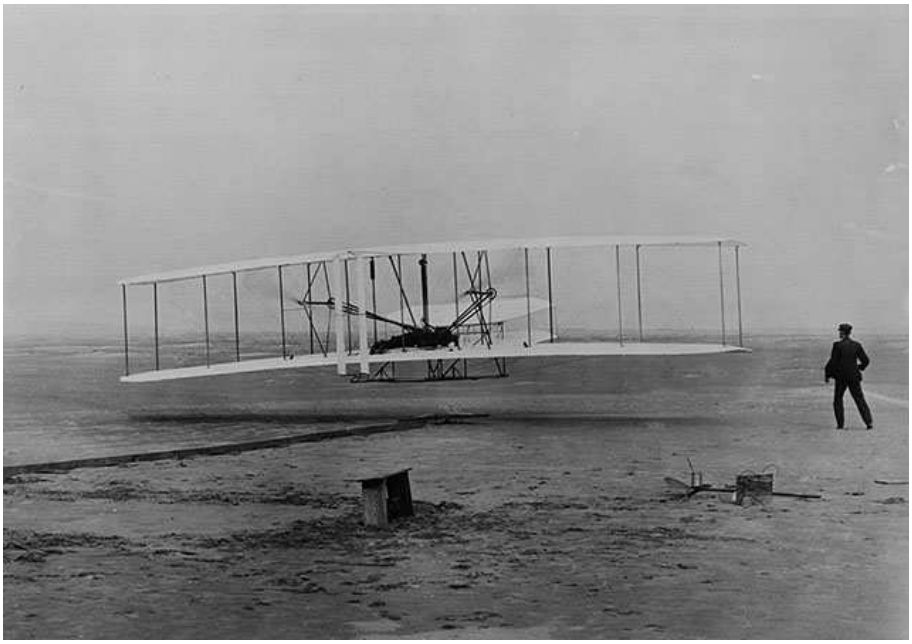

Figure 3.1 "The Wright Flyer" (http://www.nasm.edu/galleries/gal100/wrightflight.jpg)

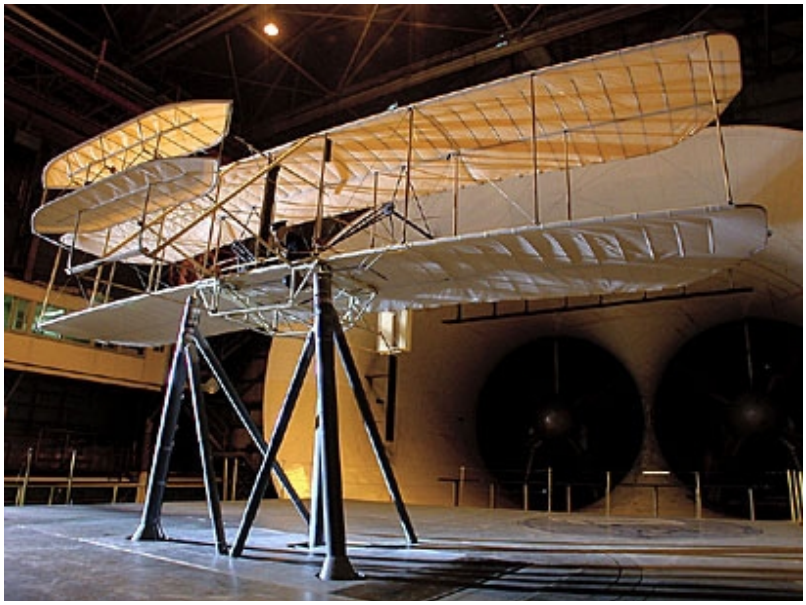

Figure 3.2 "The Wright Experience" project during the centenary : wind gallery test for 1903 Wright Flyer model [1]

The Wright brothers came up with this revolutionary system by twisting an empty bicycle tube box with the ends removed [6]. By twisting the surface of each 'wing', they

changed its orientation with respect to the oncoming wind. Such changes in position resulted in changes in the direction of flight. They tested their theory using a small kite, and later used this method to control the Wright Flyer.

Since first Wright brothers fly, airplane designer have started to find new solution for improving airplane efficiency and performances. Typically, aircraft wings are designed so that they are optimized for an assigned flight condition, but they vice versa cannot assure same efficiency during other flight conditions.

These drawbacks, through deflections of appropriate conventional control surfaces (hinged on leading or trailing edge), can be reduced.

So these control surfaces influence the field of motion all around the wing, modifying her camber in certain regions, so determining aerodynamic forces and momentum variation on the wing.

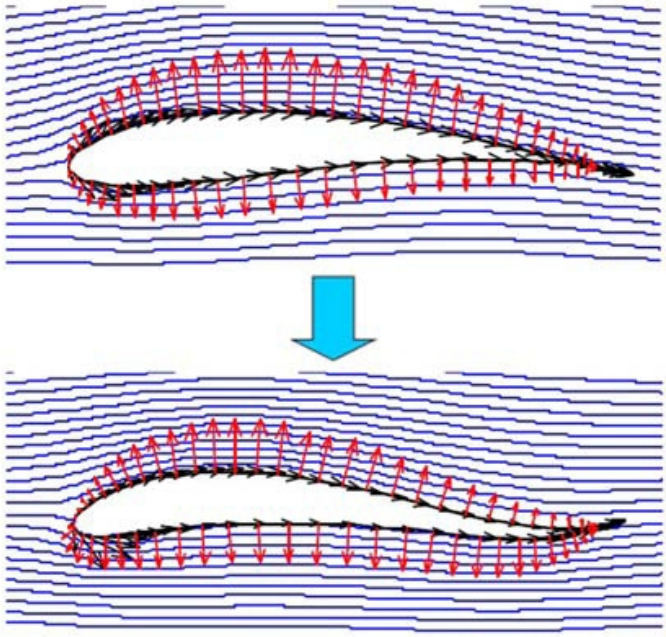

Figure 3.3: Example of a wing profile morphing producing aerodynamic forces and momentum variations

Since 1980, a lot of researchers have investigated about system actuation and shape control structures using adaptive materials (generally these technologies are named "Smart") for a flight efficiency and performances improvement, in order to be able to modify wing shape according to specific flight conditions.

A "Smart structure" involves distributed systems and actuators and one or more micro-processors analyzing sensor output and by means of control theory for actuator activation

so, strains and /or localized displacement can be obtained for a structure behaviour alteration. In this context a lot of disciplines are integrated in terms of vibration and damping structural control, aeroelastic stability control, shape control and stress distribution involving many fields of applications from surgery, civil, biomedical, aerospace, mechanics and so on.

From a biological point of view, birds are a natural example of wing morphing at work. It would be negligent for scientists and engineers to overlook birds for motivations on morphing wing designs [1] Birds are able to fold, sweep, twist, and change the cross-section of their wings during flight. The aspect of particular interest with regards to these wing mechanisms is that they are highly integrated in terms of structure and function. For example, a bird's wing is able to lift and propel while providing the necessary forces and moments to trim (i.e. balance).

Different configurations that birds use for different flight conditions are shown in Figure 3.4. This figure shows that the bald eagle extends his wings to maximize his wing span and wing area. This configuration minimizes the amount of effort required (i.e. power) to soar at low speeds (i.e. loiter). Conversely, the bald eagle tucks his wing to minimize his wing span and wing area in order to reduce drag. This configuration allows for higher speed flight (i.e. dash).

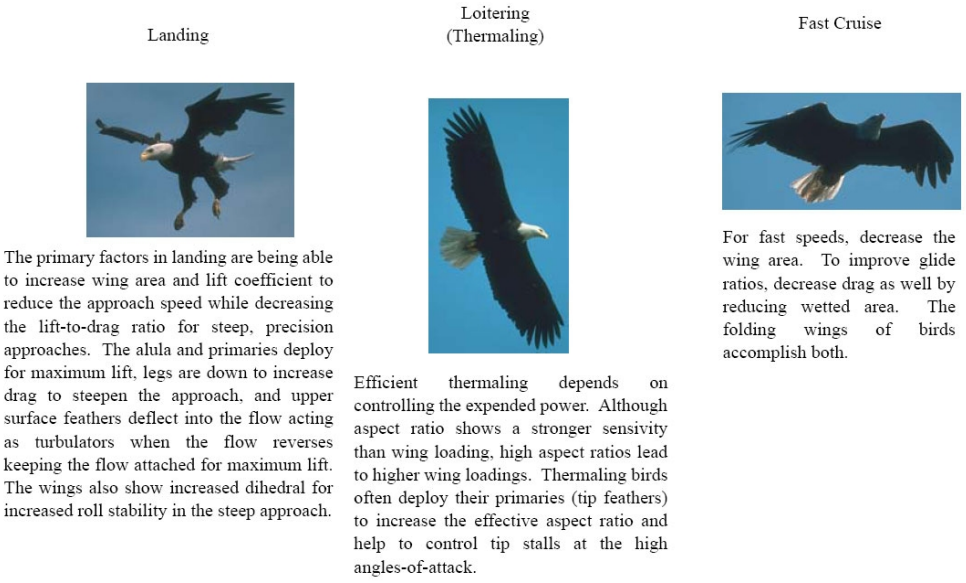

Figure 3.4 :Summary of bird flight conditions and geometry changes [1].

The concept of changing the geometry or shape of an aircraft's wing or other components

during flight has been around since the beginning of controlled flight [1]. The Wright brothers used wing twisting techniques for roll control when flight was in its infancy. Other early morphing technologies included retractable landing gears for reduced drag and foldable wings for increased transportability. Trailing edge flaps and fowler flaps have been used to change the wing camber and area during flight, typically at low speed segments such as takeoff and landing, thrust vectoring has also provided benefits during takeoff and landing segments, in addition to increasing an aircraft's manoeuvrability. Variable sweep angle wings have also been used on a number of aircraft configurations to account for the optimal geometry contrasts between subsonic and supersonic flight conditions. A timeline of when different morphing capabilities were introduced is presented in Figure 3.5.

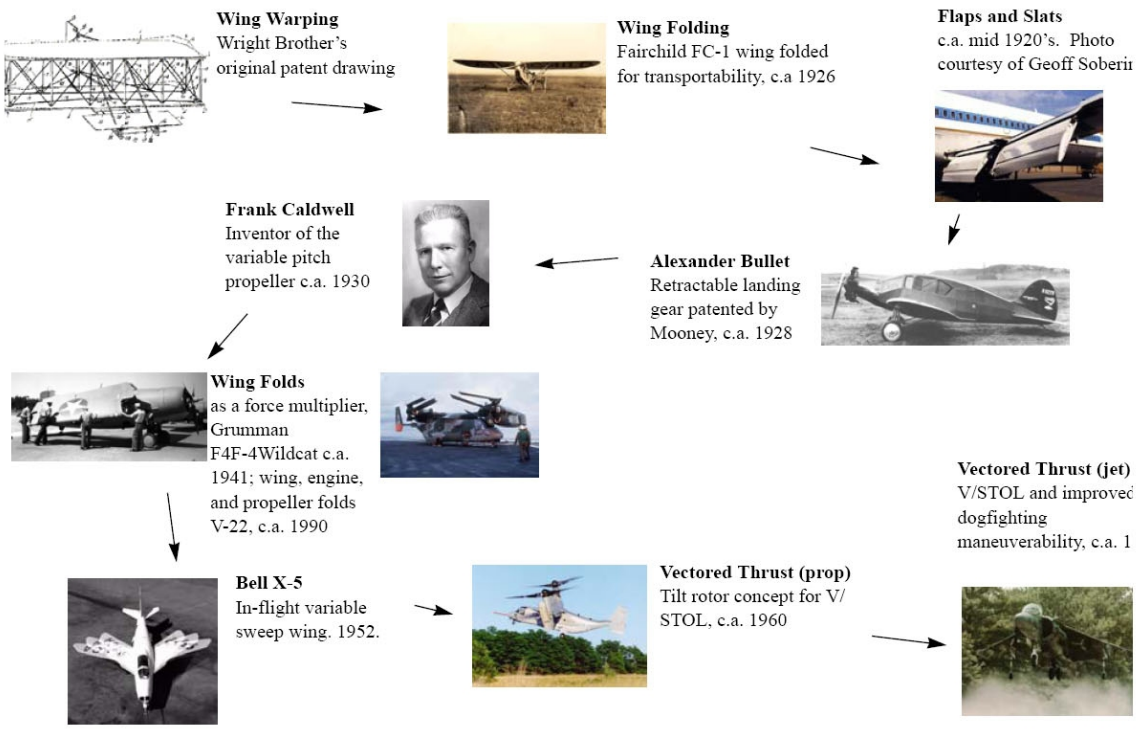

Figure 3.5: History of aircraft morphing technologies [1]

The ability of wing surface to change its geometry (morphing) during flight has been of great interest to researchers and designers over the years: an adaptive wing allows to diminish the number of compromises that a designer is forced to accept to ensure the operation of the airplane in multiple flight conditions [2]

By using an adaptive wing, whose geometry varies according to changing circumstances of external aerodynamic loads, it is possible to fully explore the potential of airflow in each part of the aircraft mission profile, resulting in an increase of aerodynamic performance during cruising flight as well as during manoeuvre, and in a more efficient structural design [3-8]; therefore, having to choose at the design stage between high efficiency or high manoeuvrability, as the need to consider aerodynamic optimization for a single flight condition would no longer be necessary.

For this reason many companies and universities follow a multidisciplinary optimization and systems approach to morphing solutions, also focusing on the integration of computational fluid dynamics (CFD) and computational structural dynamics (CSD) models for geometric optimization; moreover, morphing wing airfoil and configuration geometry, design methodology, effectors, flight control, aeroelasticity and stability are taken into consideration too (an overview can be found in [10]).

Moreover, estimated 1& reduction in airfoil drag would save the U.S. fleet of wide-body transport aircraft $140 million/year, at fuel cost of 0.70 $/gal (source NASA Dryden Studies). For a medium range transport aircraft with an adaptive wing, the projected fuel saving should be about 3-5%, depending on mission distance.

Usually in literature this possibility to change the wing shape is also referred to by the name M.A.W. (Mission Adaptive Wing) as shall be presented in the following.

At present, the use of multiple aerodynamic devices (such as flaps, slats, etc.) represents a simplification of such general idea. The use of traditional control system (with a fixed geometry and/or location) allows to obtain high aerodynamic performance in a fixed range number of flight conditions, when the aircraft comes out of that range, these traditional systems can be neutral or negatively influence the development of aerodynamics, with obvious consequences (lower efficiency).

Currently, several research programs are underway to further understand the potential for morphing wing technologies such as hinge-less control surfaces, variable wing twist, and seamless variable camber. These new technologies could provide drastic changes in an aircraft wing's shape and size, which could produce an abundance of different performance benefits. The scope of all of the possible advantages that a morphing wing could provide has yet to be truly realized. NASA's Aircraft Morphing Program and DARPA's Morphing Aircraft Structures program are currently engaged in large-scale coordinated efforts for the development of morphing wing aircraft (Roth and Crossley,

2003).

One of the more interesting examples to come out of the DARPA Morphing Aircraft Structures Program is the Lockheed Unmanned Air Vehicle (UAV) with in-flight wing folding capability. The main performance improvements that morphing provides this aircraft come from its variable wing area, wetted area, and aspect ratio, which allow efficient operation at both high and low speeds and altitudes. The Lockheed UAV folding wing concept combines desirable attributes from several different types of aircraft platforms, as shown in Figure 3.6. This new design combines the aircraft services of reconnaissance, loiter, attack, and stealth (i.e. low observability). The combination of these attributes allows the Lockheed UAV to perform a hunter-killer mission (i.e. to search and destroy a specified target). Generally a "package" or group of aircraft with different functions is required to perform this type of mission, but the Lockheed UAV concept can conduct this type of mission solo. This in turn reduces the amount of aircraft, ground support, and overall cost required to perform such a mission.

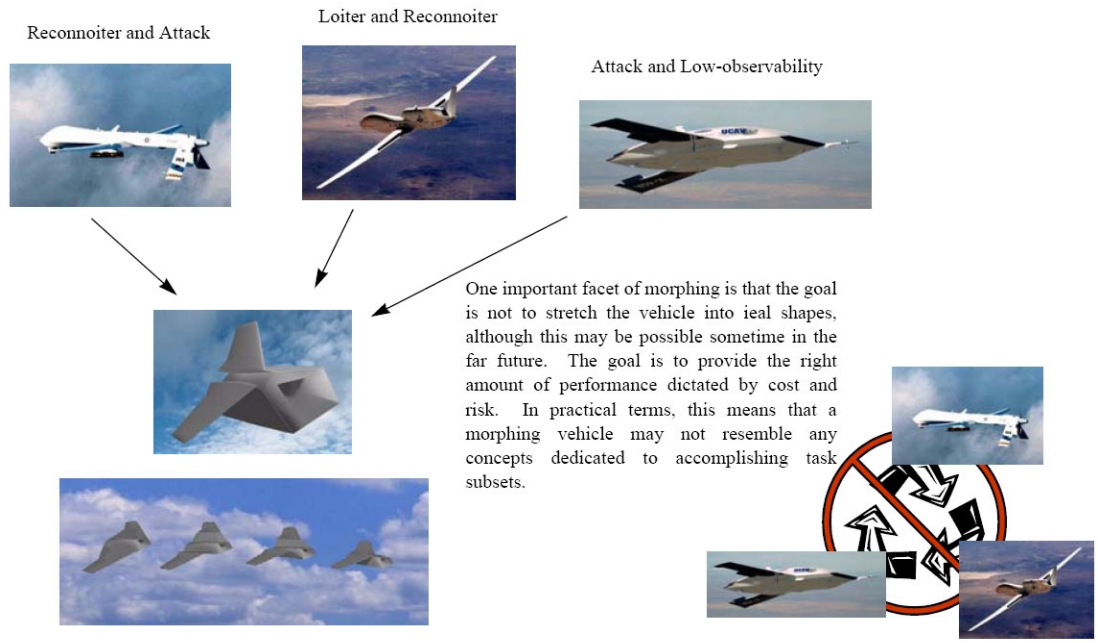

Figure 3.6: DARPA morphing aircraft structures Lockheed hunter-killer aircraft concept [2].

3.3 Methodology for structural wing morphing

In this section different methods for realizing the adaptive wing will be discussed, as a result of the earlier studies found in literature.

Research activities carried out on a wing morphing by means of Shape Memory Alloys (S.M.A.) will be presented in the next paragraph.

At present, several studies are underway aimed at understanding the potential of adaptive wing technologies: these new technologies have the ability to alter substantially the shape and size of the wing, which can lead to many benefits.

Aircraft wings that can change their geometry during different flight conditions can maximize the efficiency and performance of the airplane [1], intended as increased payload or range, noise or weight reduction, less polluting emissions, etc.

The idea of changing the wing shape or geometry is far from new. Referring to the Wright Flyer. The first heavier than air aircraft with the engine, it could change the curvature of the wing by means of some cables actuated directly by the pilot.

As **Renken** [11] has highlighted, since 1970, aircrafts have used devices able to increase lift during take-off and landing but thanks to a heavier aircraft and cruise velocity growth also wing stiffness is increased because of various aeroelastic problems (divergence, flutter, etc.): in order to solve these problems ailerons and flaps have played a rule for wing twisting.

In the middle of Seventies researchers seriously took into account a development of a morphing wing. Mostly of these researches have been based on two concepts active control of camber along wing span and on flexible wing use, able to exploit aeroelastic forces in order to obtain desiderated strains.

Until now a lot of studies have focused attention on wing morphing. However they are not aiming at obtaining only one purpose.

In fact, wing geometry modification for shock waves control during transonic flight (turbulence control, wake control in laminar flow separation, vortex, active flutter control) [2] have been studied.

Adaptive wing is able to assure a relevant aircraft performance improvement.

However, a similar aircraft realization a new design and technical challenge requires.

Traditional approaches based on extremely rigid and light structure where aerodynamic optimization is related to a defined flight condition have to be updated in order to develop

structures intrinsically deformable and always adaptable real time and in flight according to operative condition imposed by the mission requirements.

It is clear that wing morphing is strictly linked to smart materials availability and also to actuation solution in any case able to assure necessary structure strain ability (by internal stiffeners and surfaces under aerodynamic loads), even if structural integrity and sustainability to applied loads is constantly warranted.

In this context, S.M.A. may be a valid solution for realization of distributed actuators able to assure desiderated local shape variations.

Focusing our attention on adaptive wing concept with the purpose of wing profile geometric optimization in the following all previous researches, about wing camber modification for an aerodynamic improvement or traditional control substitution, shall be illustrated.

In particular, aerodynamic efficiency improvement of hingeless wing profile (without hinged flap) shall be considered.

Moreover, the conventional hinged mechanisms are effective in controlling the airflow, but they are not efficient, as the hinges or other junctions usually create discontinuities in the surface, resulting in unwanted fluid dynamic phenomena.

This hingeless solution is part of wing and it is able to act an aerodynamic force and momentum variation, adapting to different flight conditions also exploiting a control function. In addition morphing gradually and continuously activated several aerodynamic benefits with respect to traditional control solution can provide.

This avoids use of traditional control surfaces that during deployment are additional obstacle to the flow, so inducing additional drag.

Scientific research developed during the last years for an adaptive wing design has provided success which here shall be presented.

Wing shape modification is not new, in fact the Wright flyer was able to modify wing camber. There are several examples also for recent aircraft as F-14 Tomcat or Tornado with the swept angle variation in order to have relevant performances each time at higher or lower speed (so reducing flow compressibility problems).

Even when a commercial airplane deploys its conventional flaps, in practice it is changing the geometry of the wings. However, these examples of geometry changes are still limited, with narrow benefits compared with those which can be obtained employing a wing that is inherently deformable and adaptable in many ways or by changing several

parameters.

Some efforts in the construction of an airplane that can also change the wing geometry, as for F-14 or Tornado, led to some penalties in terms of weight, cost and maintenance, sustainable only for high performance/military aircrafts.

Recent developments in the SMART materials field may allow to overcome these limitations and enhance the benefits coming from similar design solutions [13].

Some modern designs of morphing aircraft can be seen in use today. These include the B-1B *Lancer*, the F-14 *Tomcat*, the AFTI/F-111 Mission Adaptive Wing, and the F/A-18A *Hornet* with Active Aeroelastic Wing (AAW). Both the B-1B (figure 3.7) and the F-14 (figure 3.8) use "swingwing" technology so that the wing can have variable sweep. This is done primarily for supersonic aircraft, where swept wings are highly beneficial when travelling at high speeds.

The AFTI/F-111 (figure 3.9) and the F/A-18A (figure 3.10) however create a seemless camber change to maneuver more quickly, achieve better lift to drag ratios, and to have greater ranges in flight.

The B-1B officially went into operation on October 1, 1986. It has a blended wing-body configuration and can change its wingspan from a more 78 feet to almost 140 feet by changing the sweep of its wing [19]. In the unswept position, the B-1B can take off in shorter distances and increase its range. In the swept position the B-1B can achieve speeds above the speed of sound. This can be used for high-speed penetration into hostile territory or to escape potential threats. The morphing aspect of this bomber has left it with several world records for speed, payload, and distance.

Figure 3.7 : B-1B Lancer(http://www.fas.org/nuke/guide/usa/bomber/b1-dvic162.jpg[19]

Figure 3.8 : F-14 *Tomcat*(http://www.fas.org/man/dod-101/sys/ac/f-14-053.jpg)[20].

The F-14 *Tomcat* also utilizes swing wing technology much like the B-1B. It was designed to be an air-superiority fighter for the Navy. The swept wings of the F-14 play a slightly different role than the B-1B because the F-14 is a carrier based aircraft.

The variable swept wings are shoulder mounted and are programmed for automatic sweep during flight, although a manual override is available. The wing pivot structure spans the entire center of the airplane. It is 22 feet wide, and is electron welded out of titanium[20].

One drawback of this structure is that its enormous size greatly increases the weight of the plane. The span of the airplane can increase from 38 feet to 64 feet in the unswept position. The normal sweep range for the wings is 20 to 68 degrees. It has an over-swept position of 75 degrees that allows for hangar storage within the carrier [20]. Not only does the morphing aspect help decrease storage space, but when completely unswept, it helps the F-14 take off and land in the short span of the carrier deck. When in the swept position the F-14 can reach velocities greater than twice the speed of sound. Both the F-14 and the B-1B use the swing wing to their advantage and are more versatile in their operations because of this morphing capability.

In this context it is clear that during flap deployment for a liner wing geometry is changing. However, these examples are related only to limited benefits with respect to those ones achieved by using a wing completely deformable and adaptable to various aspect.

Often an aircraft realization able to modify, even if partially, wing geometry has penalized his the development because of weight, costs and maintainability. Recent studies in smart materials can overcome these limitations and amplify advantages through all innovative design solutions.

A lot of methods exist in order to change a wing geometry in different studies:

- Variable camber (local or global);
- Inflatable wing;
- Wing span variation.

- ***Variable camber (local or global)***

Wing camber variation derives from the possibility, during a subsonic flight, to continuously adapt wing profile to flight conditions, so increasing wing profile Lift/Drag ratio[14]; there are aerodynamic benefits according to a gradual activation.

In these situation a gradual wing camber variation limited to determined areas (leading. edge L.E and trailing edge T.E.) occurs, or equivalently, whole wing as control surface (in such case a twisting on the wing appears as for the Wright Flyer) is used.

Moreover, some applications also realized a small curvature change on the wing upper surface to increase the aircraft performance in transonic regime [2].

Though wing camber variation solution was born contemporary to aeronautics, the design of new devices able to exploit determined deformations and control systems for their regulation, is not simple: a lot of studies have been carried out.

Probably, the first example in literature of a variable camber wing has been presented by **Parker** [15] in 1920. This concept involved changing the wing configuration through aerodynamic loads on the wing. This scheme divided the wing into three sections using two wing spars, one at the leading edge and the other at the two-third chord. The portion of the wing between the spars was flexible and the portion aft of the second spar was rigid. The ribs were allowed to slide over the rear spar. Thus, when the wing was placed under aerodynamic load the portion between the spars was carried upward while the rear portion being rigid and fixed to it, moved downward resulting in a camber wing.

The wing was covered with fabric continuously expect where the flexible channel was connected to the tailpiece, a 1-inch space was left open to allow the lower portion of the fixed tail to slide to when the wing was deformed.

The wind tunnel test results showed that the wing had a maximum lift coefficient of 0.76 and minimum drag of 0.007.

Since 1978 the **Frost & al**. patent [16] designed a wing L.E. variation by the activation of an internal structure as a flexible beam, surface panels were flexible. Internal structure activation took place by means of screw adequately commanded inducing an opposite motion between upper and lower wing side, so determining a L.E. bending.

A similar concept is due to **Statkus & al**.[17] where two groups of four linking bars allow the camber control: the first group allows the horizontal and vertical motion control of the structure, while the second one allows rotation angle and momentum applied on a flexible skin surface.

A more recent patent has been issued to **Perez** in 2002 [18], who conceived a mechanism for adjusting the curvature of airfoils, based on a plurality of torsion boxes connected by means of a drive chord, the length of which may be changed using a control command.

In the middle of ’80 the **A.F.T.I.** (Advanced Fighter Technology Integration)/F-111 MAW

(Mission Adaptive Wing) program was one of the first attempts at a smooth variable camber wing. This was a joint project between the United States Air Force (USAF) and National Aeronautics and Space Administration (NASA)[4]. The project called for a significant improvement in aircraft performance by adapting a plane's airfoil shape to each task required by the aircraft's mission. Their solution was a mission adaptive wing (MAW) that allows the leading edge of the wing to travel from +2 to -21 degrees and the trailing edge of the wing to travel from +4 to -22 degrees.

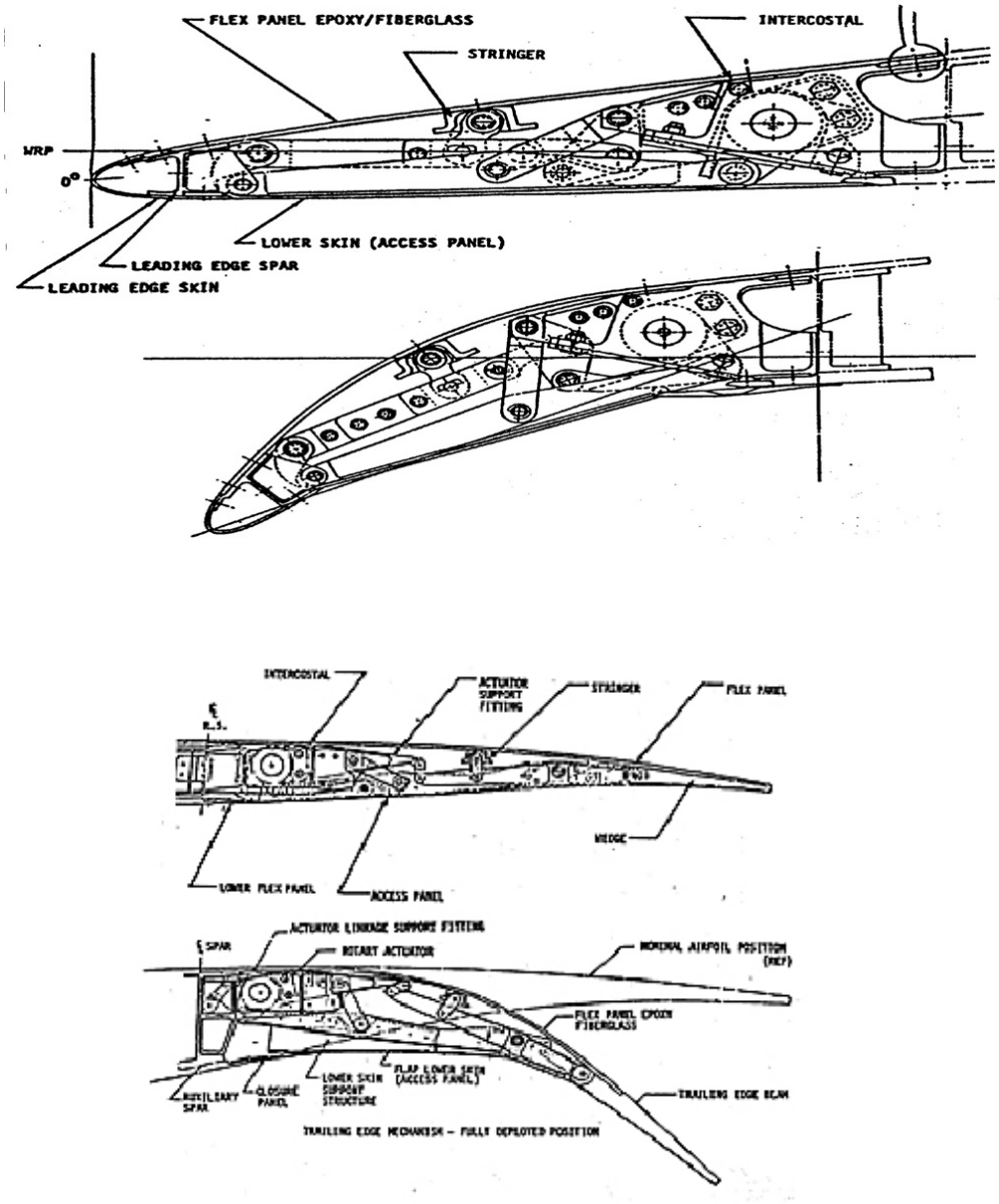

Figure 3.9 : MAW wing concept [9]

The benefits calculated by several studies confirm that the power required to actuate the morphing wing is calculated as a percentage increase in mission fuel required. Both of these 'penalties' are considered over a wide range of values in order to demonstrate the sensitivity to these effects. The optimisation metric of minimum weight of fuel burned is used to represent energy efficiency, instead of the conventional minimisation of vehicle weight [9]. Results for this work are presented in figure 3.10 showing the benefits in terms of mission fuel burned by a morphing concept compared with the similarly optimised non-morphing (fixed-wing) configuration [9] as presented in the figure the mission profile improvement.

In the following results showing benefits related to using MAW solution.

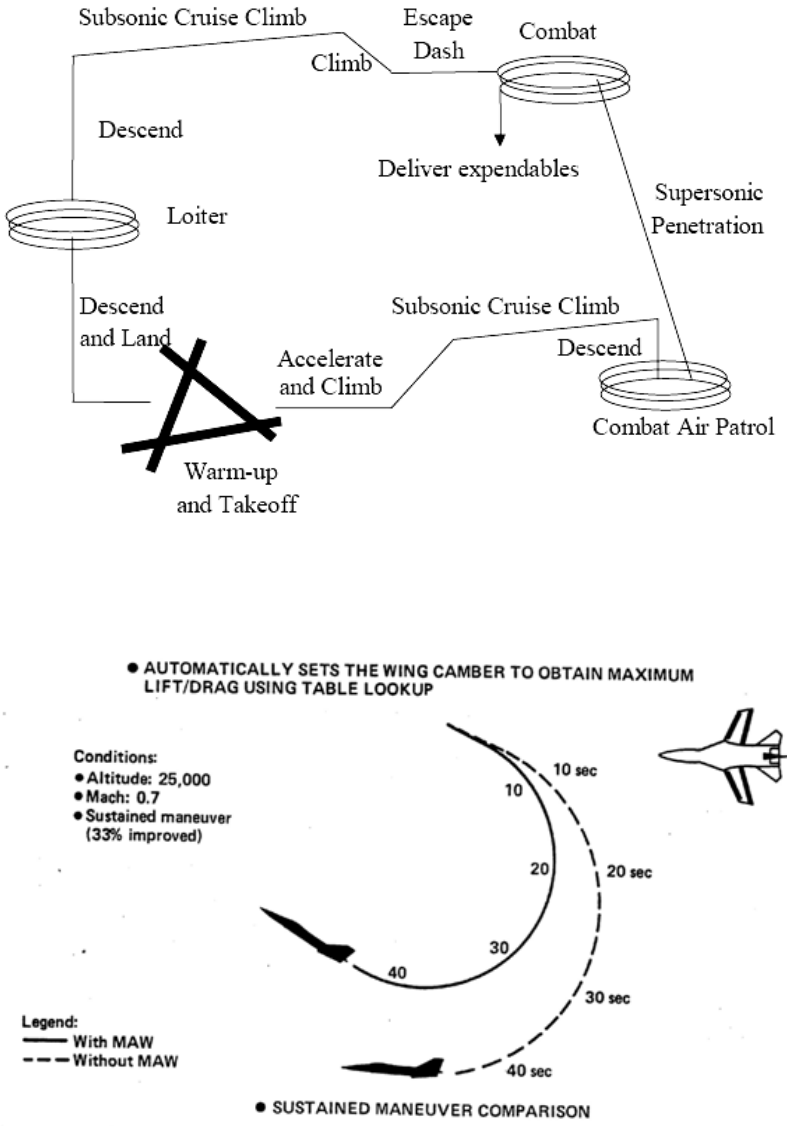

Figure 3.10 : MAW mission profile description [9]

The MAW consists of variable camber leading and trailing edges, controlled by surface actuation linkages, and hydraulic servo systems driven by digital computers. For the camber variation each wing has three trailing edge and one leading edge segments. On the variable camber edges a flexible fiberglass skin is used to cover the wing. While the upper edge is smooth and continuous, the lower edge of the wing has overlapping tapered edges and sliding panels that can accommodate for the chord changes with camber variation. The pilot can choose either manual or automatic modes for the flight control of the wing. In both modes the outboard and midspan MAW trailing edge surfaces respond to roll stick inputs from the pilot to provide flap assistance for roll control[4].

The control system implemented four different operative typology on the basis of dynamic pressure , normal acceleration , Mach number an fuel onboard measurement in order to achieve different optimizations:

- Maneuver Camber Control (MCC) mode maximized Lift/Drag ratio;
- Cruise Camber Control (CCC) mode maximized cruise speed in defined altitude and engine throttle conditions;
- Maneuver Load Control (MLC) measured the aerodynamic momentum produced by the wing and optimized camber in order to shift aerodynamic load towards wing root;
- Maneuver Enhancement/Gust Alleviation (MEGA) mode maximized aircraft response to pilot commands.

The AFTI/F-111 MAW project proved to be successful. The aircraft performance was greatly enhanced with the variable camber wing. However, despite this apparent success, the MAW program faded out in the late 1980's.

During the flight test the AFTI/F-111 have confirmed a performance improvement of 20-30% range enhancement, 20% aerodynamic efficiency growth and 15% increase of wing air load at a constant bending momentum.

Figure 3.11 : AFTI/ F-111 Mission Adaptive Wing(http://www.fas.org/man/dod-101/sys/ac/946-710.jpg).

The Active Aeroelastic Wing (AAW) project at NASA's Dryden Flight Research Center is a two-phase flight research program that is investigating the potential of aerodynamically twisting flexible wings to improve roll maneuverability of high-performance aircraft at transonic and supersonic speeds. Traditional control surfaces such as ailerons and leading-edge flaps are used as active trim tabs to aerodynamically induce the twist. From flight test and simulation data, the program is developing structural modeling techniques and tools to help design lighter, more flexible high aspect-ratio wings for future high-performance aircraft, which could translate to more economical operation or greater payload capability.

The program uses a modified F/A-18A Hornet as its testbed aircraft, with wings that were modified to the flexibility of the original pre-production F-18 wing. Other aircraft modifications include a new actuator to operate the outboard portion of a divided leading edge flap over a greater range and rate, and a research flight control system to host the aeroelastic wing control laws.

AAW flight tests began in November 2002 with checkout and parameter-identification flights and in the same year the aircraft has flown in the sud east zone of NASA Dryden Flight Research center in Edwards, California. Based on data obtained during 50 research

flights over a five-month period, new AAW flight control software was then developed over the following year. A second series of research flights began in late 2004 evaluated the AAW concept in a real-world flight environment, using the newly created control laws in the aircaft's research flight control computer. About 45 research missions were flown over a four-month period in the second phase of flight testing that concluded in March, 2005. Extensive analysis of data acquired during the project is continuing at NASA Dryden.

The Active Aeroelastic Wing Program is jointly funded and managed by the Air Force Research Laboratory and NASA Dryden Flight Research Center, with Boeing's Phantom Works as prime contractor for wing modifications and flight control software development. The F/A-18A aircraft was provided by the Naval Aviation Systems Test Team and modified for its research role by NASA Dryden technicians.

Figure 3.12 : F/A-18A Hornet with Active Aeroelastic Wing (http://www.fas.org/man/dod-101/sys/ac/946-710.jpg).

Researchers at the University of Maryland [21] have designed and implemented a multisection wing model **mandarin-type** based on the NACA 0012 airfoil able and

capable of variable curvature.

Each rib is divided into six sections, ach able to rotate up to 5 deg with respect to the previous one without significant discontinuities on the wing surface; the camber change is obtained by means of pneumatic actuators. Wind tunnel tests showed that the lift produced by a similar wing is comparable to that of the same one piece airfoil, but the surface drag is higher due to the increased required skin flexibility.

Monner & al. [22] within the ADIF project carried out by EADS-Airbus, DaimlerChrysler F&T and DLR, developed a typical example of "Compliant Structure" that is one piece structure which is able to spread forces so that it can deform in pre-determined areas and results rigid to deformation elsewhere.

So, the trailing edge is composed of a flexible structure realized with plate elements connected with a cinematic mechanism.

Each rib is actuated in a single point: the rotation of the commanded plate element is gradually transferred by means of the mechanism to the other elements, to obtain the desired shape. This solution is actually under development for a possible application on the Airbus A-340 aircraft.

Basing on a similar idea, the Second University of Naples developed and simulated a servo-actuated articulated rib [23] (figure 3.13-3.14).

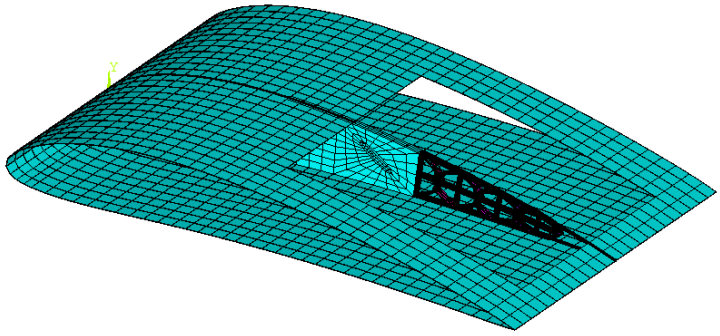

Figure 3.13 : FE model of adaptive wing with elements of deformable rib [23]

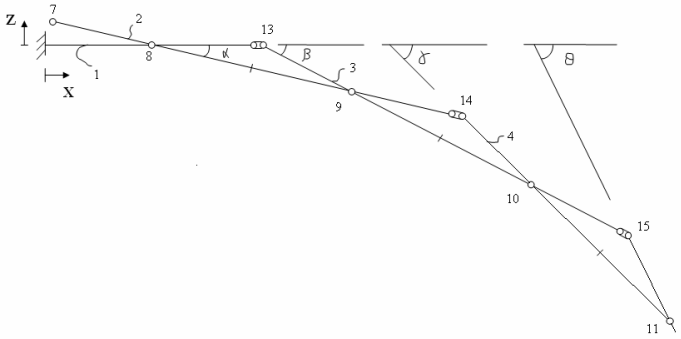

Figure 3.14 : Cinematic scheme of adaptive rib [23]

An analogous inspiration is the project named 3AS (Active Aeroelastic Aircraft Structures) born in 2003 and based on a consortium of 15 European aerospace industrial partners, partially sustained by European Community, with the purpose of developing structural design concept by means of aircraft efficiency improvement.

So instead of design of very stiff and heavy structure in contrast with aeroelastic deformations, during design phase it is better to transform these deformations into an advantage.

Aeroelastic behavior exploitation in a smart way allow using of aerodynamic loads to produce required deformations so determining a structural weight reduction, a lower aerodynamic drag, less control surfaces etc.: this implies a deep comprehension of interaction between structure and aerodynamic loads [25].

- ***Inflatable wing***

Inflatable wings are the most relevant morphing implementation allowing wide wing shape variations.

They are the ideal solution where wings have to be folded up when the aircraft is not in use: then, even if inflatable wings can be realized in different dimension, they give a particular importance for the UAV (Unmanned Air Vehicle) because these aircraft have to be stowed in a very small areas and a relevant characteristic is the weight/volume ratio that makes the inflatable wings a smart solution with respect to the folding wings [26].

The main disadvantages of these wings is related to the absence of actuators for the roll control (ailerons): this lack can be overcome in different ways for example by using wing twisting. Even if the inflatable wing concept was born almost 100 years ago their development and use only in the last decades has happened.

Inflatable wings have been successfully demonstrated in 1950 by Goodyear GA-468, developed as search and rescue military aircraft.

A lot of aircrafts have been developed since 1970 as the Stingray, ultralight (the developer proposed to inflate the wings by helium to have additional lift) (figure 3.15).

Goodyear Model GA-468 Inflatoplane

Stingray

Figure 3.15 : Inflatable wing aircraft [32].

In 1970 first UAV were developed by **ILC Dover Inc**. as "Apteron" that flew successfully but it has never been manufactured: from then, several designs with inflatable wings have been developed [27](figure 3.16).

In 2001 NASA Dryden researcher conducted flight tests with UAV "I2000"[28] (figure 3.17). This UAV had inflatable wings and his camber give a response according to a pressure input: the wings are characterized by inflatable tubes with sponge with the purpose of defining the wing profile shape.

Wing test tunnel done at NASA Dryden flight Research Center assessed that inflatable wings have a similar behaviour of solid wings with similar dimensions and geometry.

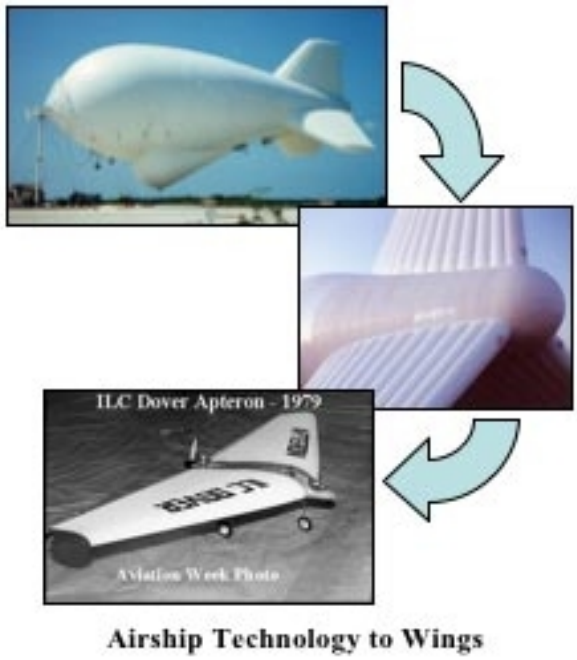

Figure 3.16 : "Apteron" technology from naval experience[27].

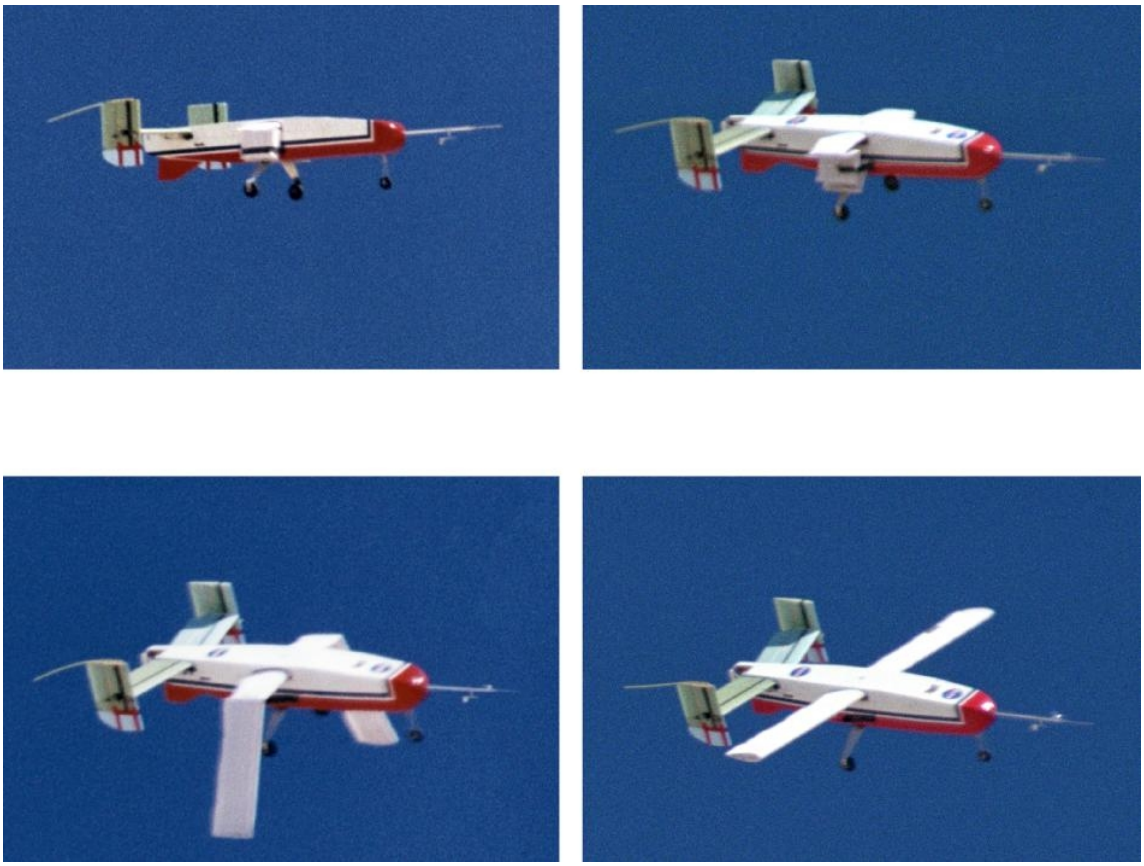

Figure 3.17 : In flight deployment of inflatable wings of "I2000" [28].

This 64 inch span inflatable wing contains five high pressure inflatable cylindrical spars than run span wise from tip to tip and chord is 7.25 inch. Between the spars and to trailing edge of the wing is open-cell foam bonded to the spars and to a rip-stop nylon outer skin.

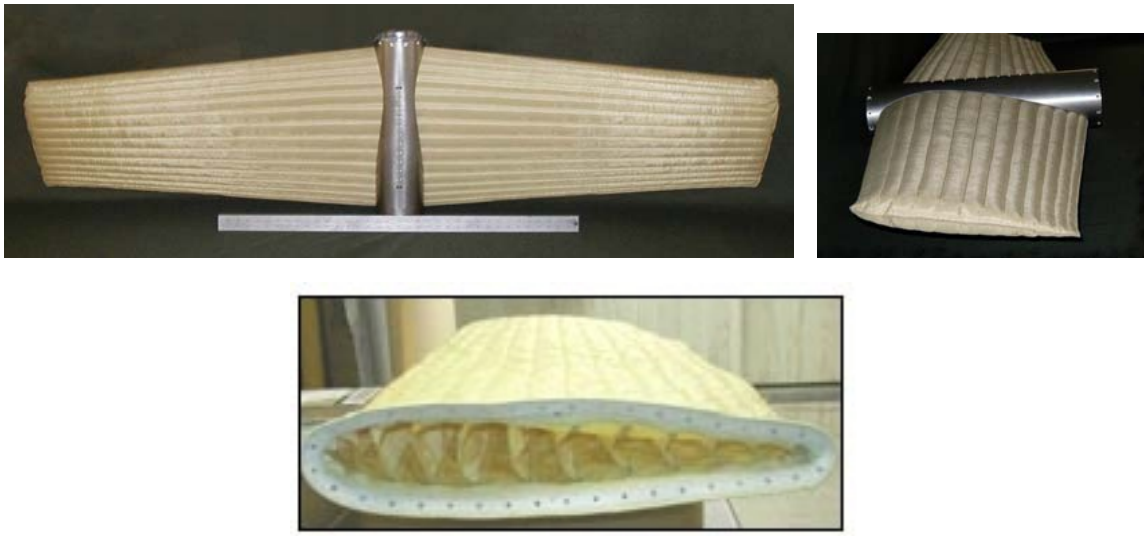

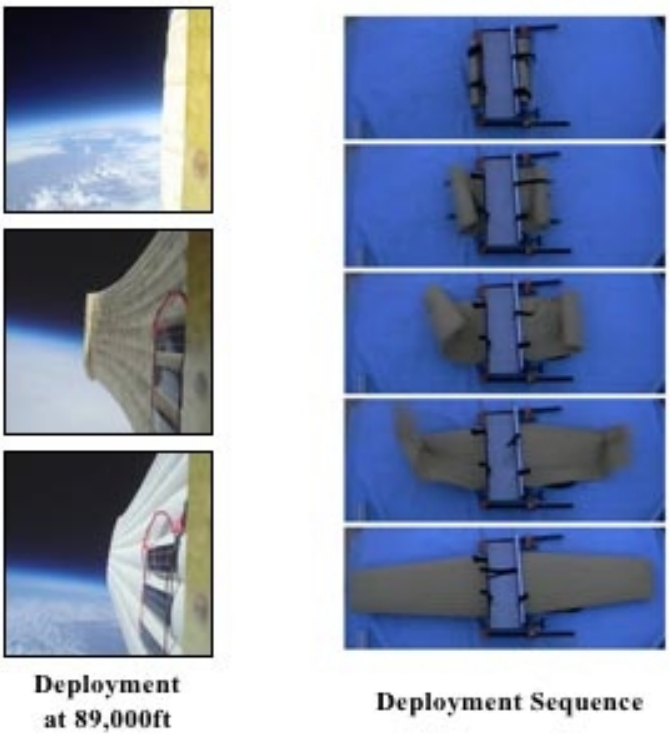

Figure 3.18 : Inflatable wings example in aeronautical and space environment

Additionally, a rib at each tip rigidly connects all the spars to establish wing torsional stiffness. Thermally activated adhesives are used to bond the spars, foam and nylon skin into a contiguous wing structure. The airfoil profile is a NACA 0021 and does not contain any control surface.

This inflatable wing consists of a manifold at the center of the wing to hold the wing spars in position. A small commercial off-the-shelf tank (COTS) with a volume of approximately 35 cubic inches was selected as the high pressure tank source.

Nitrogen gas was selected as the gas source at 1800 psig and was reduced to a wing pressure between 150 psig to 300 psig using ad adjustable pressure regulator.

By using this high pressure inflation system, the inflatable wing can be rapidly deployed on the ground or in the flight within less than a second.

Recent studies at Kentacky University [29] have developed two different typology of inflatable wings. The first one at a constant pressurization able to keep the expanded shape and under stiffening after inflating: the second one wings are composed of a composite material that stiffen after the UV rays exposition [30].

There are also studies for inflatable wings able to act twisting or bending, so deleting all problems related to the lack of roll control.

The Mars Aircraft realization System (M.A.R.S.) is the part of the program at Oklahoma State University (OSU) to develop, construct and test airplane designs for flight on planet Mars [31]. It is a component of BIG BLUE V.

BIG BLUE (Baseline Inflatable wing Glider, Balloon-Launched Unmanned Experiment) is a high-altitude experiment developed, designed, built, conducted and evaluated primarily by undergraduate students in the College of Engineering at the University of Kentucky (UK). The goal of BIG BLUE is to demonstrate the feasibility of inflatable wings for flight in the low-density atmosphere of planet Mars.

While most design use folding wings, MARS uses inflatable wings to overcome the packing problem in the spacecraft carrier.

In the high altitude flight test discussed herein, the completed and semi-autonomous aircraft ascends via weather balloon to a targeted altitude of 100,000 feet in order to simulate the density present in the Martian atmosphere.

The inflatable wings are inflated to a minimum of around 5 psig and a release mechanism is triggered that allows the aircraft to parachute to an altitude of 5,000 feet above ground level, where it is flown under autonomous guidance, and then lands under human control.

The inflatable wings have been manufactured by ILC Dover, Inc. out of polyurethane coated rip-stop nylon.

The airfoil profile is NACA 4318. each wing semi-span has a root chord of 19.5 inches and a tip chord of 13.5 inches with a semi-span of 36 inches. The wings have been constructed in two semi-spans such that they could be mounted externally to a fuselage, but they did not include mounting attachments.

The wings have been attached to a balsa sandwich wing mount using a light weight low temperature fiberglass tape with a silicon based adhesive.

The wing mounts have been in turn connected to one another using two carbon fiber rods.

Full three axis control has been affected only by the tail control surface. A small scuba air tank was selected as the pressure tank source. The fuselage has been initially constructed out of a composite using a balsa sandwich. While this design has been used for low altitude flight testing, later designs used a composite with a card stock sandwich to reduce weight and was used for the high altitude mission.

➢ ***Wing span variation***

Aircraft able to modify wing span may have good aerodynamic efficiencies within a wide range of speeds. Typical examples are military aircraft with variable geometry wing, as illustrated before for F-14 or Tornado, where it was possible to modify the swept angle and so the angle of attack with the flow so reducing compressibility effects at higher speeds.

Today several studies are object of investigation where by means of telescopic wings wing span is possible. In other words these aircraft have wings separated in different parts, each one extensible and/or retractable according to the required performances.

In this way wide wing surfaces at low speed flight is possible so reducing fuel consumption and contemporary relevant maneuverability at higher speeds, closing the wings. Proposals for telescopic wings during at early of '40 may be found.

In 1990, the naval research laboratory built and tested an experimental non-recoverable ship-launcher expendable radar decoy named **F.L.Y.R.T.** (Flying Radar Target) [32-33] as shown in figure 3.19. The first test flight occurred in September 1993. FLYRT was launched with rigid folded wings and tail surfaces from MK 36 launcher by using a solid propellant rocket motor, which burned for about 1.6 seconds. The fully expanded rigid wing has a span of 2.4 meters and weight of 60 kg .

Immediately after launch, the tail fins were unfolded mechanically to control the vehicle during ascent. After the booster had been jettisoned, the UAV coasted to the apogee of the launch trajectory, where the rigid wings were unfolded to the electric motor stated.

Figure 3.19 : F.L.Y.R.T. during operative mission [32-33].

A total of 13 drones were built before the program ended, and the decoy successfully demonstrated the defense of a variety of ships against simulated radar threats.

However, there is no evidence of constructed devices., recently in 1997 **Gevers Aircraft Inc.** company have designed a telescopic wing (with variable wing span) on a amphibious vehicle[32]. When the wings are closed, they allow a higher cruise speed, while after deployment relevant performances are assured.

About the same concept the U.M.A.A.V. (Unmanned Morphing Aerial Attack Vehicle) aircraft developed by **AeroVisions Inc.** [34] for the D.A.R.P.A. Morphing Aircraft Structures program. This aircraft with maximum wing span is able to glide at low speed with a minimum fuel consumption.

The intermediate configuration allows higher cruise speed during before the landing phase. The reduced wing span phase assures higher maneuver speed and allows to use this aircraft for faster attacks. In figure 3.20 different configurations with a radio-commanded demonstrator developed by AeroVision Inc. are shown.

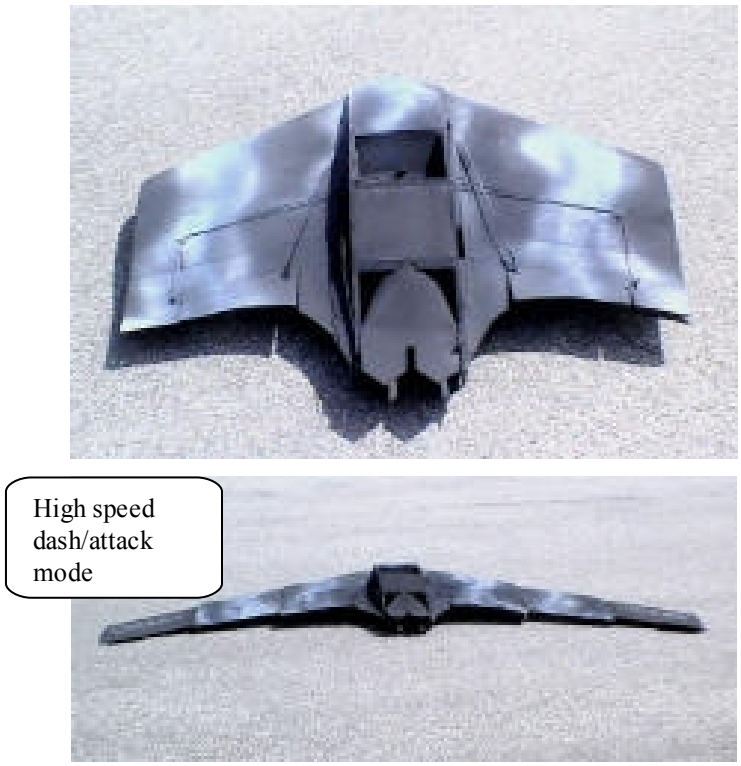

Figure 3.20 : UMAAV model with variable wing span in loiter mode(1), fast cruise mode(2), high speed dash/attack configuration (3) [34].

Another project in these context is **A.L.I.C.E.** (Air launched Integrated Counter-measure, Expendable) [35]. It is an unmanned platform developed by AFRL Vehicle Research section that can be air launched from a tactical aircraft at speeds up to 0.8 mach and altitudes up to 45,000 ft. the design is shown in figure 3.21. after launched from the tactical aircraft, ALICE glides using tail control surfaces until it reaches a speed of approximately 250 knots.

The rigid wing and propeller then deploy and heavy fuel engine starts. ALICE will cruise approximately 200 nautical miles in one hour before the outer rigid wing panels deploy for loiter. In the loiter mode it will operate at 65 knots with a two hour endurance and it is able to carry a 25 lb payload. Research efforts included development of the polymorphic wing, a JP-8 fueled rotary engine, a high efficiency starter/generator, a folding variable pith propeller and an advanced EW payload.

Figure 3.21 : ALICE mission profile from launch to loiter phase [35].

Neal III & al. [36] at the Virginia Polytechnic Institute studies the design and development of the MORPHEUS wind tunnel model (figure 3.22), within the adaptive planform vehicle experiment (APVE), that combines large and small wing shape variations for fundamental research in modeling and control morphing for vehicle maneuverings. Planform variations include major changes in wingspan, sweep, and tail configuration such that the aspect ratio, planform area and static margin are significant modified. Control morphing refers to smaller motions that alter lesser portions of the flow field to maneuver without significantly affecting the aircraft dynamics. For MORPHEUS this consists of independent wing twist, which replaces elevons on conventional vehicles.

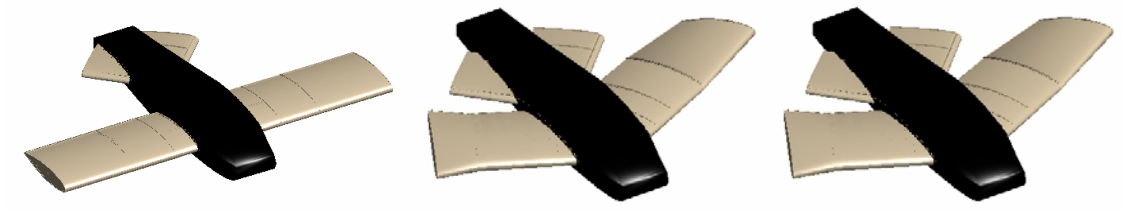

(a) **(b)** **(c)**

Figure 3.22 : MORPHEUS concept: (a) loiter, (b) dash and (c) asymmetric manoeuvring configurations[36].

In this same area (span morphing) can be inserted the **A.M.P**. (Aircraft Morphing Program) of NASA and **M.A.S.** (Morphing Aircraft Structures) program of DARPA that have been engaged in a large scale cooperation for the development of an airplane with an adaptive wing [37].

The research program at DARPA aims at achieving an airplane wing that can drastically change its shape, so as to meet, within the same mission, the conflicting requirements of loitering at low speeds on a particular area and a high maneuverability at transonic speeds: an UAV having similar characteristics would present a great adaptability to many different missions and be able to perform multiple functions.

Such an aircraft would have the advantages of several different platforms: those of a fighter plane, fast and with high maneuverability at high speed (but low aerodynamic efficiency), combined with those typical of a surveillance aircraft, aerodynamically efficient but not particularly fast and maneuverable; in addition, one could decide when to prefer one or other characteristics [38]. This brings immediate benefits in those missions where different skills are generally requires, and thus involve multiple aircraft. A similar aircraft would be able to carry out the mission alone, with a great reduction of costs and resources involved. DARPA is currently developing two parallel projects.

The Lockheed Martin project called **"Agile Hunter"** (figure 3.23) [24, 39] involves the design and implementation of an UAV with the ability to fold the inner sections of the wing (also called Z-wing) near the fuselage, so as to hide part of an area and reduce drag during the transonic flight at low altitude: in fact, the wing folds into two parts that rotate in the opposite way during the deployment or withdrawal.

Improvement in data collection are related to the following: at Mach 0.6 a morphing capability from 0 to 130 deg is demonstrated over 65 second period (with a controllable, reliable and precise actuation), with angle of attack (AoA) adjusted to maintain lift and inboard motor torque near zero [40, 41].

The Z-Wing program has been stopped after the company experienced several problems during the initial flight testing.

However, studies are already underway for all adoption of a Shape Memory Polymer, named Veritex (figure 3.24), a composite based on Veriflex produced by CRG Inc. [42]: when heated, these materials become elastic allowing rotation around the hinges; when cooled, they stiffen, finally, they "remember" their original shape when reheated again [43].

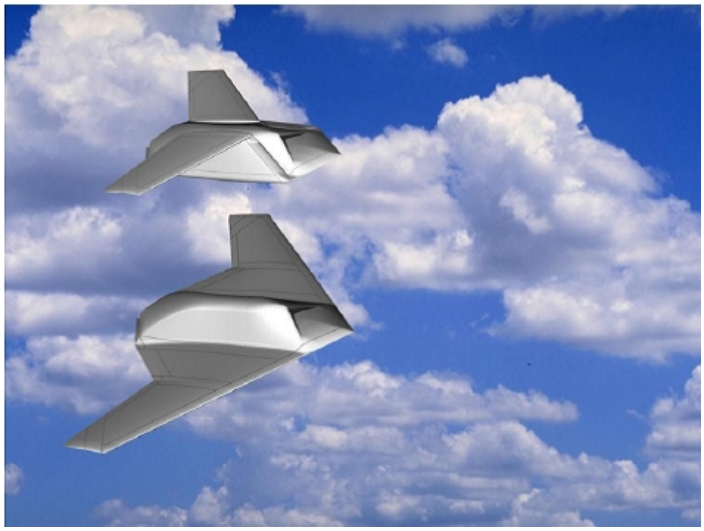

Figure 3.23 : Z-wing concept by Lockheed Martin [43].

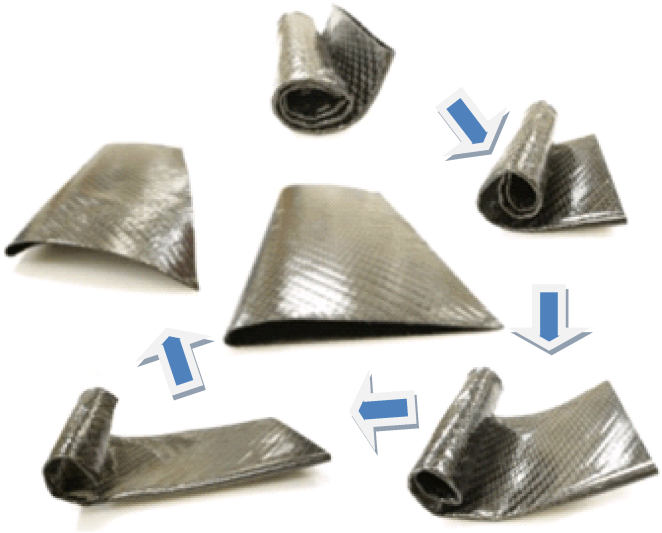

Figure 3.24 : Veritex wing sample working cycle. When heated the wing unfolds and recovers its initial shape [42].

A Multi-Purpose Unmanned Aerial Vehicle (**M.P.U.A.V.)** was also briefly considered by Lockheed Martin called The Cormorant [10] as shown in figure 3.25.

The idea is that the drone could handle all-weather reconnaissance, battle damage assessment, or specialized mission support for the submarine. This UAV could be launched from a submarine, then perform wing shaping for a different mission and return to the boat.

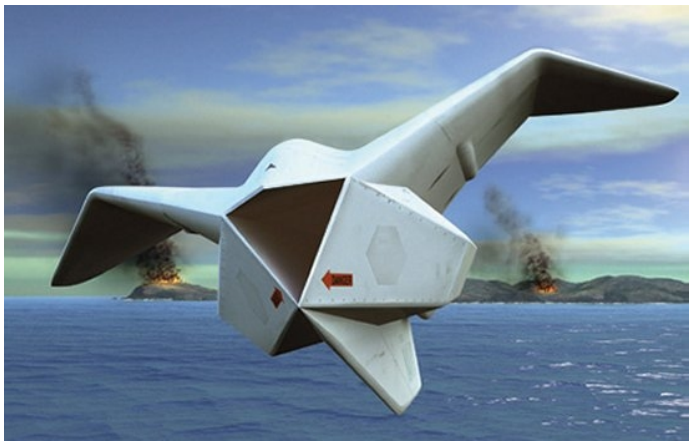

Figure 3.25 : The Cormorant concept by Lockheed Martin [10].

Another project for adaptive wing as Z-wing is the DARPA project named Vulture Program well known as **Odysseus** [9] The solar-powered concept aircraft is as radical as the mission it is designed to accomplish, combining three self-sufficient "constituent aircraft" in a unique Z wing configuration (figure 3.26) that spans almost 500 feet (150 meters). The modular design provides several advantages - the shape of the aircraft can be adjusted to maximize the solar collection properties during the day and spread flat for aerodynamic efficiency at night-time, when energy stored in onboard batteries is used to drive the aircraft's electric motors. Because each of the constituent vehicles is capable of autonomously docking at altitude, the design also facilitates the replacement of one section of the plane whilst it is still aloft, meaning continuous flight can be maintained even if something goes awry.

Designed to fly in the stratosphere, Odysseus will be used for surveillance and reconnaissance, communications relay and environmental monitoring with the potential for roles in global climate change research and regional-scale telecommunications.

Each autonomous section of the plane has three high efficiency electric brushless motors turning low Reynolds number propellers giving the aircraft the ability to cruise at 63 m/s during daytime and 45 m/s during nighttime and carry a payload of 500kg. The onboard batteries are designed to be recharged each day via double sided cells optimized for energy collection efficiency at high latitudes, and adding to the redundancy built in to the plane's architecture, Odysseus' electronics are adapted from spacecraft designs which have already proven their reliability in missions lasting several years.

One of three contractors recently chosen for the Vulture program (along with Boeing and Lockheed Martin), Aurora Flight Sciences will develop a half scale demonstrator

followed by a full scale prototype aircraft in 5 years [9].

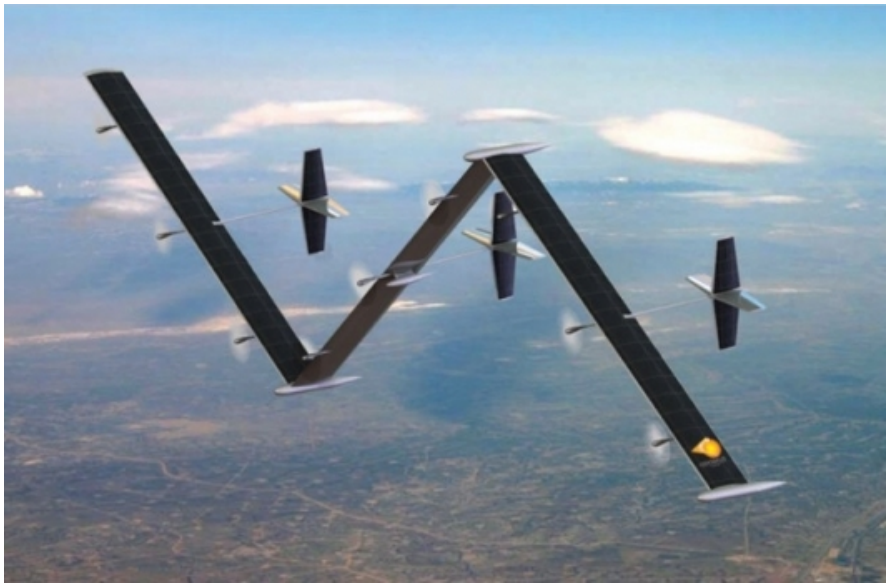

Figure 3.26 : Odysseus'radical Z-wing configuration [9].

The NextGen Aeronautics design, instead, has a wing structure capable of being transformed from a high-span configuration for slow speed flights to a configuration with reduced wing span to fly at high speeds (figure 3.27, 3.28).

This UAV was originally referred to as a "BatWing" but has since origin been named **MFX-1** by NextGen.

In this solution, the wing is based on a moveable truss-like structure that can be handled by appropriate actuators, so as to adjust the wing span, area and shape (figure 3.29). The metallic wing structure is then covered with silicone elastomer reinforced with titanium or steel to prevent unwanted deformations. The real problem is to attack these surfaces together; an alternative approach could be based on the use of sliding panels.

The MFX-1 wing features have several technical innovations including innovative flexible wing skin designs which can undergo strains in excess of 100% while withstanding air loads of up to 400 pounds per square foot, and kinematic, light-weight wing substructure which enables the wing to morph.

The geometry change is implemented using an efficient, internal electro-mechanical actuation system.

In August 2006, NextGen successfully flight tested MFX-1 in Camp Roberts, California.

The UAV sustained an area change of 40 %, span change of 30 % and sweep varying from 15 to 35 degrees during the flight.

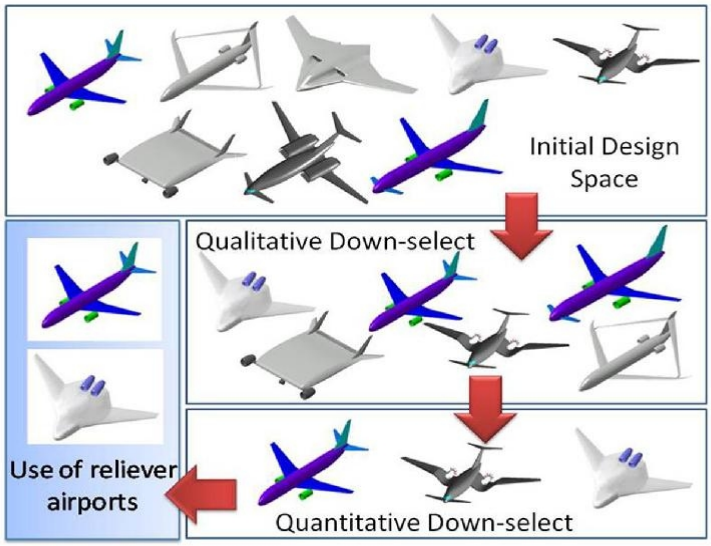

Figure 3.27 : NextGen aircraft design concept [38].

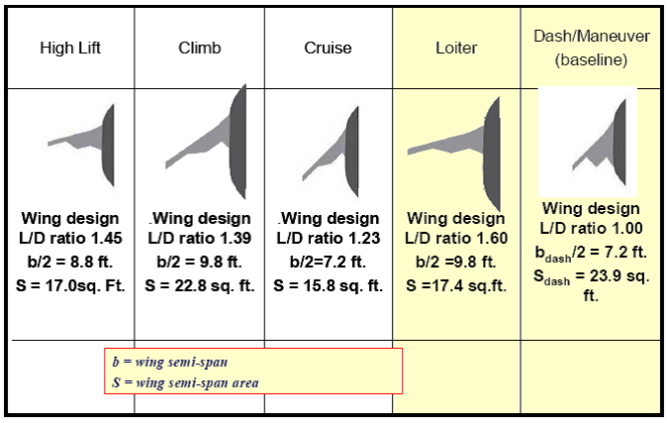

Figure 3.28 : NextGen design various operative configurations [24].

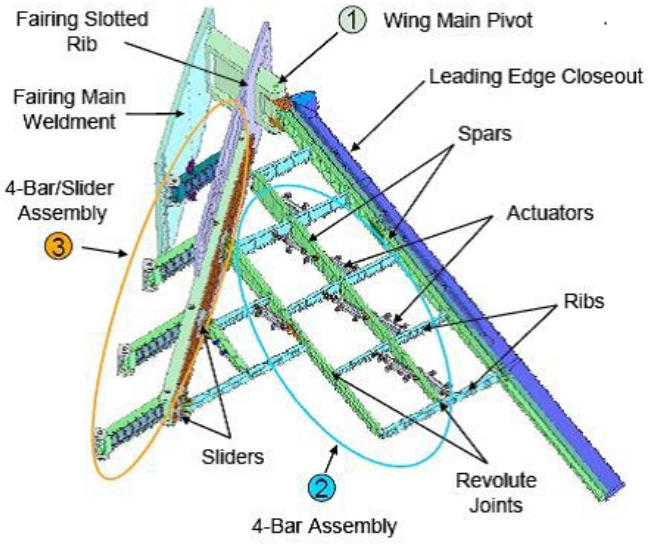

Figure 3.29 : NextGen Aeronautics "Batwing"design [53].

It is also attained airspeeds of about 100 knots during the test cycle. This was the first recorded successful test of an aircraft that morphed during flight [48] (figure 3.30).

Figure 3.30 : :NextGen Aeronautics flying MFX-1[10].

After the success of MFX-1, NextGen developed a larger 300 pound morphing UAV named MFX-2.

MFX-2 used twin jet engines for propulsion and also encompassed a flight control system that allowed autonomous flight. A September 2007 flight test of the aircraft once again garnered success while demonstrating a 40 % change in wing area, 73 %change in span and 177 % change in aspect ratio.

3.4 Adaptive wing actuated by SMA

The possibility of changing the airfoil shape by means of Shape Memory Alloy (S.M.A.) is very attractive: by directly implementing these materials within the structural elements, an actuation capability is integrated within the structure, with significant benefits in terms of:

- weight, because there is no need for the traditional hydraulic lines for the control surfaces actuation;
- reliability and maintenance, as it reduces the number of required components;
- structural and aerodynamic efficiency, as the use of SMA can allow for both load bearing and deformable structures, with the possibility of implementing a continuous, gradual, adaptive, in real-time actuation.

However, the use of SMA for morphing wing applications is still in an experimental

phase: what makes these technologies inapplicable in a commercial context is the lack of an established modeling, suitable for engineering design on a large scale, as well as the intrinsic limits of shape memory materials, for which the ratio of applied force/application rate is rather limited. Many studies, therefore, are still facing small model aircraft or aircraft (such as U.A.V.s).

Alasty & al. [50] studied the effect of a variable shape wing applied to an ultra-light aircraft, in order to improve aerodynamic efficiency and flight control. Given the size (less than a meter of wing span) and the low weight of this aircraft, the use of SMA has proven more appropriate than traditional actuators thanks to the favorable characteristics of a high strength and low weight, as well as a reduced footprint. The structure was made of balsa wood with nylon sticks. Wings were composed of two parts, a rigid front element and a deformable rear.

Actuators in SMA are used in pairs, so each wire acts in opposition to another: this concept is often found in literature with the name of antagonistic configuration.

Conclusions made from the authors demonstrate an increment of maneuverability characteristics of the radio controlled aircraft with respect to previous works.

Benavides & Correa [51] at University of Missouri-Rolla realized a wing section, based on the symmetric Gottingen 776 airfoil (figure 3.31), having a deformable trailing edge actuated by SMA wires: during wind tunnel test it has been verified the improvements in terms of Lift / Drag ratio and lift coefficient of this solution with respect to a traditional one. The wing section used six NiTiNOL wires that could pull, upon electrical activation, the upper part of the trailing edge downward: in this manner, the thrust produced by the upper part induces a deformation of the lower surface, with a deflection equivalent to that produced by a flap. Following the cooling of the SMA wires, ten springs carry the profile to its initial configuration.

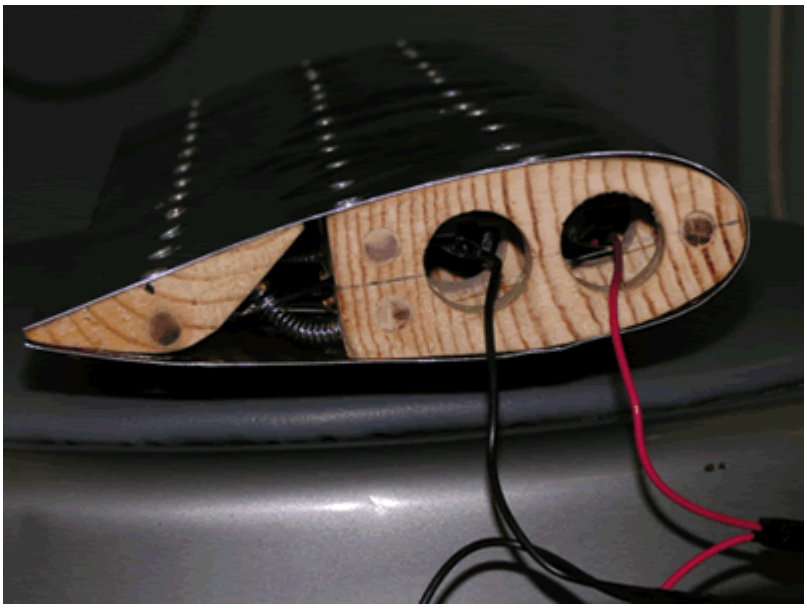

Figure 3.31 : Wing section with deformable trailing edge actuated by SMA wires [48].

Song & Ma [52] used SMA wires to control the flap movement of a model airplane wing mainly to achieve weight reduction (figure 3.32) two SMA actuators are used: one to move the flap up and the other one to move the flap down; by alternatively activating the SMA actuators, the flap can stay at a desired position. A sliding mode based on nonlinear robust controller is designed and implemented on a real-time data acquisition and control platform to control the position of the flap. Experimental results show that a high control accuracy has been achieved for both the position regulation and tracking tasks, even with uncertainties and disturbances.

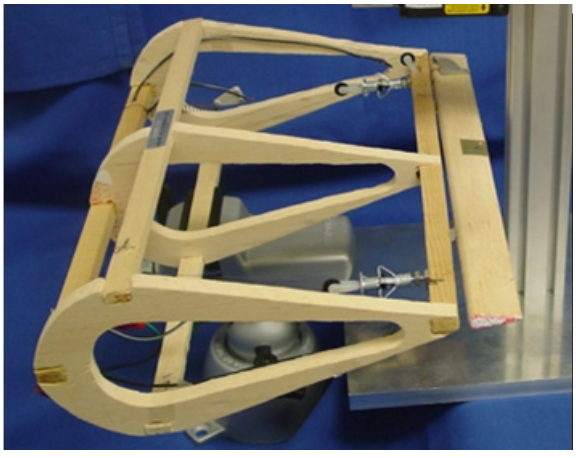

Figure 3.32 : Wing model with SMA actuated flap [88].

Eggleston & al. [48] experimented the use of SMA wires on a model aircraft (after

having also explored the idea of using torsion bars in SMA) for the roll control on a morphing wing.

The first concept developed for the variation of the wing curvature was based on NiTiNOL wires: a polyurethane rod is connected to a wood element (representative of the wing box) and is bent due to the SMA wires activation, connected to it through four Flexane sheets; the rod exercises the elastic recovery when the wires are not heated, returning to the initial configuration. Having more wires on both sides of the rod, it can be alternatively deflected to one side or the other (simulating an aileron) (figure 3.33).

The final chosen configuration is similar to the first model. The wings are stiffened by Plexiglass elements, where SMA wires are arranged on both sides (through aluminium supports that are needed to prevent the Plexiglass overheating upon activation).

The final model is shown in figure 3.34: from wind tunnel tests, it showed a significant improvement in aerodynamic characteristics.

Figure 3.33 : Morphing wing concept: activation through SMA wires [48].

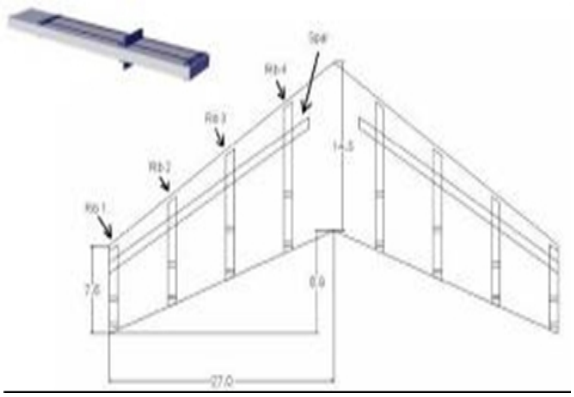

Figure 3.34 : Ultra-light aircraft with adaptive wings [54].

Kudva & al [50, 51] have worked on SMA applications for a morphing wing on a more extensive way. In particular, they developed those concepts which have then been implemented in the "Smart Wing" program sponsored by DARPA. They mainly focused on the wing torsion (through an SMA torsion tube) and leading edge and trailing edge actuation (with SMA wires).

The wing twist was obtained using two concentric SMA torque tubes, one of which tied to the wing tip and the other one to the aircraft body: by means of a relative rotation the entire wing can undergo a twisting action (figure 3.35).

Instead, to achieve the hingless aileron, SMA wires were adopted in an antagonistic configuration: the aerodynamic surfaces to be controlled (either upper or lower one) internally integrate SMA wires, ensuring a two-way antagonistic deflection.

Figure 3.35 shows in more detail what has been achieved.

Due to the considerable complexity of the thermo-mechanical behaviour of SMAs, a fiber optic interferometric system was implemented for determining the actual deformation.

Surely one of the most interesting studies carried out to date in terms of integtration of SMA within a morphing wing has been developed under the "**Smart Wing"** program by the cooperation of DARPA, AFRL, NASA and Northrop Grumman [51-53], aimed at the realization of an UCAV (Unmanned Combat Air Vehicle) (figure 3.36).

Starting from what has already been described (see Kudva & al.), this experimental study implemented both concepts of SMA tubes to attain wing twist and flexible leading and trailing edges actuated by SMA wires (figure 3.37)

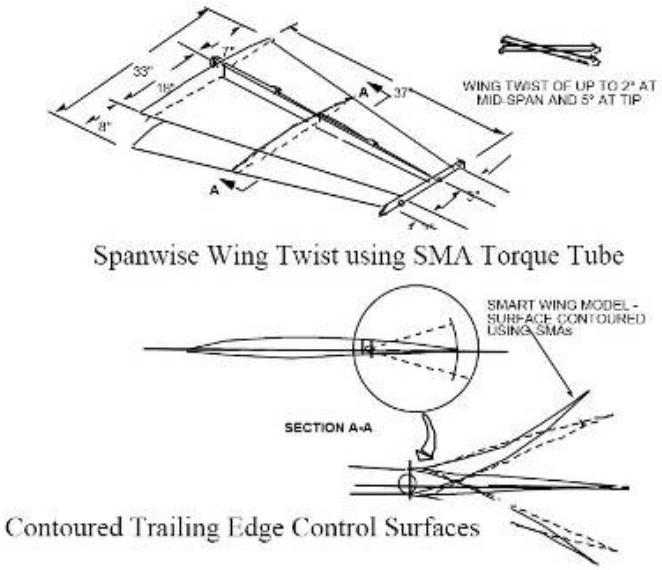

Figure 3.35 : Smart Wing program: wing model and wing twist actuation through SMA torque tube trailing edge model and actuation with SMA wires [51,52].

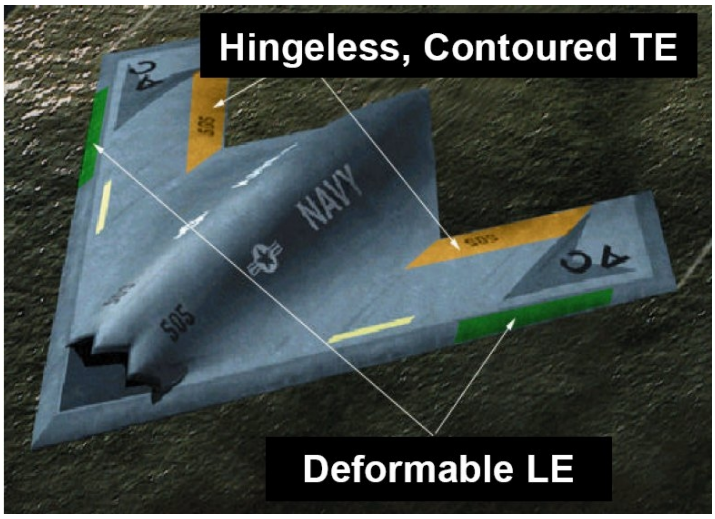

Figure 3.36 : UCAV developed in Smart Wing program by Lockheed Martin [51,52]

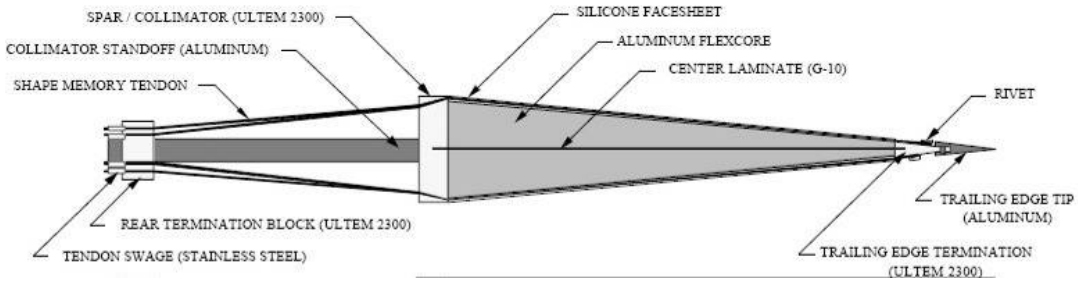

Figure 3.37 : Manufacture details of the UCAV trailing edge actuated by SMA wires by Lockheed Martin [51,52].

The choice of an antagonistic configuration for the SMA wires actuating the wing edges was no accident: though a single set of wires could be sufficient fort actuation and the central laminate adequate to restore the structure at rest upon cooling, this solutions showed a better efficiency under static loads. The mid laminate also provides the necessary support for the SMA wires termination and constraint, in addition to being the load-bearing structural element of the wing edge; the aerodynamic surface is then defined by means of Flexcore filling and an elastomeric skin.

From wind tunnel tests, it was noticed an improvement between 8% and 12% in lift and roll control over a traditional wing. A wing twist up to 5 deg was also attained, together with a deflection of up to 4.5 deg for the leading edge and 15 deg for the trailing edge (figure 3.38)

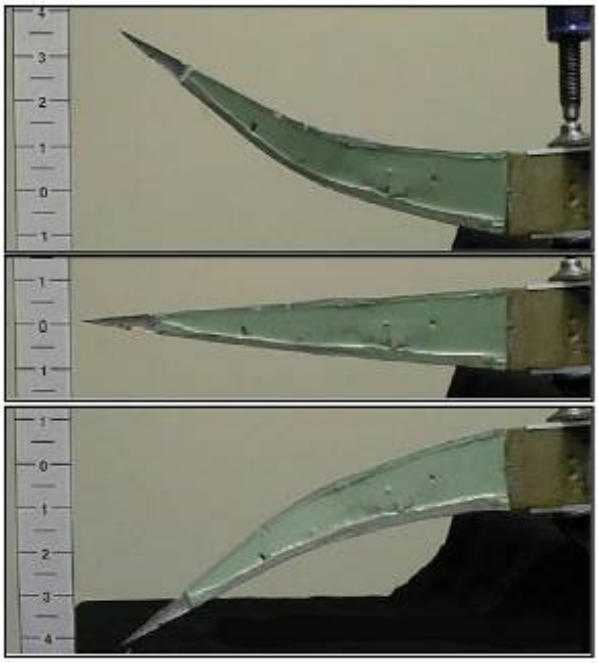

Figure 3.38 : Experimental test on the trailing edge tip deflection [51,52].

A study on the morphing wing was conducted by **T.I.I.M.S.** (Texas Institute for Intelligent Bio-Nano Materials and Structures for Aerospace Vehicles) [54] on a NACA 0015 airfoil made of ABS plastic, whose structure was divided into three independent sections each able to rotate freely with respect to the other ones by means of concentric tubes, so as to attain wing twisting (figure 3.39).

To actuate the three independent wing sections, NITiNOL ribbons an wires were used.

Each section is equipped with two SMA ribbons and an aluminium strip with a SMA wire, to achieve the actuator shown in figure 3.40.

The combined strength of the SMA ribbons and wires under thermal activation is able to generate a twisting moment, allowing a relative rotation between two consecutive wing sections and a global wing twist effect (also if attained by means of rigid)

Figure 3.41 shows the actuator position within the three wing sections: with only two actuators for section, an experimental rotation of 5.5 deg was measured for each section.

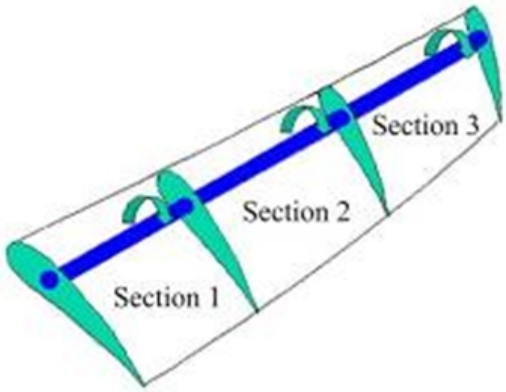

Figure 3.39 : Concept developed at TIIMS for the adaptive wing [54].

Figure 3.40 : Actuator developed at TIIMS for the adaptive wing, comprised of an aluminium strip and SMA wires [54].

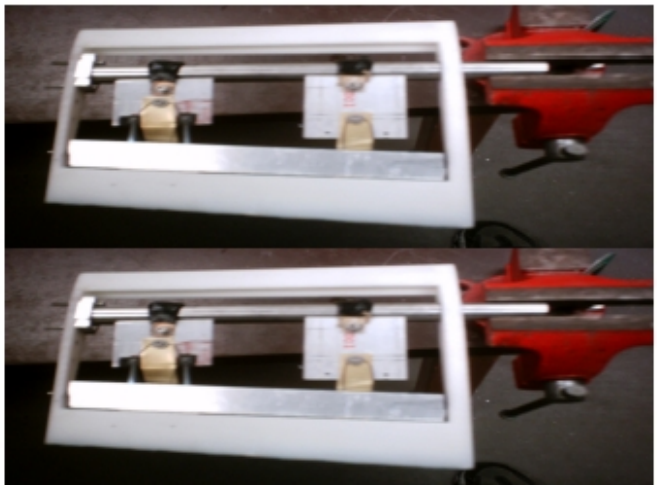

Figure 3.41 : Wing section prototype adopted for the experimental tests [54].

The Aerospace Engineering Department **(D.I.A.S.)** at University "Federico II" of Naples, in collaboration with the Italian Aerospace Research Center **(C.I.R.A.)**, also conducted some studies in the morphing wing field, with particular reference to a "Hingless Wing" concept for an UAV [55, 56].

The main focus of the study was to create, on the selected NACA 63_2-415 airfoil, a morphing leading edge capable of 10 deg deflection, as obtained by aerodynamic optimizations for take-off and landing conditions.

To achieve this deflection, an actuation system based on seven SMA wires was adopted together with a three hinge mechanism (figure 3.42), and a partial return of the lower surface in the airfoil itself was allowed (the ventral area of the leading ledge is not attached to the front spar, but free to slide in the wing).

Accommodating the SMA wires along the wing span greater available length and volume is allowed: this way, a sufficient number of wires could be placed according to the requested actuation forces (estimated by a FE analysis in 336N under maximum external loads) and their action calibrated.

Figure 3.43 shows some details about the three hinge mechanism, it is constrained to the wing front spar on one side (fixed hinge) and to a suitable structural element on the other one (free hinge); upon activation, the two hinges get closer and the skin undergoes a suitable curvature.

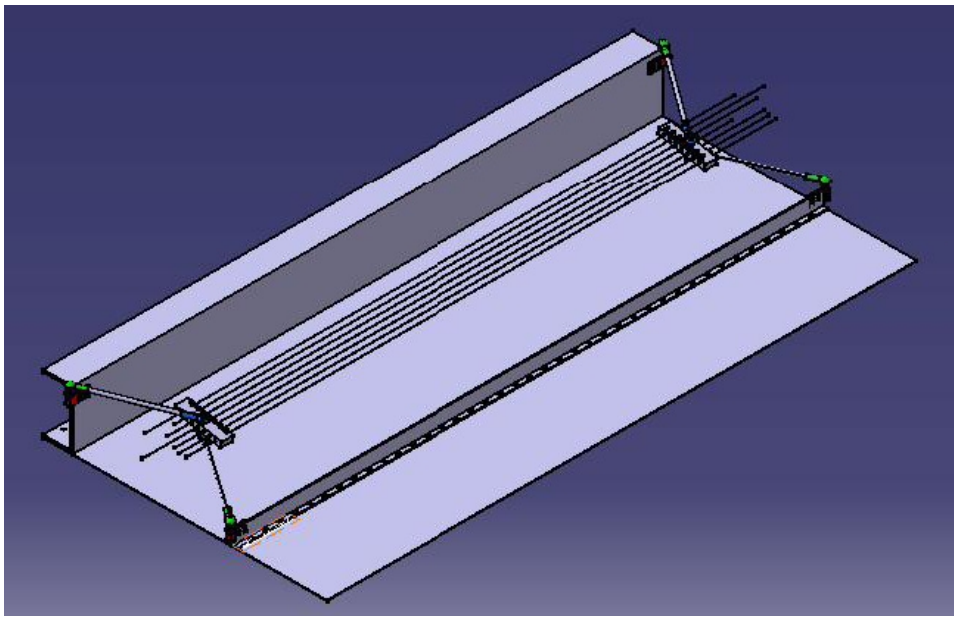

Figure 3.42 : Leading edge CAD model developed at CIRA [55, 56].

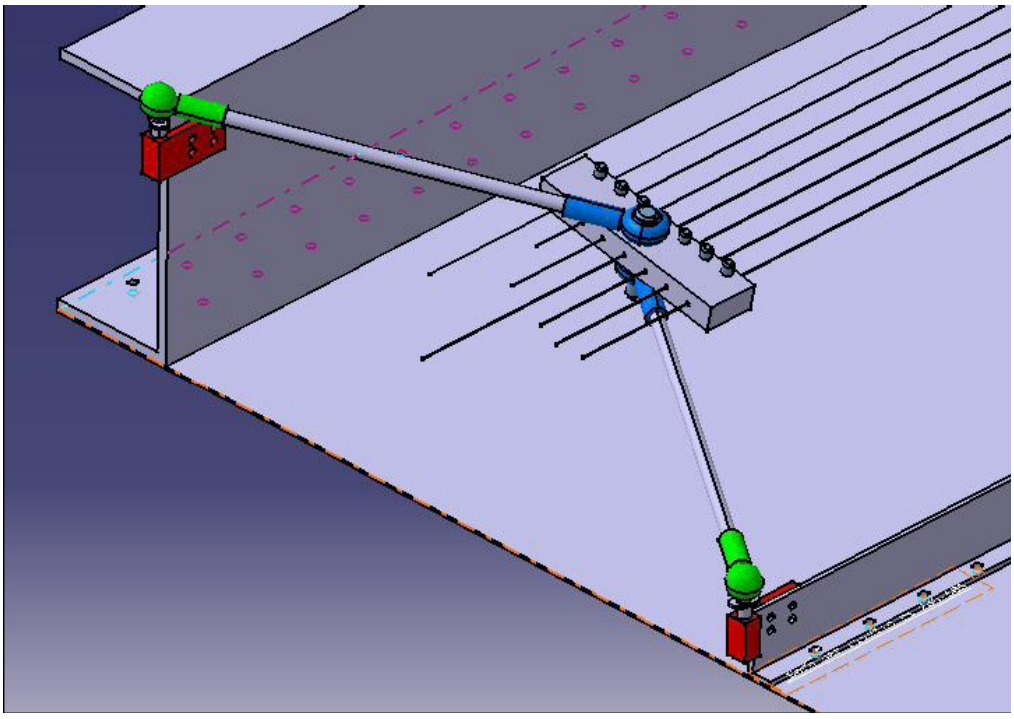

Figure 3.43 : Detail of the three hinge arc system adopted for actuation [55, 56].

3.5 Other morphing aerospace applications

In the previous paragraphs, many studies have been illustrated regarding aeronautical morphing, focused on the variation of main geometrical parameters of a fixed wing. However, the idea of changing the shape of an aerodynamic surface is of a great interest nowadays and spread in all the branches of aerospace field: in this paragraph some applications not centred on geometry change of fixed wing aircrafts will be discussed.

Winglets

Wingtip devices aim the reduction of induced drag, which is responsible for 30-40% of the total drag of a transport aircraft at long range cruise condition and for considerably downgrading the climb performance on aircraft. Winglets alongside with tip tanks, raked wingtips, aligned fans belong to this class of devices. In the case of winglets, the reduction of the induced drag is accomplished by acting like a small sail whose lift component generates a traction force, draining energy from the tip vortices [57].

The wingtip might be considered a dead zone regarding to the aerodynamic efficiency, because it generates a lot of drag and no significant lift. The winglet contributes to accelerate the airflow at the tip in such a way it generates lift and improves the wing loading distribution, which is related to the induced drag. In addition, the aircraft will fly at a slightly lower angle of attack for the same lift coefficient.

Despite the benefits of winglets, there are some drawbacks that need to be addressed.

For example, bending moment at the wing root is higher and may require additional structural wing reinforcements. The winglet also generates viscous and induced drag reduction caused by the winglet itself on the configuration. Winglets could also contribute to slightly worsening of the aircraft Dutch-roll.

Considering the large amount of investigations on suitable winglets design and aerodynamic performance evaluation [58-68], together with the necessity to adapt its geometry to the different flight conditions an aircraft can encounter in its mission, morphing technologies and smart materials have been focused also in the development of active or adaptive winglets: in this case, the main advantage of morphing techniques is related to the low invasiveness in traditional structures, whose main load-bearing elements can be designed traditionally, and the greater aerodynamic benefits that can be achieved.

Studies in this regard have been carried out at the University of Bristol [69-72], with a

pair of **winglets with adaptive cant angle**, independently actuated, mounted at the tips of a flying wing. Computations and wind tunnel tests (figure 3.44) demonstrate that variable cant angle winglet appears to be a multi-axis effectors with a favourable coupling in pitch and roll with regard to turning manoeuvres.

Figure 3.44 : Experimental model as mounted in the wing tunnel with (a) both winglets planar and (b) both winglets upright [69].

The investigated concept appears also to be a promising alternative to conventional control surfaces such as ailerons, elevators and rudders as far as basic manoeuvres are concerned. However, a single pair of adaptive winglet cannot substitute for all the conventional control surfaces at the same time if one wants to get a full control envelope: an alternative is to use a second pair of adaptive winglets on top of the first one to control the aircraft in pitch without elevators (figure 3.45 and figure 3.46).

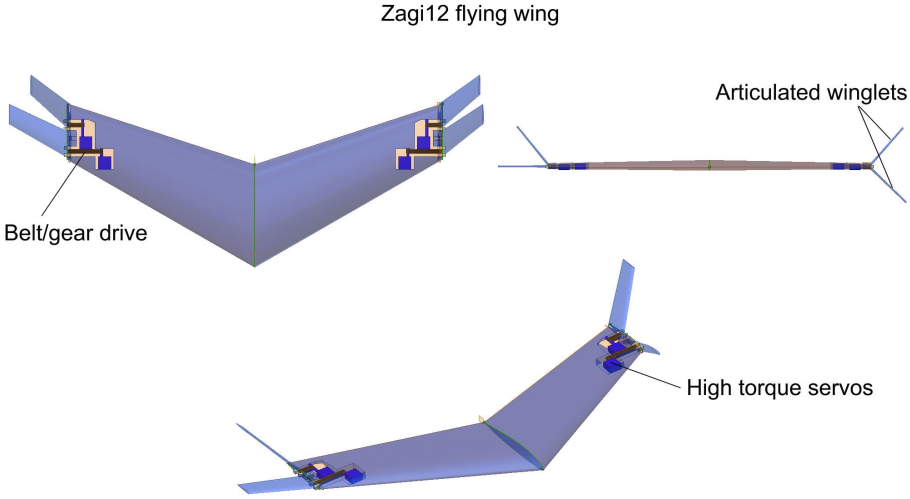

Figure 3.45 : Wind tunnel model schematics of adaptive winglet prototype [70].

Figure 3.46 : Experimental model as mounted in the wind tunnel: (a) front and (b) rear view [70]

Moreover, further studies are focused on the development of a small scale flying wing with active winglets from its actual discrete surfaces concepts [71], actuated via single torque actuator, to a seamless continuous concept actuated via a distribution of actuators (figure 3.47).

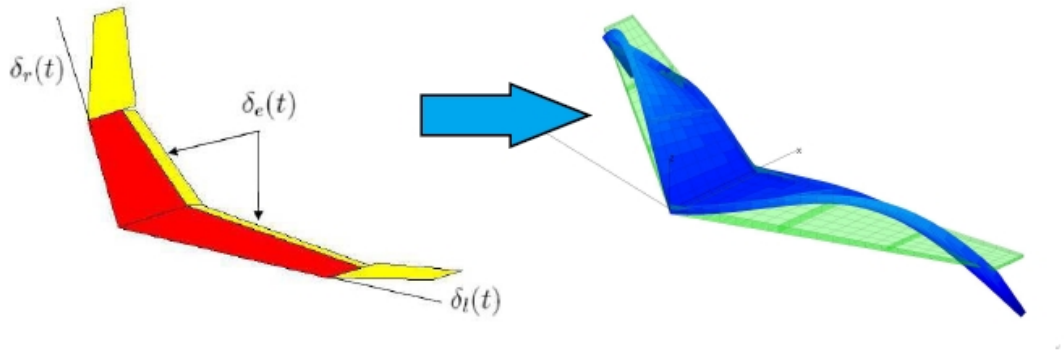

Figure 3.47 : Discrete and continuous wing morphing concept[72].

Propulsion systems: inlets, nozzles, chevrons

The usefulness of active materials in tailoring propulsion systems has been demonstrated through the Smart Aircraft and Marine Project System DemonstratiON **(S.A.M.P.S.O.N.)** program [75]. One of the uses of SMAs in this program has been to change the geometry of an F-15 engine inlet. The shock structure inside the inlet of an air-breathing hypersonic (or scramjet) engine is controlled largely by the inlet geometry: the ability to change that geometry in flight allows the control of flow behaviour and the enhancement of engine performance. The inlet must compress and decelerate the entering air to speeds and

pressures appropriate for combustion.

Typically, this deceleration is achieved through a series of oblique shocks in the inlet and the isolator. The geometry of the inlet determinates the structures of these oblique shocks, and therefore the amount of compression and the total energy loss as the flow is decelerated.

Figure 3.48 : The SAMPSON F-15 inlet cowl as installed in the NASA Langley Transonic Wind Tunnel [76].

The experiment conducted within the SAMPSON program has been carried out on a full scale F-15 inlet, and the experimental set up arranged at NASA Langley can be seen in figure 3.48 [76, 77].

A total force of approximately 26.700N has been achieved through the use of SMA bundles containing 34 wires/rods. This generated force rotated the inlet cowl through 9 deg. Another concept tested by the SAMPSON program has been the concept of changing the shape of the inlet lip through a more complex system of SMA actuation.

A similar study has been done by **Timpano & al.** [78] on a morphing inlet based on cellular-core sandwich panels, which provide a useful platform for aerodynamic shape change without introducing seals or gaps into the structure.

A morphing supersonic nozzle has been designed, built and tested in the wind tunnel (figure 3.49). The nozzle has the capability of changing its aerodynamic shape smoothly

and continuously during operation, thus changing the Mach number in the test section of the nozzle: seven actuators (linear stepper motors) have been used to achieve the three prescribed shapes.

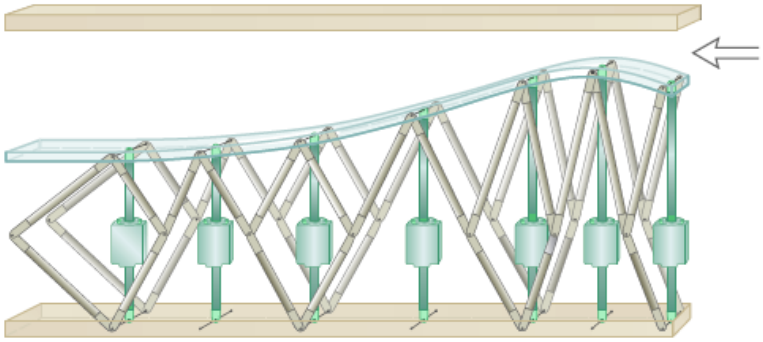

Figure 3.49 : Morphing nozzle (half-nozzle configuration)[78].

A variable area exhaust nozzles for a jet engine, actuated by means of SMAs, has been investigated by **Song & al.** [79]. A significant reduction in noise and improved fuel consumption can be achieved by varying the area of a commercial jet engine's fan nozzle. A larger diameter at take-off and approach can reduce jet velocity reducing noise. Adjusting the diameter in cruise, to account for operating conditions such as varying Mach number and altitude, can optimize fan loading and reduce fuel consumption. The difficulty of using SMA actuators for controlling variable area exhaust nozzles lies in the fact that the temperature near the exhaust nozzle is far higher than the transformation temperature of an SMA actuator.

Due to the flexibility and small volume of SMA wire actuators, they have been remotely replaced away from the exhaust nozzle area, in a region where the temperature is lower than that of its transformation temperature (figure 3.50). Experimental results on the proof-of-concept prototype demonstrate that the proposed design meets the desired area variation requirements (figure 3.51) and shows the promise of a lightweight and simple exhaust nozzle design by using shape-memory alloy actuators.

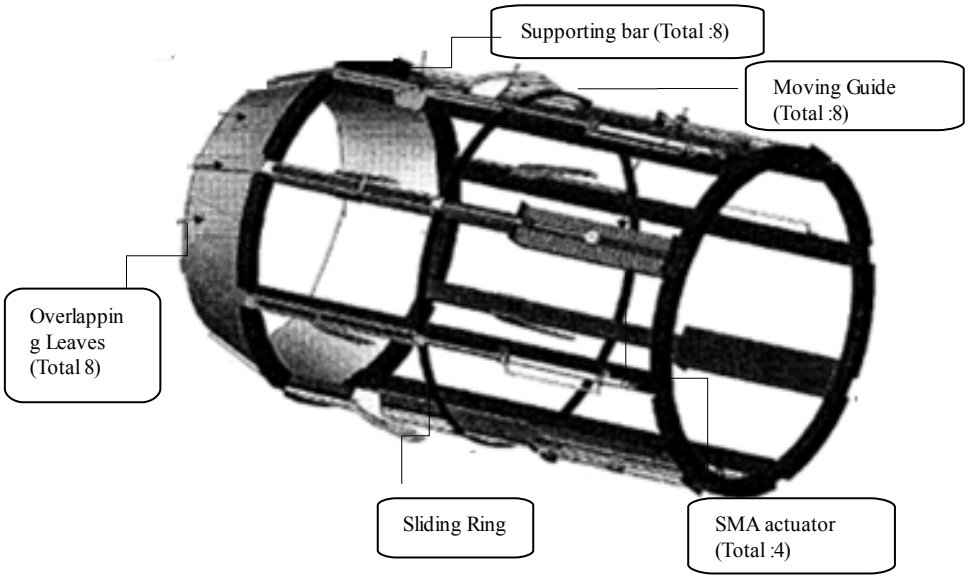

Figure 3.50 : Variable area exhaust nozzle model [79].

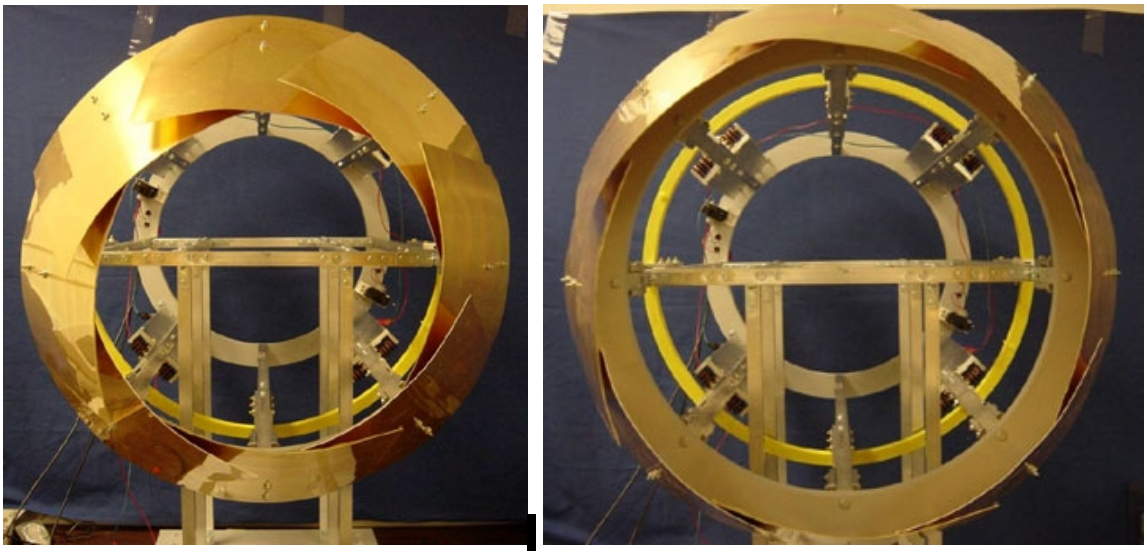

(a) **(b)**

Figure 3.51 : Exhaust nozzle experimental prototype: (a) fully closed and (b) fully open state [77].

A similar study has been carried out by Boeing [76], with two examples of Variable Area Fan Nozzles **(V.A.F.N.)** employing SMA flexure actuators that have been built and tested (the first was a scaled version used for noise tests and the second was a full scale functional display). This variable are jet nozzle has a variable area capable of 20% area change.SMA flexure actuators were used to position 12 interlocking panels at the nozzle exit. The nozzle has an outlet diameter of 7 cm (2.75 inches). There are 12 interlocking Aluminum panels that make up the last 2.86 cm (1.125 inches) of the nozzles.

SMA actuators designed to expand and contract the nozzle when heated are attached to

alternating panels. The interlocks and actuator forces are designed such that each panel's edge stays in contact with the edges of the adjoining panels. A SMA actuator, made of Ni-40Ti (60% by wt. Nickel), was attached to each panel. The actuator base is attached to the support ring and the tip is attached near the free end of each panel. A small resistive heater is bonded on the surface of each actuator. The expanding actuators are trained to curve away from the centre line of the nozzle when heated pulling the panels trip with it. The contracting actuators are trained to bend towards the centre line when heated, pushing the panels trip into the nozzle flow; the actuators were 1.9 cm wide (0.75 inches) x 4.4 cm long (1.75 inches) and tapered from 2 mm (0.08 inches) thick at the base and 1 mm (0.04 inches) thick at the tip. A closed loop control system was used to maintain a range of constant diameters with varying the flow conditions and to vary the diameter under constant flow conditions. Acoustic data by side line microphones and flow field measurements at several cross sections using PIV showed significant effect on the flow and noise reduction. Engine noise levels during take-off and landing have become more highly regulated worldwide. To reduce this noise, some designers are installing chevrons onto engines to mix the flow of exhaust gases and reduce engine noise. Research is being preformed into methods by which SMA beam components can be embedded inside chevrons. The SMA beams bend the chevrons into the flow during low-altitude flight or low speed flight, these SMA beam components cool into martensite, thereby straightening the chevrons and increasing engine performance [79]. The current Boeing design for these variable geometry chevrons **(V.G.C.)** can be seen in figure 3.52 and details are illustrated in figure 3.53.

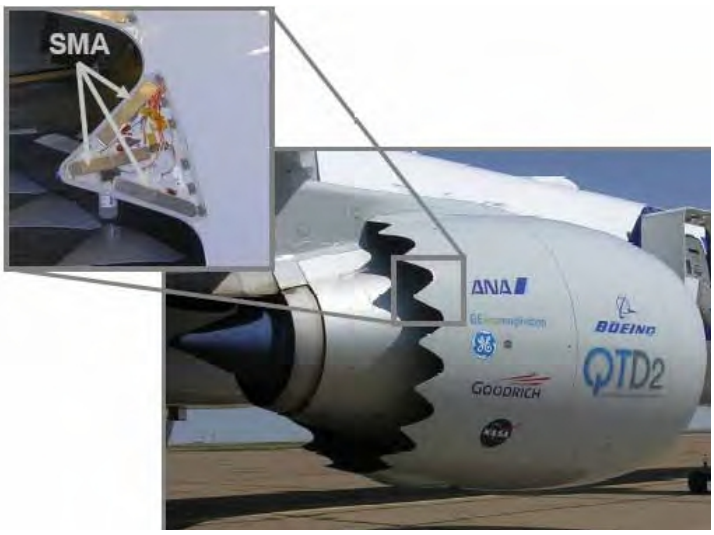

Figure 3.52 : Boeing variable geometry chevron, flight testing [80].

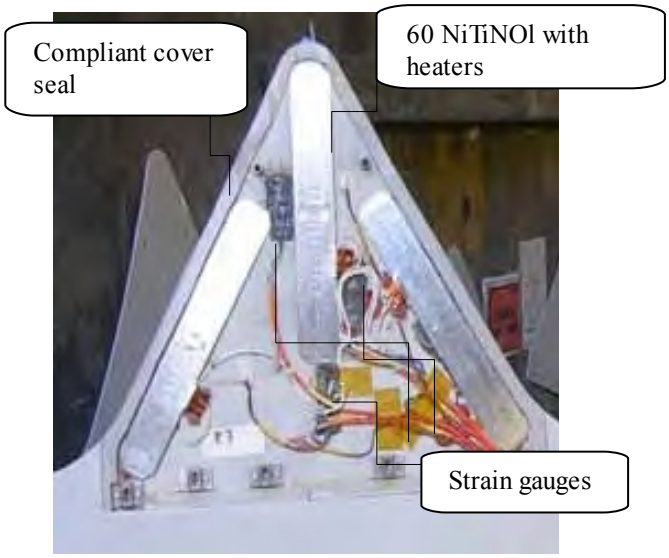

Figure 3.53 : Individual chevron components [80].

Variable Geometry Chevrons (VGCs) have been successfully flight6 tested on a Boeing 777-300ER with GE-115B engines, demonstrating full-scale aerostructure morphing using SMA actuators. Chevrons, serrated aerodynamic devices along the trailing edge of a jet nozzle, have been shown to greatly reduce jet noise by encouraging advantageous mixing of the free, fan and primarily streams.

A different solution to the **active chevron** problem has been proposed by NASA. In this design, SMA strips are installed on each side of the chevron centroid during the fabrication process [81]. Upon heating, the SMA strips contract alternatively, leading to asymmetric stresses within the chevrons and therefore create a bending moment.

Helicopter rotor blades

Aeronautical engineers have faced a plethora of issues in their path to obtain stable flight of rotary-wing aircraft. A major component of these issues has to do with the complex flow field that a rotor blade is exposed to: even in hover, each section of the rotor blade is exposed to a different oncoming flow velocity; engineers have designed the blade to have a pre-built twist which compensates for the varying flow velocity.

However, the optimum amount of this pre-twist varies with flight condition: considering this fact, classical rotor blade designs are therefore actually a compromise and not an optimum design.

Apart from the performance issues that plague rotating wing aircraft, the rotor blades emanate a significant amount of vibration and noise as well. These problems are caused

by a number of factors including the increased asymmetrical loading of the rotor disk as well as blade tip shocks that occur with increasing speed. Furthermore, the noise emitted by the rotor blades is compounded by the interaction of the blades with the tip vortices of the proceeding blades (BVI noise), figure 3.54.

These problems, while not necessarily imperative to performance improvements, are essential to be solved in order to obtain a "smooth" ride.

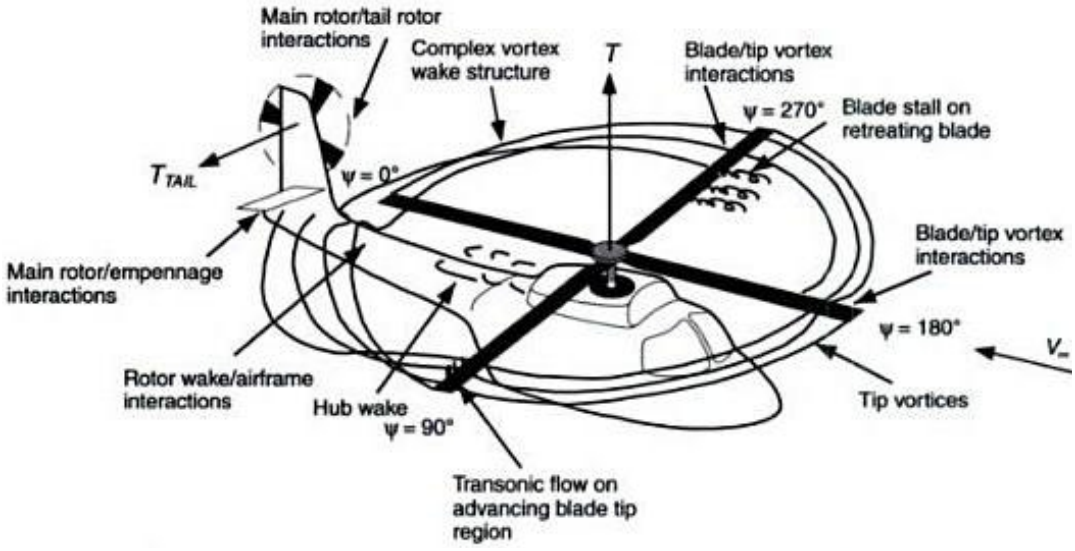

Figure 3.54 : Complex flow-field of an helicopter [82].

As for aircrafts, current researchers focus on improvements in terms of increased speed, payload and manoeuvrability, along with reductions in costs, vibrations and noise.

These are among the objectives of the DARPA Mission Adaptive Rotor **(M.A.R.)** initiative, which will kick off by the end of 2009 [83]. The program aims to develop "on-the-fly" morphing rotor technology and demonstrate the benefits of actively reconfiguring the rotor in flight: DARPA has identified a wide range of potential ways of reconfiguring the rotor in flight, including varying blade diameter, sweep and chord; morphing tip shapes and variable camber airfoils; variable blade twist; anhedral/dihedral, tip speed, stiffness and damping. DARPA is looking for technologies that can increase rotorcraft payload by 30% and range by 40%. While reducing acoustic detection range by 50% and vibration by 90% over the fixed geometry rotors.

Some studies can be found in literature which illustrate the aerodynamic and acoustic benefits of an active twist rotor [84-86], the rotor power reduction in presence of trailing edge flaps [87] or the envelope expansion using expendable chord sections [88]. Many

researches are focused on how to achieve these morphing characteristics from a structural perspective, focusing on specific geometrical parameters.

Some solutions for rotor twist have been presented by **Riemenschneider & al.** [93]; warp induced systems to obtain the variable twist of rotor blades nave been investigated by **Mistry** [90], focusing on the use of an I-beam spar located within the blade which acts as both a load bearing member and the actuating mechanism (through the application of differential axial loads, Vlasov bimoments) or via the forced warping of the skin (actuated using a mechanism based on the power screw concept).

Another example on rotor blade twisting obtained by means of SMA has been developed within the Reconfigurable Rotor Blade **(R.R.B.)** program funded by NAVAIR, with a goal of demonstrating the potential to improve rotorcraft performance by optimizing the configuration of major structures in flight [91, 92].

The NiTi actuation system employed 55 NiTiNOL (Ni-55Ti) rotary actuators in a quarter scale rotor blade. The actuators have been integrated into the rotor blade as structural elements controlling blade twist. The basic concept of the RRB is illustrated in figure 3.55, which shows as actuator assembly in red located inside the spar near the root of the blade. The passive torque tube in blue transmits the torque from the actuator assembly to the tip of blade causing the blade to twist. A lightweight spring mechanism, the Strain Energy Shuttle, provided an energy storage element between the SMA actuator and the passive torque tube. The Strain Energy Shuttle reduced the actuator system weight by half. Figure 3.56 shows the actuator system before assembly in the rotor blade. In 2007 the actuator has been tested in the V/STOL Wind Tunnel using ¼ scale three blade hub assembly mounted on the Boeing Advanced Rotor Test Stand. The wind tunnel test was a high-fidelity assessment of the SMA actuator. It represents one of the first attempts to incorporate SMAs into an actuator which provides more than 60 in-lb of torque and 30 in-lb of energy and is able to withstand a rotor environment. The actuator provided approximately 250 twist transitions during 75 hours of testing with no less of performance or operational anomalies.

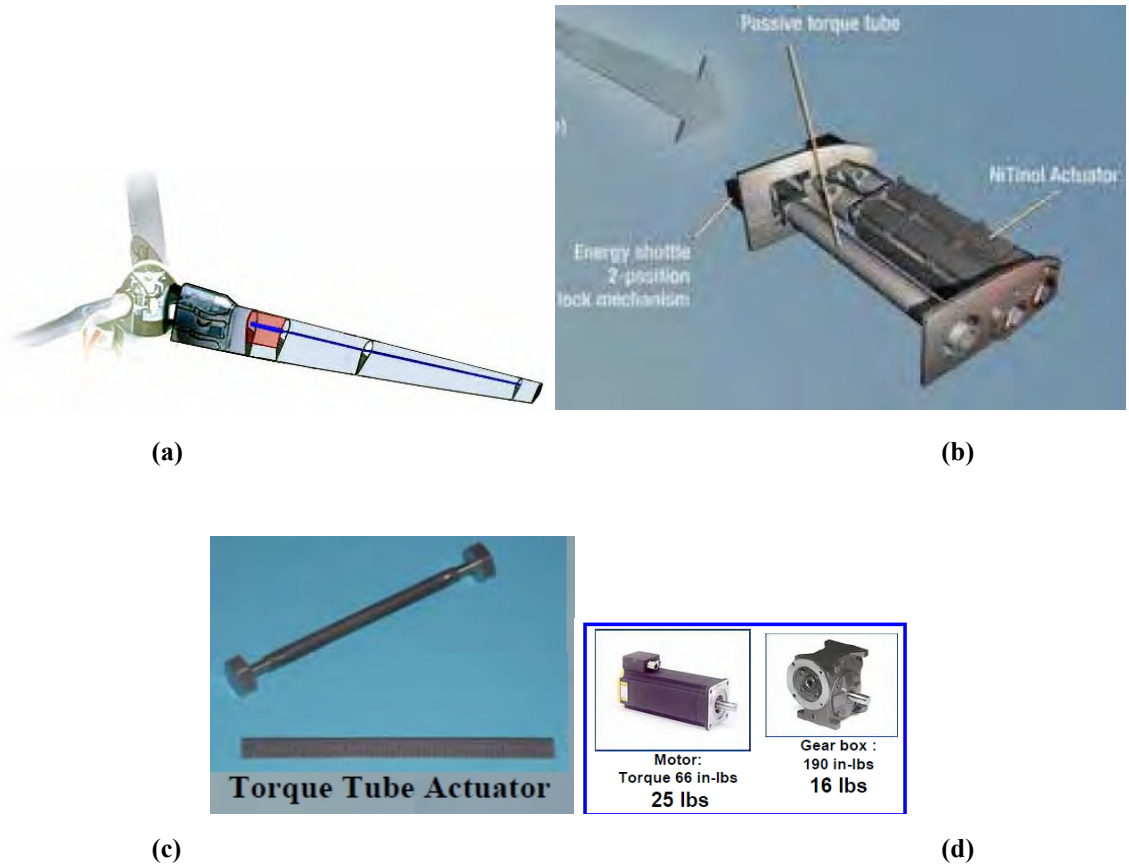

(a) **(b)**

(c) **(d)**

Figure 3.55 : Reconfigurable Rotor Blade (RRB) program: (a) blade system showing placement of actuator system (red region) at base of rotor, (b) scheme of actuator system, including antagonistic actuator, passive torque tube and strain energy shuttle, (c) tube torque actuator particular, (d)motor and gear box characteristics[78].

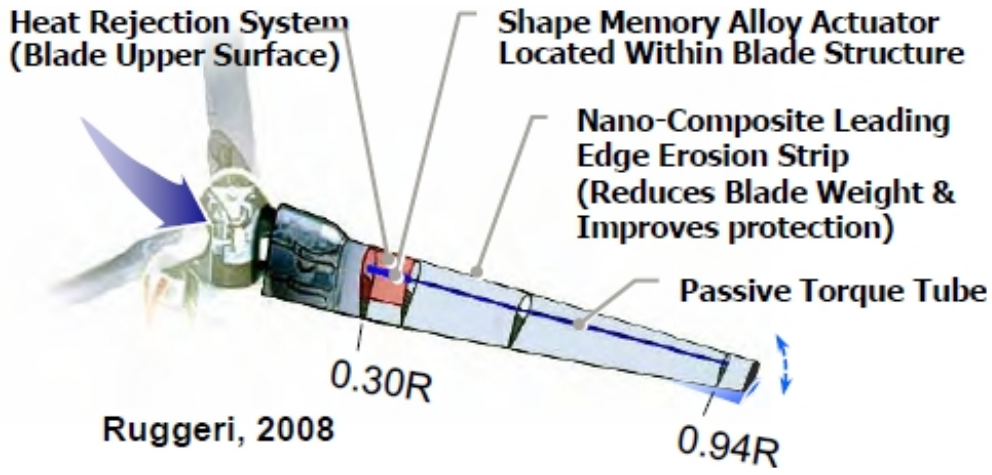

(a)

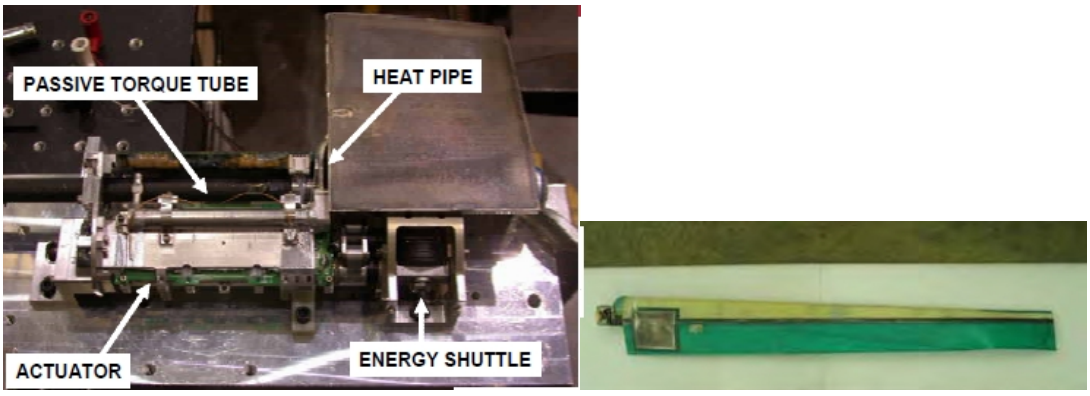

(b) (c)

(d)

Figure 3.56 : Reconfigurable Rotor Blade (RRB) program : (a) scheme of rotor and actuator system position, (b) actuator system prior installation, (c) particular of actuation, (d) 1/4 scale rotor blade in Boeing V/STOL Tunnel[78].

A Twistable Section Closed by Actuation **(T.W.I.S.C.A.)** concept has been developed jointly by DLR and ONERA for the Active Twist Blade (ATB) project [93].

The concept utilizes the warp-twist coupled behaviour of beams to produce the twist of rotor blades and intended for high frequency, low amplitude twist changes of the beam. The concept utilized an open section spar at the leading edge of the blade. A mini-prototype model for this concept was developed which utilizes a PTZ actuator at the trailing edge. This model was able to produce a tip twist of approximately 0.7 degrees for an input voltage of almost 800V.

Boeing's **Smart Active Rotor**, with piezoelectric actuated blade flaps (figure 3.57), was tested in wind tunnel at NASA Ames Research Centre in 2008

The effectiveness of the active flap control on noise and vibration was conclusively demonstrated. Preliminary results show significant reductions in blade-vortex-interaction (BVI) and in-plane noise as well as vibratory hub loads. Up to 80% reduction in vibratory hub loads and up to 6dB noise reduction were measured. Trailing-edge flap deflections were controlled within 0.1 degrees of the commanded value. The impact of the active flap on control power and rotor smoothing was also demonstrated[94].

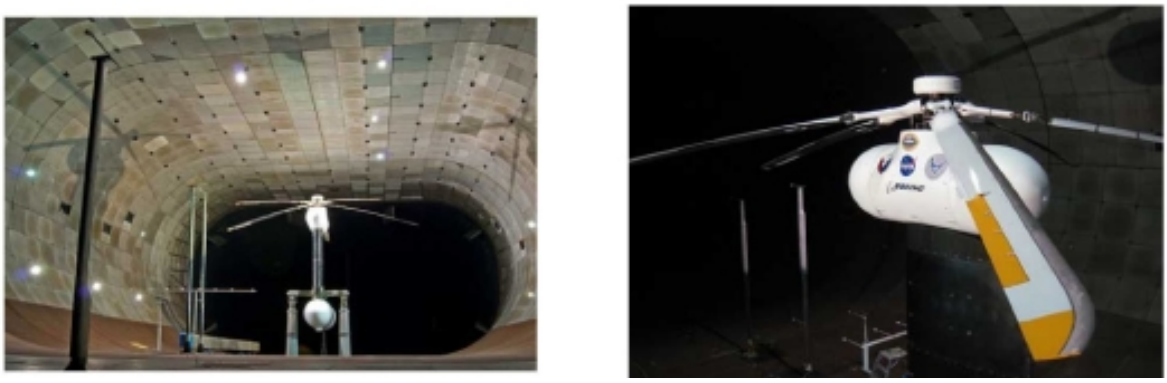

(a) **(b)**

Figure 3.57 : (a) SMART rotor in the 40- by-80-foot wind tunnel of the National Full-Scale Aerodynamic Complex at NASA Ames Research Center, (b) close-up view of the SMART rotor, blade, and flap with piezoelctrics actuated on-blade flap [78].

Ameduri & al. [95], within the European "Friendcopter" project, studied how to achieve blade twist through a SMA based device suitably integrated along spanwise direction. A max angular rotation of 6 deg was reached on an experimental prototype with a transmitted corresponding moment of 21.6 Nm.

The Boeing Company has been actively developing a robust solid state Active Hinge Pin Actuator **(A.H.P.A.)** that can reliably apply high torque and angular displacement with a low space, weight and power burden. It uses SMA technology adapted and developed into a solid state actuator [96]. Previous research has shown that small tabs on the rotor blades can reduce blade vortex interaction (BVI) noise; however, these tabs also increase drag and decrease overall performance.

The ideal solution is to integrate deployable tabs on the rotor blade that can be extended when quiet operation is desired and stowed when they are not needed.

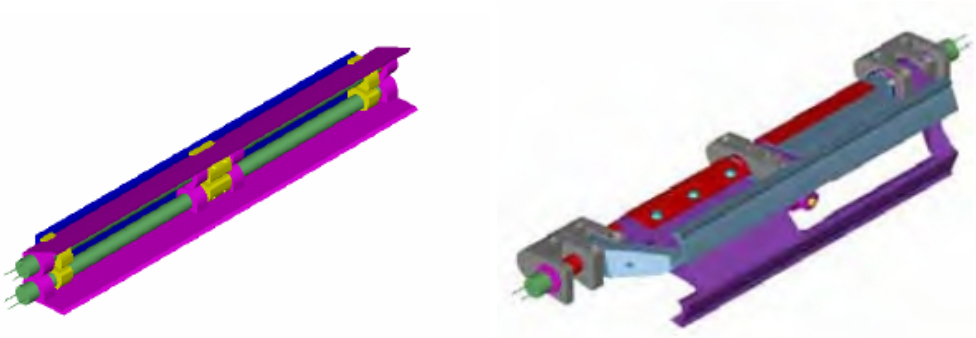

(a) (b)

Figure 3.58 : Active Hinge Pin Actuator (AHPA). (a) two torque tubes solution that each control one flap, and (b) double acting hinge[96].

This application demonstrates the integration of a compact, low cost, reproducible, rugged and efficient torsional actuator that can survive the harsh rotor blade environment. An AHPA was developed meeting displacements, force and frequency requirements of a BVI noise reduction tab within acceptable weight and size limits. Two deployment device configurations were built and tested in both a centrifuge and 2D wind tunnel (figure 3.58 and figure 3.59).

Figure 3.59 : NACA 0015 Blade Section with Integrated Double Acting Hinge[96].

Space applications

Morphing applications are of great interest also in the space field especially due to size and volume constraints at launch. For these reasons, morphing technologies are mainly focused on deployable structures, with particular reference to inflatable structure and trusses.

A comparison of several inflatable structures for space applications can be found in **Bell** [96-97]. Pressurized "soft" membrane structure can offer important advantages for space habitat applications (volume-efficient launch packaging, large diameter interior volumes that increase as a function of the radius squared rather than relying upon linear extension, flexible conformability for use as connectors between imperfectly aligned "hard"

modules). Inflatable modules also present certain special constraints and requirements compared with conventional hard shell structures. One of the most significant of these relates to problematic pre-integration of hardware and utility systems, requiring that hookups be manually undertaken following inflation by flight crew. Some innovative concepts developed by Sasakawa International Center for Space Architecture (**S.I.C.S.A**.) are shown in figure 3.60.

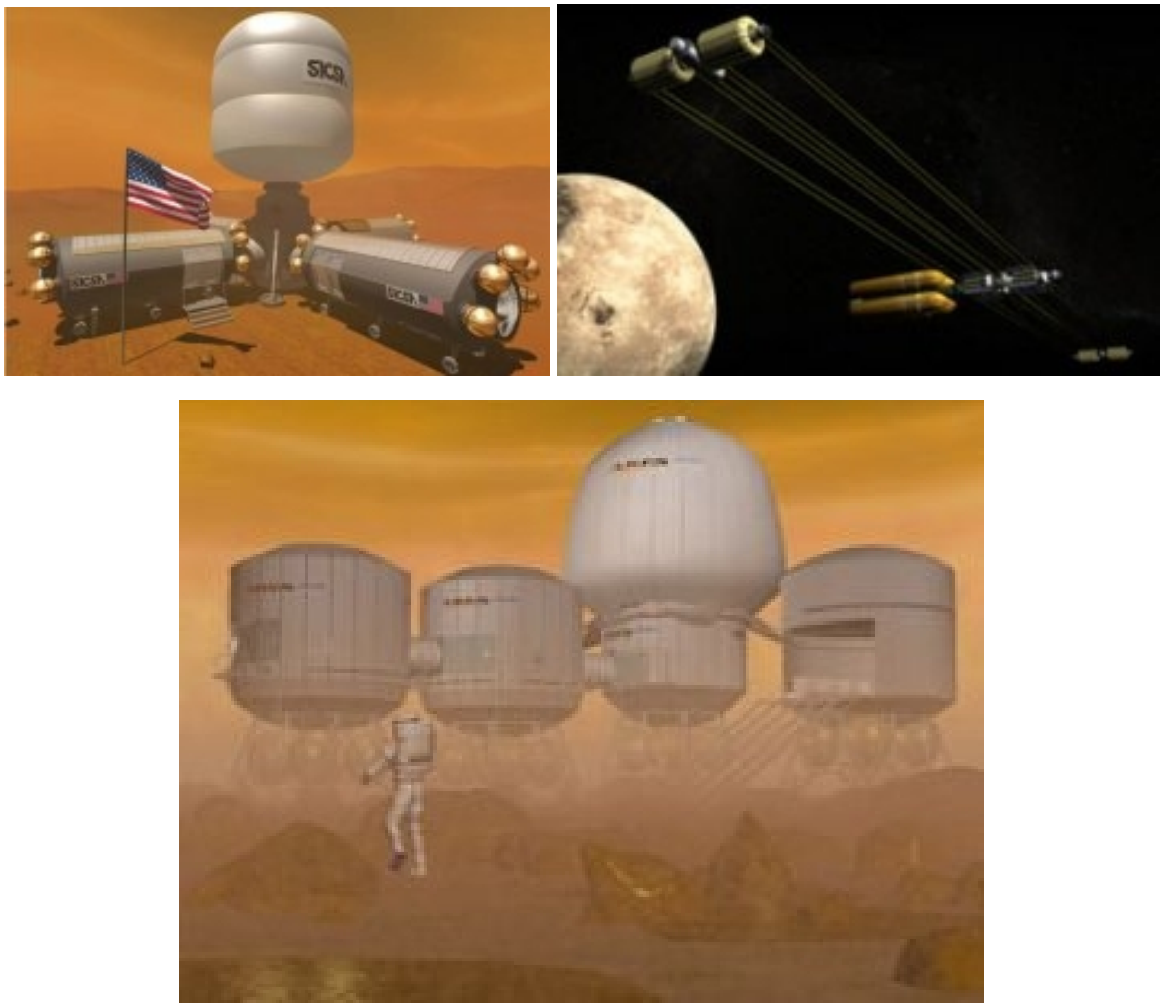

Figure 3.60 : SICSA's Inflatable Structures concepts [97].

Sofla & al. [98] developed a rotational joint for use in shape morphing. The joint isa chain mechanism comprising up to six pivoted linkages that provide a compact mechanism for the connection of up to six structures at a node (figure 3.61, 3.62, 3.63).
The joint mechanism has a total of three degrees of freedom leading to inter-relationship of the six rotation angles at the pivots: by knowing three of the angles as input, the other three rotation angles are determined. Twenty different arrangements for the joint mechanism are possible for any set of three known angles, making the joint capable of

having several different shapes, the hexa-pivotal joint is easy to manufacture and can be fabricated to the desired size and strength. No offset between the links is another advantage of the joint which makes it easily programmable for precise positioning applications (figure 3.64).

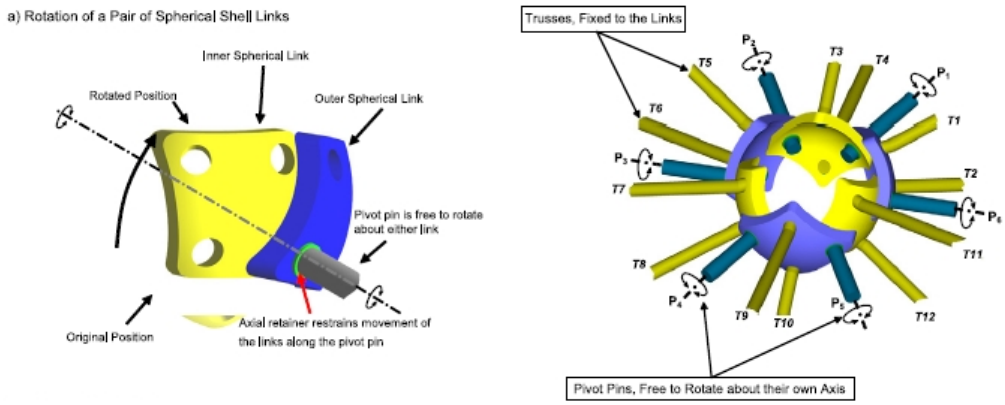

(a) **(b)**

Figure 3.61 : Rotational joint scheme: (a) two concentric spherical links detail and (b) a hexa - pivotal joint consisting of six spherical links[98].

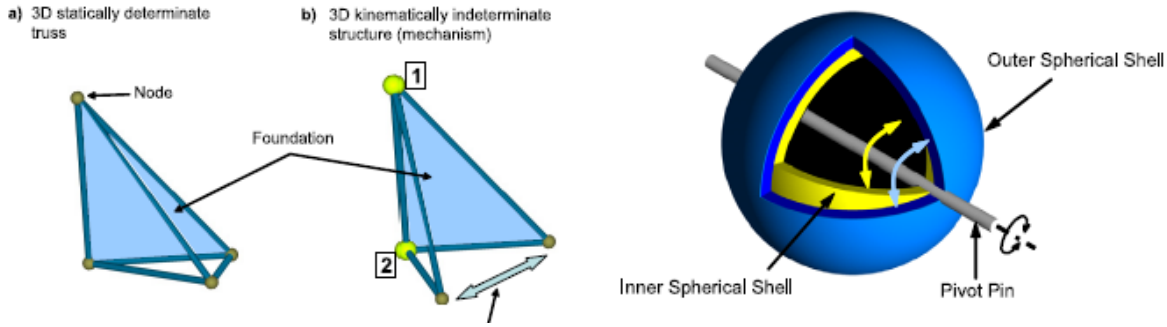

(a) **(b)**

Figure 3.62 : Rotational joint scheme: (a) tetrahedral space truss unit attached on one side to a rigid foundation and (b) a pivot pin passing through the center of two concentric spherical shells anbles free rotation of the two shells about the pin.[98].

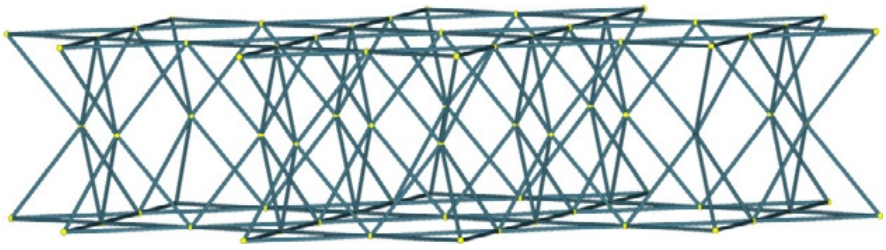

Figure 3.63 : Example of 3D plate for shape morphig plate structure. The welded node constructions causes stresses to develop in the trusses during actuation. This limits actuation authority and increases the susceptibility of the structure to failure by fatigue [98].

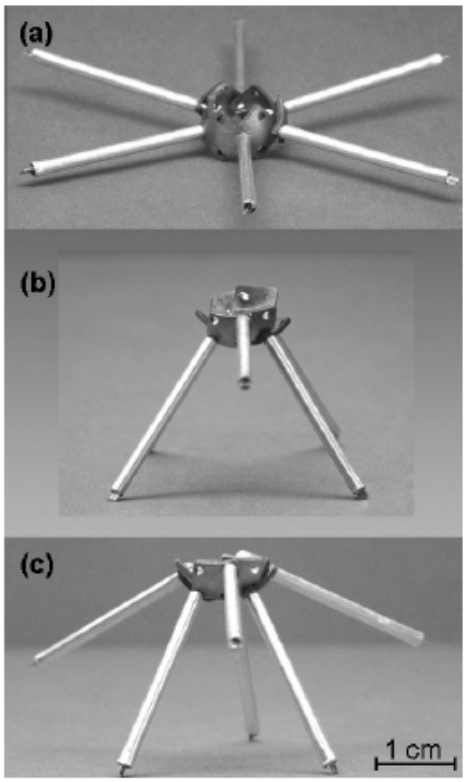

Figure 3.64 : Three symmetric arrangement of a hexa-pivotal joint[98].

Another research has been conducted by ILC. Dover Inc. They have fabricated and tested several types of beam structures including tubular elements, iso-grid, and space frame truss structures manufactured from thermoplastic and shape memory polymer (SMP) materials. The SMP materials have been found to be enabling in the development of small diameter tubular truss elements when it is impractical to reliably inflate all the elements of the truss. Instead, an outer shell is used to deploy the heated structure and the SMP elements take a formed tubular shape naturally, providing optimal structural efficiency. Use of these materials in the joints of truss elements has also eliminated the need for bulky hardware fittings that decrease packing efficiency and add system mass.

SMP generated shape restoration forces are very low, and are not usually practical as a provider of force to deploy more than the material mass alone. The self deployment stress, or force, generated by the SMP polymers is relatively low (10-30Kgf/cm^2 as opposed to 1500-3000Kgf/cm^2 for alloys such as Nitonol). Therefore, structures that use SMP materials will also require a deployment force augmentation system such as with inflatable structures, if the structure is to experience even small exterior forces during the deployment cycle (figure 3.65) [120].

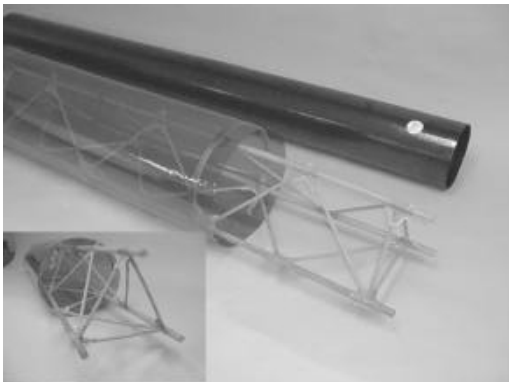

Figure 3.65 : Shape Memory Thermoplastic Inflatable Space Frame [120].

Finally, some early studies begin to appear for aircrafts having adaptive wings thought as automatic robots to be sent to other planets, like the "**Daedalon**" developed by **Lafleur & al.** [99] and sponsored by N.I.A.C. (NASA Institute for Advanced Concepts). The morphing wing concept is here assumed to integrate the re-entry phase into the Martian atmosphere with the flight before touch-down; in this manner, in addition to increase the aerodynamic efficiency at different stages of descent, it is possible to avoid the typical constraints associated with packaging of the wings.

The mission (figure 3.66) provides that, once the initial more intense descent into the atmosphere finishes, Daedalon can get rid of its thermal shield and starts its wing morphing (in a continuous manner, in a 10 minutes time range) from an initial configuration suited for the high initial speeds, up to a final configuration suitable for propelled flight in the Martian atmosphere at mach 0.7 and 500m altitude: in this way it is possible to search for the most suitable landing site (it is expected a flight range of 54 minutes). According to this study, the morphing wing is operated through spars (six along the wing span and two along its longitudinal axis; other four spars go down, to support the thermal shield) able to rotate and having telescopic capabilities (figure 3.67); the wing is not characterized by surfaces that can deform, but it is also assuming telescopic or sliding panels that can overlap or unfold.

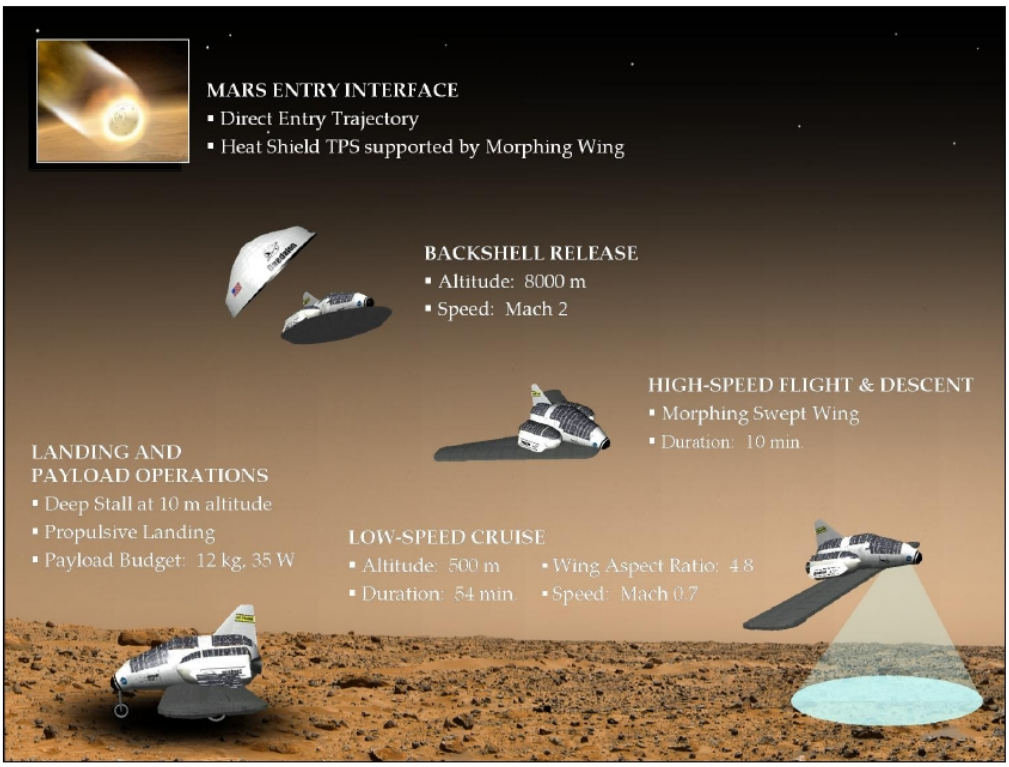

Figure 3.66 : Hypothetical mission profile for Daedalon during descent on Mars [99].

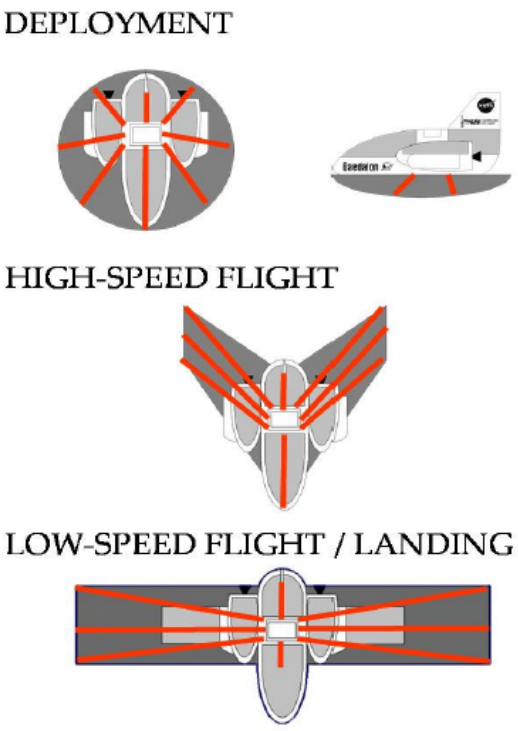

Figure 3.67 : Morphing wing concept for Daedalon [99].

3.6 Morphing skins

Historically, the wing skin on early aircraft was made of fabric; however, with increasing flight speeds and hence aerodynamic loads, stiffer and more robust materials were needed. Today, the majority of aircraft uses stiffened metallic (typically aluminum alloy) panels as an outer skin, although high specific strength and stiffness fiber reinforced polymer composites in the form of glass or carbon fiber/epoxies are increasingly being employed. The stiffeners are usually Z or T-shaped. The panels are supported by ribs in the chordwise direction and by spars in the spanwise direction.

Propellers or rotor blades often include a sandwich structure with a honeycomb core and a metallic or composite faces. While most of the axial and bending loads are counteracted by the stringers, ribs and spars, the skin needs to withstand a combination of tensil, compression and shear forces (semi-monocoque structures i.e. stressed skin concept) and needs to be able to distribute the aerodynamic pressure loads to the underlying structure.

This highlights the difficulties inherent in replacing the current stiff and strong skins with a more flexible solution, needed for morphing applications.

A morphing skin can be envisaged as an aerodynamic fairing to cover an underlying morphing structure. In this case, the skin must be able to withstand a change in shape in at least one of the following two ways: change in chamber or in surface area. This shape change can be instigated either by external or integrated actuators, which in the latter case would make the skin self-actuating or active (and potentially “smart”).

An adaptive structure can be defined as possessing the ability to change shape whilst maintaining a continuous form, whereas a passive structure, such as an hinged aileron, has discrete components which move relative to each other. A smart structure is able to sense external stimuli (pressure, velocity, density or temperature change), process the information and respond in a controlled manner, in real-time. The major problematic, when a morphing skin is chosen, is its smoothness. In literature, a lot of investigated morphing solutions exhibit a skin with many wrinkles. However, from an aerodynamic point of view, this can represent a source for undesired drag increase (which could also cause the morphing configuration to be less effective than traditional one). The morphing skin can be realized either by materials that exhibit specific properties or by means of innovative structural concepts. In this paragraph a review of suitable materials, concepts and structures that can be used for a morphing skin are illustrated.

Morphing skins tailoring materials properties

Elastomers (or rubbers) are a class of polymer with a low density of cross-links [100]. Hence they have the ability to undergo large elastic deformations without permanent changes in shape. However, the few cross-links give them a memory effect so that they return to their original shape on unloading [101]. Many studies mention elastomers as being a prmising solution for morphing skins [101-103]. As an example, in the DARPA Smart Wing programme, a high strain to failure silicone skin was used [103].

The low tensile modulus of elastomers (0.5 to 50 MPa) makes them easily deformable up to 1000% (elongation at break) of their original length. At the same time, the load required is relatively low; tensile strength can have values up to around 50MPA [100].

Since the stress-strain curve of elastomers is non-linear, its modulus of elasticity varies with strain, strain rate and temperature. Below the glass transition temperature (T_g) polymers behave like glass and are brittle, above T_g they are in a rubbery state. Hence the T_g for useful elastormers to be used as stretchable morphing skins must be well below their operation temperature range. A further property exhibited in general by polymers is visco-elasticitìy, which means that when subjected to a load the strain does not occur instantly (i.e. the strain is time dependent) [100].

While these properties potentially make elastomers good candidates for flexible skins, they are unsuitable for carrying loads, which means that it would be difficult to design elastomeric skins that can sustain and transfer aerodynamic loads to the underlying structure [101]. At the same time, working against the strain of material should be avoided as much as possible, since it is likely that it will induce fatigue problems as well as requiring excessive actuation power to hold the undeformed skin in place.

Kikuta [13] is one of the few investigators that experimentally tested a few thermoplastic polyurethanes, co-polyester and woven materials that are commercially available to investigate the materials' viability as morphing skins. According to the author's results none of the selected materials satisfy all of the requirements of a morphing skin. A material that was able to strain and recover well was not able to carry a high load and vice versa. The best polymer tested was found to be Tecoflex 80A (thermoplastic polyurethane). A suggestion was made to combine a material like Spandura (woven material) with a polyurethane like Tecoflex 80A, that way the high strength required would be achieved by the fibers and the elasticity by the polymer.

Auxetics are materials that have a negative Poisson's ratio: when stretched they become

thicker perpendicularly to the applied force (figure 3.68). This occurs due to their hinge-like structures which flex when stretched. Such materials are expected to have interesting mechanical properties such as high energy absorption and fracture resistance. Auxetics may be useful in applications such as body armor, packing material, knee and elbow pads, robust shock absorbing materials and sponge mops.

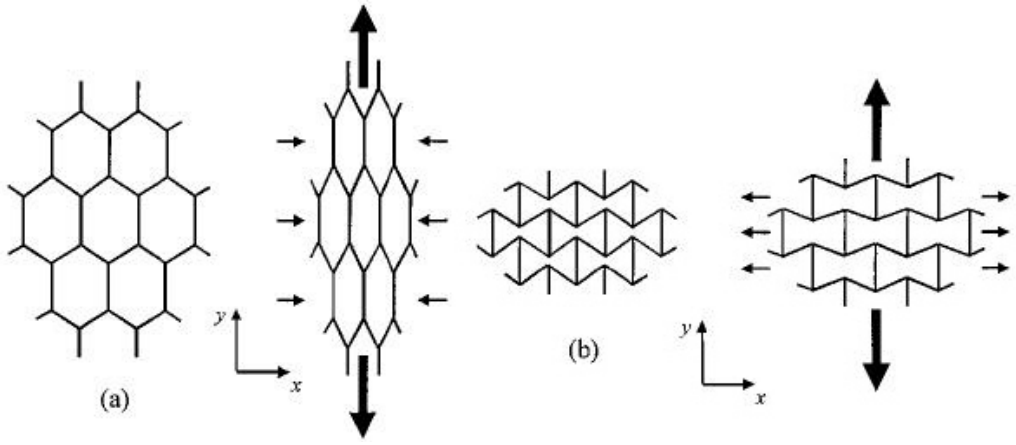

Figure 3.68 : (a) Positive Poisson's ratio honeycomb; (b) Auxetic honeycomb [136]

Research on a morphing aerofoil concept using an hexagonal chiral honeycomb structure (a cellular network featuring a negative Poisson effect) was conducted by **Bornengo &al.** [104]. Finite element analysis (FEA) of a chiral honeycomb made from acrynolitrili butadiene styrene (ABS) plastic and used as concept for a Formula 1 car wing box predicted a trailing edge deflection of 5 mm due to the pressure distribution of the air flow. **Wei & Edwards** [105] looked at ways of making composite materials with auxetic inclusions in order to improve the low modulus of elasticity in auxetic materials.

Gandhi and his collaborators in many studies [106-109] suggest using zero-Poisson's ratio cellular structures as morphing skins. They present an analytical model and FE model showing that by using hybrid (negative and positive Poisson's ratio materials) and accordion cellular honeycomb cores(figure 3.69), the Poisson's ratio is zero and hence would be ideal for morphing. Additionally these honeycombs give low in plane and out of plane stiffness.

A novel cellular platform, inspired by the amorphous silica configurations, has been investigated by **Lira & al.** [110] and called "SILICOMB". Their work was concerned with the investigation of the in plane mechanical and dielectric properties of a novel centre-symmetric cellular structure. Multiple geometry parameters to be used to design the honeycomb are identified and discussed.

Auxetic polymer foams appear to offer some potential for use as a "gap filling"material in a morphing application. Due to their low modulus they can be easily deformed whilst simultaneously expanding when elongated. An example would be to use such materials between a hinged aileron and the main wing of an aircraft top maintain a smooth aerodynamic profile and minimise drag.

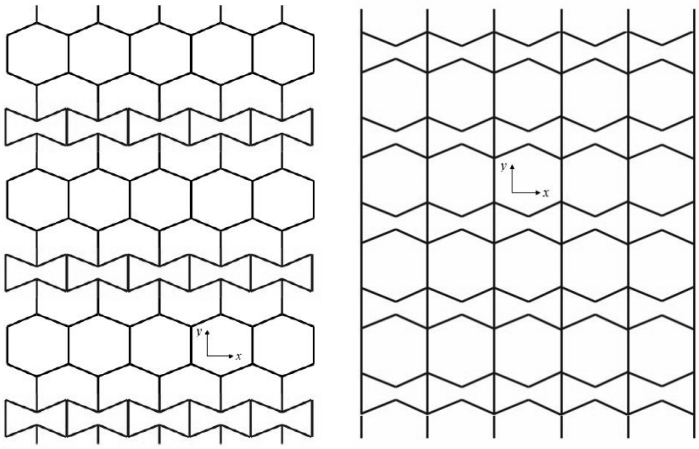

Figure 3.69 : Hybrid (left) and accordion (right) cellular structures [136]

Multi-stable composite

They could potentially be used for morphing skin applications (figure 3.70). Multi-stability of thin laminates, a property usually considered unfavourable, is due to residual stresses forming during the cure cycle of a non-symmetric lay-up or due to Gaussian curvature effects. Generally bi-stable composites exhibit large deformations but only require low actuation forces. This makes them in the current form difficult to use as morphing skins, since aerodynamic loads may be greater than the forces needed to snap the laminates from one stable configuration to the other one.

However, there are still many phenomena related to these materials currently not clearly understood and object of researches, such as how different parameters (fibre angle, lay-up sequence, ply geometry) affect multi-stability and how they interact.

Solving these questions may allow multi-stable laminates as viable option for morphing skins.

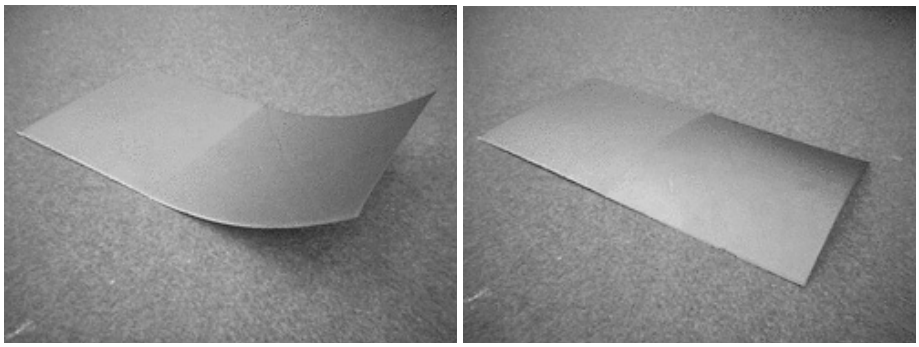

Figure 3.70 : Multi-Stable Composite [136]

Great interest has been posed by the International Scientific Community on these materials, as illustrated by the works of **Hyer** [111-112], **Kebadze & al**. [113] **Hufenbach & al** [114] and **Iqbal & Pellegrino** [115], the research on multi-stable composite and its applications at the University of Bristol is documented for example in **Weaver** [116], **Potter & al.** [117], **Mattioni & al.** [118], who mentioned the use of snap-through buckling as a deployment mechanism in anisotropic composite structures.

Norman & al. [119] manufactured multi-stable corrugated panels made from copper-beryllium alloy via cold working. Bi-stable panels consisted of corrugated state and a coiled state parallel to the corrugations that occurs when the corrugations are pressed flat the panel. Tri-stable panels have two states where the panel is twisted along an axis not aligned with the corrugations in two different directions and a coiled state like the bi-stable panels. Applications could include flexible display screens or roll-able keyboards, or adaptive wings/skin panels for UAVs and spacecrafts. Although these panels have been manufactured in metal, there should be no reason why similar multi-stable composite corrugated panels could not be made. Furthermore this work is interesting since it combines anisotropy and multi-stability.

Shape Memory Alloys (SMA)

They are metal alloys able to recover their original shape after large deformations [120]. Depending on the alloy material properties and on the external conditions, shape recovery can occur in two ways: Shape memory effect and Super-elasticity or Pseudoelasticity as discussed in chapter 2.

Some researchers have embedded SMA actuators in laminates tro obtain self-actuating structures. So for example, **Zhen & al.** [121] embedded pre-strained SMA TiNiCu wires

into a glass/epoxy and a Kevlar/epoxy prepreg. **Dano & Hyer** [122] attached SMA wires to a bi-stable composite plate to initiate snap-through phenomena. The wires could not be directly surface mounted but rather attached to supports in order to have a larger moment arm. **Barrett & Gross** [123] embedded SMA wires in a very low modulus silicone matrix (no additional reinforcements were used). Cellular structures made from SMA have also been investigated by **Shaw & al.** [124].

In many applications SMAs are used as actuators of suitably designed morphing structures.

Shape Memory Polymers (SMP)

They are polymeric smart materials that have the ability to return from a deformed state (temporary shape) to their original (permanent) shape induced by an external stimulus (trigger), such as temperature change [125, 126] (figure 3.71).

In addition to temperature change, the shape memory effect of SMPs can also be triggered by an electric or magnetic field, UV light or a change in pH. As well as polymers in general, SMPs also cover a wide property-range from stable to biodegradable, from soft to hard and from elastic to rigid, depending on the structural units that constitute the SMP. SMPs include thermoplastic and thermoset (covalently cross-linked) polymeric materials. SMPs are known to be able to store up to three different shape in memory [120, 125, 126] (figure 3.71)

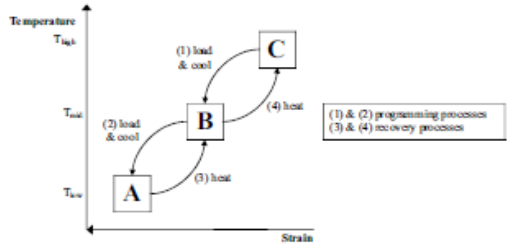

Figure 3.71 : Temperature-strain diagram of triple shape SMPs [136]

Polymers exhibiting a shape memory effect have both a current (temporary) form and a stored (permanent) form. Once the latter has been manufactured by conventional methods, the material is changed into another, temporary form by processing through heating, deformation, and finally, cooling. The polymer maintains this temporary shape until the shape change into permanent form is activated by a predetermined external stimulus.

The secret behind these materials lies in their molecular network structure, which contains

at least two separate phases.

SMPs can be elongated up to 1100% [127] and their mechanical properties can be varied over a wide range. Potential applications include: self-repairing auto bodies, kitchen utensils, switches, sensors intelligent packing, tools and tools and medical applications.

However, not many applications have been implemented to date since only few SMPs have been investigated and even less are available on the market.

SMPs may also be useful in the production of aircrafts which would morph during flight.

Three main products have been developed, based on a fully-cured thermoset SMP that can change shape due to thermo-molecular relaxation rather than a thermally-induced crystalline phase transformation as with SMA. The first product is Veriflex which is the styrene based SMP itself (figure 3.72): it was used as a skin material for a morphing aerofoil section.

The second is Veritex TM (figure 3.73) which is a composite that can be fabricated with nearly any fibre type and with Veriflex as the matrix resin.

And finally CRG's third product is a low density foam based on Veriflex called VerilyteTM (figure 3.74). it could be used as core material in a sandwich structure that can be reshaped when soft at high temperature and carry out structural functions at low temperature. The method used by the manufacturer to heat the SMP is electrical resistive heating using nichrome wires.

Figure 3.72 : Veriflex honeycomb structure self-recovering under an IR heat lamp [136]

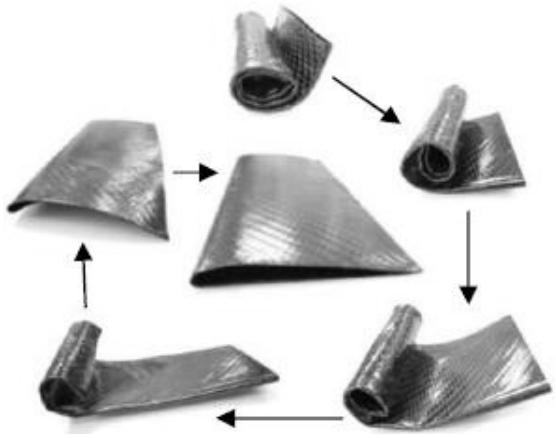

Figure 3.73 : Veritex TM aerofoil self-recovering from rolled state [136]

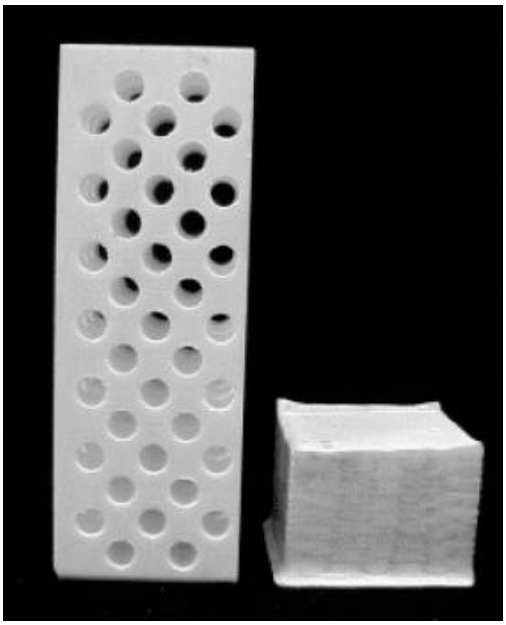

Figure 3.74 : Verilyte TM

McKnight & Henry [128, 129] used SMPs to achieve variable stiffness materials for reconfigurable structures. In their first paper they design a laminate with constant and variable stiffness elements. The function of the constant stiffness element is to carry the structural loads while the function of the variable stiffness element is to provide variable connectivity between the constant stiffness elements.

In the structural mode, the variable stiffness elements rigidly connect the stiff elements which creates high stiffness (similar to traditional structural composites). In the morphing mode, the variable stiffness material becomes soft leaving the stiff element effectively disconnected, in this mode large axial, shear and bending deformations can be achieved (figure 3.75, 3.76). They used high yield spring steel for the stiff elements and a thin film polyurethane SMP (produced by Mitsubishi Heavy Industries., Diaplex 5510 [129]) for the variable stiffness elements to manufacture their samples. The key design variables were length and thickness of stiff elements, spacing of elements, thickness of variable stiffness elements, fraction of stiff elements within segmented layer and volume fraction of stiff elements.

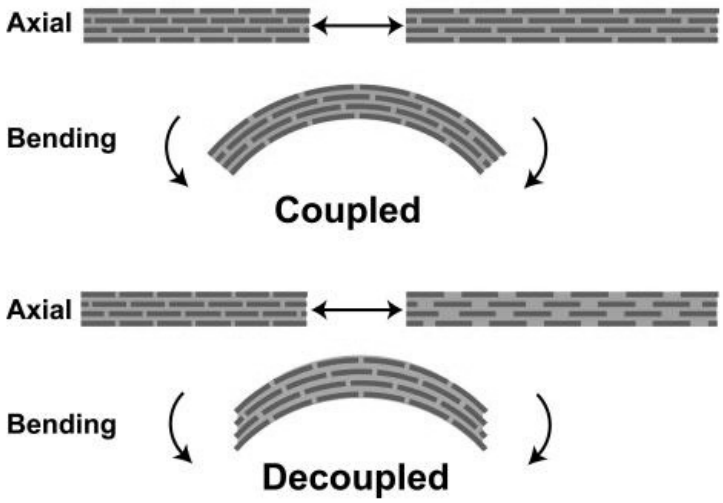

Figure 3.75 : High stiffness (top) and low stiffness (bottom) structure [128].

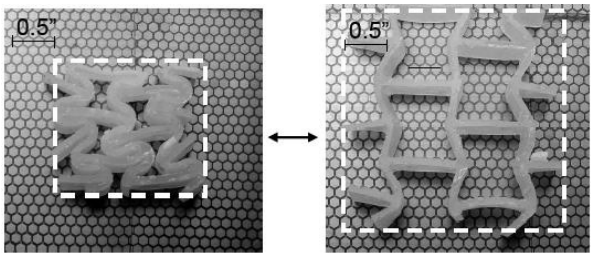

Figure 3.76 : Auxetic cellular material [128].

Morphing skins tailoring innovative structural concepts

Skins for morphing applications can also take advantage of innovative structural concepts to accomplish their objective of an adaptive, high strain capability together with structural load-bearing requirements.

Deployable structures

These structures allow big surface area changes which are desirable during change from high to low speed flight configuration (e.g. trailing edge flap deployment during landing). There are different classes of deployable structures: rollable, collapsible, foldable, inflatable and overlapping/stacked/nested structures; many examples have already been presented in the previous paragraphs.

In order to change the form of a structure with minimal actuation force it needs to be relatively soft in the direction the structure will be deformed in. this is where **stiffness tailoring** comes in useful i.e. designing the structure in such a way that low stiffness is present in the planes where deformation occurs and high stiffness is present in the planes where loads need to react against. Materials that exhibit such a radical variation in

stiffness for two orthogonally opposed directions are called (extreme) orthotropic structures [102, 130].

Many researches are present in this field. Potter & Wisnom [130] aim was to design and manufacture composite components with minimal torsional rigidity but with high bending stiffness fotr which a potential application would be a bearingless rotor hub for a heavy helicopter. Murray & al. [108] presented results from simple analytical and experimental analysis on reinforced elastomeric skin called flexible matrix composite membrane.

They suggested using this composite as skins for one-dimensional wing morphing i.e. chord/camber or span morphing. Yokozeki & al. [102] demonstrated the use of corrugated composite sheets as a candidate material for flexible wing skins (figure 3.77).

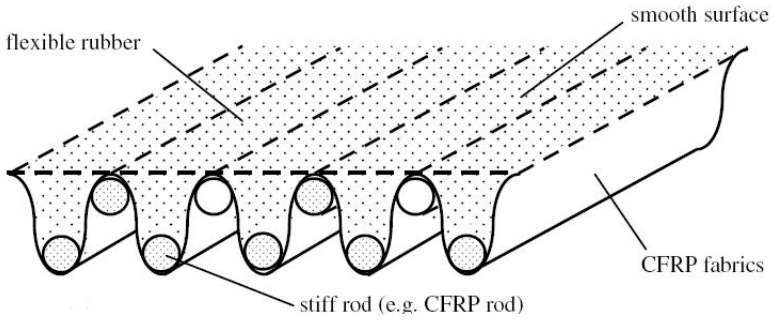

Figure 3.77 : Reinforced corru8gated structure with elastomeric surface [102].

Butler [131] also picked up Yokozeki 6 al.'s idea by manufacturing and testing corrugated composite laminate specimen made from Kevlar/914 pre-preg.

Another structural concept, inspired by the fish skins, is the idea of **segmented structures**. Ramarakhyani & al. [132] explained that due to the multiple discrete elements, called scales, which slide relative to each other, such a structure can deform (figure 3.78).

This arrangement provides a high local lateral stiffness i.e. on their own scales are fairly stiff and hence can transmit the loads via myotomes (muscles) to the underlying structure (vertebral structure) while overall the structure can defeorm.

However a significant aerodynamic concern is the non-continuous profile where the scales overlap. A detailed description of the morphology and functions of fish scales can be found in Varma [134], Long & al. [133] and Bechert & al. [135].

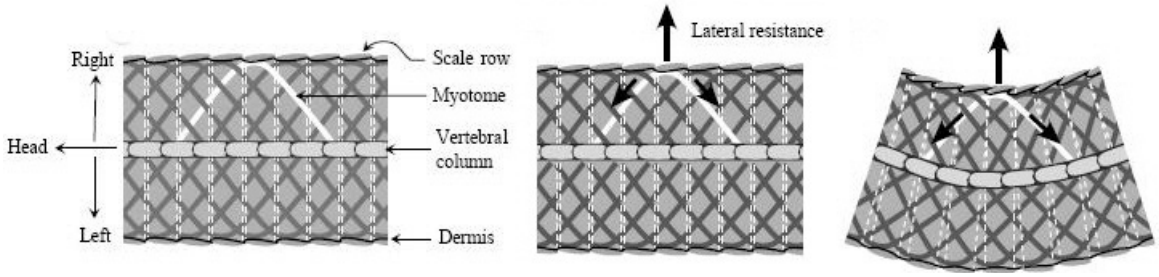

Figure 3.78 : Function model of fish scales[133].

Ramrakhyani & al. [132] suggested the use of **folded inner skin** (figure 3.79), that provides lateral support to very flexible outer skins e.g. elastomers, as potential morphing skin solution. The folded inner skins would expand and contract with the main load-bearing substructure.

They also mention using a **multilayered skin** (figure 3.80) that consists of multiple thin layers of conventional material (e.g. metal or composite) that are not bonded together.

In this configuration transverse shear stresses are not transmitted from one layer to another one which reduces bernding stiffness compared to a monolithic skin-in effect the through-thickness shear modulus is very low. This allows large bending curvatures to develop but the skin can withstand the same tensile loads as a monolithic structure of the same thickness.

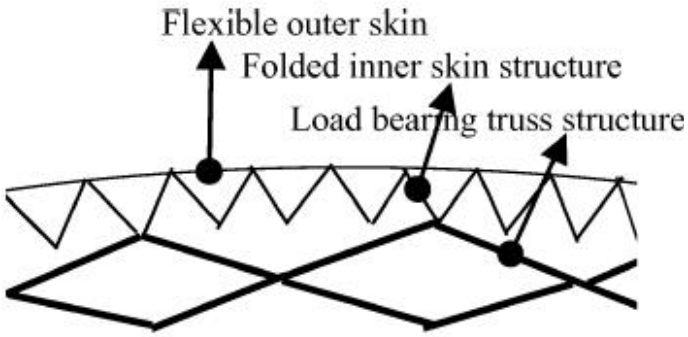

Figure 3.79 : Folded inner skins[132].

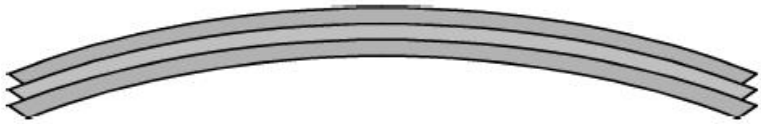

Figure 3.80 : Multilayered skins[132].

3.7 Conclusions

As it can be seen from this bibliographic research, most solutions for wing morphing have regarded small aircrafts, radio controlled scale models for UAVs (Unmanned Aerial Vehicle)

Among these studies, the most promising make extensive use of the SMART materials (SMA, piezo-electric, flexible composites, etc.). As regards the use of Shape Memory Alloys, they have generally been adopted in the form of wires due to modeling and manufacturing limitations.

At the end of this overview of morphing wing technologies, the following conclusions can be done:

- wing morphing is a promising technology, because it allows to fully explore the aerodynamic potential of an aircraft wings by enabling the wing shape adaptability to the several flight conditions that can be encountered in a typical mission profile;
- the opportunity of taking advantage of aero-elastic deformations can allow performance and maneuverability increase, in addition to a structural efficiency improvement;
- new design criteria must be adopted for wing morphing, usually antithetical to the traditional ones, which allow highly deformable or compliant structures;
- many actual studies are focused on the exposed aerodynamic surfaces, which must be deformable while ensuring a smooth skin for flow continuity and complying with the structural integrity;
- the development of innovative SMART materials, their commercial availability and modeling assessment can only enlarge future perspectives on wing morphing applied to real aircrafts;
- as of today, Shape Memory Alloys allow highly integrated actuation systems within the wing structure, but their relatively low actuation energy constrained many works to model aircrafts or UAVs, also become of the use of SMAs in the form of wires only;
- considering the actual studies on wing morphing with SMAs, benefits in terms of maintenance, weight reduction, cost and complexity reduction

seem clear, thus justifying more researches in this field.

According to studies at NASA, it will take another 20-30 years before skies could be furrowed by aircraft more and more similar to birds, having wings with no attached control surfaces and that can change their shape in a smart way.

3.8 References

[1] Browman J., Sanders B., Weisshaar T., 2002, „Evaluating the Impact of Morphing Technologies on Aircraft Performance“ – AIAA Journal 2002-1631.

[2] Stanewsky E., 2001, “Adaptive Wing and Flow Control Technology” – Progress in Aerospace Sciences, Elsevier Science Ltd., vol.37, pp.583-667.

[3] DASA- Airbus DA-Report, 1999, No.EF-069/99

[4] Siclari M. J., Van Nostrand W., Austin F., 1996, “The design of Transonic Airfoil Sections fora n Adaptive Wing Concept Using a Stocasthic Oprimization MOthod” – 34th Aerospace Sciences Meeting and Exhibit, Reno, NV, AIAA 1996-0329.

[5] Smith S. B., Nelson D. W., 1990, “Determination of the Aerodynamic Characteristics of the Misdsion Adaptive Wing” – AIAA Journal, vol.27 no.11.

[6] Thornton S.V., 1993, “Reduction of the Structural Loads Using Maneuver Load Control on the Advanced Fighter technology Integration (AFTI)/F-111 Mission Adaptive wing” – NASA TM 4526.

[7] Szodruch J., 1985, “The influence of Camber variation on the Aerodynamics of Civil Transport Aircraft” – 23th Aerospace Sciences Meeting, Reno, NV, AIAA 85-0353.

[8] Martins A.L., Catalano F.M., 1998, “Viscous Drag Optimization for a Transport Aircraft Mission Adaptive Wing” – 21st ICAS Congress, Melbourne, Australia, Paper A98-31499.

[9] http://www.gizmag.com/auroras-radical-odysseus-solar-powered-aircraft-unveiled/9261/picture/44136

[10] Rodriguez A.R., 2007, “Morphing Aircraft Technology Survey” – 45th AIAA Aerospace Sciences Meeting and Exhibit, January 8-11, Reno, NV, AIAA J.2007-1258.

[11] Renken J.H., 1985, “Mission – Adaptive Wing camber Control Systems for Transport Aircraft” – 3rd Applied Aerodynamics Conference, Colorado Springs, Co, AIAA 85-5006.

[12] Von Spakovsky and Butt J., Sanders B., Moorhouse D., **“**Benefits and design challenges of adaptive structures for morphing aircraft” and US Air Force Research LaboratoryWright-Patterson AFB Ohio, USA**M.** Virginia Polytechnic Institute and State UniversityVirginia, USA pp.159-160.

[13] Kikuta M.T., 2003, “Mechanical Properties of Candidate Materials for Morphing Wings” – Master’s Thesis, Univ. Of Virginia, Blacksburg, VA.

[14] Spillman J., 1992, “The Use of Variable Camber to Reduce Drag, Weight and Copsts

of transport Aircraft" – Aeronautical Journal, January 1992, vol.96, pp.1-8.

[15] Parker H.F., 1920, "The Parker Variable Camber Wing" – Annual Report national Advisory Committee for Aeronautics, report no.77.

[16] Frost & al., 1978, "Airfoil variable Cambering Device and Method" – United States patent no.4,247,066, general Dynamics Corporation, Forth worth, TX.

[17] Statkus F.D., 1980, "Continuous Skin Variable Camber Airfoil Edge Actuating Mechanism" – U.S. Patent no. 4,351,502, The Boeing Copmpany, Seattle, WA.

[18] Perez J., 2002, "Mechanism for at least regionally Adjusting the Curvature of Airfoil Wings" – U.S. patent no. 2002/0100842 A1.

[19] Federation of American Scientists. B-1B *Lancer*. http://www.fas.org/nuke/guide/usa/bomber/b-1b.htm, October 1999.

[20] Federation of American Scientists. F-14 *Tomcat*. http://www.fas.org/man/dod-101/sys/ac/f-14.htm, April 2000.

[21] Poonsong P., 2004, "Design and Analysis of a Multi-Section variable camber Wing" – Master's thesis, Univ. of Maryland, MD.

[22] Monner H.P., Bein T., Hanselka H., Breitbach E., 1998, "Design Aspects of the Adaptive Wing – The Elastic Trailing Edge and the Local Spoiler Bump" – Royal Aeronautical Society, Multidisciplinary Design and Optimization, London, October 1998.

[23] M. Santangelo*, L. Iuspa, L. Blasi "ANALISI CINETO-STATICA DI UNA STRUTTURA ALARE ADATTIVA HINGELESS" Associazione Italiana per l'Analisi delle Sollecitazioni (AIAS) XXXV National Conference– 13-16 September 2006, Marche. Polythecnic Univ.

[24] McGowan A,M., 2008, "Overview. Morphing Activities in the USA" – Advanced Coures on Morphing Aircraft materials, Mechanism and Systems, November 17-20, Lisbon, Portugal, invited lecturer.

[25] Thornton S.V., 1993, "Reduction of Structural Loads Using Manoeuvre Load Control on the Advanced Fighter technology Integration (AFTI)/F-111 Mission Adaptive wing" – NASA TM 4526.

[26] Simpson A., Jacob J., Smith S., 2005, "Inflatable and Warpable Wings for Mesoscale UAVs" – AIAA Journal 2005-7161.

[27] Cadogan D., Smith T., Lee R., Scarborough S., Graziosi D., 2003, "Inflatable and Rigidizable Wing Components for Unmanned Aerial Vehicles" – 44th AIAA/ASME/ASCE/AHS/ASC Structures, Structural Dynamics and Materials Conference, Norfolk, VA, AIAA Journal 2003-6630.

[28] Murray J.E., Pahle J.W., Thornton S.V., Vogus S., Frackowiak T., Mello J.D., Norton B., 2002, "Ground and Flight evaluation of a Small –Scale Inflatable Winged Aircraft" – 40th Aerospace Sciences Meeting & Exhibit, Reno, NV, AIAA Journal 2002-0820.

[29] Lin J.K., Sapna G.H., Cadogan D.P., Scarborough S.E., 2002, "Inflatable Rigidizable Isogrid Boom Development" – 43rd AIAA/ASME/ASCE/AHS/ASC Structures, Structural Dynamics and Materials Conference, Gossamer Spacecradft Forum, Denver, CO, AIAA Journal 2002-1297.

[30] Chandler J., Jacob J., 2007, "Design and Flight Testing of a mars Aircraft Prototype Using Inflatable Wings" – 58th International Astronautical Congress, September 27, Hyderabad, India.

[31] Kheong L.W., Jacob J.D., 2008, "In Flight Aspect Ratio Morphing Using Inflatable Wings" – 46th AIAA Aerospace Sciences Meeting and Exhibit, January 8-11, 2008, Reno, NV, AIAA Journal 2008-425.

[32] Gevers Aircraft Inc., 1997, "Multi-Purpose Aircraft", US patents Office, patent number 5,645,250.

[33] Munson K., 2000, "Jane's Unmanned Aerial Vehicles and Targets", Jane's issue 15.

[34] AeroVisions Inc., website. http://www.canosoaurus.com/05UMAAV/UMAAV01.htm

[35] AFRL, Vehicle Reseacrh Section, Air Launched IOntegrated Countermeasure, Expendable (ALICE), website: http://www.nrl.navy.mil/vrs/factsheets/index.php .

[36] Neal III D.A., Farmer J., Inman D.J., 2006, "Development of a Morphing Aircraft Model for Wind Tunnel Experimentation" – 47th AIAA/ASME/ASCE/AHS/ASC Structures, Structural Dynamics and Materials Conference, May 1-4, Newport, Rhode island, AIAA J. 2006-2141.

[37] Roth B.D., Crossley W.A., 2003, "Application of optimization Techniques in the Conceptual Design of Morphing Aircraft" – AIAA Journal 2003-6733.

[38] Flight group – Airline Industry news, aviation jobs 6 airline recruitment, website: http://www.flightinternastionsl.com/Articles/2005/09/13/Navigation

[39] Bye D.R., McChure P.D., 2007, "Design of a Morphing Vehicle" – 48th AIAA/ASME/ASCE/AHS/ASC Structures, Structural Dynamics and Materials Conference, April 23-26, Honolulu, Hawaii, AIAA J. 2007-1728.

[40] Love M.H., Zink P.S., Stroud R.L., Bye D.R., Rizk S., WhiteD., 2007, "Demonstration of Morphing Technology through Cround and Wind Tunnel Tests" – 48th AIAA/ASME/ASCE/AHS/ASC Structures, Structural Dynamics and Materials

Conference, April 23-26, Honolulu, Hawaii, AIAA J. 2007-1729.

[41] Ivanco T.G., Scott R.C., Love M.H., Zink S., Weisshaar T.A., 2007, "Validation of the Lockheed Martin Morphing Concept with Wind Tunnel Testing" - – 48th AIAA/ASME/ASCE/AHS/ASC Structures, Structural Dynamics and Materials Conference, April 23-26, Honolulu, Hawaii, AIAA J. 2007-2235.

[42] Cornerstone Research Group Inc., website: http://www.crgrp.net/veriflex.htm

[43] Perkins D.A., Reed J.L., Havens E., 2004, "Morphing Wing Structures for Loitering Air Vehicles" – 45th AIAA/ASME/ASCE/AHS/ASC Structures, Structural Dynamics and Materials Conference, Palm Springs, California, AIAA Journal 2004-1888.

[44] Flanagan J.S., Strutzenberg R.C., Myers R.B., Rodrian J.E., 2007, "Development and flight testing of a Morphing Aircraft, the NexGen MFX-1" - 48th AIAA/ASME/ASCE/AHS/ASC Structures, Structural Dynamics and Materials Conference, April 23-26, Honolulu, Hawaii, AIAA J. 2007-1707.

[45] Alasty A., Alemohammad S.H., Khiabani R.H., Khalighi Y., 2004, "Manoeuvrability Improvement for an Ultra Light Airplane Model Using variable Shape Wing" – AIAA Atmospheric Flight Mechanics Conference and Exhibit, Providence, Rhode Island, AIAA Journal 2004-4831.

[46] Benavides J.C., Correa G., 2004, "Morphing Wing Design Using NITiNOL Wire" Univ. of Missouri-Rolla (UMR), Intelligent System Centre, website: http://www.isc.mst.edu/reu/2004indprojects/2004-6html

[47] Song G., Ma N., 2007, "Robust control of a shape memory alloy wire actuated flap" – Smart materials and Structures, vol. 16, pp.N51-N57.

[48] Eggleston G., Hutchinson C., Johnston C., Koch B., Wargo G., Williams K., 2002, "Morphing Aircraft Design Team" – Virginia Tech Aerospace Engineeriong Senior Design Project.

[49] Kudva J.N., Lockyer A.J., Appa K., 1996, "Adaptive Aircraft Wing" – AGARD SMP Lecture series 205, Smart Structures and Materials: Implications for Military Aircraft of New Generation, AGARD-LS-205.

[50] Kudva J.N., Jardine P., Martin C., Appa K., 1996, "Overview of the ARPA/WL" "Smart Structure and Material Development – Smart Wing Contract" – SPIE, vol.2721.

[51] Kudva J.N., Carpenter B., 2000, "Smart Wing Program" – DARPA Technology Interchange Meeting, June 2000.

[52] Kudva J.N., 2001, "Overview of the DARPA/AFRL/NASA Smart Wing phase II

Program" - Smart Structures and Materials Conference, USA, SPIE n.4332-48, pp.383-389.

[53] Florance J.P., Burner A.W., Fleming G.A., Hunter C.A., Graves S.S., 2003, "Contribution of the NASA Langley Research Centre to the DARPA//AFRL/NASA/Northrop Grumman Smart Wing Program" – 44th AIAA/ASME/ASCE/AHS Structures, Structural Dynamics and Materials Conference, Norfolk, Virginia, AIAA Journal 2003-1961.

[54] Gonzales L., Rediniotis O., 2005, "Morphing Wing Using SMA" – T.I.I.M.S. 3rd Annual Meeting.

[55] Lecce L., 2004, "Deliverable 4 – relazione di Progetto del dimostratore bidimensionale" – Deept. Internal report no.04/64, Dept. of Aeronautical Design, Univ. of Napoli "Federico II", Napoli (italian)

[56] Lemme M. Caruso A., 2004, "Deliverable 3 – Modellazione FEM del dimostratore bidimensionale di un bordo d'attacco deformabile con attuazione tramite fili di SMA" – Dept. intenra,l report no.04/72, Dept. of Aeronautical Design, , Univ. of Napoli "Federico II", Napoli (italian)

[57] De Mattos B.S., Macedo A.P., da Silva Filho D.H., 2003, "Consideration about Winglet Design" – 21st Applied Aerodynamic Conference, June 23-26, Orlando, Florida, AIAA J. 2003-3502.

[58] Smith M.J., Komerath N., Ames R., Wong O., 2001, "Performance Ana,lysis of a Wing with Multiple Winglets" – AIAA Journal 2001-2407.

[59] Maughmer M.D., Swan T.S., Willit S.M., 2002, "Design and testing of a Winglet Airfoil for Low-speed Aircraft" – Journal of Aircraft, vol.39, no.4, pp.654-661.

[60] Soltani, M.R., Ghobarian K., Nazarinia M., 2004, "Flow Analysis Over and behind a Wing with Different Winglet Shapes" – 42nd AIAA Aerospace Sciences Meeting and Exhibit, January 5-8, Reno, NV, AIAA Journal 2004-723.

[61] Ogurek D.J., Ashworth J., 2004, "Experimental Investigation of various Winglet Designs for a Wing in Ground Effect" – 22nd Applied Aerodynamics Conference and Exhibit, August 16-19, Providence, Rhode Island, AIAA J. 2004-4720.

[62] Daccache E., Lee T., 2007, "Effect of a winglet on Normal Blade-Vortex Interaction" – Journal of Aircraft, vol.44, no.1, pp.264-273.

[63] Ning S.A. Kroo I., 2008, "Tip Extensions, Winglet and C-wings: Conceptual Design and Optimization" 26th AIAA Applied Aerodynamics Conference, August 18-21,

Honolulu, Hawaii, AIAA J. 2008-7052.

[64] Mann A., Elsholz E., 2005, "The M-DAW project Investigations in Novel Wing Tip Device Design" – 43rd AIAA Aerospace Sciences Meeting and Exhibit, January 10-13, Reno, NV, AIAA Journal 2005-461.

[65] Hantrais-Gervois J-L., Rapin M., 2006, "Aerodynamic and Structural Behaviour of a Wing equipped with a Winglet at Cruise" – 44th AIAA Aerospace Sciences Meeting and Exhibit, January 9-12, Reno, NV, AIAA Journal 2006-1489.

[66] Elsholz E., Barakat S., 2006, "CFD Analysis of twist Correction on Commercila Aircraft Wing with Different Tip Devices in ETW Windtunnel" – 44th AIAA Aerospace Sciences Meeting and Exhibit, January 9-12, Reno, NV, AIAA Journal 2006-513.

[67] Allen A., Breitsamter C., 2008, "Transport Aircraft Wake Influencede bu a Large Winglet and Winglet Flaps" – Journal of Aircraft vol. 45, no.2, pp. 686-699.

[68] Slingerland R., Verstraeten J.G., 2008, "Drag Characteristics for Optimally Spanloaded Planar, Wingletted and C-wings" - 46th AIAA Aerospace Sciences Meeting and Exhibit, January 7-10, Reno, NV, AIAA Journal 2008-161.

[69] Bourdin P. Gatto A., Friswell M.I., 2006, "The Application of variable Cant Angle Winglets for Morphing Aircraft Control" – 24th Applied Aerodynamic Conference, June 5-8, San Francisco, California, AIAA J. 2006-3660.

[70] Bourdin P. Gatto A., Friswell M.I., 2007, "Potential of Articualted Split Wingtips for Morphing-Based Control of a Flying Wing" - 25th Applied Aerodynamic Conference, June 25-28, Miami, Florida, AIAA J. 2007-4443.

[71] Ursache n.M., Melin T., Isikveren A.YT., Friswell M.I., 2007, "Morphing Winglets for Aircraft Multi-phase Improvement" – 7th AIAA Aviation Technology, Integration and Operations Conference (ATIO), September 18-20, Belfast, Northern Ireland, AIAa J. 2007-7813.

[72] Ameri N., Livne E., Lowenberg M.H., Friswell M.I., 2008, "Modelling Continuously Morphing Aircraft for Flight Control" AIAA Guidance, Navigation nad Control Conference and Exhibit, August 18-21, Honolulu, Hawaii, AIAA J. 2008-6966.

[73] Pitt D., Dunne J., White E., Garcia E., 2001, "SAMPSON smart inlety SMA powered adaptive lip design and static test" – Proceedings of the 42th AIAA Structures, Structural Dynamics and Materials Conference, April 16-20, Seattle, WA, pp.1-11

[74] Wax S., Fisher G., Sands R., 2003, "The past, present and future of DARPAs investment strategy in smart materials" – Journal of the Minerals, Metals and Materials

Society, vol.55, no.12, pp.17-23.

[75] Pitt D.M., Dunne J.P., White E.V., 2002, "Design and Test of a SMA Powered Adaptive Aircraft Inlet Internal Wall" – 43rd AIAA/ASME/ASCE/AHS/ASC Structures, Structural Dynamics and Materials Conference, April 22-25, Denver, Colorado, AIAA Journal 2004-1356.

[76] Timpano K.H., Zaidi S., Martinelli L., Miles R.B., Steeves C.A., Evans A.G., 2008, "Design and Test of a Morphing Supersonic Nozzle" – 46th AIAA Aerospace Sciences Meeting and Exhibit, January 7-10, Reno, NV, AIAA Journal 2008-851.

[77] Song G., Ma N., Lee h.-J., Arnold S., 2007, "Design and control of a proof-of-concept variable area exhaust nozzle using shape-memory alloy actuators" – Smart material and Structures, vol.16, pp.1342-1347.

[78] Calkins F.T., Mabe J.H., Ruggeri R.T., 2008, "Overview of Boeing's Shape Memory Alloy based Morphing Aerostructures" – Proceedings of ASME Conference on Smart Materials, Adaptive Structures and Intelligent Systems (SMASIS 2008), October 28-30, Ellicott City, Maryland, paper SMASIS 2008-648.

[79] Mabe J., Cabell R., Butler G., 2005, "Design and control of a morphing chevron for take-off and cruise noise reduction" – Proceedings of the 26th Annual AIAA Aeroacustics Conference, Monterey, CA, pp.1-45.

[80] Mabe J., Calkins F.T., Butler G.W., 2006 "Boeing's variable geometry chevron, morphing aerostructure for a jet noise reduction" – 47th AIAA/ASME/ASCE/AHS/ASC Structures, Structural Dynamics and Materials Conference, Newport, Rhode Island, pp.1-19AIAA Journal 2006-2142.

[81] Turner T.L., Buehrle R.D., Cano R.J., Fleming G.A., 2006, "Modeling, fabrication and testing of a SMA hybrid composite jet engine chevron concept" – Journal of Intelligent Material Systems and Structures, vol.17, pp.483-497.

[82] Leishman G., 2006, "Principles of helicopter Aerodynamics" – Cambridge University press.

[83] Warwick G., 2009, "Morphing Methods" – Aviation Week 6 Space Technology, October 5, 2009, p.55.

[84] Boyd Jr. Douglas D., 2009, "Aerodynamic and Acoustic Study of an Active twist Rotor using a Loosely Coupled CFD/CSD Method" 35th European Rotorcraft Forum, Hamburg, Germany, September 22-25, article 1160.

[85] bailly J., Delrieux Y., 2009, "Improvement of Noise Reduction and Performance for a

Helicopter Model Rotor Blade by Active Twist Actuation" – 35th European Rotorcraft Forum, Hamburg, Germany, September 22-25, article 1157.

[86] Zhang Q., Hoffmann F., 2009, "Benefit Studies for Rotor with Active Twist Control Using Weak Fluid-Structure Coupling" - 35th European Rotorcraft Forum, Hamburg, Germany, September 22-25, article 1217.

[87] Leon O., Gandhi F., 2009, "Rotor Power Reduction using Multiple Spanwise Segmented Optimally-Actuated Trailing Edge Flaps" 35th European Rotorcraft Forum, Hamburg, Germany, September 22-25, article 1309.

[88] Leon O., Hayden E., Gandhi F., 2009, "Rotorcraft Operating Envelope expansion Using Extendable Chord Sections" – Proceedings of the American helicopter Society 65th Annual Forum, Grapevine, Texas, May 27-29.

[89] Riemenschneider J., Opitz S., Weirach P., Mercier des Rochettes H., Buchaniek L., Joly D., 2009, "Structural design and testing of Active Twist Baldes – A comparison" - 35th European Rotorcraft Forum, Hamburg, Germany, September 22-25, article 1163.

[90] Mistry M.P., 2008, "Induced Warp Systems to Obtain Active Twist of Rotor Blades" – Master thesis, The Pennsylvania State University, State College.

[91] Ruggeri R.T., Bussom R.C., Arbogast D.J., 2008, "Development of a ¼ scale NiTiNOL actuator for reconfigurable structures" – SPIE Smart Materials and Structures, paper 6930-21.

[92] Blushnell G.S., Arbogast D.J., Ruggeri R.T., 2008, "Shape control of a morphing structure (rotor blade) using a shape memory alloy actuator system, future of SMA" – SPIE Smart Materials and Structures.

[93] Riemenschneider J., Keye S., Weirach P., Mercier des Rochettes H.,2004, "Overview of the Common DLR/ONERA Project 'Active Twist Blade' (ATB)" - 30th European Rotorcraft Forum, Marseilles, France, September 14-16, pp.20.1-9.

[94] Straub F., Anand V.R., Birchette T., Lau B.H., 2009, "SMART Rotor development and wind tunnel test" - 35th European Rotorcraft Forum 2009 (ERF 2009), Hamburg, Germany, September 22-25, article 1200.

[95] Ameduri,S., Pagano A., Altmikus A., Cokonasj V., Prachar A., Zachariadas Z., Drikakis D., 2009, "Helicopter Blade Twist Control through SMA Technology: Optimal Shape Prediction, Twist Actuator Realisation and Main Rotor Enhabced Performance Computation" - 35th European Rotorcraft Forum 2009 (ERF 2009), Hamburg, Germany, September 22-25, article 1297.

[96] Mabe J.H., Gravatt L., Bushnell G., Gutmark E., DiMiccio R.G., Harris C., 2008, "Shape Memory Alloy Actuators for Deployable rotor Blade Aerodynamic Devices" – 46th AIAA Aerospace Sciences Meeting and Exhibit, January 7-10, Reno, NV, AIAA Journal 2008-1451.

[97] Bell L., 2009, "Deployable Soft Space Structures. Concepts and Application Requirements" – 50th AIAA/ASME/ASCE/AHS/ASC Structures, Structural Dynamics and Materials Conference, May 4-7, Palm Spring, California, AIAA Journal 2009-2168.

[98] Sofla A.Y.N., Elzey D.M., Wadley H.N.G., 2007, "A rotational joint for shape morphing space truss structures" – Smart materials and Structures, vol.16, pp.1277-1284.

[99] Lafleur J.M., Olds J.R., Braun R.D., 2005, "Daedalon: A Revolutionary Morphing Spacecraft Design for Planetary Exploration" 1st Space Exploration Conference: Continuing the voyage of Discovery, Orlando, Florida, AIAA Journal 2005-2771.

[100] Callister W.D.J., 2006, "Materials Science and Engineering. An Introduction" – Seventh edition, Wiley.

[101] Keihl M.M., Bortolin R.S., Sanders B., Joshi S., Tidwell Z., 2005, "Mechanical properties of shape memory polymers for morphing aircraft applications" – International Society for Optical Engineering.

[102] Yakozeki T., Takeda S-I., Ogasawara T., Ishikawa t., 2006, "Mechanical properties of corrugated composites for candidate materials of flexible wing structures" Composites Part A. Applied Science and Manufacturing, vol.37, no.10, pp.1578-1586.

[103] Kudva J.N., 2004, "Overview of the DARPA smart wing project" – Journal of Intelligent material Systems and Structures, vol.15, no.4, pp.261-267.

[104] Bornengo D., Scarpa F., Remillat C., 2005, "Evaluation of hexagonal chiral structure for morphing airfoil concept" – Journal of Aerospace Engineering, vol.219, no.3, pp.185-192, Proceeding of the Institution of Mechanical Engineers, Part G.

[105] Wei G., Edwards S.F., 1998, "Auxeticity windows for composites" – Physica A, vol.258, no.1-2, pp.5-10.

[106] Olympio K.R., Gandhi GF., 2007, "Zero-v cellular honeycomb flexible skins foro ne-dimensional wing morphing" - 48th AIAA/ASME/ASCE/AHS/ASC Structures, Structural Dynamics and Materials Conference, April 23-26, Honolulu, Hawaii, AIAA Journal 2007-1735.

[107] Gandhi F. Anusonti-Inthra P., 2004, "On the Design of Flexible Skins for Morphing Aircraft Structures" – Proceedings of the 15th International Conference on Adaptive

Structures and technologies (ICAST), October 24-27, Bar Harbor, Maine.

[108] Murray G., Gandhi F., Bakis C., 2007, "Flexible Matrix Composite One-Dimensional wing Morphing" - 48th AIAA/ASME/ASCE/AHS/ASC Structures, Structural Dynamics and Materials Conference, April 23-26, Honolulu, Hawaii, AIAA Journal 2007-1737.

[109] Gandhi F. Anusonti-Inthra P., 2008, "Skin Design for Variable Camber Morphing Airfoils" Smart Materials and Structures, vol.17, 015025, 8pp.

[110] Lira C., Scarpa F., Olszewska M., Celuch M., 2009, "The SILICOMB cellular structure: Mechanical and dielectric properties" – Phys. Status Solidi B, vol.246, no.9, pp.2055-2062, doi: 10.1002/pssb.200982036.

[111] Heyer M.W., 1981, "Calculations of the room-temperature shapes of unsymmetric laminates" – Journal of Composite Materials, vol.15, pp.296-310.

[112] Heyer M.W., 1982, "The room-temperature shapes of 4-layer unsymmetric cross-ply laminates" – Journal of Composite Materials, vol 16, pp.318-340.

[113] Kebadze E., Guest S.D:, Pellegrino S., 2004, "Bistable prestressed shell structures" – International Journal of Solids and Structures, vol.41, no.11-12, pp.2801-2820.

[114] Hufenbach W., Gude M., Kroll L., 2002, "Design of multistable composites for application in adaptive structures" – Composites Science and Technology, vol.62, no.16, pp.2201-2207.

[115] Iqbal K., Pellegrino S., 2000, "Bi-stable composite shells" – American Inst. Aeronautics and Astronautics.

[116] Potter K., Weaver P., Seman A.A., Shah S., 2007, "Phenomena in the bifurcation of unsymmetric composite plates" – Composites Part A: Applied Science and Manufacturing, vol.38, no.1, pp.100-106.

[117] Mattioni F., Weaver P.M., Friewell M.I., Potter K.D., 2007, "Modelling and applications of thermally induced multistable composites with piecewise variation of lay-up in the planform" - 48th AIAA/ASME/ASCE/AHS/ASC Structures, Structural Dynamics and Materials Conference, April 23-26, Honolulu, Hawaii, AIAA Journal 2007-2262.

[118] Norman A.D., Guest S.D., Seffen K.A., 2007, "Novel Multiostable Corrugated Structures" - 48th AIAA/ASME/ASCE/AHS/ASC Structures, Structural Dynamics and Materials Conference, April 23-26, Honolulu, Hawaii, AIAA Journal 2007-2228.

[119] Otsuka K., Wayman C.M., 1999, "Shape Memory Materials" – Cambridge

University press.

[120] David P. Cadogan, Stephen E. Scarborough AIAA 2001-1417 Rigidizable Materials for use in Gossamer Space Inflatable Structures ILC Dover, Inc. Frederica, DE p.9

[121] Zheng Y.J., Cui L.S., Schrooten J., 2005, "Basic design guidelines for SMA/epoxy smart composites" – materials Science and Engineering a Structural Materials Microstructure and Processing, vol.390, no.1-2, pp.139-143.

[122] Dano M.L., Hyer M.W., 2003, "SMA-induced snap-through of unsymmetric fiber-reinforced composite laminates" – International Journal of Solids and Structures, vol.40, no.22,pp.5949-5972.

[123] Barrett R., Gross R.S., 1996, "Super-active shape memory alloy composites" – Smart Materials and Structures, vol.5, no.3, pp.255-260.

[124] Shaw J.A:, Churchill C., Triantafyllidis N., Michailidis P., Grummon D., Folts j., 2007, "Shape memory alloy honeycombs: experiments & simulation" - 48th AIAA/ASME/ASCE/AHS/ASC Structures, Structural Dynamics and Materials Conference, April 23-26, Honolulu, Hawaii, AIAA Journal 2007-1739.

[125] Hu J., 2007, "Shape memory polymers and textiles" – Woodhead publishing limited.

[126] Bellin I., Kelch S., Langer R., Lendlein A., 2006, "Polymeric triple-shape materials" – Proceedings of the National Academy of Sciences of the United States of America, vol.103, no.48, pp.18043-18047.

[127] Lendlein A., Kelch S., 2002, "Shape memory polymers" – Angewandte Chemie-International edition, vol.41, no.12, pp.2035-2057.

[128] McKnight G., Henry C., 2005, "Variable stiffness materials for reconfigurable surface applications" – International Society for Optical Engineering.

[129] The Intelligent Material DIAPLEX, Mitsubishi heavy Industries, website: http://www.diaplex.com

[130] Potter K.D., Wisnom M.R., 2002, "Composites of extreme anisotropy initial experiments" – Plastics, Rubber and Composites, vol.31, no.5, pp.226-234.

[131] Butler G., 2007, "Investigation of corrugated composite laminates for use in morphing wing skin applications" – Department of Aerospace, Univ. of Bristol

[132] Ramrakhyani D.S., Lesieutre G.A., Frecker M., Bharti S., 2005, "Aircraft structural morphing using tendon-actuated compliant cellular trusses" – Journal of Aircraft, vol.42, no.6, pp.1615-1621.

[133] Long J.H., Hale M.E., Mchenry M.J., Westneat M.W., 1996, "Functions of fish skin: Flexural stiffness and steady swimming of longnose gar Lepisosteus osseus" – Journal of Experimental Biology, vol.199, no.10, pp.2139-2151.

[134] Varma K.B.R., 1990, "Morphology and dielectric properties of fish scales" – Current Science, vol.59, no.8, pp.420-422.

[135] Bechert D.W., Bruse M., Hage W., 2000, "Experiments with three-dimensional riblets as an idealized model of shark skin" Experiments in Fluids, vol.28,no.5, pp.403-412.

[136] C. Thill, J. Etches, I. Bond, K. Potter and P. Weaver "Morphing skins" Advanced Composites Centre for Innovation and Science (ACCIS)Department of Aerospace Engineering, University of Bristol, UK

CHAPTER 4
A PELTIER CELL AS COOLING SYSTEM

4.1 Introduction

In the previous chapter a general wing morphing description has been presented and in particular also a material overview has been provided.

In this section a new cooling concept approach is described by means of a Peltier cell used as a cooling system on the S.M.A. ribbon for a flap actuator. An overview of semiconductor materials and their use into Peltier cell and all pro and contra of this type of application is provided.

In the following, after a brief Peltier effect description and operability a possible solution for the S.M.A. cooling has been presented.

4.2 Semiconductor materials

Semiconductor materials are named such as materials that have an intermediate resistivity between conductor and insulating materials. The most commonly used materials are german and silicon with a resistivity, respectively, of 0.6 and $2 \text{ x } 10^3 \Omega m$.

This chemical elements are tetravalent with four valence electrons and each atom joins together for a crystal aggregation where each atom joins his four valence electrons with four adjacent atoms. So that, all around each atom there are 8 rotating electrons, 4 of each ones of the same originating atom and 4 of adjacent atom.

A very stable crystal structure is obtained, thanks to covalent bond by means of electron in common lock up adjacent atoms.

However, already at room temperature some valence electrons get sufficient energy to run out from their atoms and to become free electrons, each ones leaving in the crystal lattice a hole. In the semiconductor this hole allows a positive charge; if an electrical field is applied to a semiconductor, silicon for example, free electrons follow opposite direction with respect to the electrical field when the electrical current is in the semiconductor.

Valence electrons still joined with the atoms are driven to follow opposite direction to the electrical field, but the motion is obstructed by the atom attractive force.

However, if a valence electron is driven by the field towards an adjacent atom with a hole, this valence electron is captured by the adjacent atom, counteracting the hole, but

generating another hole in the originating atom.

In other words, the hole has moved according to electrical field, so hole can be considered as a positive charge.

So that, an electron in atom adjacent to the generated hole repeats this described process and for this reason the presence of electrical field determines a hole movement according to the field direction.

At the end it is clear that in a semiconductor subjected to an electrical field a current with the same field orientation is generated. Finally, current determines a free electron motion in opposition to electrical field orientation and whereas a hole motion according to field orientation.

In pure semiconductor free electron and hole number is the same. This condition is strongly altered if in a semiconductor impurity is added; for example in a silicon crystal lattice small quantity of pentavalent element (phosphorus, antimony etc.) are added, impurity atoms get into the crystal lattice, with no alteration, substituting the same number of silicon atoms.

However only 4 of 5 valence electrons of new atoms need to define covalent bonds among adjacent reticular atoms, while the fifth electron immediately becomes free electron and no hole in the crystal lattice takes place.

This implies that pentavalent impurity presence determines a free electron number increase in the semiconductor remaining hole number the same.

So that, semiconductor is doped type n (negative) where free electrons are majority charges and the vacancies are minority charges.

Whereas, if small quantity of trivalent element (boron, gallium etc.) are added new atoms get into the crystal lattice substituting the same silicon atom number; bonds among adjacent atoms are defective because external atoms share the process only by 3 valence electrons, so, for each impurity atom, a hole takes place but no valence electrons become free electrons. Trivalent impurity determines a hole number growth but no free electron number increase happens.

So that, semiconductor is named doped type p (positive), vacancies are majority charges and electrons are minority charges.

4.3 Properties of a p-n junction

In this section in order to define the great commercial importance and diffusion of this type of devices a more complete p-n junction description shall be provided.

A p–n junction is formed by joining p-type and n-type semiconductors together in very close contact. The term junction refers to the boundary interface where the two regions of the semiconductor meet. If they were composed of two separate pieces this would introduce a grain boundary, so p–n junctions are created in a single crystal of semiconductor by doping, for example by ion implantation, diffusion of dopants, or by epitaxy (growing a layer of crystal doped with one type of dopant on top of a layer of crystal doped with another type of dopant).

P-N junctions are elementary "building blocks" of almost all semiconductor electronic devices such as diodes, transistors, solar cells, LEDs, and integrated circuits; they are the active sites where the electronic action of the device takes place. For example, a common type of transistor, the bipolar junction transistor, consists of two p–n junctions in series, in the form n–p–n or p–n–p.

The discovery of the p–n junction is usually attributed to American physicist Russell Ohl of Bell Laboratories [1]. Schottky junction is a special case of a p-n junction, where metal serves the role of the n-type semiconductor.

The figure 4.1 shows the p-n junction.

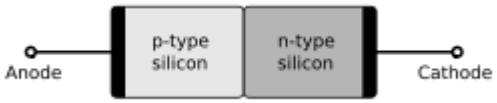

Figure 4.1: A p–n junction with anode and cathode

Normally, p–n junctions are manufactured from a single crystal with different dopant concentrations diffused across it. Creating a semiconductor from two separate pieces of material would introduce a grain boundary between the metals which severely inhibits its utility by scattering the electrons and holes. However, in the case of solar cells, polycrystalline silicon is often used to reduce expense, despite the lower efficiency.

The p–n junction possesses some interesting properties which have useful applications in modern electronics. A p-doped semiconductor is relatively conductive. The same is true of an n-doped semiconductor, but the junction between them is a nonconductor. This nonconducting layer, called the depletion zone, occurs because the electrical charge carriers in doped n-type and p-type silicon (electrons and holes, respectively) diffuse into the other type of material (i.e. electrons in p-type and holes in n-type) and eliminate each other in a process called recombination. By manipulating this non-conductive layer, p–n junctions are commonly used as diodes: circuit elements that allow a flow of electricity in one direction but not in the other (opposite) direction. This property is explained in terms of forward bias and reverse bias, where the term bias refers to an application of electric voltage to the p–n junction.

In a p–n junction, without an external applied voltage, an equilibrium condition is reached in which a potential difference is formed across the junction. This potential difference is called built-in potential Vbi.

After joining p-type and n-type semiconductors, electrons near the p–n interface tend to diffuse into the p region. As electrons diffuse, they leave positively charged ions (donors) in the n region. Similarly, holes near the p–n interface begin to diffuse into the n-type region leaving fixed ions (acceptors) with negative charge. The regions nearby the p–n interfaces lose their neutrality and become charged, forming the space charge region or depletion layer (see figure 4.2).

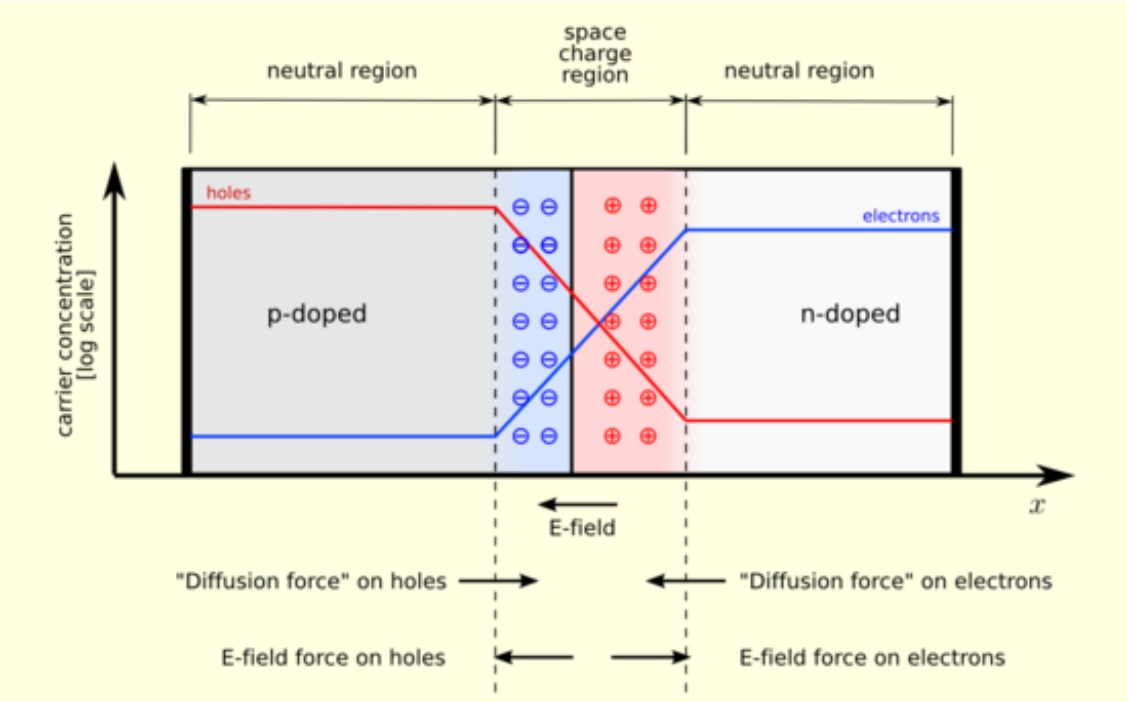

Figure 4.2: A p–n junction in thermal equilibrium with zero bias voltage applied. Electrons and holes concentration are reported respectively with blue and red lines. Gray regions are charge neutral. Light red zone is positively charged. Light blue zone is negatively charged. The electric field is shown on the bottom, the electrostatic force on electrons and holes and the direction in which the diffusion tends to move electrons and holes.

The electric field created by the space charge region opposes the diffusion process for both electrons and holes. There are two concurrent phenomena: the diffusion process that tends to generate more space charge, and the electric field generated by the space charge that tends to counteract the diffusion. The carrier concentration profile at equilibrium is shown in figure 4.2 with blue and red lines. Also shown are the two counterbalancing phenomena that establish equilibrium.

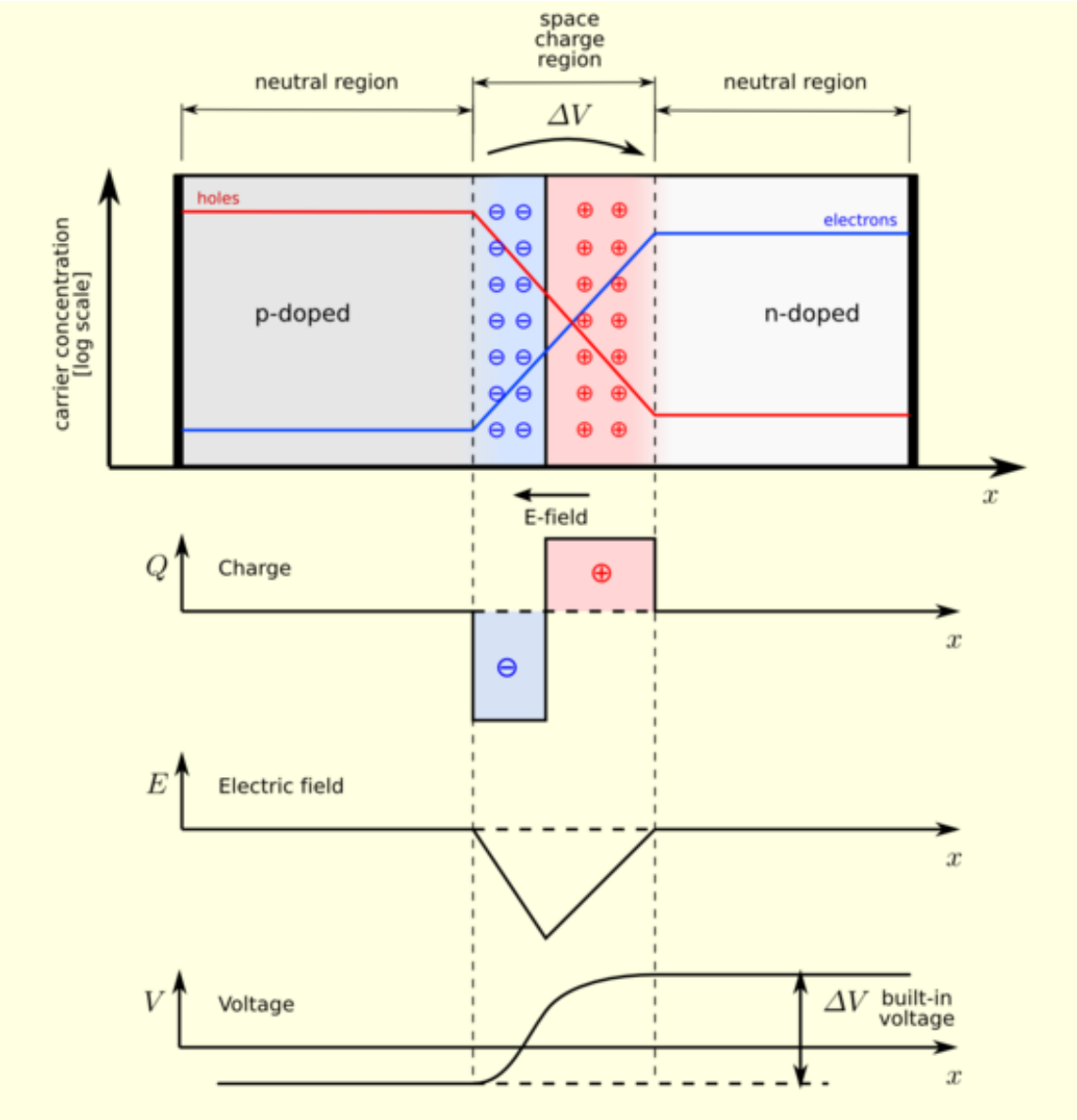

Figure 4.3: A p–n junction in thermal equilibrium with zero bias voltage applied. Under the junction, plots for the charge density, the electric field and the voltage are reported

The space charge region is a zone with a net charge provided by the fixed ions (donors or acceptors) that have been left uncovered by majority carrier diffusion. When equilibrium is reached, the charge density is approximated by the displayed step function. In fact, the region is completely depleted of majority carriers (leaving a charge density equal to the net doping level), and the edge between the space charge region and the neutral region is quite sharp (see figure 4.3 Q(x) graph). The space charge region has the same charge on both sides of the p–n interfaces, thus it extends farther on the less doped side (the n side in figures 4.2 and 4.3).

With a battery connected this way, the holes in the P-type region and the electrons in the

N-type region are pushed towards the junction. This reduces the width of the depletion zone. The positive charge applied to the P-type material repels the holes, while the negative charge applied to the N-type material repels the electrons. As electrons and holes are pushed towards the junction, the distance between them decreases. This lowers the barrier in potential. With increasing forward-bias voltage, the depletion zone eventually becomes thin enough that the zone's electric field can't counteract charge carrier motion across the p–n junction, consequently reducing electrical resistance. The electrons which cross the p–n junction into the P-type material (or holes which cross into the N-type material) will diffuse in the near-neutral region. Therefore, the amount of minority diffusion in the near-neutral zones determines the amount of current that may flow through the diode.

Only majority carriers (electrons in N-type material or holes in P-type) can flow through a semiconductor for a macroscopic length. With this in mind, consider the flow of electrons across the junction. The forward bias causes a force on the electrons pushing them from the N side towards the P side. With forward bias, the depletion region is narrow enough that electrons can cross the junction and inject into the P-type material. However, they do not continue to flow through the P-type material indefinitely, because it is energetically favorable for them to recombine with holes. The average length an electron travels through the P-type material before recombining is called the diffusion length, and it is typically on the order of microns [2].

Although the electrons penetrate only a short distance into the P-type material, the electric current continues uninterrupted, because holes (the majority carriers) begin to flow in the opposite direction. The total current (the sum of the electron and hole currents) is constant in space, because any variation would cause charge buildup over time (this is Kirchhoff's current law). The flow of holes from the P-type region into the N-type region is exactly analogous to the flow of electrons from N to P (electrons and holes swap roles and the signs of all currents and voltages are reversed).

Therefore, the macroscopic picture of the current flow through the diode involves electrons flowing through the N-type region toward the junction, holes flowing through the P-type region in the opposite direction toward the junction, and the two species of

carriers constantly recombining in the vicinity of the junction. The electrons and holes travel in opposite directions, but they also have opposite charges, so the overall current is in the same direction on both sides of the diode, as required.

4.4 The Thermoelectric effect : theory

The thermoelectric effect is the direct conversion of temperature differences to electric voltage and vice versa. A thermoelectric device creates a voltage when there is a different temperature on each side. Conversely when a voltage is applied to it, it creates a temperature difference (known as the Peltier effect). At atomic scale (specifically, charge carriers), an applied temperature gradient causes charged carriers in the material, whether they are electrons or electron holes, to diffuse from the hot side to the cold side, similar to a classical gas that expands when heated; hence, the thermally induced current takes place.

This effect can be used to generate electricity, to measure temperature, to cool objects, or to heat them or cook them. Because the direction of heating and cooling is determined by the sign of the applied voltage, thermoelectric devices make very convenient temperature controllers.

Traditionally, the term thermoelectric effect or thermoelectricity encompasses three separately identified effects, the Seebeck effect, the Peltier effect, and the Thomson effect. In many textbooks, thermoelectric effect may also be called the Peltier–Seebeck effect. This separation derives from the independent discoveries of French physicist Jean Charles Athanase Peltier and Estonian-German physicist Thomas Johann Seebeck. Joule heating, the heat that is generated whenever a voltage is applied across a resistive material, is somewhat related, though it is not generally termed a thermoelectric effect (and it is usually regarded as being a loss mechanism due to non-ideality in thermoelectric devices). The Peltier–Seebeck and Thomson effects can in principle be thermodynamically reversible [3] whereas Joule heating is not.

Figure 4.4: A commercial Peltier cell

Seebeck effect

The Seebeck effect is the conversion of temperature differences directly into electricity. Seebeck discovered that a compass needle would be deflected when a closed loop was formed of two metals joined in two places with a temperature difference between the junctions. This is because the metals respond differently to the temperature difference, which creates a current loop, which produces a magnetic field. Seebeck, however, at this time did not recognize there was an electric current involved, so he called the phenomenon the thermomagnetic effect, thinking that the two metals became magnetically polarized by the temperature gradient. The Danish physicist Hans Christian Ørsted played a vital role in explaining and conceiving the term "thermoelectricity".

The effect is that a voltage, the thermoelectric EMF (electro-magnetic force), is created in the presence of a temperature difference between two different metals or semiconductors. This causes a continuous current in the conductors if they form a complete loop. The voltage created is of the order of several microvolts per kelvin difference. One such combination, copper-constantan, has a Seebeck coefficient of 41 microvolts per kelvin at room temperature. In the circuit:

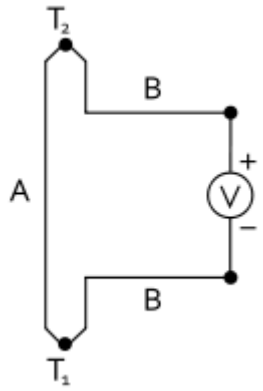

Figure 4.5: Circuit scheme (Seebeck effect).

(which can be in several different configurations and be governed by the same equations), the voltage developed can be derived from:

$$V = \int_{T_1}^{T_2} \left(S_B(T) - S_A(T) \right) dT \tag{4.1}$$

S_A and S_B are the Seebeck coefficients (also called thermoelectric power or thermopower) of the metals A and B as a function of temperature, and T_1 and T_2 are the temperatures of the two junctions. The Seebeck coefficients are non-linear as a function of temperature, and depend on the conductors' absolute temperature, material, and molecular structure. If the Seebeck coefficients are effectively constant for the measured temperature range, the above formula can be approximated as:

$$V = (S_B - S_A) \cdot (T_2 - T_1) \tag{4.2}$$

The Seebeck effect is commonly used in a device called a thermocouple (because it is made from a coupling or junction of materials, usually metals) to measure a temperature difference directly or to measure an absolute temperature by setting one end to a known temperature. A metal of unknown composition can be classified by its thermoelectric effect if a metallic probe of known composition, kept at a constant temperature, is held in contact with it. Industrial quality control instruments use this Seebeck effect to identify metal alloys. This is known as thermoelectric alloy sorting.

Several thermocouples connected in series are called a thermopile, which is sometimes constructed in order to increase the output voltage since the voltage induced over each individual couple is small.

This is also the principle at work behind thermal diodes and thermoelectric generators (such as radioisotope thermoelectric generators or RTGs) which are used for creating power from heat differentials.

The Seebeck effect is due to two effects: charge carrier diffusion and phonon drag.
If both connections are held at the same temperature, but one connection is periodically

opened and closed, an AC voltage is measured, which is also temperature dependent. This application of the Kelvin probe is sometimes used to argue that the underlying physics only needs one junction. And this effect is still visible if the wires only come close, but do not touch, thus no diffusion is needed.

The thermopower, thermoelectric power, or Seebeck coefficient of a material measures the magnitude of an induced thermoelectric voltage in response to a temperature difference across that material. The thermopower has units of (V/K), though in practice it is more common to use microvolts per kelvin. Values in the hundreds of μV/K, negative or positive, are typical of good thermoelectric materials. The term thermopower is a misnomer since it measures the voltage or electric field induced in response to a temperature difference, not the electric power. An applied temperature difference causes charged carriers in the material, whether they are electrons or holes, to diffuse from the hot side to the cold side, similar to a classical gas that expands when heated. Mobile charged carriers migrating to the cold side leave behind their oppositely charged and immobile nuclei at the hot side thus giving rise to a thermoelectric voltage (thermoelectric refers to the fact that the voltage is created by a temperature difference). Since a separation of charges also creates an electric potential, the buildup of charged carriers onto the cold side eventually ceases at some maximum value since there exists an equal amount of charged carriers drifting back to the hot side as a result of the electric field at equilibrium. Only an increase in the temperature difference can resume a buildup of more charge carriers on the cold side and thus lead to an increase in the thermoelectric voltage. Incidentally the thermopower also measures the entropy per charge carrier in the material. To be more specific, the partial molar electronic heat capacity is said to equal the absolute thermoelectric power multiplied by the negative of Faraday's constant [4].

The thermopower of a material, represented by S (or sometimes by α), depends on the material's temperature and crystal structure. Typically metals have small thermopowers because most have half-filled bands. Electrons (negative charges) and holes (positive charges) both contribute to the induced thermoelectric voltage thus canceling each other's contribution to that voltage and making it small. In contrast, semiconductors can be doped with excess electrons or holes, and thus can have large positive or negative values of the thermopower depending on the charge of the excess carriers. The sign of the thermopower

can determine which charged carriers dominate the electric transport in both metals and semiconductors.

If the temperature difference ΔT between the two ends of a material is small, then the thermopower of a material is defined (approximately) [5] as:

$$S = \frac{\Delta V}{\Delta T} \tag{4.3}$$

and a thermoelectric voltage ΔV is seen at the terminals.

This can also be written in relation to the electric field E and the temperature gradient , by the approximate [3] equation:

$$S = \frac{E}{\nabla T} \tag{4.4}$$

In practice one rarely measures the absolute thermopower of the material of interest. This is because electrodes attached to a voltmeter must be placed onto the material in order to measure the thermoelectric voltage. The temperature gradient then also typically induces a thermoelectric voltage across one leg of the measurement electrodes. Therefore the measured thermopower includes a contribution from the thermopower of the material of interest and the material of the measurement electrodes.

The measured thermopower is then a contribution from both and can be written as:

$$S = S_B - S_A = \frac{\Delta V_B}{\Delta T} - \frac{\Delta V_A}{\Delta T} \tag{4.5}$$

Superconductors have zero thermopower since the charged carriers produce no entropy. This allows a direct measurement of the absolute thermopower of the material of interest, since it is the thermopower of the entire thermocouple as well. In addition, a measurement of the Thomson coefficient, μ, of a material can also yield the thermopower through the relation:

$$S = \int \frac{\mu}{T} dT \tag{4.6}$$

The thermopower is an important material parameter that determines the efficiency of a thermoelectric material. A larger induced thermoelectric voltage for a given temperature gradient will lead to a larger efficiency. Ideally one would want very large thermopower values since only a small amount of heat is then necessary to create a large voltage. This voltage can then be used to provide power.

Charge carrier diffusion

Charge carriers in the materials (electrons in metals, electrons and holes in semiconductors, ions in ionic conductors) will diffuse when one end of a conductor is at a different temperature from the other. Hot carriers diffuse from the hot end to the cold end, since there is a lower density of hot carriers at the cold end of the conductor. Cold carriers diffuse from the cold end to the hot end for the same reason.

If the conductor were left to reach thermodynamic equilibrium, this process would result in heat being distributed evenly throughout the conductor (heat transfer). The movement of heat (in the form of hot charge carriers) from one end to the other is called a heat current. As charge carriers are moving, it is also an electrical current.

In a system where both ends are kept at a constant temperature difference (a constant heat current from one end to the other), there is a constant diffusion of carriers. If the rate of diffusion of hot and cold carriers in opposite directions were equal, there would be no net change in charge. However, the diffusing charges are scattered by impurities, imperfections, and lattice vibrations (phonons). If the scattering is energy dependent, the hot and cold carriers will diffuse at different rates. This creates a higher density of carriers at one end of the material, and the distance between the positive and negative charges produces a potential difference; an electrostatic voltage.

This electric field, however, opposes the uneven scattering of carriers, and an equilibrium is reached where the net number of carriers diffusing in one direction is canceled by the net number of carriers moving in the opposite direction from the electrostatic field. This

means the thermopower of a material depends greatly on impurities, imperfections, and structural changes (which often vary themselves with temperature and electric field), and the thermopower of a material is a collection of many different effects.

Early thermocouples were metallic, but many more recently developed thermoelectric devices are made from alternating p-type and n-type semiconductor elements connected by metallic interconnects as pictured in the figures below. Semiconductor junctions are especially common in power generation devices, while metallic junctions are more common in temperature measurement. Charge flows through the n-type element, crosses a metallic interconnect, and passes into the p-type element. If a power source is provided, the thermoelectric device may act as a cooler, as in the figure 4.6 to the left below. This is the Peltier effect, described below. Electrons in the n-type element will move opposite the direction of current and holes in the p-type element will move in the direction of current, both removing heat from one side of the device. If a heat source is provided, the thermoelectric device may function as a power generator, as in the figure 4.6 to the right below. The heat source will drive electrons in the n-type element toward the cooler region, thus creating a current through the circuit. Holes in the p-type element will then flow in the direction of the current. The current can then be used to power a load, thus converting the thermal energy into electrical energy.

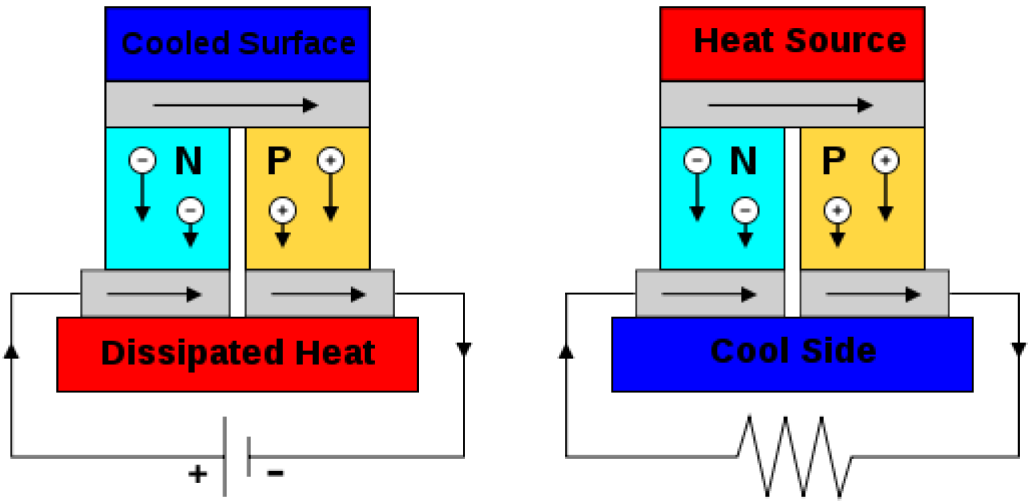

Figure 4.6: Example for heating an cooling.

Thomson effect

The Thomson effect was predicted and subsequently experimentally observed by William Thomson (Lord Kelvin) in 1851. It describes the heating or cooling of a current-carrying conductor with a temperature gradient.

Any current-carrying conductor (except for a superconductor), with a temperature difference between two points, will either absorb or emit heat, depending on the material.

If a current density J is passed through a homogeneous conductor, heat production per unit volume is:

$$q = \rho J^2 - \mu J \cdot \frac{dT}{dx} \tag{4.7}$$

where

ρ is the resistivity of the material;
dT/dx is the temperature gradient along the wire;
μ is the Thomson coefficient.
The first term ρ J² is simply the Joule heating, which is not reversible.
The second term is the Thomson heat, which changes sign when J changes direction.
In metals such as zinc and copper, which have a hotter end at a higher potential and a cooler end at a lower potential, when current moves from the hotter end to the colder end, it is moving from a high to a low potential, so there is an evolution of heat. This is called the positive Thomson effect.

In metals such as cobalt, nickel, and iron, which have a cooler end at a higher potential and a hotter end at a lower potential, when current moves from the hotter end to the colder end, it is moving from a low to a high potential, there is an absorption of heat. This is called the negative Thomson effect.

The Thomson coefficient is unique among the three main thermoelectric coefficients because it is the only thermoelectric coefficient directly measurable for individual materials. The Peltier and Seebeck coefficients can only be determined for pairs of

materials. Thus, there is no direct experimental method to determine an absolute Seebeck coefficient (i.e. thermopower) or absolute Peltier coefficient for an individual material. However, as mentioned elsewhere in this section there are two equations, the Thomson relations, also known as the Kelvin relations, relating the three thermoelectric coefficients. Therefore, only one can be considered unique.

If the Thomson coefficient of a material is measured over a wide temperature range, including temperatures close to zero, one can then integrate the Thomson coefficient over the temperature range using the Kelvin relations to determine the absolute (i.e. single-material) values for the Peltier and Seebeck coefficients. In principle, this needs only be done for one material, since all other values can be determined by measuring pairwise Seebeck coefficients in thermocouples containing the reference material and then adding back the absolute thermoelecric power (thermopower) of the reference material.

It is commonly asserted that lead has a zero Thomson effect. While it is true that the thermoelectric coefficients of lead are small, they are in general non-zero. The Thomson coefficient of lead has been measured over a wide temperature range and has been integrated to calculate the absolute thermoelectric power (thermopower) of lead as a function of temperature [6].

Unlike lead, the thermoelectric coefficients of all known superconductors are zero.

The Seebeck effect is actually a combination of the Peltier and Thomson effects. In fact, in 1854 Thomson found two relationships, now called the Thomson or Kelvin relationships, between the corresponding coefficients. The absolute temperature T, the Peltier coefficient Π and Seebeck coefficient S are related by the second Thomson relation

$$\Pi = S \cdot T \tag{4.8}$$

which predicted the Thomson effect before it was actually formalized. These are related to the Thomson coefficient μ by the first Thomson relation

$$\mu = T \cdot \frac{dS}{dT} \tag{4.9}$$

Thomson's theoretical treatment of thermoelectricity is remarkable in the fact that it is probably the first attempt to develop a reasonable theory of irreversible thermodynamics (non-equilibrium thermodynamics). This occurred at about the time that Clausius, Thomson, and others were introducing and refining the concept of entropy.

Peltier effect

The Peltier effect is the reverse of the Seebeck effect; a creation of a heat difference from an electric voltage.

It occurs when a current is passed through two dissimilar metals or semiconductors (n-type and p-type) that are connected to each other at two junctions (Peltier junctions). The current drives a transfer of heat from one junction to the other: one junction cools off while the other heats up. This effect was observed 13 years after Seebeck's initial discovery in 1834 by Jean Peltier. The Peltier effect bears the name of Jean-Charles Peltier, a French physicist who in 1834 discovered the calorific effect of an electrical current at the junction of two different metals (as in figure 4.7). When a current is made to flow through the circuit, heat is evolved at the upper junction (at T_2), and absorbed at the lower junction (at T_1). The Peltier heat absorbed by the lower junction per unit time, is equal to

$$Q = \Pi_{AB} \cdot I = \left(\Pi_B - \Pi_A\right) \cdot I \tag{4.10}$$

where Π is the Peltier coefficient Π_{AB} of the entire thermocouple, and Π_A and Π_B are the coefficients of each material. p-type silicon typically has a positive Peltier coefficient (though not above ~550 K), and n-type silicon is typically negative.

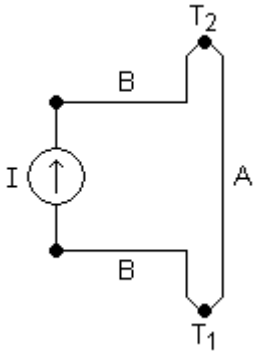

Figure 4.7: Circuit scheme (Peltier effect).

The Peltier coefficients represent how much heat current is carried per unit charge through a given material. Since charge current must be continuous across a junction, the associated heat flow will develop a discontinuity if Π_A and Π_B are different. This causes a non-zero divergence at the junction and so heat must accumulate or deplete there, depending on the sign of the current. Another way to understand how this effect could cool a junction is to note that when electrons flow from a region of high density to a region of low density, this "expansion" causes cooling (as with an ideal gas).

The carriers are attempting to return to the electron equilibrium that existed before the current was applied by absorbing energy at one connector and releasing it at the other. The individual couples can be connected in series to enhance the effect.

An interesting consequence of this effect is that the direction of heat transfer is controlled by the polarity of the current; reversing the polarity will change the direction of transfer and thus the sign of the heat absorbed/evolved.
A Peltier cooler/heater or thermoelectric heat pump is a solid-state active heat pump which transfers heat from one side of the device to the other. Peltier cooling is also called thermo-electric cooling (TEC).

The figure of merit for thermoelectric devices is defined as

$$Z = \frac{\sigma S^2}{\kappa} \tag{4.11}$$

where σ is the electrical conductivity, κ is the thermal conductivity, and S is the Seebeck coefficient or thermopower (conventionally in μV/K). This is more commonly expressed as the dimensionless figure of merit $Z \cdot T$ by multiplying it with the average temperature $T_m = \frac{T_1 + T_2}{2}$. Greater values of $Z \cdot T$ indicate greater thermodynamic efficiency, subject to certain provisions, particularly the requirement that the two materials of the couple have similar Z values. $Z \cdot T$ is therefore a very convenient figure for comparing the potential efficiency of devices using different materials. Values of $Z \cdot T = 1$ are considered good, and values of at least the 3–4 range are considered to be essential for

thermoelectrics to compete with mechanical generation and refrigeration in efficiency. To date, the best reported $Z \cdot T$ values have been in the 2–3 range [7][8][9]. Much research in thermoelectric materials has focused on increasing the Seebeck coefficient and reducing the thermal conductivity, especially by manipulating the nanostructure of the materials.

4.5 Peltier cell description

A Peltier cell is a thermoelctrical device with many junctions series assembled using the Peltier effect. A Peltier cell is essentially a solid state heat pump with the aspect of a small thin plate with a surface from heat is absorbed and the other one from heat is emitted.
The heat emission direction depends on the applied current versus as in the figure 4.8 and 4.9.

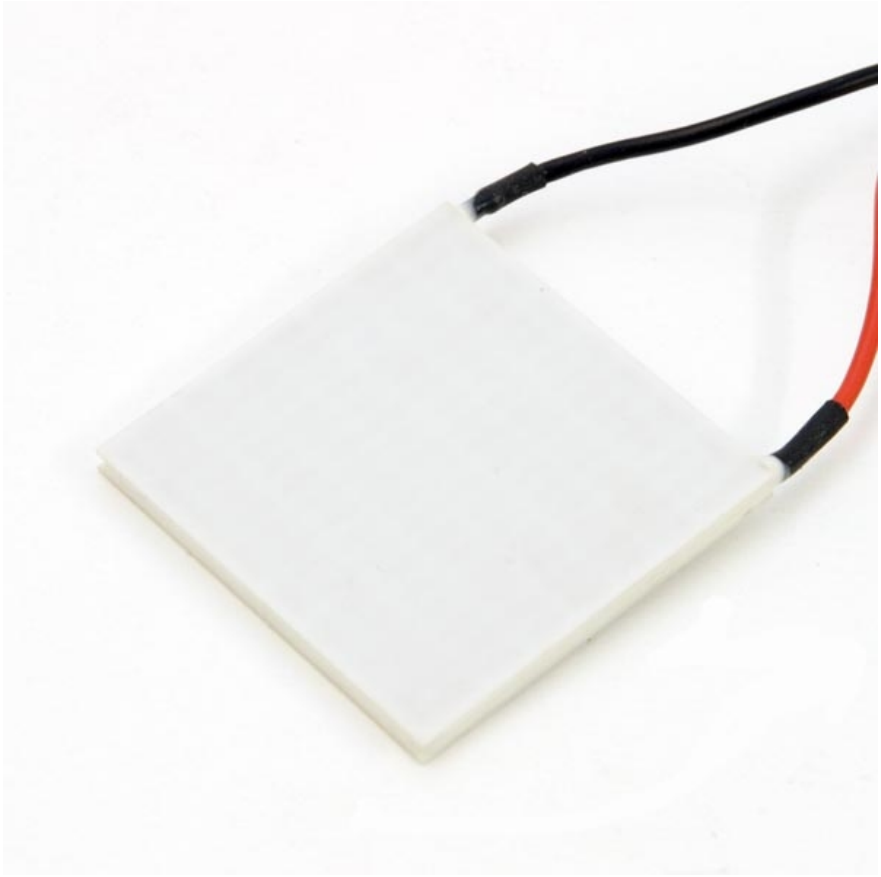

Figure 4.8: Peltier cell connected to red and black wire is supplied by 1A d.c. ; voltage is 1V. One of each face is warmed and the other ones is cooled.

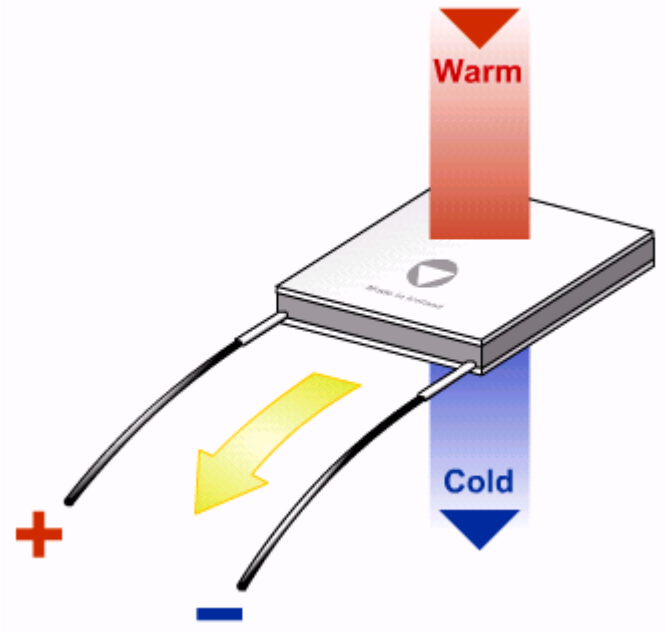

Figure 4.9: Peltier cell conceptual operation.

A common Peltier cell has 2 semiconductor materials doped type n and type p (figure 4.9), linked between by a copper plate. If a positive voltage to n type and a negative voltage to the p type is applied, upper cell plate shall cool while lower cell plate shall hot. Inverting the voltage versus thermal energy shall be inverted too. Insulated and not insulated Peltier cell exist. The first one in the upper and lower side by ceramic material are covered and allow better efficiency with respect to the second ones (figure 4.10).

In fact, in order to transfer heat against the second thermodynamic law, from cool side to hot side, Peltier cell has to produce work and has to create a temperature difference absorbing necessarily great electrical current quantity.

A cell with dimension of 30 x 30 x 4 mm and 25W, produces a potential difference of 8.5V and absorbs 4.5A. In addition because of voltage-current curve typical for the junction device in controlled current (constant current) is supplied.

When several cells have used in order to transfer heat quantity as for a laser diode cooling and differently for a sensor cooling, it is important to consider that an efficient cell operation needs to remove from “hot” side the total power as the sum of heat to remove and the power provided to the junction.

So that, when difference between hot and cool side and current absorbed is very low is a Peltier cell efficiency is maximum. For these reasons Peltier cells are mainly used only to

remove small heat quantity and they are very useful to get down temperature in non generating heat parts (passive parts).

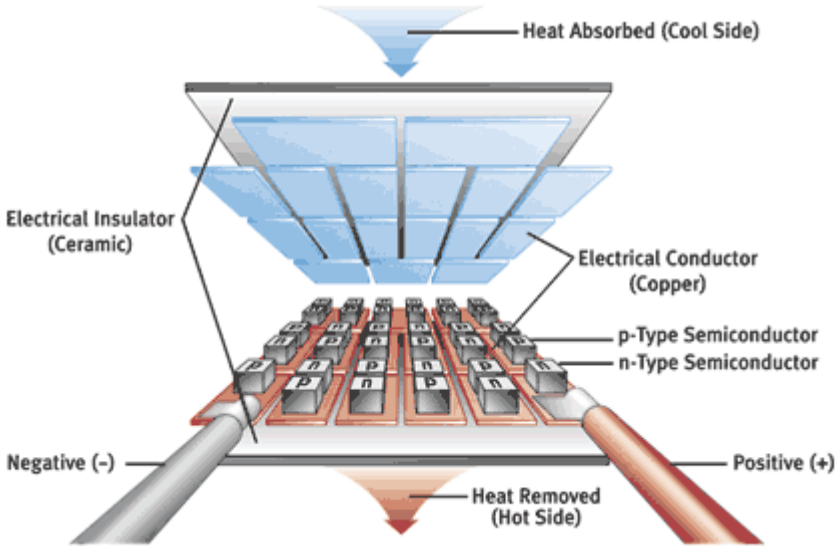

Figure 4.10: Peltier cell description with all component: particular of p-n junction assembly, ceramic plate for electrical insulation.

Peltier cell common use is related to heat removal by means of link of cool side to the body to be cooled; heat removal is helped by thermal bridge creation (thermo conductive adhesives) allowing better thermal removal. Subtracted heat also with operative heat (great part) to the hot side is transferred.

Fundamental problem in a Peltier cell is the intensity current control related to a proportional heat removal, if the thermal source changes in terms of energy emission also the removal operated by the cell has to change consequently, preferably using temperature sensor with a feedback action controlling current intensity provided to the cell, in such a way operation is within the defined temperature range.

It is possible to verify that the cooled thermal source reduces or stops heat production and in a such condition cell heat removal, if without control system, can lower in a few seconds the temperature under the freezing point.

When the cooled region is for example a computer CPU this implies that the system Peltier cell and CPU can freeze and if it is exposed to the atmosphere and to condense on the upper surface atmospheric humidity in ice.

At the same, sudden source temperature growth can increase Peltier cell removal heat and consequently temperature on the hot side. This implies that if the temperature on the hot side exceeds admissible values the cell can "cook" and then can be strongly damaged stopping her function; this leads to stop the heat removal and so all parts no more cooled can be damaged too.

At the end, cell operation when provides a variable heat removal has to be opportunely in a variable way controlled.

All provided energy to the system has to be subtracted by means of heat efficiently and safety from hot side and outside dissipated.

Only small thermal energy thanks to a heat pump transfer on hot side comes from because the much of thermal energy is parasitic energy produced by the cell for the cooling required operation.

Finally such a system has a reduced efficiency and it can be used only if it is well governed and thermal controlled in particular in case of a well defined region to be cooled or for punctual cooling assuring a local temperature range of application.

As stated before, Peltier cells are used where small parts in a few time have to be cooled.

They are used for example in order to freeze biological sample or to cool telescope or thermo room or in laser aiming at maintaining a stable work temperature and sometimes also to cool CPU by means of heatpipe for the hot cell side cooling.

These cells are the cooling element inside the portable freezer even if adequate control system has to be used during the current supply.

Peltier cell thanks to Seebeck effect are reversible too: warming a side and cooling the other at the end of the cell electrical energy shall appear directly proportional to thermal difference inside the faces. Potential difference is directly proportional to the element number inside the cell while the current is inversely proportional to the element number.

This ratio is related to the following formulas : $I = \frac{V}{N_e}$; $N_e = \frac{V}{I}$; $V = N_e \cdot I$.

where I : generated Ampère;

V: Volt at the end of the cell;

N_e: element number inside the cell.

Thanks to the Seebeck effect Peltier cells can be adopted as generator. For example Peltier cell can be used as generator for solar panels; the side to be warmed is exposed to the sun and also between the cell and the sun a Fresnel lens increase the total efficiency while the side to be cooled is on a water container in order to obtain a thermal difference of 60°C. Obviously in order to avoid short circuit and the following device damage insulated cells are only used. They produce a sufficient continue current that opportunely transformed in alternate current by means of an inverter is transferred to the network cutting down energy consumption.

Finally in order to cool the S.M.A. tape aim of the present work a Peltier cell choice can be useful. Peltier cell characteristics as stated before can be adopted during the cooling process because of reduced cell dimension and weight, punctual cooling required during the transformation from Austenite (hot phase) into Martensite (cold phase) and interchangeability.

4.6 References

[1] Ohl's discovery is in Riordan, Michael; Lillian Hoddeson (1988) "Crystal fire: the invention of the transistor and the birth of the information age". *USA: W. W. Norton & Company pp.88–97. ISBN 0393318516.* http://books.google.com/books?id=SZ6wm5ZSUmsC&pg=PA92.

[2] Hook, J. R.; H. E. Hall (2001) "Solid State Physics" John Wiley & Sons. *ISBN 0-471-92805-4.*

[3] DiSalvo, "Thermoelectric Cooling and Power Generation", *Science 1999, Web link.*

[4] Rockwood, Alan L. (1984). *"Relationship of thermoelectricity to electronic entropy". Phys. Rev. A 30: 2843–4. doi:10.1103/PhysRevA.30.2843. http://link.aps.org/doi/10.1103/PhysRevA.30.2843*

[5] Taylor, 1973 *Physics of transition metal oxides by Sadamichi Maekawa, page 323, or Thermoelectrics: Basic Principles and New Materials Developments* by Nolas et al., page 38.

[6] Roberts, R.B. (1977) "*Absolute scale of thermoelectricity". Nature 265: 226–7. doi:10.1038/265226a0 web site*

[7] Katie Walter (May 2007). "*A Quantum contribution to Technology". Lawrence Livermore National Laboratory.* http://www.llnl.gov/str/May07/Williamson.html.

[8] R. Venkatasubramanian, E. Siivola, T. Colpitts, and B. O'Quinn, *Nature 413, 597 2001 web site.*

[9] T. C. Harman, M. P. Walsh, B. E. Laforge, and G. W. Turner, J. Electron. Mater. 34, L19 2005

CHAPTER 5

S.M.A. COOLING ASSESSMENT BY PELTIER CELL

5.1 Introduction

In the previous chapter in order to define the choice of S.M.A. cooling solution a general thermoelectrical description and Peltier overview has been provided.

In the following after a brief thermodynamic laws illustration the modeling approach shall be presented. At first after the equilibrium equations and the conceptual reference scheme adopted during the assessment, a theoretical approach shall be provided aiming at describing the trade off study for the S.M.A. cooling solution by means of Peltier cell.

5.2 Heat transfer and thermodynamic

In order to define the possibility of cooling a system as S.M.A. ribbon as flap actuator with reduced energy consumption in a new design concept, a general overview of thermodynamic laws and their application has to be provided.

When a ∇T in a system exists or two or more systems with different temperatures are in contact, an energy exchange occurs.

The process by means of an energy exchange takes place and it is better known as heat exchange. During the process heat transmitting cannot be directly measured and observed but only his induced effect can be pointed out. In fact heat, as work in general, induces a system internal energy variation.

Relations among heat and other type of energy is included in a science sector well known as thermodynamic. Fundamental principles, as for all physical laws, are based on observation and have been codified by means of laws valid for all physical phenomena with no exception.

First Thermodynamic Principle defines that energy cannot be created or deleted but only transformed from one type to another one; this quantitatively governs each energy transfer but doesn't define the transformation versus.

However experience teaches that each transformation is impossible with the final result of heat transfer from a cool region to hot region. This is well known as the Second Thermodynamic Principle.

As defined by Rudolph Clausius put it, in 1850: "It is impossible for a self-acting machine unaided by an external agency to convert heat from one body to another at higher temperature." As given by Kelvin, "It is impossible by means of inanimate material

agency to derive mechanical effect from any portion of matter by cooling it below the temperature of surrounding objects." If a machine was able, by itself, to take heat energy out of the surrounding environment and use that energy to run its cooling work, it would be a perpetual motion machine. Cooling the surrounding average requires energy from an external source.

All heat transformation process requires energy exchange and conversion obeying to First and Second Thermodynamic Principles.

So that, it could be right that all heat transfer principles can be derived from fundamental thermodynamic laws even if this conclusion is wrong because classic thermodynamic stops her influence sphere into equilibrium conditions, including mechanical, chemical and thermal equilibrium. However this approach doesn't help quantitatively assessment because during most of technical process there is no equilibrium condition.

Heat exchange is related to a temperature gradient and his study involves other science fields as other transfer process like matter transfer.

Classical thermodynamic limitations

Classical thermodynamic deals with system state macroscopically and no hypothesis about matter structure are introduced.

In order to carry out a system thermodynamic analysis, the state, in terms of pressure, volume and temperature directly measured, has to be described; these variables or thermodynamic properties play an important rule into the system only if in it they are uniform, in other words when the system is in equilibrium condition.

So that, classical thermodynamic doesn't deal with process details but equilibrium status and relationships; analysis procedure adopted are purely ideal, useful only for information about equilibrium condition.

From a thermodynamic point of view heat quantity exchanged during a process is related to the difference between the system energy variation and the work carried out.

It is evident that this analysis doesn't consider neither the thermal exchange mechanism nor the required time, only defining the provided and removed heat during the transformation between determined extreme states independently by the process.

The real approach limitation during this analysis is the absence of time as variable, so that the heat exchange duration problem, even if of enormous practical importance, is not within the thermodynamic analysis.

Heat transfer in techniques

From an engineering point of view essential problem is related to the thermal power determination transferred by means of a defined temperature difference. In order to evaluate costs, capacity and dimension of such a plant able to exchange heat quantity in a determined range time, a detailed heat transfer analysis needs.

Size of boilers, radiators, freezers and heat exchangers not only depend on heat quantity transferred but especially on the velocity by which, under assigned conditions, heat has to be exchanged.

A correct operation for plant components as, for example, turbine blade or combustion chamber walls depends on the cooling efficiency of metallic parts continuously and quickly removing heat from the surface.

In order to avoid damage for mechanical systems, during electric engine transforms and bearing design, a preliminary heat exchange assessment has to be carried out too.

This seems to underline that all engineering fields are involved by the heat exchange problems and cannot be only solved by thermodynamic but a heat transfer study is required.

As in a great part of engineering fields also in heat transfer study a common adopted solution requires hypothesis and modelling approach.

Physic phenomena in general are not exactly describable, so that, it is common use to introduce approximations in order to translate a problem into a solvable equation.

Sometimes a wrong or poor information about physic properties leads to introduce approximations aiming at the problem solution; for example during high temperature mechanism design a correct fatigue resistance evaluation needs.

This approach is followed also during thermal exchange problems: some properties as thermal conductivity or viscosity depend on temperature but choosing average value calculations can result simpler within an acceptable mistake range.

Finally during heat transfer analysis fundamental requirements for hypothesis formulation is strictly connected to a complete physical knowledge.

5.3 Heat transfer form

Thermal exchange can be defined as energy transfer from a region to another one due to a temperature difference.

Temperature difference exists all around the universe and thermal exchange as gravitational phenomenon are universal; however contrarily to the gravity, thermal exchange is not regulated by only one relation but by a combination of independent physic laws. In general in literature three different form of heat exchange are distinguished: *conduction, radiation and convection.*

Only conduction and radiation should be considered as thermal exchange processes because only these ones depend on presence of temperature difference.

The last one, convection, doesn't comply with thermal exchange definition because it is depending on a matter transfer; however convection produces also an energy transfer from higher temperature region to lower temperature region in general it is used the following definition "heat exchange through convection".

It is evident that in most of physic phenomena heat flows not only by means of one of these thermal mechanism but in general according to all these ones together.

In this section a brief description of each mechanism shall be provided.

Conduction

Conduction is a thermal process through heat fluxs from a region of higher temperature region to a lower temperature region only by one means (solid liquid or gas) or by different means in physic direct contact [8].

In conduction, energy is transferred through the transport of thermal energy between neighboring molecules in a substance due to a temperature gradient.

According to kinetic theory temperature in a material is proportional to average kinetic energy and energy of each material element, for his velocity and relative molecular position, is named *internal energy.*

So that temperature is related to molecular velocity and each material internal energy.

When molecules get average kinetic energy higher than neighboring molecules, as temperature difference, molecules with higher energy give adjacent molecules with lower energy part of this energy.

Energy exchange can happen by elastic collision (in fluids) or by faster electron diffusion from higher temperature to lower temperature regions as in metals.

Conduction relevant effect is a temperature levelling even if, adding or subtracting heat in different region, a continuous heat flux from a region of higher temperature to a region of lower temperature is established.

Conduction is the only mechanism by means of heat can propagate into opaque solids; it is also important into fluids but not into solids because this process is associated to convection and to radiation too.

Radiation

Radiation is a process where heat flows from a body of higher temperature to a body of lower temperature when bodies are not in contact even if between them vacuum exists.

The term "radiation" in general is referred to each electromagnetic waves propagation phenomenon, but is related to thermal exchange only some phenomena depending on temperature, allowing energy transfer through transparent mean or by vacuum.

So radiated energy is named *radiated heat.*

Each body continuously emits heat by radiation and emission intensity depends on temperature and surface characteristic.

Radiating energy travels with a velocity of $3 \cdot 10^5 km/s$ and presents a similar phenomenology to light radiation; in fact according to electromagnetic theory light and thermal radiation differs from them only in wave length.

Radiated heat is emitted from a body by finite quantity or better known as energy quantum; transmission in space of radiated heat is similar to light propagation and can be described by wave theory, when radiations meet another body their energy is absorbed near the surface. Thermal exchange by radiation becomes more and more important according to body temperature increase and in several engineering problems, where there is an atmospheric temperature, radiation can be often neglected.

Convection

Convection is an energy transfer process by means of combined action of conduction, energy contribution and mixing; this is the most important heat exchange mechanism between a solid surface and a liquid or a gas.

Energy transmission through convection, from a surface with a higher temperature than neighboring fluid temperature, by different phases happens.

At first heat flows from surface to adjacent fluid particles through conduction; such

transmitted energy increases internal energy and particle temperature.

They migrate versus a fluid region at lower temperature and mixing and giving other particles their energy; a matter and energy flux take place, so that energy is stored up into the particles and by themselves motion it is removed.

The mechanism is not only depending on a temperature difference and it don't strictly comply with heat transfer definition [8].

Consequently an energy transfer according to the thermal gradient direction takes place classified as thermal exchange mechanism and named *heat exchange through convection*.

Heat transmission through convection according to the origin of flux is divided into *free or natural convection* and *forced convection*.

When flux only depends on density difference due to thermal gradient, free convection takes place, when flux is induced by external agents, like pumps or other systems, forced convection takes place.

Convection thermal exchange efficiency greatly depends on fluid flux so that convection analysis is based on fluid dynamic characteristic.

During each heat transfer problem solution not only exchange mechanisms have to be defined; in fact it is necessary to determine if the process is in a steady regime or not.

When in a system thermal power is not time dependent, in other words it is constant, temperature is the same in each investigation point and steady conditions take place: everywhere in the system input thermal power is exactly the output thermal power and no internal energy variation occurs.

In many engineering problems steady regime systems are studied: for example heat flux from water combustion into a boiler tube, lamp cooling in the atmosphere, heat flux into heat exchanger and so on.

However in some system area temperature is time dependent and heat transfer is no more a steady regime.

So that, temperature variation is related to internal energy variation then energy heap is typical for a transitory flux. These problems are more difficult than the steady ones and only by approximated methods can be successfully solved. For example this approach is followed during the analysis of a furnace starting phase or during thermal treatment for metals etc. In general when a system has cyclic temperature variation a transitory heat flux occurs: in this problem each system area has periodically the same temperature and energy and thermal power to a periodic variation are subjected too.

These problems belong to a periodic or quasi steady regime heat transfer and typical examples are given by building temperature variation, heat flux through cylindrical walls of an engine when gas temperature in the cylinder periodically changes.

5.4 Non steady regime conduction

In general a physical process is connected to a non steady heat conduction.

In fact during the starting phase of an heat exchange in order to have a steady regime time is necessary so that transitory conditions are over.

This is a typical engineering problem as periodical temperature variation and periodic heat flux in engine, in air conditioning problems, in control process and so on.

The S.M.A. ribbon cooling process aim of this work is an example and it can be solved by this theoretical approach simplifying and assuming the temperature only a time dependent function and in addition always uniform all over the system.

Even if in nature there are no materials with infinite thermal conductivity a lot of transitory thermal flux problems can be quickly solved with acceptable precision assuming that the internal conductive resistance of the system is so little that in the system the temperature every instant is uniform. This assumption is justified if the external thermal resistance, between the system surface and the neighboring mean, is many times higher than the internal one.

The relative importance of the thermal resistance in a solid body is related to the ratio between the internal and external resistance.

This ratio can be dimensionless written as $\frac{\bar{h}L}{k}$, Biot number, where $\bar{h}$ is the average surface conductance, L is the significant length obtained by the ratio of body volume and surface area and k is the solid body conductivity.

In body with a cylindrical planar or spherical shape the introduced error assuming that temperature every instant is uniform is lower than 5% when the internal resistance is lower than 10% of external surface resistance in other words if $\frac{\bar{h}L}{k} < 0.1$.

A typical example of this transitory thermal flux is a metallic billet cooling during the quenching, after the removal from a furnace. It is supposed that the billet is removed by the furnace at an uniform temperature T_0 and that the billet is dipped into the bath so

quickly to approximate the ambient temperature variation with a step variation.

Initial state when cooling starts is $\theta = 0$ and assume that thermal exchange coefficient $\bar{h}$ is constant during the process and that the bath temperature, at a certain distance from the billet, T_∞ is not time dependent.

Then, with the hypothesis that temperature every instant in the body is uniform, the energy balance on the billet relatively to a strictly time interval is the following.

Billet internal energy variation during $d\theta$ = net thermal flux billet -bath during $d\theta$

Mathematically is the following:

$$-c \cdot \rho \cdot V \cdot dT = \bar{h} \cdot A \cdot (T - T_\infty) \cdot d\theta \tag{5.1}$$

where

c = specific billet heat $\left[\frac{J}{kg \cdot °K}\right]$

ρ = billet density $\left[\frac{kg}{m^3}\right]$

V = billet volume $[m^3]$

T = average temperature $[°C]$

$\bar{h}$ = average heat transmission coefficient $\left[\frac{J}{m^2 \cdot s \cdot °K}\right]$

A = billet surface area $[m^2]$

dT = temperature variation due to $d\theta$

The minus sign in the equation (5.1) shows that internal energy decreases if $T > T_\infty$.

Variables T and θ can be easily separated and for a little differential time interval $d\theta$ equation (1) can be written as

$$\frac{dT}{T - T_\infty} = \frac{d(T - T_\infty)}{T - T_\infty} = -\frac{\bar{h} \cdot A}{c \cdot \rho \cdot V} \cdot d\theta \tag{5.2}$$

where being $T_\infty = \cos t$ then $d(T - T_\infty) = dT$ can be written too.

While the boundary conditions for this problem solution are T_0 is the initial temperature and T is temperature at θ time, the equation (5.2) integral gives the following solution

$$\ln \frac{T - T_\infty}{T_0 - T_\infty} = -\frac{\bar{h} \cdot A}{c \cdot \rho \cdot V} \cdot \theta \tag{5.3}$$

or the same

$$\frac{T - T_\infty}{T_0 - T_\infty} = \exp\left(-\frac{\bar{h} \cdot A}{c \cdot \rho \cdot V} \right) \theta \tag{5.4}$$

5.5 S.M.A. system actuator thermomechanical features

A considerable incentive towards this direction has been given by the advent of above mentioned smart materials, generally guaranteeing compactness, cost and weight reduction, high integration level. Among the others, a morphing application focusing on flap zone chamber control, based on S.M.A. ribbon integrated within the structure, has been carried out and a lab technology demonstrator has been built and tested [1]. However, the intrinsic limit of S.M.A., as the heating and cooling necessity for activation and deactivation, strongly penalized the frequency working range of the prototype, thus restricting tests to steady state.

While the activation time can be remarkably reduced by increasing the power supply, the deactivation cannot be made faster unless introducing a dedicated cooling system.

In the work at hand, the cooling effects due to a Peltier cell working at several regimes [4-5] bonded on a face of a S.M.A [2],. ribbon in natural convection, has been considered.

Assuming a one-dimensional domain and uniform temperature distribution along S.M.A. thickness, starting from a complete Austenite phase, the cooling process through an analytic approach has been described; at first, the time required to arrive at M_s temperature (beginning of Austenite into Martensite transformation) has been estimated; then, the temperature evolution during transition (up to reaching M_f) has been computed.

A dedicated heat balance equation has been written for the complete austenite interval and then solved, thus achieving temperature vs. time required relation. The same equation has been adapted for the case of phase transformation, by assuming as initial conditions the last ones given by the previous solution and taking into account of the arising concentration of Martensite. As S.M.A. material constitutive law, Liang and Rogers

cosine model [2] [3] has been adopted and a piece wise approximation performed, thus preserving the linearity of the governing differential equation.

As stated in chapter 2 where an overview of S.M.A. materials has been presented here a brief illustration of flap actuator and then the analytical approach followed shall be provided.

The actuator in charge of producing chamber variations of a wing of a regional aircraft is constituted by a S.M.A. ribbon.

The edges are suitably connected to elastic elements, parts of the rib structure and able to assure required rigidity against aerodynamic loads and necessary pre-stress within S.M.A.s for recovering operations.

In practice, by heating through Joule effect the ribbons, Martensite into Austenite transformation is obtained so an actuator contraction is achieved and a relative rotation of the different rib parts is induced, because they are linked each other by the elastic elements. The activation is assured by a dedicated power supplier providing an electrical current of 50 A at a voltage of 1V. By this power the activation, thanks to a pre-load of 150 MPa within S.M.A. ribbons, is achieved in 65 s, from a room temperature conditions until to a temperature of 100 °C.

While it is thinkable to reduce this interval, supplying greater power or cutting down activation temperature through an appropriate alloy dosage, cooling is an open problem: time required, 235 s in natural convection, represents a system limitation. In order to accelerate the heat subtraction some solution can be adopted. Among the others, due to their integrability, Peltier cells are seen as promising components of a forced convection system. In the specific case, one face of the S.M.A. ribbon is directly air exposed, while the other one is in contact with a Peltier cell transferring, at several working regimes (current supply), heat from the S.M.A. to the lower fluid layer. A scheme of this cooling system is depicted in Figure 5.1. The cell is mainly composed of internal positive and negative junctions couples (named “P” and “N”) allowing an electron migration copper plates (green) and two external ceramic insulation layers.

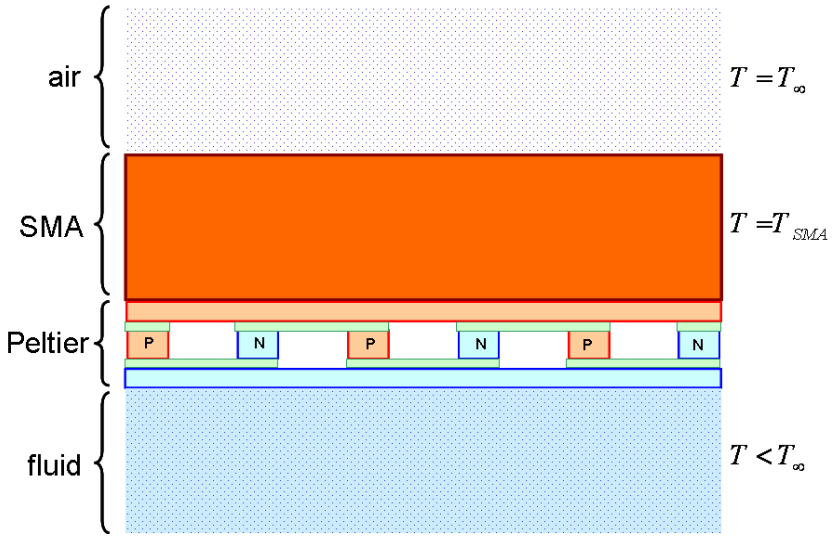

Figure 5.1: Reference scheme S.M.A. – Peltier cells – air.

In order to improve this system, the temperature of the bottom fluid layer has been assumed lower than the top one ($T<T_\infty$). This corresponds to have a heat transfer system that allows the fluid circulation, thus further accelerating the cooling process. The main geometric and mechanical features of the system are summarized in table 5.1 and 5.2

Rectangular section (m)	1.0e-3
Area (m^2)	1.0e-6
Tape length (m)	13.0e-2

Table 5.1: S.M.A. tape geometrical features

Austenite Young modulus (GPa)	40.18
Martensite Young modulus (GPa)	16.5
Austenite start, A_s, (°C)	47.3
Austenite finish, A_f, (°C)	58.9
Martensite start, M_s, (°C)	43.3
Martensite finish, M_f, (°C)	27.5

Table 5.2: S.M.A. tape properties [7]

Although the S.M.A. ribbon operates with an internal pre-load to assure its recovery when cooled, the effects on the transformation temperatures of the internal stress have been neglected. In the following paragraph, the simulation strategy, adopted for predicting the time required for completely deactivating the S.M.A., has been described.

5.6 Thermoelectric basis for the analysis

Before starting the analytic model illustration in order to understand the conceptual origin and applicability of the analysis an overview of the thermoelectric basis shall be provided.
In general a thermoelectrical couple, as a Peltier cell considered during this investigation, has the prismatic elements (pellet) composed of semiconductor material [5-6].
As discussed in previous chapter a semiconductor material, typically a solid solution of bismuth - antimony - tellurium – selenium, has a p doping in one of his prism and a n doping in the other one.
In an elementary thermoelectric couple two prisms are linked between them to one extreme side by a thin metallic plate (“cold junction”) usually copper.
At the other side the prism are linked to two other thin plates (“hot junction”) and between them a current generator is inserted.
If the current generator supplies a direct current to the thermoelectrical couple through the Peltier effect an heat transfer from cold junction to the hot junction is obtained.
In fact, through the motion from p doped to n doped material by the cold junction, electrons absorb energy in order to overcome the local potential step.
So that, absorbed energy is subtracted as heat form to the thin metallic plate and the junction is cooled by this process.
The thermoelectric couple cooling performances can be estimated evaluating the different energetic contributions to the cold junction.
They are primarily caused by:

1. Peltier effect
2. Joule effect (electrical dissipation)
3. Fourier effect (thermal conduction)

Thermal power subtracted to the cold junction by Peltier effect is proportional to current

$$Q_{pelt} = 2 \cdot a \cdot T_c \cdot I \tag{5.5}$$

By this relation it is evident that Peltier effect depends on the junction thermodynamic temperature, T_c, and by the Seebeck coefficient of thermoelectric couple, a, defined as

$$a = \frac{1}{2}\left(a_{pm} + a_{mn}\right) \tag{5.6}$$

The terms a_{pm} and a_{mn} are the Seebeck coefficient values between the type p semiconductor and the metal (copper) and between metal and type n semiconductor.
Joule effect dissipation in the thermoelectric couple can be evaluated by means of total circuit resistance composed of semiconductor prisms, then, it is related to the electric resistivity of two semiconductor materials, r_p and r_n.
They are similar and so an averaged value can be considered as

$$r = \frac{1}{2}\left(r_p + r_n\right) \tag{5.7}$$

Under the hypothesis that half dissipated heat by Joule effect goes to the hot junction and the other half goes to cold junction, this one has a thermal power according to the relation

$$Q_J = \frac{1}{2} R \cdot I^2 = \frac{1}{2}\left(r \cdot \frac{2 \cdot s}{A}\right) I^2 = \frac{1}{2}\left(r \cdot \frac{2}{G}\right) I^2 \tag{5.8}$$

In the equation (5.8) a "shape factor" G has been introduced defined as the ratio between prism transversal section area, A, and their high, s as $G = \frac{A}{s}$.

The shape factor has been assumed the same for both prisms of the couple, as in commercial thermoelectric devices. In addition, copper plates electric resistance has been neglected with respect to the semiconductor resistance.
Thermal power transferred through the couple by Fourier effect (thermal conduction) from hot junction to cold junction can be calculated by the relation

$$Q_F = \left(k_p + k_n\right) \cdot \frac{A}{s} \cdot \left(T_h - T_c\right) \equiv 2 \cdot k \cdot G \cdot \left(T_h - T_c\right) \tag{5.9}$$

T_h is the thermodynamic temperature at the hot junction, k is an averaged thermal conductivity of the thermoelectric couple as for the electric resistance.

Conductive effect through air between the junctions and the thermal radiation are neglected.

In addition during a thermoelectric modules performances assessment in general a, r and k in the semiconductor are considered constant even if they should be considered temperature dependent. Consequently also electric resistance and thermal conductivity should be written using they averaged integral value even if, in moderate temperature differences between hot and cold junction, calculated averaged temperature value can be well approximated.

Seebeck coefficient should be an average temperature value at the cold junction but the calculated average temperature value allows to balance a secondary effect, Thomson effect, when temperature gradient in the semiconductor appears.

Finally semiconductor performances are always related to material average temperature value $T_m = \frac{T_c - T_h}{2}$.

Thermal power in steady state subtracted at the cold junction of a thermoelectric couple (thanks to the electron migration), and taken out from a body or environment thermally linked with the junction, is provided by the algebraic sum of different terms due to Peltier, Joule and Fourier effects.

$$Q_C = Q_P - Q_J - Q_F = 2 \cdot \left[a \cdot T_C \cdot I - \frac{1}{2} \cdot \frac{r}{G} \cdot I^2 - k \cdot G \cdot \left(T_h - T_c\right) \right] \tag{5.10}$$

By the equation (5.10) it is evident that thermoelectric device performances depend on semiconductor material properties.

In particular materials with a maximum value of Seebeck coefficient are preferred and contemporarily with minimum electric resistance and thermal conductivity.

Unfortunately this two last properties are strictly connected and are inversely proportional each others: for example metals have lower electric resistance but higher thermal

conductivity too.

The material choice has to be balanced by these factors.

In general the thermoelectric device performances for cooling (performance coefficient, maximum temperature difference between hot and cold side, cooling power etc.) depend on "figure of merit" Z of the couple of used materials, defined as:

$$Z = \frac{a^2}{r \cdot k} \tag{5.11}$$

5.7 The Analytical Model for S.M.A. cooling

In this section a theoretical model for S.M.A. tape cooling has presented.

According to the differential equation for the conduction-convection state a new model including the thermoelectrical contribution related to the Peltier cell physic operation [3], has been developed In order to reduce time cooling of the S.M.A. tape by means of a Peltier cell bonded on the bottom of one face of the ribbon this analytical model allow to represent the phenomenology.

In table 5.3 thermodynamic characteristics are illustrated:

$c \left[\frac{J}{kg \cdot °K}\right]$	837
$k \left[\frac{J}{m \cdot s \cdot °K}\right]$	18
$\rho \left[\frac{kg}{m^3}\right]$	6500
$k_p \left[\frac{J}{m \cdot s \cdot °K}\right]$	148
$k_n \left[\frac{J}{m \cdot s \cdot °K}\right]$	59.9
$\bar{h} \left[\frac{J}{m^2 \cdot s \cdot °K}\right]$	11.63

Table 5.3: S.M.A. and Peltier thermodynamic parameters

The theoretical model is based on the two following assumption according to the thermodynamic phenomenology.

1. Biot number for SMA component is $6.0 \cdot 10^{-4}$ (Bi << 1)
2. Low thermal inertia of the Peltier cell

In this model, for the S.M.A., the internal thermal resistance has been considered negligible with respect to the external thermal resistance and so the temperature is practically uniform along the S.M.A. thickness.

In addition, there is a low thermal inertia for the Peltier cell and this hypothesis confirms that the cell, installed on the S.M.A. tape, has a negligible influence on the system thermal equilibrium.

The reference scheme adopted for this model is illustrated in Figure 5.1.

In Figure 5.1 along the S.M.A. lower face Peltier cells have been set but under the Peltier cells a fluid at a lower temperature has been considered, while above the S.M.A. only air has been foreseen.

In order to model the phenomenology, basing on such a scheme, the energy balance equation has been written.

At first, model analysis has been developed assuming Austenite as initial phase to compute the transformation time from A_f to M_s. In the following, the first analytical model is presented [5]. According to the energy balance equation for our purpose in presence of the initial Austenite phase we have the Eq. (4)

$$(c_{SMA} \cdot \rho_{SMA} \cdot L_{SMA} \cdot b_{SMA} \cdot t_{SMA}) \frac{dT_{SMA}}{dt} = \overline{h} \cdot (L \cdot b) \cdot (T_{\infty} - T_{SMA}) - 2 \cdot a \cdot I \cdot T_{SMA} + R_{pelt} \cdot I^2 + \\ + (k_p + k_n) \cdot \left(\frac{L \cdot b}{t_{pelt}} \right) \cdot \left(T_{pelt-air} - T_{SMA} \right) \tag{5.12}$$

In the table 5.4 each terms in Eq. (5.12) is explained.

$a = \frac{1}{2}(a_{pm} + a_{nm})$	Averaged Seebeck coefficients (between positive and negative electrodes
$r = \frac{1}{2}(r_p + r_n)$	Averaged semiconductor electrical resistivity
$R_{pelt} = r \cdot \frac{s}{A}$	Cell resistance
$(c_{SMA} \cdot \rho_{SMA} \cdot L_{SMA} \cdot b_{SMA} \cdot t_{SMA}) \frac{dT_{SMA}}{dt}$	S.M.A. Internal Energy variation
$\overline{h} \cdot (L \cdot b) \cdot (T_{\infty} - T_{SMA})$	S.M.A. tape output energy
$-2 \cdot a \cdot I \cdot T_{SMA}$	Peltier cell output energy

$R_{pelt} \cdot I^2$	Joule effect (electric dissipation)
$(k_p + k_n) \cdot \left(\frac{L \cdot b}{t_{pelt}} \right) \cdot (T_{pelt-air} - T_{SMA})$	Fourier effect (thermal conduction between cell – S.M.A.)

Table 5.4: Energy balance terms for the analytical model

Eq. (5.12) has been formulated according to the first and second hypothesis (Bi <<1 in the system S.M.A. – Peltier cell and low thermal inertia of Peltier cell respectively).

But for the completely problem solution the Eq. (5) has been necessary.

$$T_{pelt} = T_{\infty} \tag{5.13}$$

Through Eq. (5.12), by assuming as final temperature the Martensite start value, M_s, the time, t_{M_s}, necessary to cool down the S.M.A. up to getting incipient transformation condition, has been estimated. In Eq. (5.14) the analytical equation solution and in table 5.5 the energy balance equation coefficients are presented.

$$t_{M_s} = -\frac{A_a}{B_a} \cdot \ln\left(\frac{C_a - B_a \cdot M_s}{C_a - B_a \cdot T_0} \right) \tag{5.14}$$

$A_a = (c_{SMA} \cdot \rho_{SMA} \cdot L_{SMA} \cdot b_{SMA} \cdot t_{SMA})$ $B_a = \bar{h}Lb + \left(\frac{k_p + k_n}{t_{pelt}} \right)(Lb) + 2aI$ $C_a = \bar{h}LbT_{\infty} + \left(\frac{k_p + k_n}{t_{pelt}} \right)(Lb)T_{pelt-air} + R_{pelt} \cdot I^2$	Equation (5.14) coefficients
$t = 0$ $T_{SMA} = T_0$	Initial conditions for equation (5.14)

Table 5.5: Energy balance equation condition and coefficient for initial transformation from Austenite to Martensite start.

After the Eq. (5.14) solution for austenite phase, in order to compute the phase change occurring between M_s and M_f interval, according to our purpose, a new transformation equation has been written.

During the transformation phase from M_s to M_f, a new term in the energy balance

equation has to be considered. So that, according to Liang and Rogers model, Martensite amount ξ produced has been computed.

For the Martensite concentration during cooling phases Eq. (5.15) has been considered but in this case, assuming S.M.A. material unloaded ($\sigma = 0$). To formulate an exact solution, Eq. (3) has been approximated through a piece wise function, equal to 1 for T ≤ M_f, equal to 0 for T ≥ M_s and linearly variable as

$$\xi = \left(\frac{M_s}{M_s - M_f} - \frac{T_{SMA}}{M_s - M_f} \right) \tag{5.15}$$

for T $\in [M_f M_s,]$.

So that, from the Eq. (5.15), including the transformation phase, the energy balance equation for the S.M.A. – Peltier cell system Eq. (5.12) becomes

$$\begin{aligned} &(c_{SMA} \cdot \rho_{SMA} \cdot L_{SMA} \cdot b_{SMA} \cdot t_{SMA}) \frac{dT_{SMA}}{dt} = \overline{h} \cdot (L \cdot b) \cdot (T_\infty - T_{SMA}) + \\ &- 2 \cdot a \cdot I \cdot T_{SMA} + R_{pelt} \cdot I^2 + (k_p + k_n) \cdot \left(\frac{L \cdot b}{t_{pelt}} \right) \cdot (T_{pelt-air} - T_{SMA}) + (c_{SMA} \cdot \rho_{SMA} \cdot L_{SMA} \cdot b_{SMA} \cdot t_{SMA}) \frac{d(\xi \cdot T_{SMA})}{dt} \end{aligned} \tag{5.16}$$

with $(c_{SMA} \cdot \rho_{SMA} \cdot L_{SMA} \cdot b_{SMA} \cdot t_{SMA}) \frac{d(\xi \cdot T_{SMA})}{dt}$ the novel phase transformation term.

The solution of Eq. (5.16) is the time, t_{M_f}, computed according to the Martensite finish , M_f, temperature.

$$t_{M_f} = \frac{A_t}{B_t} \cdot \ln\left(\frac{C_t \cdot M_f + D_t}{C_t \cdot M_s + D_t} \right) + \frac{B_t}{C_t} (M_f - M_s) - \left(\frac{B_t D_t}{C_t^2} \right) \ln\left(\frac{C_t \cdot M_f + D_t}{C_t \cdot M_s + D_t} \right) + t_{M_s} \tag{5.17}$$

with

$A_t = (c_{SMA} \cdot \rho_{SMA} \cdot L_{SMA} \cdot b_{SMA} \cdot t_{SMA}) \left[1 - \frac{M_s}{M_s - M_f} \right]$ $B_t = (c_{SMA} \cdot \rho_{SMA} \cdot L_{SMA} \cdot b_{SMA} \cdot t_{SMA}) \left[\frac{2}{M_s - M_f} \right] T$ $C_t = \left(\bar{h} Lb + 2aI + \left(\frac{k_p + k_n}{t_{pelt}} \right) (Lb) \right) T_{SMA}$ $D_t = R_{pelt} I^2 + \left(\frac{k_p + k_n}{t_{pelt}} \right) (Lb) T_{pelt-air}$	Equation (5.17) coefficients
$t = t_{M_s}$ $T_{SMA} = M_s$	Initial conditions for equation (5.17)

Table 5.6: Energy balance equation condition and coefficient for initial transformation from Martensite start to Martensite finish.

From Eq. (5.17) total cooling time is presented. In this case, Eq. (5.17) provides the necessary time to cool down the S.M.A. ribbon from the Austenite to Martensite phase, considering the transformation phase time from M_s to M_f temperature cooling time too.

The computed result has been obtained by considering the Peltier cell aid too during the modelling phase.

In these plots (Figure 5.2, 5.3, 5.4, and 5.5) predicted interval needed to pass from initial temperature (Austenite) to Martensite start, M_s, (blue curve) is presented, then, by this later value, calculating the transformation time by the Eq. (5.17), the M_s to M_f time interval has been computed (red curve), and finally, the total interval time from Austenite to M_f has been found as sum of the previous time (black curve).

These data have been plotted vs. current intensity within Peltier cell.

Such a way Peltier aid to S.M.A. cooling has been shown, remarking the advantages found by using this method adopted.

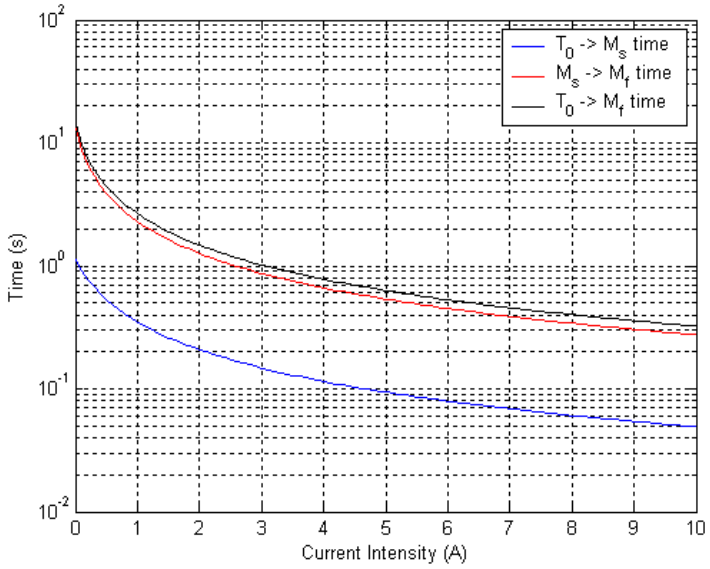

Figure 5.2: Time vs current intensity for S.M.A. tape cooling for $T_{pelt} = T_{\infty}$

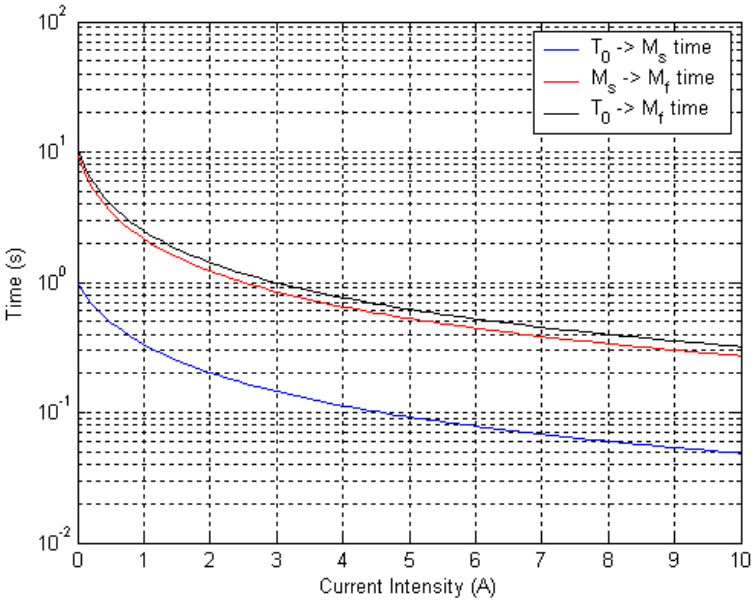

Figure 5.3:Time vs current intensity for S.M.A. tape cooling for $T_{pelt} = T_{\infty} - 10°C$

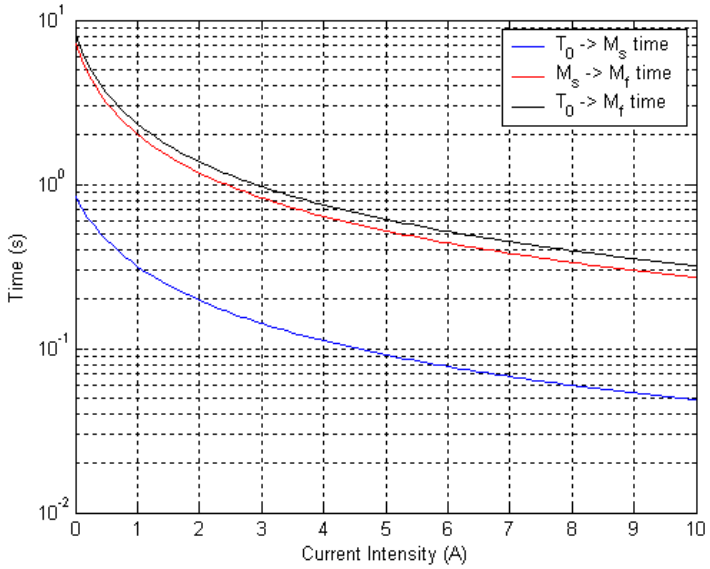

Figure 5.4:Time vs current intensity for S.M.A. tape cooling for $T_{pelt} = T_{\infty} - 20°C$

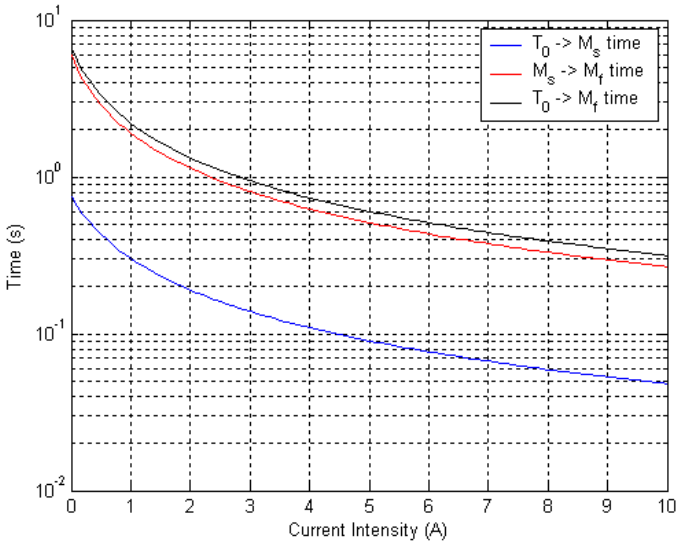

Figure 5.5: Time vs current intensity for S.M.A. tape cooling for $T_{pelt} = T_{\infty} - 30°C$

In these plots it is possible to choose a current intensity input, according to the supplied power by the Peltier cell, and, consequently, obtain the S.M.A. cooling time from Austenite to Martensite phase as reported above.

It results that for lower T_{pelt} temperature as in Figure 5.5 a sensible cooling time reduction is obtained.

So that, results here presented demonstrate a deep S.M.A. cooling time reduction by using the Peltier cell with respect to the natural convection.

5.8 Conclusions about S.M.A. cooling analytical model

In the present chapter a possible solution to the S.M.A. structure cooling problem has been proposed. In particular, among other solutions after advantages and disadvantages about the proposed solution herein described, the Peltier cell installation under the S.M.A. ribbon flap actuator has been preferred. During the solution choice advantages in terms of energy consumption, weight reduction and system integrability has been assessed. So, after a conceptual scheme presented and a brief system description of the architecture, in order to verify a new S.M.A. cooling system by using a Peltier cell installed along the S.M.A. ribbon, an analytical procedure by means of thermoelectrical differential equations has been developed.

At first, Peltier cell as cooling system, has been preferred and then a differential equation system has been written according to the hypothesis related to a negligible S.M.A. thermal inertia and uniform temperature into the S.M.A. tape, in terms of negligible internal resistance with respect to external one satisfying the following hypothesis Bi <<1.

By solving the differential equation system, cooling time from Austenite to Martensite finish phase has been computed; results have confirmed the soundness of the adopted solution by means of installation of Peltier cell along the S.M.A. tape, showing a sensible cooling time reduction with respect to a natural convection cooling system.

This proposed solution may be considered as the initial track to follow in order to satisfy a time cooling reduction in S.M.A. applications.

In order to validate the proposed theoretical model in the following chapter a numerical solution shall be presented.

5.9 References

[1] S. Ameduri, 2003, *Sistemi Integrati di Attuazione per il miglioramento delle prestazioni aerodinamiche di un profilo alare in campo transonico*, Philosophy Doctor's Thesis, Dept. Of Aerospace Engineering, University of Naples, Italy.

[2] C. Liang and C. A. Rogers, 1990 *One- Dimensional Thermomechanical Constitutive Relations For Shape Memory Material*, Journal of Intelligent Material Systems and Structures,1 (2), 207-234

[3] Tanaka K., 1986, *A Thermomechanical Sketch of Shape Memory Effect: One Dimensional Tensile Behaviour*, Res. Mech. 18(3), 251-263.

[4] S. Haidar, I. Isaac and T. Singleton *Thermoelectric Cooling Using Peltier cells in Cascade* Undergraduate laboratories, Dept. of Physics, University of Alberta, Edmonton, AB, T6G2G7.

[5] J. C. Contreras Vargas, MSc J. L. Diaz Rodriguez, Ph.D. A. P. Garcia, MSc. M. Figuerona *A Peltier Cells Research,* Universidad de Pamplona, Facultad de Ingegnerias y Arquitectura Ciutadela Universitaria, Pamplona, Notre de Santander, Colombia.

[6] R. Featherstone and Y. The, *Improving the Speed of Shape Memory Alloy Actuators by Fasten electrical Heating*, Dept. Systems Engineering Australian University Canberra, Australia.

[7] Srinivasan AV, Mc Farland DM, 2001, *Smart Structures:Analysis and Design,* Cambridge University, UK.

[8] F. Kreith, *Principles of Heat Trasfer* 3rd edition , chap. 4, translated by G. Alfano and V. Naso, Dept. of Thermodynamics and Energy, University of Naples, Italy

CHAPTER 6

S.M.A. COOLING ASSESSMENT : NUMERICAL INVESTIGATION

6.1 Introduction

In the previous chapter S.M.A. cooling solution by a Peltier cell installation under S.M.A. ribbon actuator for a flap has been proposed.

In fact, in order to substantiate Peltier cell as cooling system for a flap actuator, a theoretical model in terms of a thermoelectric differential equation system has been provided.

In the following after a brief FEM method illustration the numerical investigation shall be presented. At first a natural convection numerical analysis by FE approach has been presented and after that, followed by modeling phase of S.M.A. structure – Peltier cell system by means of FE approach, the numerical analysis has been conducted aiming at describing cooling time reduction for the S.M.A. ribbon thanks to the Peltier cell installation adopted solution.

6.2 The FE Method history

The finite element method (FEM), its practical application often known as finite element analysis (FEA), is a numerical technique for finding approximate solutions of partial differential equations (PDE) as well as of integral equations. The solution approach is based either on eliminating the differential equation completely (steady state problems), or rendering the PDE into an approximating system of ordinary differential equations, which are then numerically integrated using standard techniques such as Euler's method, Runge-Kutta, etc.

In solving partial differential equations, the primary challenge is to create an equation that approximates the equation to be studied, but is numerically stable, meaning that errors in the input and intermediate calculations do not accumulate and cause the resulting output to be meaningless. There are many ways of doing this, all with advantages and disadvantages. The Finite Element Method is a good choice for solving partial differential equations over complicated domains (like cars and oil pipelines), when the domain changes (as during a solid state reaction with a moving boundary), when the desired precision varies over the entire domain, or when the solution lacks smoothness. For instance, in a frontal crash simulation it is possible to increase prediction accuracy in

"important" areas like the front of the car and reduce it in its rear (thus reducing cost of the simulation. Another example would be the simulation of the weather pattern on Earth, where it is more important to have accurate predictions over land than over the wide-open sea.

The finite element method originated from the need for solving complex elasticity and structural analysis problems in civil and aeronautical engineering. Its development can be traced back to the work by Alexander Hrennikoff (1941) and Richard Courant [1] (1942). While the approaches used by these pioneers are dramatically different, they share one essential characteristic: mesh discretization of a continuous domain into a set of discrete sub-domains, usually called elements.

Hrennikoff's work discretizes the domain by using a lattice analogy while Courant's approach divides the domain into finite triangular subregions for solution of second order elliptic partial differential equations (PDEs) that arise from the problem of torsion of a cylinder. Courant's contribution was evolutionary, drawing on a large body of earlier results for PDEs developed by Rayleigh, Ritz, and Galerkin.

Development of the finite element method began in earnest in the middle to late 1950s for airframe and structural analysis [2] and gathered momentum at the University of Stuttgart through the work of John Argyris and at Berkeley through the work of Ray W. Clough in the 1960s for use in civil engineering. By late 1950s, the key concepts of stiffness matrix and element assembly existed essentially in the form used today. NASA issued a request for proposals for the development of the finite element software NASTRAN in 1965. The method was again provided with a rigorous mathematical foundation in 1973 with the publication of Strang and Fix's “An Analysis of The Finite Element Method”[3] has since been generalized into a branch of applied mathematics for numerical modeling of physical systems in a wide variety of engineering disciplines, e.g., electromagnetism, thanks to Peter P. Silvester [4][5] and fluid dynamics.

In more and more engineering situations today, we find that it is necessary to obtain approximate numerical solutions to problems rather than exact closed-form solutions. For example, we may want to find the load capacity of a plate that has several stiffeners and odd-shaped holes, the concentration of pollutants during nonuniform atmospheric conditions, or the rate of fluid flow through a passage of arbitrary shape. Without too much effort, we can write down the governing equations and boundary conditions for these problems, but we see immediately that no simple analytical solution can be found.

The difficulty in these three examples lies in the fact that either the geometry or some other feature of the problem is irregular or "arbitrary." Analytical solutions to problems of this type seldom exist; yet these are the kinds of problems that engineers are called upon to solve.

The resourcefulness of the analyst usually comes to the rescue and provides several alternatives to overcome this dilemma. One possibility is to make simplifying assumptions to ignore the difficulties and reduce the problem to one that can be handled. Sometimes this procedure works; but, more often than not, it leads to serious inaccuracies or wrong answers. Now that computers are widely available, a more viable alternative is to retain the complexities of the problem and find an approximate numerical solution.

Several approximate numerical analysis methods have evolved over the years; a commonly used method is the finite difference scheme [1]. The familiar finite difference model of a problem gives a pointwise approximation to the governing equations.

This model (formed by writing difference equations for an array of grid points) is improved as more points are used. With finite difference techniques we can treat some fairly difficult problems; but, for example, when we encounter irregular geometries or an unusual specification of boundary conditions, we find that finite difference techniques become hard to use.

Unlike the finite difference method, which envisions the solution region as an array of grid points, the finite element method envisions the solution region as built up of many small, interconnected sub-regions or elements. A finite element model of a problem gives a piecewise approximation to the governing equations. The basic premise of the finite element method is that a solution region can be analytically modeled or approximated by replacing it with an assemblage of discrete elements. Since these elements can be put together in a variety of ways, they can be used to represent exceedingly complex shapes.

As an example of how a finite difference model and a finite element model might be used to represent a complex geometrical shape, consider the turbine blade cross section in Figure 6.1.

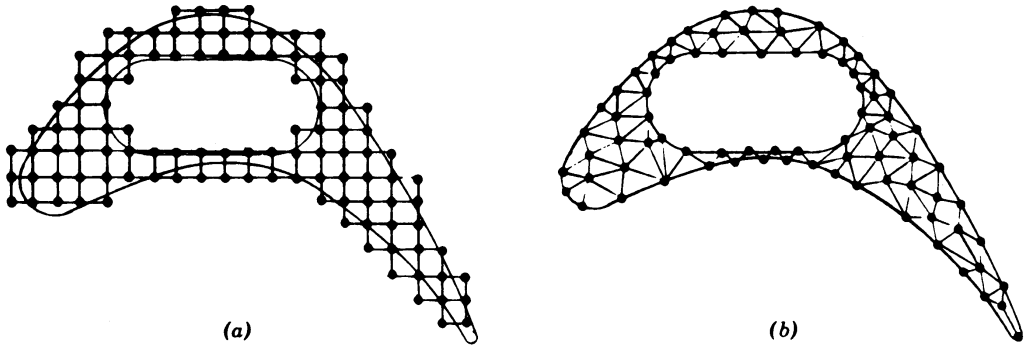

Figure 6.1: (*a*) Finite difference and (*b*) finite element discretizations of a turbine blade profile.

For this device we may want to find the distribution of displacements and stresses for a given force loading or the distribution of temperature for a given thermal loading. The interior coolant passage of the blade, along with its exterior shape, gives it a nonsimple geometry. A uniform finite difference mesh would reasonably cover the blade (the solution region), but the boundaries must be approximated by a series of horizontal and vertical lines (or "stair steps"). On the other hand, the finite element model (using the simplest two-dimensional element—the triangle) gives a better approximation to the region. Also, a better approximation to the boundary shape results because the curved boundary is represented by straight lines of any inclination. This example is not intended to suggest that finite element models are decidedly better than finite difference models for all problems. The only purpose of the example is to demonstrate that the finite element method is particularly well suited for problems with complex geometries. Still another numerical analysis method is the boundary element method (boundary integral equation method) [2–4]. This method uses Green's theorem to reduce the dimensionality of the problem; a volume problem is reduced to a surface problem, a surface problem is reduced to a line problem. The turbine blade cross section example of Figure 6.1 would have no interior mesh, but rather a mesh of connected points along the exterior boundary and a mesh of connected points along the interior boundary. This method is computationally less efficient than finite elements and is not widely used in industry. It is popular for acoustic problems [5] and is sometimes used as a hybrid method in conjunction with finite elements.

6.3 NASTRAN code

NASTRAN is a finite element analysis (FEA) program that was originally developed for NASA in the late 1960s under United States government funding for the Aerospace industry [6]. The MacNeal-Schwendler Corporation (MSC) was one of the principal and original developers of the public domain NASTRAN code. NASTRAN source code is integrated in a number of different software packages, which are distributed by a range of companies.

The 1964 annual review of NASA's structural dynamics research program revealed that the research centers were separately developing structural analysis software that was specific to their own needs. The review recommended that a single generic software program should be used instead [7]. In response, an ad hoc committee was formed. The committee determined that no existing software could meet their requirements. They suggested establishing a cooperative project to develop this software and created a specification that outlined the capabilities for the software [8].

A contract was awarded to Computer Sciences Corporation (CSC) to develop the software. The name of the program is an acronym formed from NASA Structural Analysis. The NASTRAN system was released to NASA in 1968. In the late 1960s, the MacNeal-Schwendler Corporation (MSC) started to market and support its own version of NASTRAN, called MSC/NASTRAN (which eventually became MSC.Nastran). The original software architecture was developed by Joe Mule (NASA), Gerald Sandler (NASA), and Stephen J. Burns (University of Rochester).

NASTRAN software application was written to help design more efficient space vehicles such as the Space Shuttle. NASTRAN was released to the public in 1971 by NASA's Office of Technology Utilization. The commercial use of NASTRAN has helped to analyze the behavior of elastic structures of any size, shape, or purpose. For example, the automotive industry uses the program to design front suspension systems and steering linkages. It is also used in designing railroad tracks and cars, bridges, power plants, skyscrapers, and aircraft. The program alone was estimated to have returned $701 million in cost savings from 1971 to 1984. NASTRAN was inducted into the U.S. Space Foundation's Space Technology Hall of Fame in 1988, one of the first technologies to receive this prestigious honor [9-10].

The NASTRAN program has evolved over many versions. Each new version contains enhancements in analysis capability and numerical performance. In addition, many errors

from previous versions are corrected. Today, NASTRAN is widely used throughout the world in the aerospace, automotive and maritime industries. It has been claimed that NASTRAN is the industry standard for basic types of analysis for aerospace structures, e.g. linear elastic static and dynamic analyses.

In November 2002 MSC Software reached a final agreement with the FTC to resolve an antitrust case against the company in connection with two acquisitions of rival CAE vendors, Universal Analytics, Inc. (UAI) and Computerized Structural Analysis & Research Corp. (CSAR). The FTC had alleged the acquisitions represented anticompetitive activities. Under the terms of the settlement, MSC divested a clone copy of its current Nastran software. The divestiture was through royalty-free, perpetual, non-exclusive licenses to UGS Corporation.

Commercial versions of NASTRAN are currently available from MSC Software, NEi Software (NEi Nastran) and Siemens PLM Software (NX Nastran). Siemens AG purchased the former UGS Corporation from private equity concerns and their rights to the commercial version of NX NASTRAN in 2006.

NASTRAN is written primarily in FORTRAN and contains over one million lines of code. NASTRAN is compatible with a large variety of computers and operating systems ranging from small workstations to the largest supercomputers.

NASTRAN was designed from the beginning to consist of several modules. A module is a collection of FORTRAN subroutines designed to perform a specific task—processing model geometry, assembling matrices, applying constraints, solving matrix problems, calculating output quantities, conversing with the database, printing the solution, and so on. The modules are controlled by an internal language called the Direct Matrix Abstraction Program (DMAP).

Each type of analysis available is called a solution sequence.

6.4 Numerical basis of the FE Method

We have been alluding to the essence of the finite element method, but now we shall discuss it in greater detail. In a continuum problem of any dimension the field variable (whether it is pressure, temperature, displacement, stress, or some other quantity) possesses infinitely many values because it is a function of each generic point in the body or solution region. Consequently, the problem is one with an infinite number of unknowns. The finite element discretization procedures reduce the problem to one of a finite number of unknowns by dividing the solution region into elements and by expressing the unknown field variable in terms of assumed approximating functions within each element. The approximating functions (sometimes called interpolation functions) are defined in terms of the values of the field variables at specified points called nodes or nodal points. Nodes usually lie on the element boundaries where adjacent elements are connected. In addition to boundary nodes, an element may also have a few interior nodes. The nodal values of the field variable and the interpolation functions for the elements completely define the behavior of the field variable within the elements.

For the finite element representation of a problem the nodal values of the field variable become the unknowns. Once these unknowns are found, the interpolation functions define the field variable throughout the assemblage of elements. Clearly, the nature of the solution and the degree of approximation depend not only on the size and number of the elements used but also on the interpolation functions selected. As one would expect, we cannot choose functions arbitrarily, because certain compatibility conditions should be satisfied. Often functions are chosen so that the field variable or its derivatives are continuous across adjoining element boundaries. These are applied to the formulation of different kinds of elements. Thus far we have briefly discussed the concept of modeling an arbitrarily shaped solution region with an assemblage of discrete elements, and we have pointed out that interpolation functions must be defined for each element. We have not yet mentioned, however, an important feature of the finite element method that sets it apart from other numerical methods. This feature is the ability to formulate solutions for individual elements before putting them together to represent the entire problem. This means, for example, that if we are treating a problem in stress analysis, we find the force–displacement or stiffness characteristics of each individual element and then assemble the elements to find the stiffness of the whole structure. In essence, a complex problem reduces to considering a series of greatly simplified problems.

Another advantage of the finite element method is the variety of ways in which one can formulate the properties of individual elements. There are basically three different approaches. The first approach to obtaining element properties is called the direct approach because its origin is traceable to the direct stiffness method of structural analysis. Although the direct approach can be used only for relatively simple problems, it is the easiest to understand when meeting the finite element method for the first time. The direct approach suggests the need for matrix algebra in dealing with the finite element equations.

Element properties obtained by the direct approach can also be determined by the variational approach. The variational approach relies on the calculus of variations and involves extremizing a functional. For problems in solid mechanics the functional turns out to be the potential energy, the complementary energy, or some variant of these, such as the Reissner variational principle. Knowledge of the variational approach is necessary to work beyond the introductory level and to extend the finite element method to a wide variety of engineering problems. Whereas the direct approach can be used to formulate element properties for only the simplest element shapes, the variational approach can be employed for both simple and sophisticated element shapes.

A third and even more versatile approach to deriving element properties has its basis in mathematics and is known as the weighted residuals approach.

The weighted residuals approach begins with the governing equations of the problem and proceeds without relying on a variational statement.

This approach is advantageous because it thereby becomes possible to extend the finite element method to problems where no functional is available. The method of weighted residuals is widely used to derive element properties for nonstructural applications such as heat transfer and fluid mechanics.

Regardless of the approach used to find the element properties, the solution of a continuum problem by the finite element method always follows an orderly step-by-step process. To summarize in general terms how the finite element method works we will succinctly list these steps now.

1. Discretize the Continuum.

The first step is to divide the continuum or solution region into elements. In the example the turbine blade has been divided into triangular elements that might be used to find the temperature distribution or stress distribution in the blade. A variety of element shapes

may be used, and different element shapes may be employed in the same solution region. Indeed, when analyzing an elastic structure that has different types of components such as plates and beams, it is not only desirable but also necessary to use different elements in the same solution. Although the number and the type of elements in a given problem are matters of engineering judgment, the analyst can rely on the experience of others for guidelines.

2. Select Interpolation Functions.

The next step is to assign nodes to each element and then choose the interpolation function to represent the variation of the field variable over the element. The field variable may be a scalar, a vector, or a higher-order tensor. Often, polynomials are selected as interpolation functions for the field variable because they are easy to integrate and differentiate.

The degree of the polynomial chosen depends on the number of nodes assigned to the element, the nature and number of unknowns at each node, and certain continuity requirements imposed at the nodes and along the element boundaries. The magnitude of the field variable as well as the magnitude of its derivatives may be the unknowns at the nodes.

3. Find the Element Properties.

Once the finite element model has been established (that is, once the elements and their interpolation functions have been selected), we are ready to determine the matrix equations expressing the properties of the individual elements. For this task we may use one of the three approaches just mentioned: the direct approach, the variational approach, or the weighted residuals approach.

4. Assemble the Element Properties to Obtain the System Equations.

To find the properties of the overall system modeled by the network of elements we must "assemble" all the element properties. In other words, we combine the matrix equations expressing the behavior of the elements and form the matrix equations expressing the behavior of the entire system. The matrix equations for the system have the same form as the equations for an individual element except that they contain many more terms because they include all nodes.

The basis for the assembly procedure stems from the fact that at a node, where elements are interconnected, the value of the field variable is the same for each element sharing that node. A unique feature of the finite element method is that the system equations are

generated by assembly of the individual *element* equations. In contrast, in the finite difference method the system equations are generated by writing nodal equations.

5. Impose the Boundary Conditions.

Before the system equations are ready for solution they must be modified to account for the boundary conditions of the problem. At this stage we impose known nodal values of the dependent variables or nodal loads.

6. Solve the System Equations.

The assembly process gives a set of simultaneous equations that we solve to obtain the unknown nodal values of the problem.

If the problem describes steady or equilibrium behavior, then we must solve a set of linear or nonlinear algebraic equations. If the problem is unsteady, the nodal unknowns are a function of time, and we must solve a set of linear or nonlinear ordinary differential equations.

7. Make Additional Computations If Desired.

Many times we use the solution of the system equations to calculate other important parameters. For example, in a structural problem the nodal unknowns are displacement components.

From these displacements we calculate element strains and stresses.

Similarly, in a heat-conduction problem the nodal unknowns are temperatures, and from these we calculate element heat fluxes.

6.5 S.M.A. system actuator theoretical model basis

According to the previous consideration about S.M.A. features in Chapter 2 in 1990, Liang and Rogers [11] developed a new phenomenological model base on the Tanaka's one: they adopted his constitutive equation but, for the phase kinetics, they assumed a simpler cosine relationship to describe the martensite fraction as a function of stress and temperature. They also assumed the material properties to be constant during the transformation.

The equation describing the martensite concentration during heating and cooling phases are:

$$\xi = \frac{\xi_M}{2} \cdot \cos\left[\alpha_A \left(T - A_s\right) + b_A \cdot \sigma\right] + \frac{\xi_M}{2} \qquad (6.1)$$

where $\alpha_A = \frac{\pi}{A_f - A_s}$ and $\alpha_M = \frac{\pi}{M_f - M_s}$ are combinations of material constant A_f, A_s, M_f, M_s are material characteristic temperatures, respectively known as austenite final austenite start martensite final and martensite start.

They refer to phase transformations of the material and define when a particular crystal structures appears or the conversion is complete.

Two other combination of the material constants are $b_A = -\frac{\alpha_A}{C_A}$ and $b_M = -\frac{\alpha_M}{C_M}$, being C_A and C_M the slopes of the straight lines approximating the functions relating the four temperatures to the acting stress.

Finally, ξ_A and ξ_M are the martensite and austenite volume fractions in the alloy before heating and cooling, respectively.

For our purpose the cooling term has been considered during the analysis.

As stated in the chapter 5 a numerical investigation has been conducted about this actuator only considering the conduction – free convection contribution for the S.M.A. cooling as presented in Figure 2.

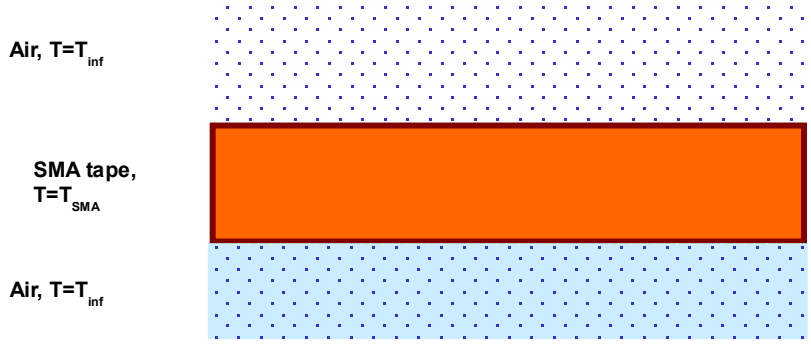

Figure 6.2: Reference scheme S.M.A. tape – air.

The main geometric and mechanical features of the system are the same of the Chapter (as in the following tables 6.1, 6.2 and 6.3).

Rectangular section (m)	1.0e-3
Area (m^2)	1.0e-6
Tape length (m)	13.0e-2

Table 6.1: S.M.A. tape geometrical features

Austenite Young modulus (GPa)	40.18
Martensite Young modulus (GPa)	16.5
Austenite start, A_s, (°C)	47.3
Austenite finish, A_f, (°C)	58.9
Martensite start, M_s, (°C)	43.3
Martensite finish, M_f, (°C)	27.5

Table 6.2: S.M.A. tape properties

$c \left[\frac{J}{kg \cdot °K}\right]$	837
$k \left[\frac{J}{m \cdot s \cdot °K}\right]$	18
$\rho \left[\frac{kg}{m^3}\right]$	6500
$\bar{h} \left[\frac{J}{m^2 \cdot s \cdot °K}\right]$	11.63

Table 6.3: S.M.A. thermodynamic parameters

Although the S.M.A. ribbon operates with an internal pre-load to assure its recovery when cooled, the effects on the transformation temperatures of the internal stress have been neglected. In the following paragraph, the simulation strategy adopted for predicting the time required for completely deactivating the S.M.A., has been described.

Before the numerical simulation a theoretical model for S.M.A. tape cooling quite similar

to the previous one already described in chapter 5 has been presented. In particular a numerical simulation by a FE approach has been developed in order to determine S.M.A. tape cooling time in an unsteady conduction - free convection regime.

The theoretical model as already considered in chapter 5 is based on the following assumption according to the thermodynamic phenomenology: Biot number for S.M.A. component is $6.0 \cdot 10^{-4}$ (Bi << 1).

In addition in this model, for the S.M.A., the internal thermal resistance has been considered negligible with respect to the external thermal resistance and so the temperature is practically uniform along the S.M.A. thickness.

In Figure 6.2 the S.M.A tape has been shown.

In order to model the phenomenology, basing on such a scheme, the energy balance equation has been written.

At first, model analysis has been developed assuming Austenite as initial phase to compute the transformation time from A_f to M_s. In the following, the first analytical model is presented. According to the energy balance equation [12] for our purpose in presence of the initial Austenite phase we have the Eq. (6.2)

$$(c_{SMA} \cdot \rho_{SMA} \cdot L_{SMA} \cdot b_{SMA} \cdot t_{SMA}) \frac{dT_{SMA}}{dt} = \overline{h} \cdot (L) \cdot (T_{\infty} - T_{SMA}) \qquad (6.2)$$

In the table 6.4 each terms in Eq. (6.2) is explained and we find t_{M_s}.

$(c_{SMA} \cdot \rho_{SMA} \cdot L_{SMA} \cdot b_{SMA} \cdot t_{SMA}) \frac{dT_{SMA}}{dt}$	S.M.A. Internal Energy variation
$\overline{h} \cdot (L \cdot b) \cdot (T_{\infty} - T_{SMA})$	S.M.A. tape output energy

Table 6.4: Energy balance terms for the analytical model

$t = 0$ $T_{SMA} = T_0$	Initial conditions for equation (6.2)

Table 6.5: Energy balance equation condition and coefficient for initial transformation from Austenite to Martensite start.

During the transformation phase from M_s to M_f , a new term in the energy balance equation has to be considered. So that, according to Liang and Rogers model, Martensite amount ξ produced has been computed.

For the Martensite concentration during cooling phases Eq. (6.3) has been considered but in this case, assuming S.M.A. material unloaded ($\sigma = 0$). To formulate an exact solution, Eq. (6.3) has been approximated through a piece wise function, equal to 1 for T $\leq M_f$, equal to 0 for T $\geq M_s$ and linearly variable as

$$\xi = \left(\frac{M_s}{M_s - M_f} - \frac{T_{SMA}}{M_s - M_f} \right) \tag{6.3}$$

for T $\in [M_f M_s,]$.

So that, from the Eq. (6.3), including the transformation phase, the energy balance equation for the S.M.A. – air system Eq. (6.2) becomes

$$(c_{SMA} \cdot \rho_{SMA} \cdot L_{SMA} \cdot b_{SMA} \cdot t_{SMA}) \frac{dT_{SMA}}{dt} = \overline{h} \cdot (L) \cdot (T_\infty - T_{SMA}) + (c_{SMA} \cdot \rho_{SMA} \cdot L_{SMA} \cdot b_{SMA} \cdot t_{SMA}) \frac{d(\xi \cdot T_{SMA})}{dt} \tag{6.4}$$

with $(c_{SMA} \cdot \rho_{SMA} \cdot L_{SMA} \cdot b_{SMA} \cdot t_{SMA}) \frac{d(\xi \cdot T_{SMA})}{dt}$ the novel phase transformation term, from solution t_{M_s} , we find the t_{M_f} .

with

$t = t_{M_s}$ $T_{SMA} = M_s$	Initial conditions for equation (6.4)

Table 6.6: Energy balance equation condition and coefficient for initial transformation from Martensite start to Martensite finish.

In the following a numerical approach by means of FE Method shall be described.

6.6 The S.M.A.FEM model

The numerical model has been realized by using the FE approach and so that after the geometry definition the discrete model has been developed.

In Nastran for the heat transfer analysis a model definition has to be done.

Conduction elements are defined by the configuration generated when geometric grid points are connected in specific orientations and, for heat transfer, obey Fourier's Law.

These elements can be characterized geometrically as being either one, two, or three dimensional, or axisymmetric. Besides being associated with geometry, these elements have the material properties for thermal conductivity, density, and specific heat associated with them.

Elements defining the geometry can the different accordingly to the analysis to be conducted in particular 1D element as for example CBAR or 2D as CQUAD4 largely used in structural problem.

These elements include one-dimensional elements, shell elements, axisymmetric elements, and solid elements as in the table.

1D	2D	3D
CBAR	CQUAD4	CHEXA
CBEAM	CQUAD8	CPENTA
CBEND	CTRIA3	CTETRA

Table 6.7: FE type modelling

Wherever a boundary condition is applied to the surface of a conduction element, it must be interfaced with a surface element. Surface elements provide the geometric connection between the structural conduction elements and the applied convection, radiation, or heat flux loads. In particular, surfaces that participate in radiation enclosures derive their cavity identity and their radiation material property pointers from the surface element description. Similarly, free and forced-convection Bulk Data entries are identified through their mating surface element identification numbers.

Surface element geometries are associated with surface types. Of the three forms of surface elements, the CHBDYG and the CHBDYP have their TYPE explicitly defined on their Bulk Data entries. The CHBDYE deals with the geometry type implicitly by

reference to the underlying conduction element.

In Nastran the Executive Control Section begins with the first Executive Control statement and ends with the CEND delimiter. It identifies the job and the type of solution to be performed. It also declares the general conditions under which the job is to be executed, such as maximum time allowed and the type of system diagnostics desired. If the job is to be executed with a solution sequence, the actual solution sequence is declared along with any alterations to the solution sequence that may be desired. If Direct Matrix Abstraction is used, the complete DMAP sequence must appear in the Executive Control Section. The Executive Control statements and examples of their use are described in the "**File Management Statements**".

The Case Control Section follows CEND and ends with the BEGIN BULK delimiter. It defines the subcase structure for the problem, defines sets of Bulk Data, and makes output requests for printing, punching, and plotting.

In MSC.Nastran, transient thermal analysis is solved by Solution Sequence 159. Since Solution 159 can be used for both structural (default) and thermal analyses, the user must include the command

ANALYSIS = HEAT

The S.M.A. – air reference scheme (Figure.6.2) has been considered to introduce the numerical simulation. A FE approach has been adopted to estimate the S.M.A. tape cooling time using as FE pre –post processor Femap 9.2 and the MSC\Nastran as solver code.

The FE model has been created according to the material properties of S.M.A. tape and considering a thermal convection between the tape and external air.

A thin S.M.A. layer has been modelled by means a CHEXA element with 8 nodes.

In order to solve the problem the boundary conditions on the two S.M.A. faces exposed to the air have been defined; in addition also material properties on the faces and the related boundary conditions surfaces with reference to the heat transfer, as in the present problem, have been determined.

The heat transfer problem by using FE approach has been studied by means of a Transient Heat Transfer (SOL 159) because of the time dependent investigation.

The thermal distribution on the S.M.A. tape is uniform and is $100°C$ necessary for the alloy activation, but the reference temperature to be reached by the tape after the thermal

exchange is $20°C$ that is the external air temperature considered during our analysis.

The model has been created considering the free convection for the two surfaces according to the heat transfer connection to a surface element for the heat exchange simulation.

In order to determine the rate of heat produced in the material, because of the heating of the tape for the flap deflection during the activation phase (through Joule effect), a rate of heat power inside the FE model has been considered.

In this FE approach, for the thermal convection exchange between the tape and the air, a control node (n.99) at an appropriate distance with respect to the FE model dimension has been placed. The control node is at a temperature of $20°C$.

Another problem to be considered during the simulation has been the transformation from A_f to M_s and from M_s to M_f modelled by means of a nonlinear approach.

By the FE simulation and analysis by means of transient heat transfer solution a thermal history has been considered.

The solution provided by the MSC\Nastran code has provided the thermal behaviour of the single node of the FE model.

In order to show the results, obtained by the numerical simulation, a tool developed in Matlab language, able to extract and evaluate numerical outputs, has been created.

This tool is able to extract and assess numerical results deriving from Nastran analysis and it is able to plot the results of the all nodes of the FE model as shown in the Figure 6.3 where the green curve is the temperature of the reference node 99 constant at $20°C$ and the red curve is the thermal evolution of the S.M.A. surfaces during the thermal convection cooling down. It is evident (figure 6.3) the two knees on the red curve depending on the transformation phase described from Austenite to Martensite.

The complete S.M.A. tape cooling time, t_{M_f} is $200s$ as final value.

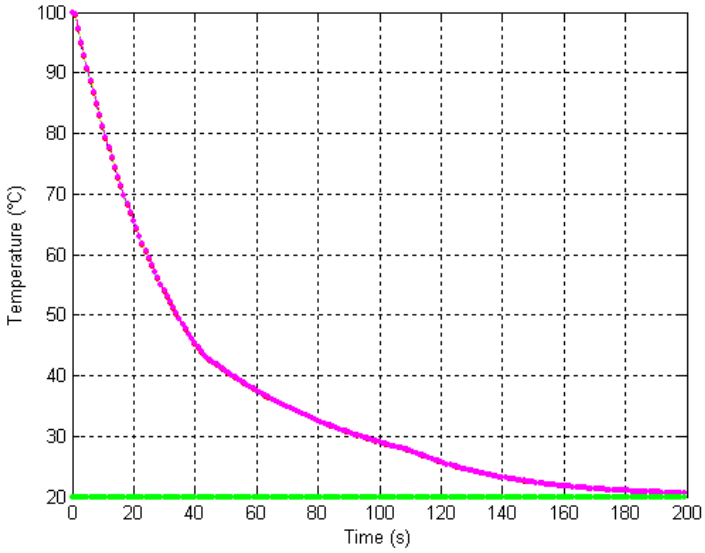

Figure 6.3: FE numerical simulation, Green curve : reference temperature, Red curve: S.M.A. cooling temperature

In this brief description a free convection analysis has been conducted in order to know the S.M.A. cooling tendency.

So, a novel approach has been adopted in this study by highly integrating the S.M.A.s' elements within the architecture for the flap deflection; this tape have both a structural and actuation role, working as actuators of the structure, whose integrity depends on S.M.A.s' structural capability of sustaining external loads.

In the present paper a possible solution to the S.M.A. structure cooling problem has been proposed. In particular, after a problem definition in terms of thermal convection equilibrium according to thermodynamic equation a FE approach has been followed.

In fact, even if the S.M.A. materials provide advantages in terms of energy consumption, weight reduction and system integrability in particular in aeronautical field, the cooling problem, during the de-activation phase, is actually under investigation. So that, after a conceptual scheme presented and a brief system description of the architecture, in order to explain the actuator system for the flap deflection, a numerical investigation has been presented.

At first, according to the hypothesis related to a negligible S.M.A. thermal inertia and uniform temperature into the S.M.A. tape (Bi <<1) a FE model has been created.

This approach for the thermal natural convection has been developed in order to predict the S.M.A. tape cool down during the de-activation phase. The actuator activation time,

through heating by means of Joule effect in order to have the alloy transformation, from Martensite into Austenite phase, is negligible with respect to the cooling time, for the transformation from Austenite into Martensite, actually under investigation, so this investigation defines a study for the prediction of the cooling time necessary when the actuator is in thermal natural convection regime during the flap deflection.

This proposed study may be considered as the initial track to follow in order to satisfy a time cooling reduction in S.M.A. applications.

In the next section the introduction of a Peltier cell under the S.M.A. ribbon shall be considered in order to define a cooling time reduction with respect to the free convection phase according to this numerical study her conducted.

6.7 The Peltier cell as S.M.A. cooling system: numerical investigation

As stated before in the following in order to cut down the cooling time of the S.M.A. ribbon by the Peltier effect contribution.

A numerical simulation by pre-post processor Femap and Solver MSC\NASTRAN has been conducted. In fact this ribbon is a flap actuator and, in order to explain his function, it has to be activated and deactivated in a few second. As more times remembered in this work a S.M.A. feature is the long deactivation time in terms of cooling of the ribbon that make unable this solution for an aeronautical use.

In this study a novel approach to this problem is presented by a numerical simulation of S.M.A. and Peltier cell installation.

In particular while in thw previous analysis only free convection has been considered and the cooling time is 200 seconds too much for a flap actuator with this type of innovative material, the Peltier cell contribution as possible cooling system has been investigated aiming at obtaining a cooling time reduction.

Then, in order to evaluate the soundness of this solution and the possible applicability for aeronautical scope a numerical simulation has been conducted.

At first, under the S.M.A. tape a Peltier cell as a solid geometry has been included.

The modeling phase for the Peltier cell simulation from a geometrical point of view is similar to the S.M.A. tape because it is composed of a solid element CHEXA with 8 nodes. This solid model has peculiar material properties related to the features of the Peltier cell in order to comply with the real cell and functions.

In the figure 6.4 a model of the S.M.A. – Peltier cell has been provided.

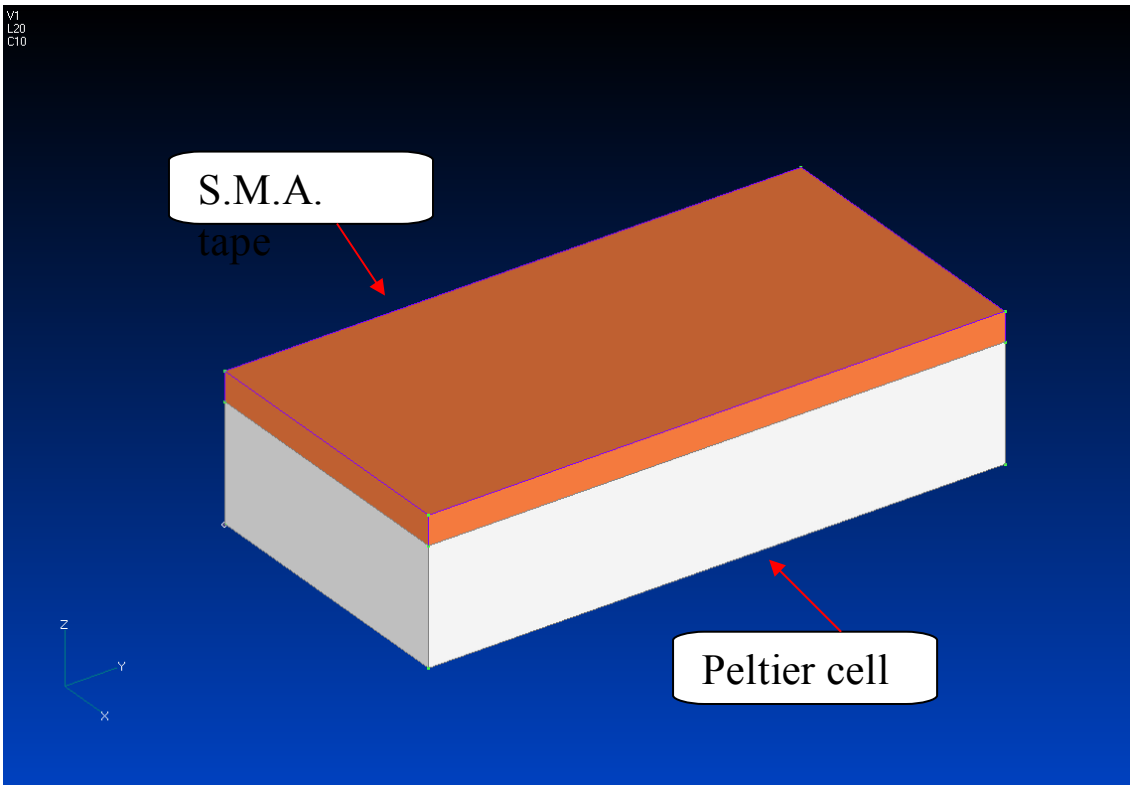

Figure 6.4: FE numerical model. S.M.A. tape is represented by the orange rectangular solid but the Peltier cell is the grey solid under the S.M.A. tape.

After the geometry definition (GRID), element for S.M.A. and Peltier cell (PSOLID) and material properties (MAT4) assignment, the heat transfer has been simulated. In addition, boundary conditions for the interface side S.M.A. – Peltier cell for the numerical simulation have been defined.

The boundary conditions in Nastran are expressed by the CHBDYE in the Bulk Data Section in order to declare which face of the solid element are involved during the convection process as in the present analysis.

In fact, the boundary conditions for the S.M.A. – Peltier cell system have been assigned to the lower Peltier cell face and to the upper side S.M.A. face in order to have a numerical simulation of the free convection with air.

According to the analytical model where during the Peltier cell cooling operation there are three contribution due to Peltier effect (thermoelectrical effect), Fourier effect (conduction effect between S.M.A. - cell) and Joule effect (dissipation effect).

It is important to focus that the Fourier effect between S.M.A. Peltier cell is a conduction effect between the two faces in contact each other.

For the Joule effect simulation an internal heat power generation inside the Peltier cell has been considered by means of QVOL entry where the intensity of internal heating can be applied defining a volumetric heat addition in a conduction element as the Peltier cell in this study. This entry is related to a control node to refer all the heat flux during the heat transfer simulation phase; in particular, a node located at a very long distance (10 times) with respect to the system dimension is the reference node for the free convection S.M.A.-air and Peltier cell – air as in this analysis has been developed.

While the Joule effect is an internal heat source related to a dissipation contribution $R \cdot I^2$ due to the internal cell resistance that represents the disadvantage during the operation phase of the Peltier cell, there is another contribution already included in the theoretical model in the previous chapter 4.

This term is related to the Peltier effect that occurs between the two faces of the cell and that is responsible of the required cooling effect.

This contribution is related to the Seebeck coefficient and to the temperature difference between the two Peltier sides, the cool one in the upper cell side under the S.M.A. tape, and the hot one on the lower cell side exposed to air convection.

The most difficult term to be considered and numerically simulated in the FE approach has been the $-2 \cdot a \cdot I \cdot T_{SMA}$ as explained in the theoretical model analysed before.

In order to obtain this result in the numerical model a non linear approach has been followed; in fact in the Nastran file .dat a NOLIN 1 entry has been included for the Peltier effect contribution.

In this entry different fields are included in particular there is a dedicated field for the node definition where Peltier cell and S.M.A. tape a re connected.

In the field 2 and 7 of the NOLIN1 entry the model node of the Peltier cell interested by the heat exchange are defined, then, in field 4 of the entry there is the scale factor of the thermoelectric effect of the Peltier cell.

For the unsteady thermal analysis SOL 159 (Transient Heat Transfer), with a nonlinear approach as in the present work case, has been used.

In the following a non linear approach for the transient analysis shall be provided.

During the analysis because of a lot of parameters to be considered and able to change are interested in this model a modular approach has been preferred.

In fact, in the Nastran .dat file named “core_parameter.dat” file as main file have been recalled other .dat files (Grid, Material, Load,) for a more usable function of the code.

In order to make easier the numerical simulation phase and obtain a computational cut down as expected result, a numerical tool in Matlab language has been written.

This tool is very friendly use because in it all geometrical and mechanical features are included for the S.M.A. tape and for the Peltier cell too.

In such a way even if some parameters have to be modified during the analysis process according to new experimental cases of interest, the tool can automatically update the Nastran file input values.

In particular this tool can give Nastran the instruction for the analysis solution automatically and with a sensible time cost reduction in a computational point of view allowing to have a plot with different case of interest for the S.M.A. cooling process by the Peltier cell. In fact depending on different current intensity of the Peltier cell the cooling effect is subjected to variation and this has to be foreseen during this type of study.

By means of the tool a parameterized analysis of the Peltier cell performances accordingly to different current intensity values in the following have been presented.

In particular, this Matlab tool is able to calculate and to present different plots for the S.M.A. tape cooling time related to different current intensity of the Peltier cell and the results have confirmed a time reduction with respect to the numerical simulation in a free convection regime as illustrated in the previous analysis.

The tool in fact can provide necessary information for developing of a new cooling approach through a Peltier cell, achieving a sensible cooling time reduction comply to a conventional flap deflection time requirements.

The different calculations obtained for a range of current supply of [0,0.2,0.4,0.6,0.8,1.0,1.2,1.4,1.6,1.8,2.0,2.2,2.4,2.6,2.8,3.0] have confirmed a cut down cooling time.

After that, thanks to the operability of the tool a new analysis approach has been followed in order to define what are the most influent parameters for the S.M.A. tape cooling time.

In the following some calculations by an iterative approach have been developed changing S.M.A. main geometric parameters as S.M.A. tape thickness very important during a thermal analysis.

In order to determine and focus the numerical law of the S.M.A. cooling time versus current supplied by the Peltier cell an intersection among the transition phase curve obtained for martensite start and martensite finish conditions, respectively, has been

proposed in this numerical analysis.

This approach has confirmed the tendency of cooling time reduction foreseen during the previous analytical investigation in particular how much the cooling time is dependent on current supplied by the Peltier cell within an application range as before stated.

In the following an additional comparison has been presented in particular showing the decreasing trend of the S.M.A. tape cooling time confirming the soundness of the design and numerical simulation soundness.

Two analysis have been conducted with a S.M.A. thickness of 1mm and 2 mm verifying the effect on cooling time. In other words a cooling time decreasing is observable according to an increasing current supplied by the Peltier cell installed under the S.M.A. tape.

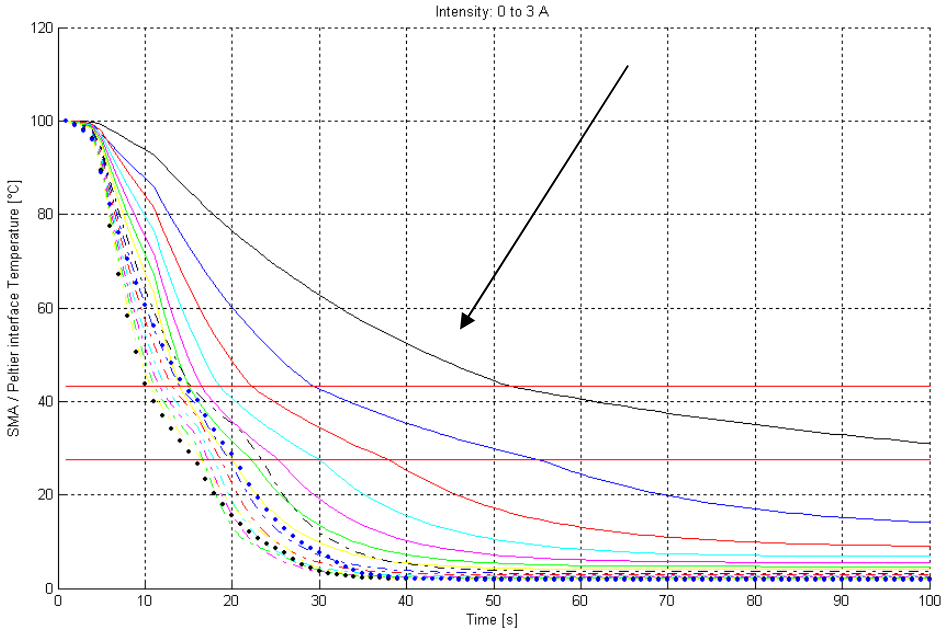

Figure 6.5: S.M.A. tape cooling time versus current supplied by Peltier cell. Arrow indicated the decreasing effect on the cooling time. With a current supply from 0 to 3 A. This analysis have been conducted for sigma =0MPa and a S.M.A. thickness of 1 mm and sigma =0MPa.

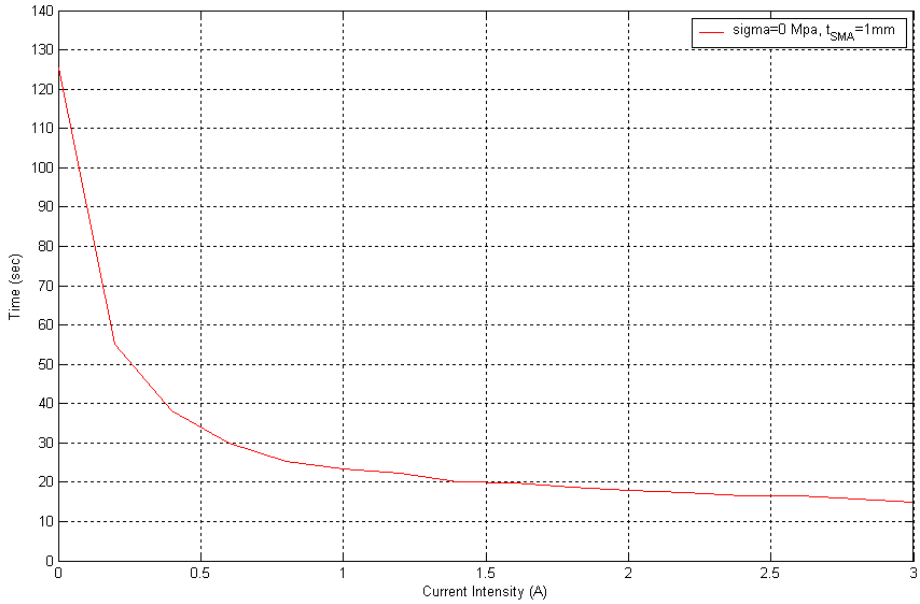

Figure 6.6: S.M.A. tape cooling time versus current supplied by Peltier cell. The current is supplied from 0 to 3 A. This analysis have been conducted for sigma =0 MPa and a S.M.A. thickness of 1 mm obtaining intersection between M_f direct line with cooling curves by Peltier cell effect from FE investigation.

By this analysis it is evident that cooling time fro the S.M.A. tape obtained by Peltier cell effect reaches 15 seconds as in the figure 6.6 presented.

This result confirms that the numerical investigation by FE approach is in line with other requirements well lower than cooling time obtained by natural convection study before presented (figure 6.3).

In fact, in natural convection only experimental data have been confirmed but the additional Peltier contribution has revealed soundness of the designed model and the goodness of the proposed solution for cooling time reduction.

After this numerical simulation here proposed another investigation has been conducted considering different boundary conditions. In particular the simulation has concerned a pre-load of $\sigma = 50MPa, 100MPa, 150MPa, 200MPa$ on the S.M.A. tape and repeating the analysis in two different cases when S.M.A. tape is 1mm and 2mm thick.

According to the linear approach for the Liang & Rogers' model $C_A = C_M$ has been considered but now in this formulation S.M.A. tape has been considered with an initial pre-load compliance with design requirements scope of this work.

In this approach according to constitutive law the following value of C_m has been

considered: $C_A = C_M = 12 \cdot 10^6 \frac{Pa}{°C}$.

From this value the pre-load contribution has been found adding to the initial martensite temperature according to this formulation: $\sigma = C_M \cdot T$ and from this relation we can found temperature value to be added to M_S temperature.

So, considering these conditions numerical investigations has been conducted and here assessed. In fact, in the following a comparison with the unloaded case shall be presented. This analysis determines a S.M.A. tape cooling time reduction with respect to the unloaded conditions because of the capacity of the material to recover the initial shape from austenite into martensite during the cooling phase.

In fact, a pre-load is able to make easier the transformation from hot phase (austenite) into cool phase (martensite) and this is evident in the following plots (from figure 6.7, to 6.14).

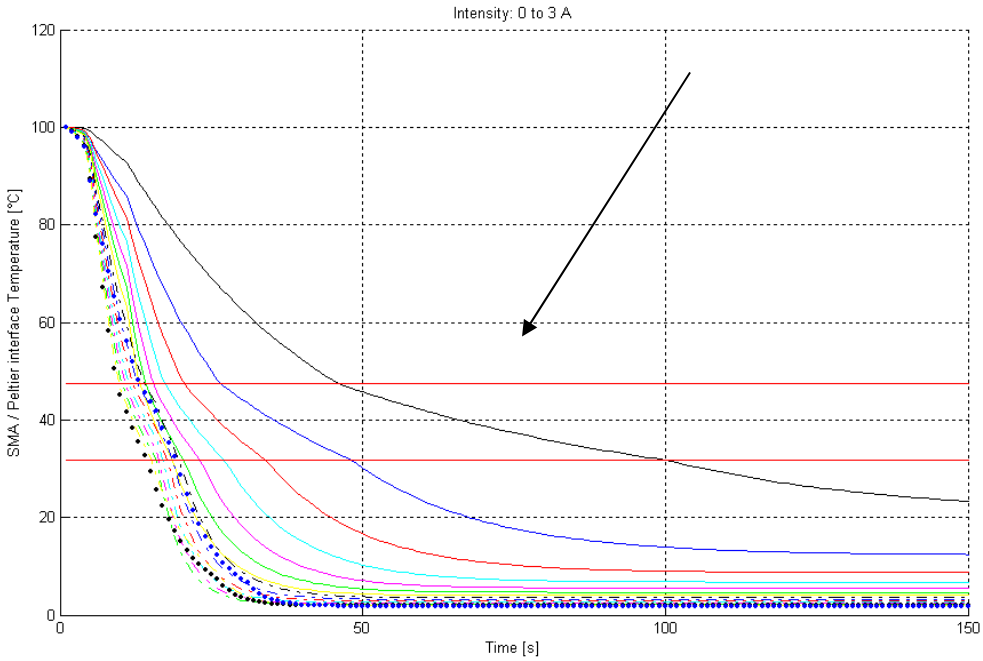

Figure 6.7: S.M.A. tape cooling time versus current supplied by Peltier cell. Arrow indicated the decreasing effect on the cooling time. With a current supply from 0 to 3 A. This analysis have been conducted for a S.M.A. thickness of 1 mm and sigma=50MPa.

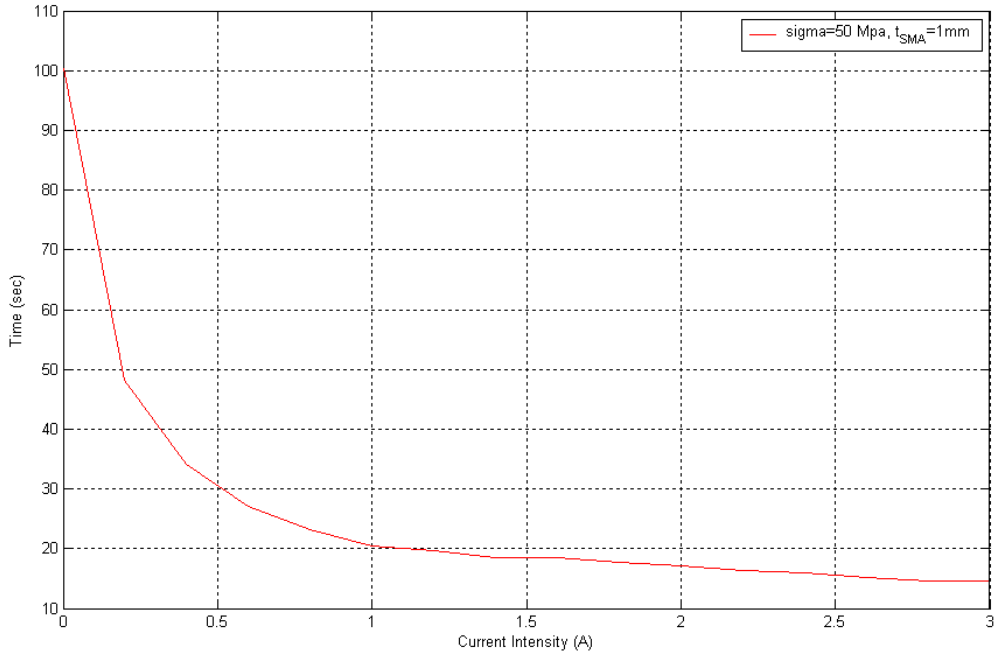

Figure 6.8: S.M.A. tape cooling time versus current supplied by Peltier cell. The current is supplied from 0 to 3 A. This analysis have been conducted for sigma =50 MPa and a S.M.A. thickness of 1 mm obtaining intersection between M_f direct line with cooling curves by Peltier cell effect from FE investigation.

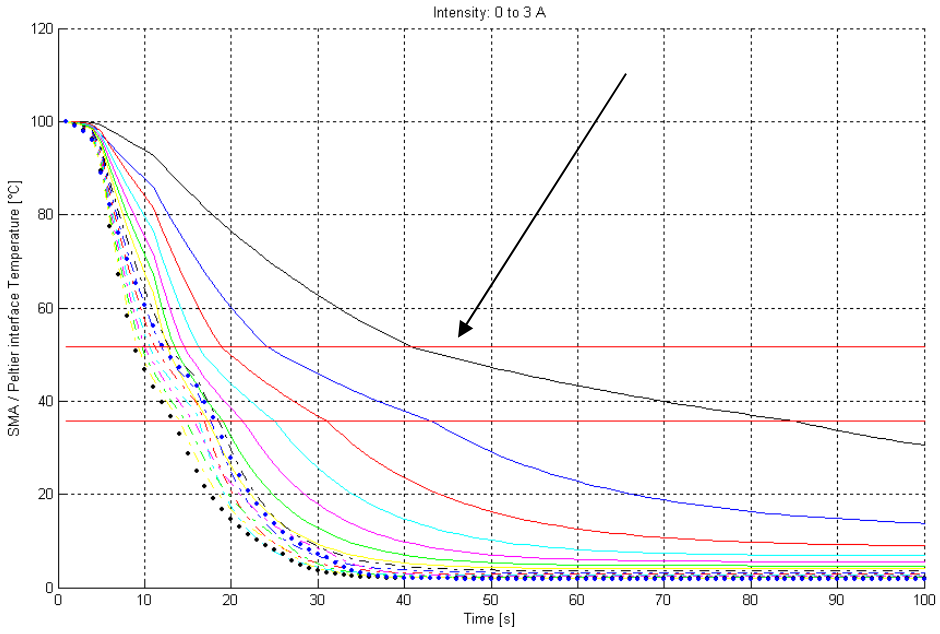

Figure 6.9: S.M.A. tape cooling time versus current supplied by Peltier cell. Arrow indicated the decreasing effect on the cooling time. With a current supply from 0 to 3 A. This analysis have been conducted for a S.M.A. thickness of 1 mm and sigma=100MPa.

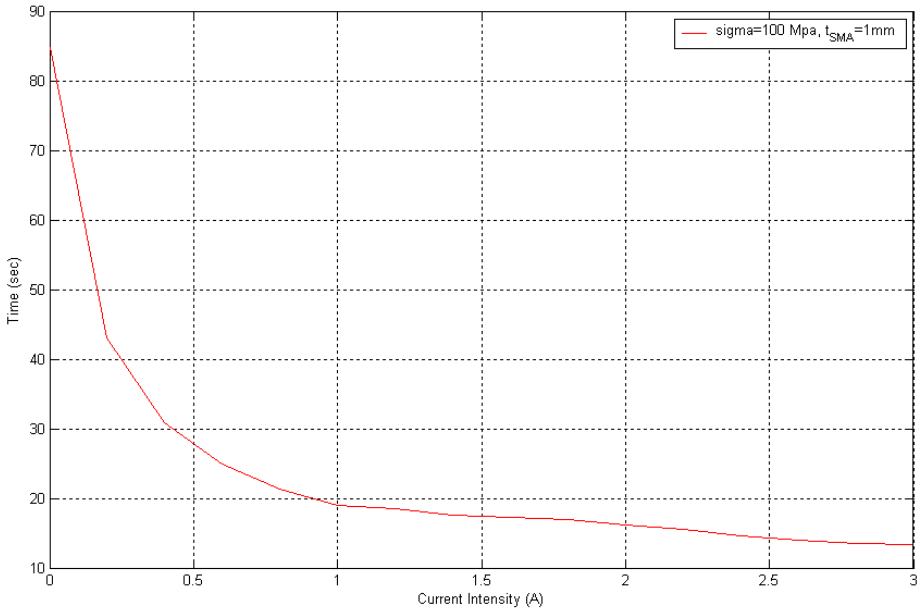

Figure 6.10: S.M.A. tape cooling time versus current supplied by Peltier cell. The current is supplied from 0 to 3 A. This analysis have been conducted for sigma =100 MPa and a S.M.A. thickness of 1 mm obtaining intersection between M_f direct line with cooling curves by Peltier cell effect from FE investigation.

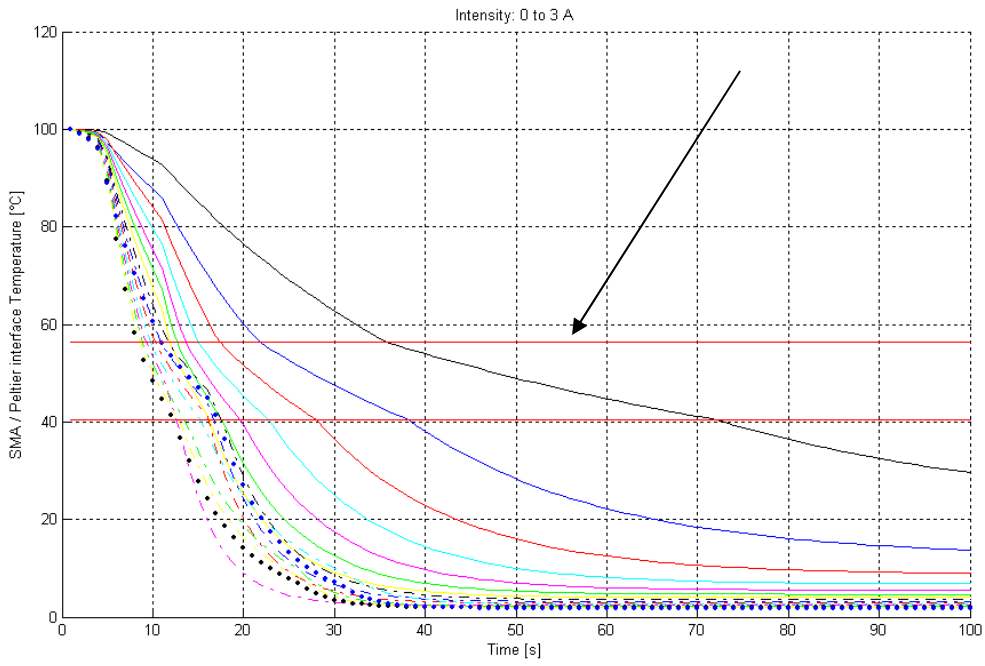

Figure 6.11: S.M.A. tape cooling time versus current supplied by Peltier cell. Arrow indicated the decreasing effect on the cooling time. With a current supply from 0 to 3 A. This analysis have been conducted for a S.M.A. thickness of 1 mm and sigma=150MPa.

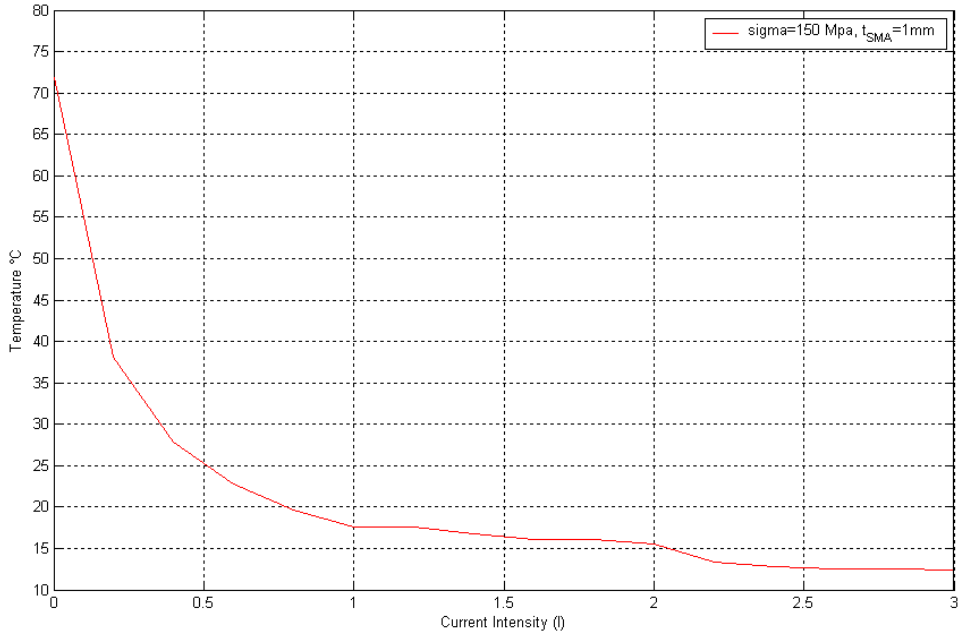

Figure 6.12: S.M.A. tape cooling time versus current supplied by Peltier cell . The current is supplied from 0 to 3 A. This analysis have been conducted for sigma =150 MPa and a S.M.A. thickness of 1 mm obtaining intersection between M_f direct line with cooling curves by Peltier cell effect from FE investigation.

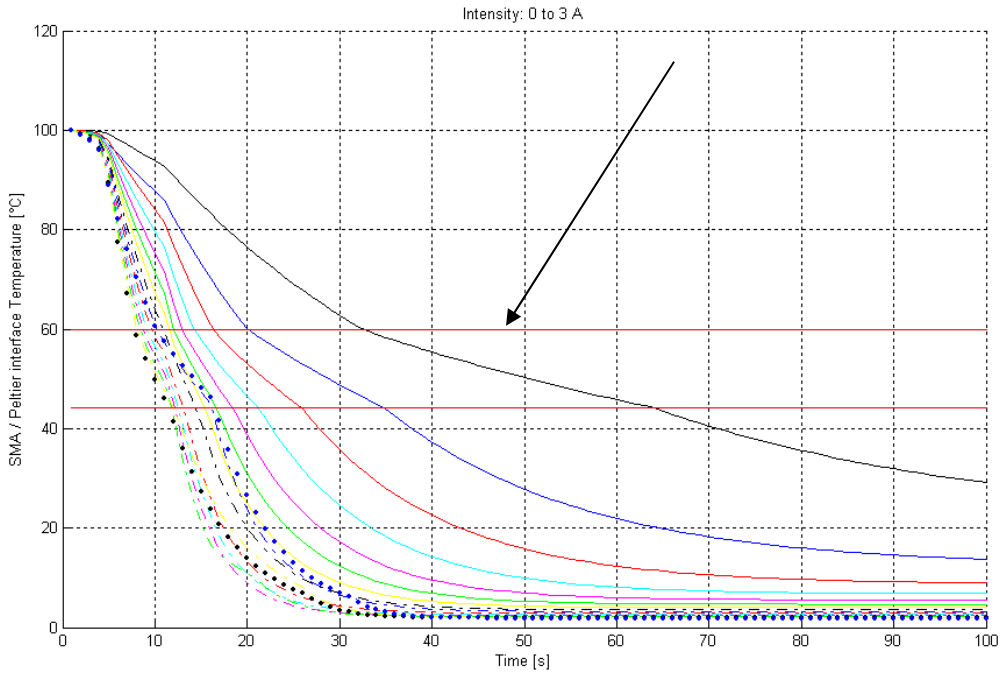

Figure 6.13: S.M.A. tape cooling time versus current supplied by Peltier cell. Arrow indicated the decreasing effect on the cooling time. With a current supply from 0 to 3 A. This analysis have been conducted for a S.M.A. thickness of 1 mm and sigma=200MPa

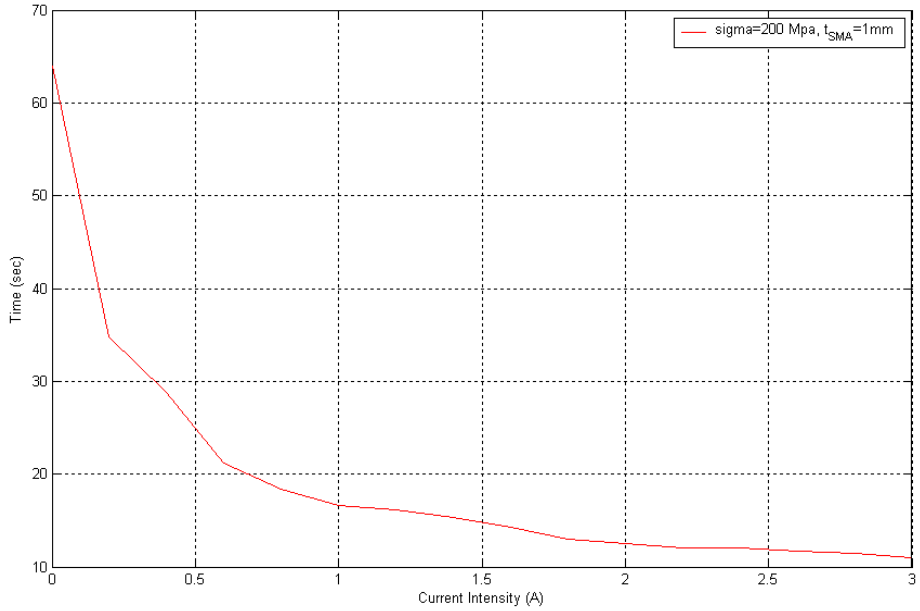

Figure 6.14: S.M.A. tape cooling time versus current supplied by Peltier cell. The current is supplied from 0 to 3 A. This analysis have been conducted for sigma =200 MPa and a S.M.A. thickness of 1 mm obtaining intersection between M_f direct line with cooling curves by Peltier cell effect from FE investigation.

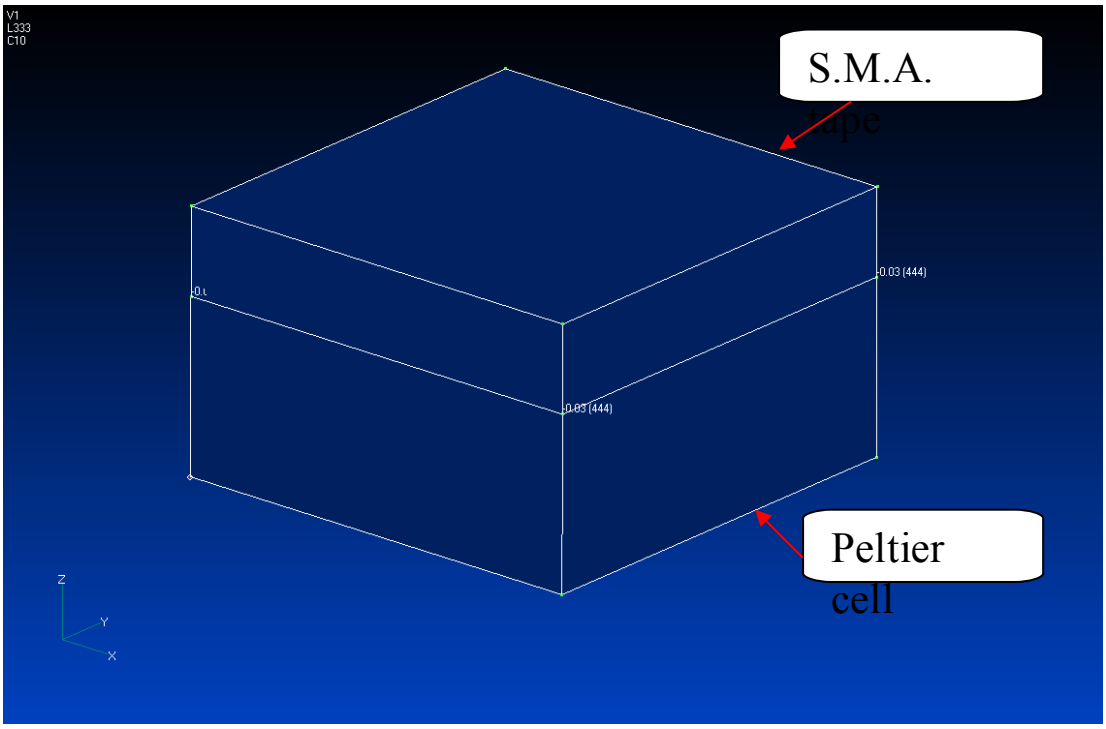

Figure 6.15: S.M.A. tape (upper side)- Peltier cell (lower side) FE model for S.M.A. tape thickness of 2mm.

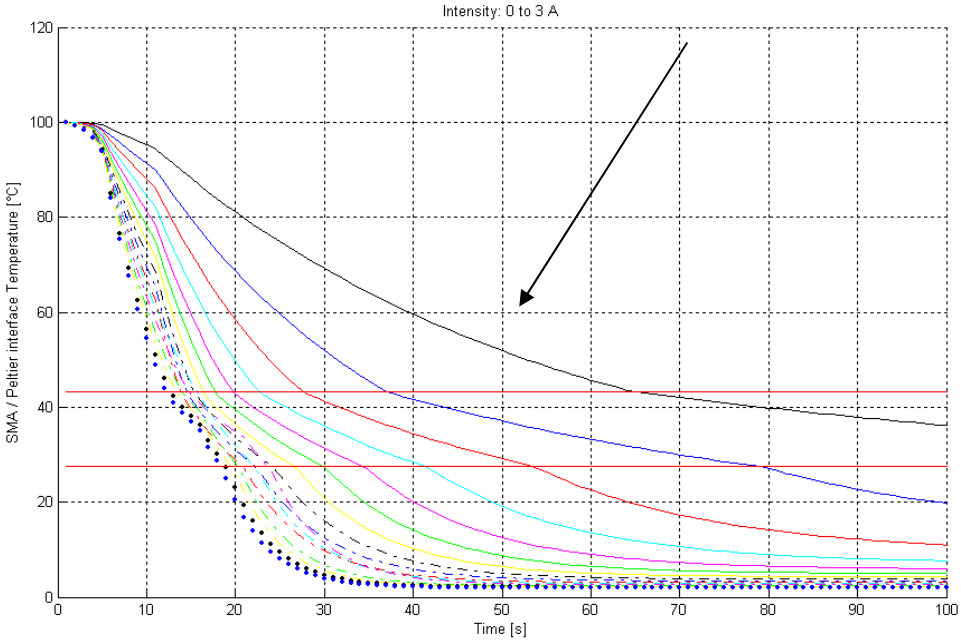

Figure 6.16: S.M.A. tape cooling time versus current supplied by Peltier cell. Arrow indicated the decreasing effect on the cooling time. With a current supply from 0 to 3 A. This analysis have been conducted for a S.M.A. thickness of 2 mm and sigma=0MPa.

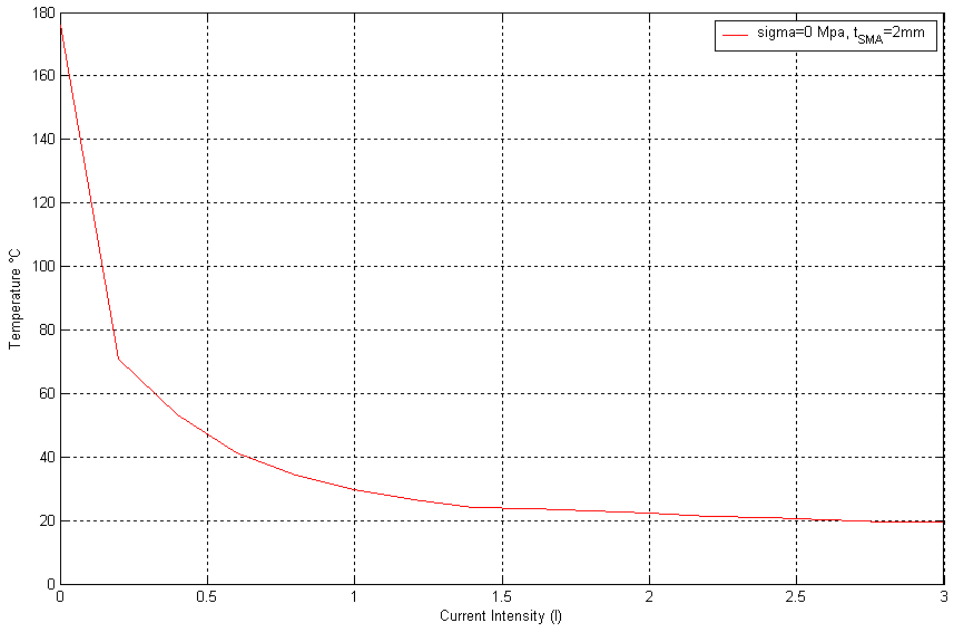

Figure 6.17: S.M.A. tape cooling time versus current supplied by Peltier cell. The current is supplied from 0 to 3 A. This analysis have been conducted for sigma = 0 MPa and a S.M.A. thickness of 2 mm obtaining intersection between M_f direct line with cooling curves by Peltier cell effect from FE investigation.

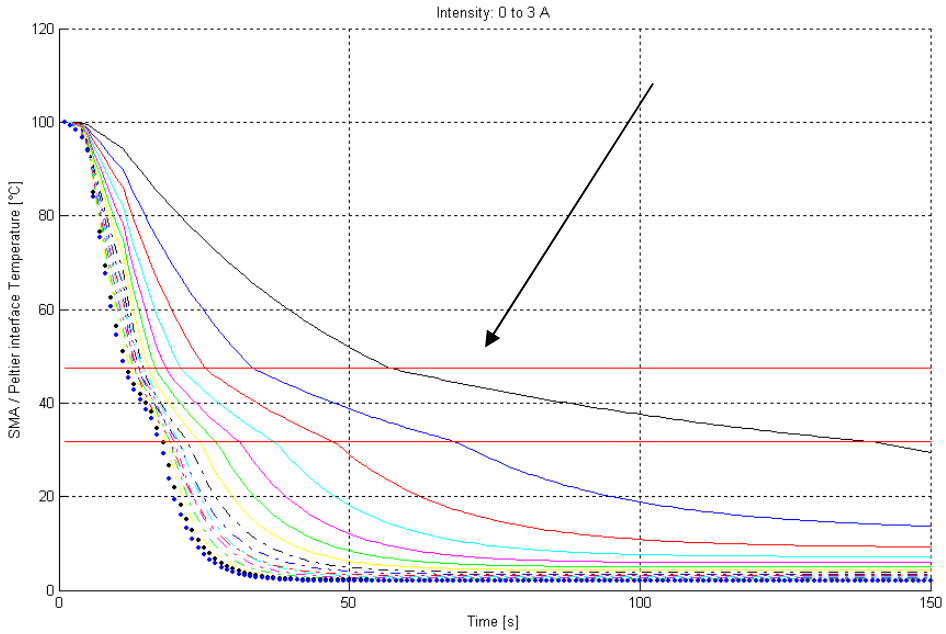

Figure 6.18: S.M.A. tape cooling time versus current supplied by Peltier cell. Arrow indicated the decreasing effect on the cooling time. With a current supply from 0 to 3 A. This analysis have been conducted for a S.M.A. thickness of 2 mm and sigma=50MPa.

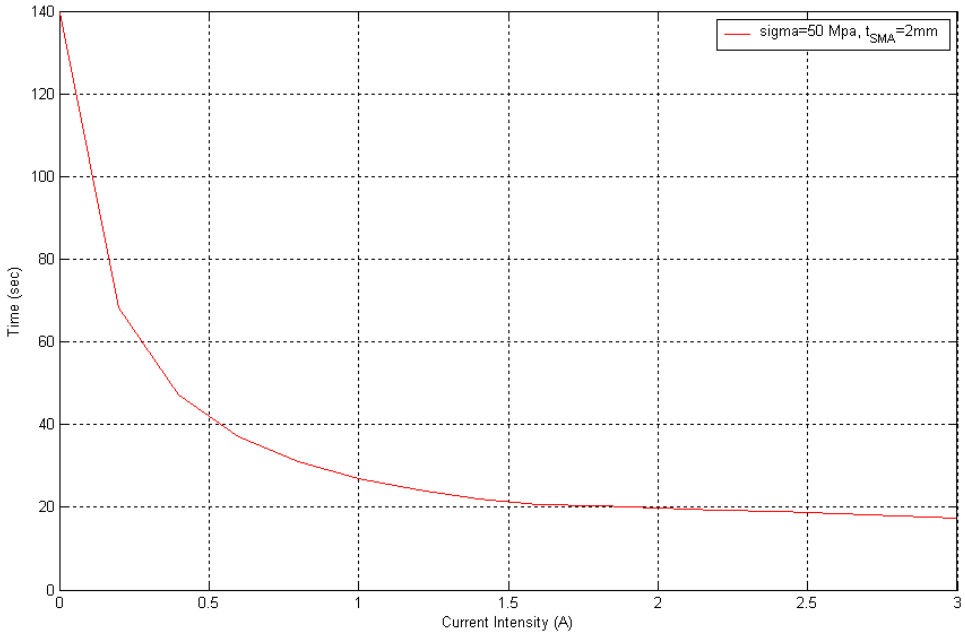

Figure 6.19: S.M.A. tape cooling time versus current supplied by Peltier cell. The current is supplied from 0 to 3 A. This analysis have been conducted for sigma = 50 MPa and a S.M.A. thickness of 2 mm obtaining intersection between M_f direct line with cooling curves by Peltier cell effect from FE investigation.

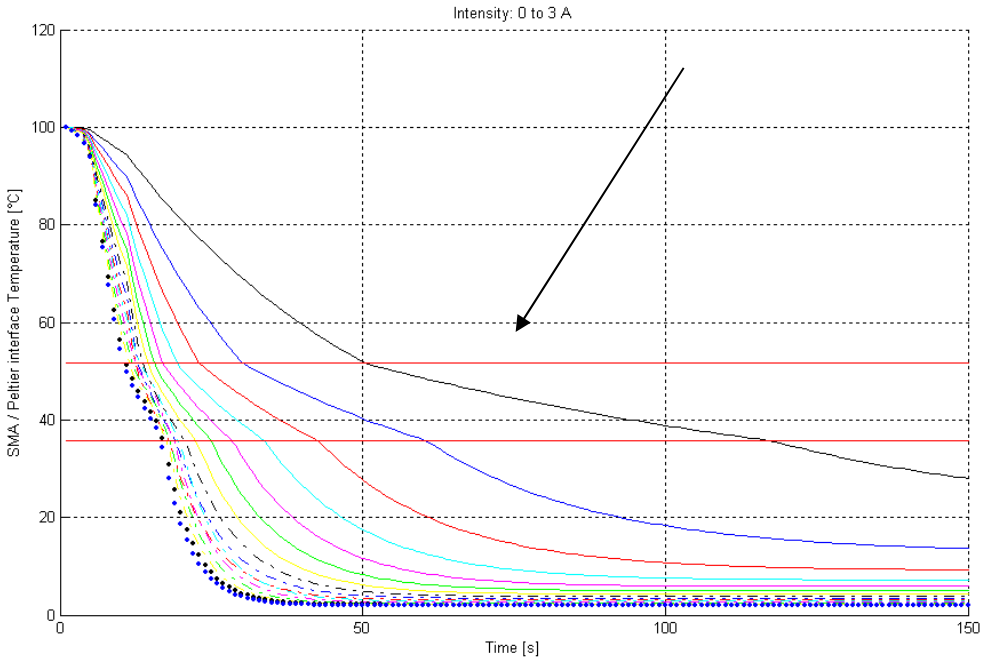

Figure 6.20: S.M.A. tape cooling time versus current supplied by Peltier cell. Arrow indicated the decreasing effect on the cooling time. With a current supply from 0 to 3 A. This analysis have been conducted for a S.M.A. thickness of 2 mm and sigma=100MPa.

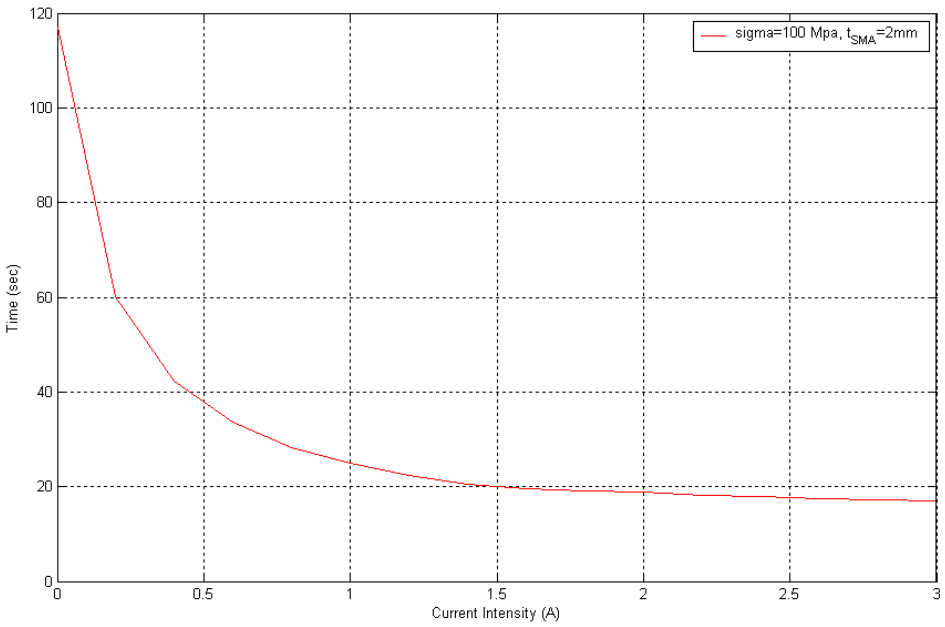

Figure 6.21: S.M.A. tape cooling time versus current supplied by Peltier cell. The current is supplied from 0 to 3 A. This analysis have been conducted for sigma = 100 MPa and a S.M.A. thickness of 2 mm obtaining intersection between M_f direct line with cooling curves by Peltier cell effect from FE investigation.

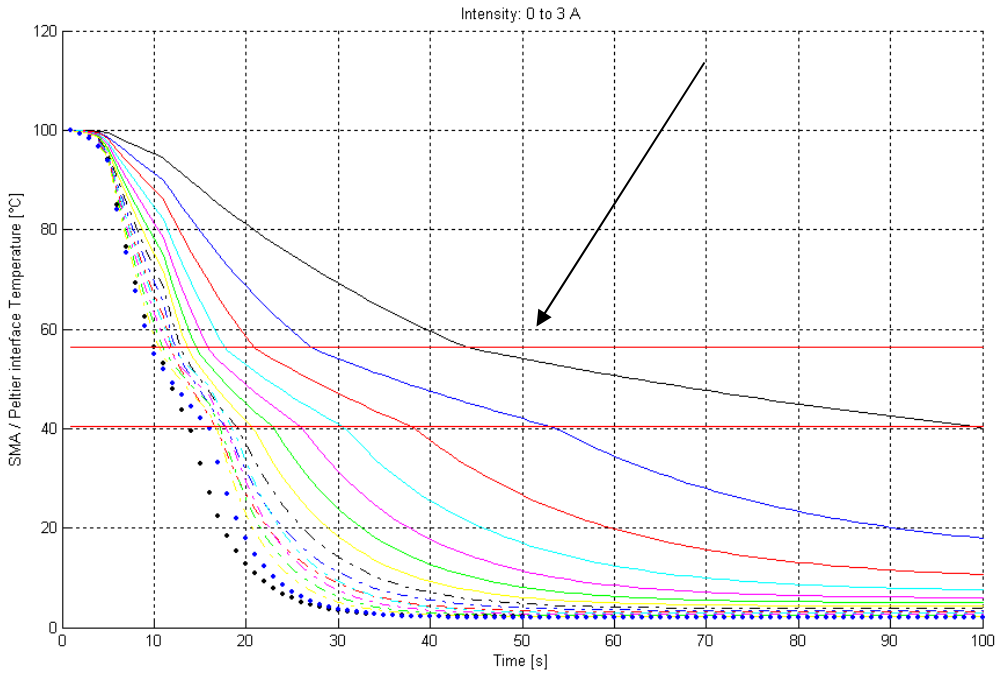

Figure 6.22: S.M.A. tape cooling time versus current supplied by Peltier cell. Arrow indicated the decreasing effect on the cooling time. With a current supply from 0 to 3 A. This analysis have been conducted for a S.M.A. thickness of 2 mm and sigma=150MPa.

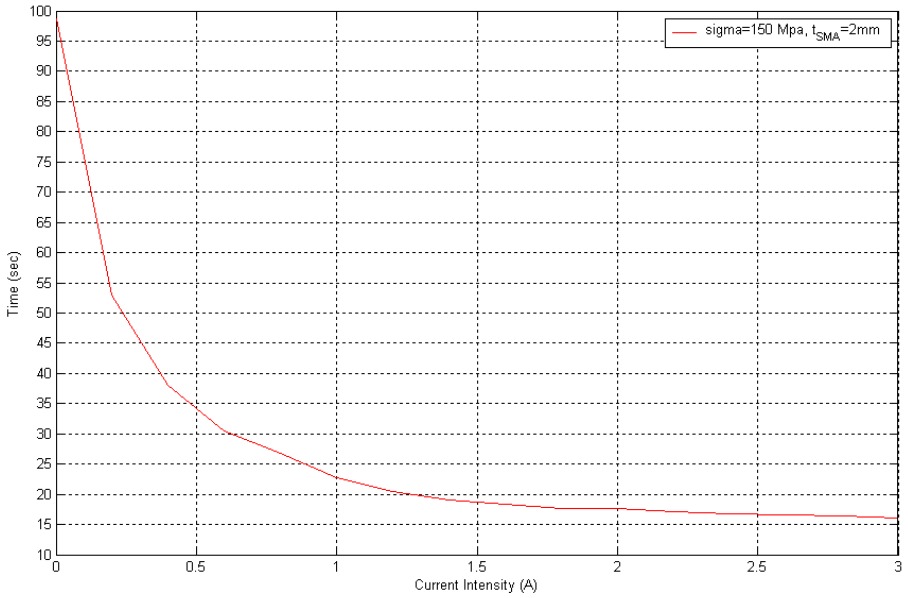

Figure 6.23: S.M.A. tape cooling time versus current supplied by Peltier cell. The current is supplied from 0 to 3 A. This analysis have been conducted for sigma = 150 MPa and a S.M.A. thickness of 2 mm obtaining intersection between M_f direct line with cooling curves by Peltier cell effect from FE investigation

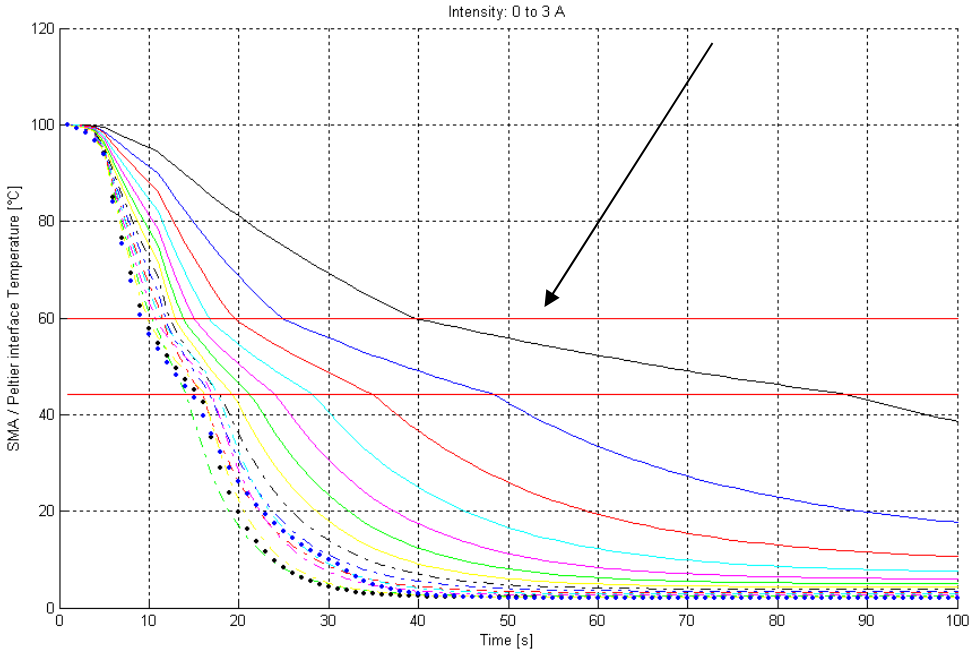

Figure 6.24: S.M.A. tape cooling time versus current supplied by Peltier cell. Arrow indicated the decreasing effect on the cooling time. With a current supply from 0 to 3 A. This analysis have been conducted for a S.M.A. thickness of 2 mm and sigma=200MPa.

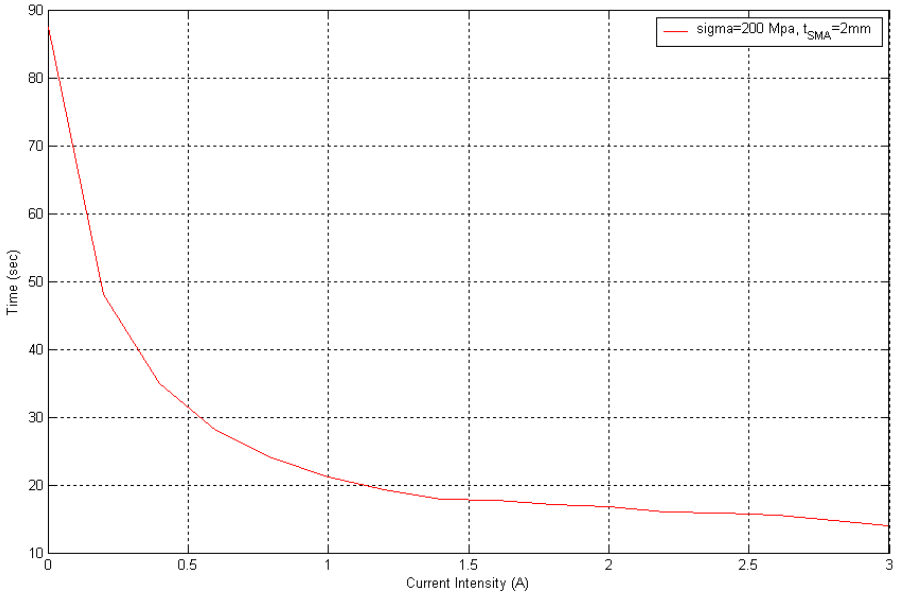

Figure 6.25: S.M.A. tape cooling time versus current supplied by Peltier cell. The current is supplied from 0 to 3 A. This analysis have been conducted for sigma = 200 MPa and a S.M.A. thickness of 2 mm obtaining intersection between M_f direct line with cooling curves by Peltier cell effect from FE investigation.

In this second numerical approach considering a S.M.A. thickness of 2mm it is evident a reduced cooling time but still in this simulation when a pre-load is considered as in the previous case with a thickness of 1 mm a faster cooling has been achieved (from figure 6.15 to 6.25).

This confirms the correct approach followed during the analysis because during a pre-loading S.M.A. tape show a tendency to recover easier the original shape impressed in this case martensite.

In addition, it is necessary to note that in a S.M.A. tape of 2 mm thick the initial temperature of investigation results to be lower than the one of 1mm thick because the inertial terms due to thermal effects are relevant.

6.8 Conclusions about S.M.A. cooling numerical model

In this section a FE model analysis has been presented in order to verify and assess the analytical approach and consideration inside the theoretical model developed.

In particular, the numerical approach has followed all the hypothesis already validated inside the analytical model and all contribution related to the cooling effect of the Peltier cell; this solution can be adopted as innovative cooling system for these materials.

In fact, at first a numerical investigation through a FE model where a natural convection between external air and S.M.A. tape has been presented in order to estimate the S.M.A. tape cooling time in free convection.

The simulation has confirmed a cooling time of 200 sec as already tested during a previous experimental phase conducted.

So, after this approach a new numerical investigation has been presented by a simulation of a cooling system composed of a Peltier cell under the S.M.A. tape to be cooled.

The FE model has reproduced all the contributions related to the phenomenology of a Peltier cell operation according to the analytical model description by using a transient heat transfer simulation (SOL 159).

The FE model has been generated aiming at a verification of the soundness of the solution adopted and in order to assess the cooling time reduction by a Peltier cell solution.

In this context a lot of simulation have been presented thanks to a tool in Matlab language able to provide numerical simulation step by step starting from Nastran analysis.

In this way the tool is able to load the input file and then to go on the thermal simulation through SOL159;

In addition the can provide all the results followed by the FE analysis by a visualization of cooling time versus input supply current provided by the Peltier cell.

The simulation has been conducted for different pre-load condition on the S.M:A. tape in order to assess the soundness of the model and to verify that with an applied load a cooling time reduction is observed.

This fact is related to the trend of material to easier recover the martensite status in presence of pre-load condition on it.

Finally a comparison of all results has been provided in order to assess the FE model and to have information for the experimental test to be conducted.

6.9 References

[1] ^http://www.openchannelfoundation.org/projects/NASTRAN

[2]http://www.nasa.gov/centers/dryden/news/XPress/stories/2008/10_08_technology.html "NASA Press Release 2008"

[3] ^ MacNeal, Richard H., page i., "The NASTRAN Theoretical Manual", December 1972.

[4] http://www.sti.nasa.gov/tto/spinoff2002/goddard.html "NASA Spinoff Magazine 2002"

[5] http://www.deskeng.com/articles/aaaxdw.htm "Review of Current Nastran Options"

[6] D. A. Anderson, J. C. Tannehill, and R. H. Pletcher, *Computational Fluid Mechanics and Heat Transfer*, Hemisphere, Washington, DC, 1984.

[7] F. J. Rizzo, "An Integral Equation Approach to Boundary Value Problems of Classical Elastostatics," *Q. Appl. Math.*, Vol. 25, 1967, pp. 83–95.

[8] F. J. Rizzo and D. J. Shippy, "An Advanced Boundary Integral Equation Method for Three-Dimensional Thermoelasticity," *Int. J. Appl. Mech.*, Vol. 11, 1977, pp. 1753–1790.

[9] C. Brebbia, J. C. F. Telles, and L. C. Wrobel, *Boundary Element Technique*, Springer-Verlag, Berlin, 1984.

[10] R. P. Banaugh and W. Goldsmith, "Diffraction of Steady Acoustic Waves by Surfaces of Arbitrary Shape," *J. Acoust. Soc. Am.*, Vol. 35, No. 10, 1963, pp. 1590.

[11] C. Liang and C. A. Rogers, 1990 *One- Dimensional Thermomechanical Constitutive Relations For Shape Memory Material*, Journal of Intelligent Material Systems and Structures,1 (2), 207-234.

[12] F. Kreith, *Principles of Heat Trasfer* 3rd edition , chap. 4, translated by G. Alfano and V. Naso, Dept. of Thermodynamics and Energy, University of Naples, Italy.

CHAPTER 7

S.M.A. COOLING ASSESSMENT : EXPERIMENTAL INVESTIGATION

7.1 Introduction

In the previous chapter S.M.A. cooling by a Peltier cell system through a FE approach has been developed. In order to evaluate and assess each result found by numerical investigation also an experimental phase has been illustrated in this work.

The experimental investigation has been conducted at the CIRA (Italian Aerospace Research Center) Smart Structures Laboratory.

After a description of experimental set-up two analysis have been conducted. The first one has involved a common material as aluminum showing a real advantage by using a Peltier cell as cooling system.

Aim of this work is develop a cooling system by Peltier cell for S.M.A. material and in this experimental phase mainly advantages have been confirmed by this innovative followed approach.

Finally, in order to estimate soundness of conducted numerical simulation a correlation between numerical and experimental results have been presented.

The comparison has shown a good correlation and the possibility to improve this system during future applications involving this approach within a flap deflection system for a regional aircraft

7.2 The set-up and systems

In order to start with the experimental phase, a previous set-up has been prepared.

All the instrumentation system involved during the test have been previously verified in order to have a clearer view of all characteristic parameters for the test.

At first, the instrumentation has been composed of a supply system, control system sensors (thermocouples) and of software able to import all results found by the test.

The specimen to be tested have been aluminum and S.M.A. respectively for each test, while a Peltier cell as heating and cooling system has been used.

The supply system is Delta Elektronika [1] and his features has been shown in the table below and in figure 7.1.

Device	Weight	Input voltage	Efficiency	High Programming speed	Input current
Delta Elektronika BV	3.1 Kg	92-265VAC, 48-62Hz	86% ayt 230VAC, 825 at 115VAC	0 to 30 V in 1ms	0 to 10 A

Table 7.1: Supply system features [1]

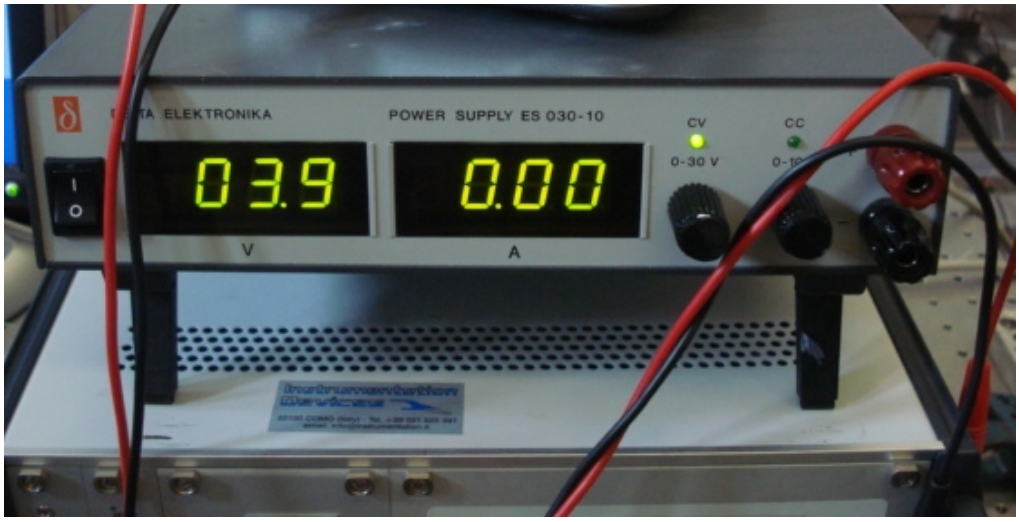

Figure 7.1: The supply system : Delta Elektronika.

This system has been used during the test for the intensity current supply during the heating and cooling phase.

A defined input range has been defined from 0 to 1 A in order to avoid difficult related to an heat increase during the test.

In particular because of a Peltier cell has been used for heating and cooling system particular attention has been focused on this aspect in order to have no problem for the cell operability.

According to Peltier double function in heating and cooling, this system have been set-up to work as a polarity inverters of the input voltage (CC).

Depending on each use it has been possible, during the test, to switch on for invert heating and cooling function for the cell.

The acquisition system involved for the test (figure 7.2) CRONOS PL8 [2] has the aim of producing an elaboration of data information derived from the input and heating-cooling

phase definition.

Figure 7.2: The acquisition data system :Cronos PL8 [2]

In the table 7.2 relevant technical information have been provided.

Device	Bit/sec	Data carrier	Max aggregate sampling rate	Modular system
CRONOS PL 8	100MB/sec	2GB	400Hz	Two active LEDs at Ethernet terminal

Table 7.2: Acquisition data system features [2]

After this description in order to have enough information about the temperature history of the test case involved, four thermocouples have been set.

As illustrated in the figure 7.3 the thermocouples, aiming at recordering the temperature of the system, have been positioned in different areas on the specimen (aluminum or S.M.A) to be tested for this experiment.

The four K thermocouples (T) have been located as follows:

- T1 at the external temperature as reference measure sensor
- T2 at the interface between material and Peltier cell
- T3 at the upper face of material (Aluminum or S.M.A.)
- T4 at the lower Peltier cell face

This configuration has allowed a typical heat measure on the test specimen with a good precision level according to previous investigations [4].

This technique allows to measure the temperature variation for each place of interest.

In addition in order to cool the hot side of the Peltier cell a small fan has been used, able to reduce temperature on the lower face of the cell during the material cooling phase

process as illustrated in figure 7.4.

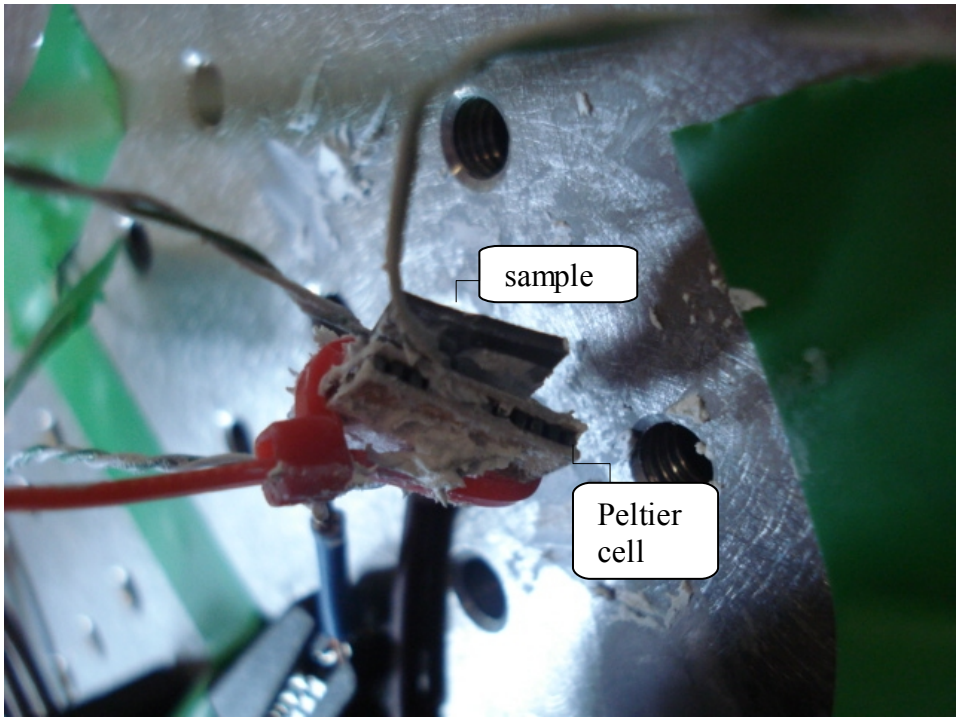

Figure 7.3: The set up: Peltier cell specimen and thermocouples.

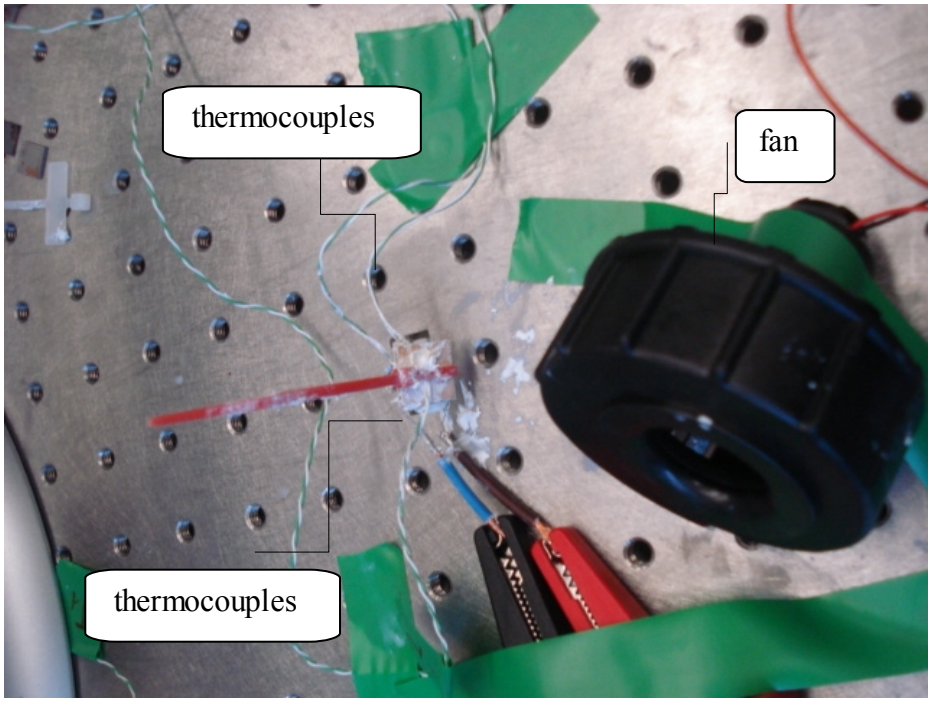

Figure 7.4: The set up: Peltier cell specimen, thermocouples and fan (in black).

In the following a Peltier cell description [3] shall be provided in order to define the rule and the operability during the test phase.

In this test the Peltier cell has been used for the experimental set-up for the two samples. The dimension of the cell and her properties are presented in table 7.3.

Producer	Marlow
Model	MI1023T-01
Max Voltage	8.0 V
Max Current	1.8 A
ΔT max	64°C to 27°C
Heat flow surface	13.16 x 13.16 mm^2
Qmax	9.2 W
Thickness	4 mm

Table 7.3: Peltier cell features [3]

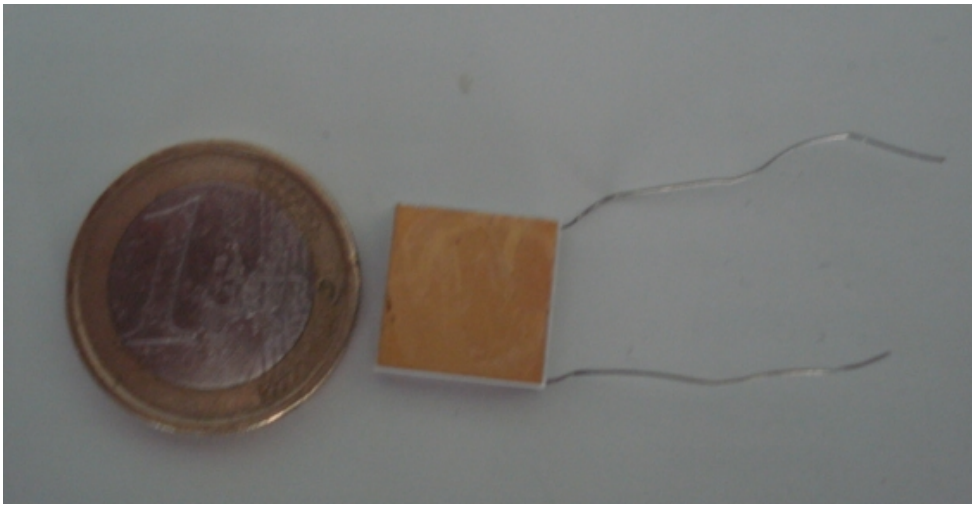

Figure 7.5: The Peltier cell with respect to a 1 euro money size.

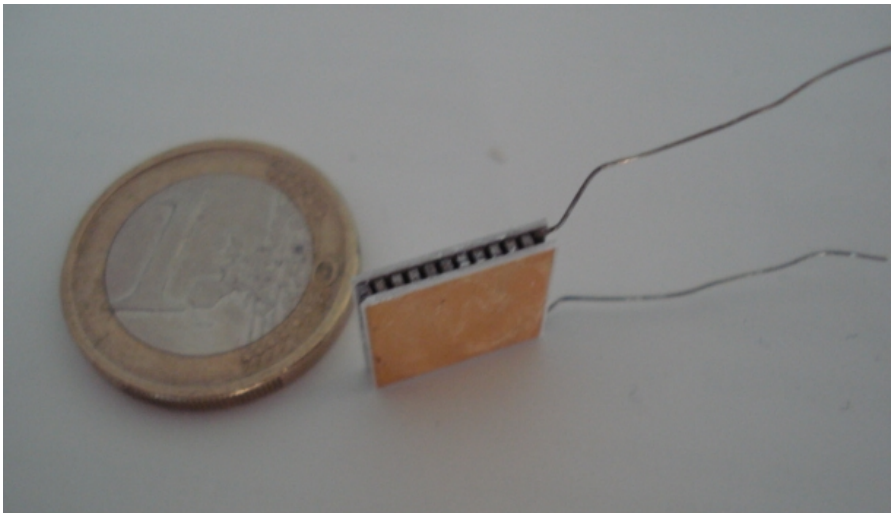

Figure 7.6: The Peltier cell with respect to a 1 euro money (thickness).

The software used for the acquisition and following elaboration of data provided by the test has been FAMOS. This software is able to reproduce real time the temperature trend derived by the thermocouples located at appropriate places for the measurements as shown in figure 7.7. After that, the software is also able to provide a plot of the curves involved during the process and it is able to give a tabular data to be imported inside a more common tool as Microsoft Excel as has been done in this context.

So that, all relevant plots have been found to evaluate the temperature profile of the system under investigation.

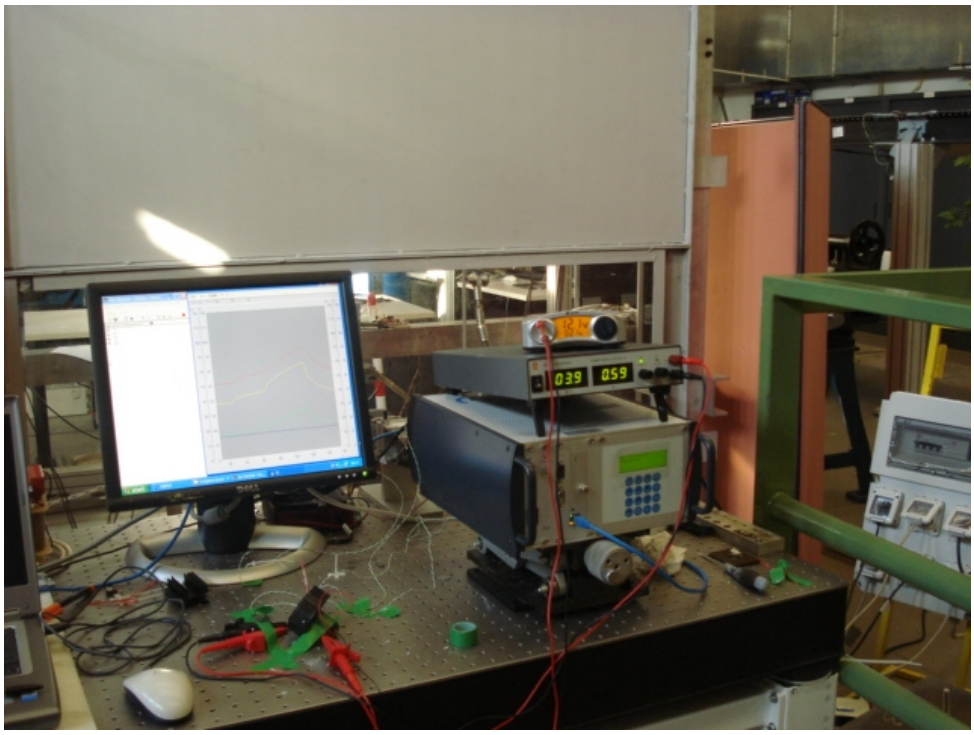

Figure 7.7: The software FAMOS used for import data analysis

7.3 Experimental tests by using Peltier cell on aluminum

In this section a description of all activities developed during the experimental tests shall be presented.

Aim of this work as stated before is to show a comparison between numerical and experimental results about the new cooling system adopted for S.M.A. material by using a Peltier cell. All the experimental tests have been conducted in order to assess and validate the prediction about the soundness of this innovative cooling system for non conventional material as S.M.A.

At first, before starting with the test on S.M.A. material, a previous analysis on aluminum

material has been conducted aiming at finding some information about material behavior and system applicability.

For our purpose a little specimen in aluminum material has been bonded to the Peltier cell by a thermal paste.

The aluminum sample has a thickness of 1mm thick and the Peltier cell is 4 mm thick.

The thermocouples have been set in relevant places allowing to have sufficient information about the thermal state of the system as previously defined.

For our purpose to study and evaluate the efficacy and efficiency of this innovative cooling system using a Peltier cell, the main problem has been relative to the difficult of reaching the temperature for the activation of the alloy (about 100-130°C) as required by the transition phase.

Generally the sample heating phase is obtained by using a separated heat source able to provide adequate energy for the sample heating; this process is often achieved by means of Joule effect with a resistive system able to heat the materials and induce the transformation.

During this experimental analysis instead of traditional heating approach, the same Peltier cell has been used for heating and cooling phase, providing a consistent energy reduction and also deleting additional system to be involved.

This approach has been followed because during the test only by switching on the polarization of the supply system has been possible to invert the heat flow for heating or cooling needs. So that, during the heating phase the upper face of the cell was hot, so transferring heat to the sample material to be heated and then, vice versa, during the cooling phase by inverting the current flow inside the cell the upper cell face has cooled the sample lower face determining a cooling effect on it.

In this way the lower face of the cell has to be cooled because all heat has to be subtracted in order to avoid the cooling process stop on the sample and the consequent cell break. In this experimental test a little fan has been used for heat subtraction with a very low energy consumption and supplied by a voltage of 12V.

Before starting with the acquisition data, some cycles able to test the instrumentation involved have been done.

After that with a test case composed of aluminum, Peltier cell, thermocouples, supply system and acquisition system the experimental phase has been started.

At first, heating and cooling cycles for aluminum have been done as presented in figure

7.8, 7.9, 7.10, 7.11, 7.12.

In order to define the aluminum behaviour under these conditions with a Peltier cell bonded under the material and all systems ready the experimental test has started.

Two tests have been conducted on this set-up.

As stated before heating and cooling have been provided by the same Peltier cell but during the first test a current intensity of 0.5 A only for the heating phase has been provided while in the cooling phase the current supply for the cell has been 0 A as in figure 7.8.

The four T1, T2, T3 and T4 are the thermocouples involved during the test as sensors for the temperature profile on specific part of the samples as already specified in previous paragraph.

Aim of this work is related to the investigation of the cooling time advantage by using a Peltier cell bonded under a material like aluminum as in this case; in the plot the trend of the cooling curve is presented and it demonstrates that within a time of 50 sec equilibrium conditions (at a temperature of room of 20°C) are reached.

The total duration of the process has been of 500 sec with an sample acquisition rate of 500 ms; this setting for all tests has been considered.

In order to clarify these results in figure 7.9 also the derivative function of T2 has been calculated aiming at defining the cooling rate of the process without the Peltier cell aid.

In the second investigation on an aluminum sample too, during the cooling phase a current intensity of 0.5 A supplied by the Peltier cell has been provided.

In this second experiment, as shown in figure 7.10, the cooling time of the aluminum is faster than the previous one time (about 30 sec) and in particular it is evident that the T2 curve (at the interface position between the Peltier cell and aluminum sample) reaches a lower temperature (about 18°C).

This is very important because as in the previous experiment at a current intensity of 0 A only the equilibrium condition has been reached at the room temperature 20°C in this new test aluminum temperature is at 18°C and this is relevant in a cooling time reduction point of view.

This relevant result is also confirmed by the 7.11 figure where the T2 derivative is presented showing that the cooling rate at a 0.5 A current is well defined because the lower value is more evident than the previous one.

In figure 7.12 a comparison between the two T2 derivative curves at 0A (blue curve) and

at 0.5 A current intensity (red curve) are shown.

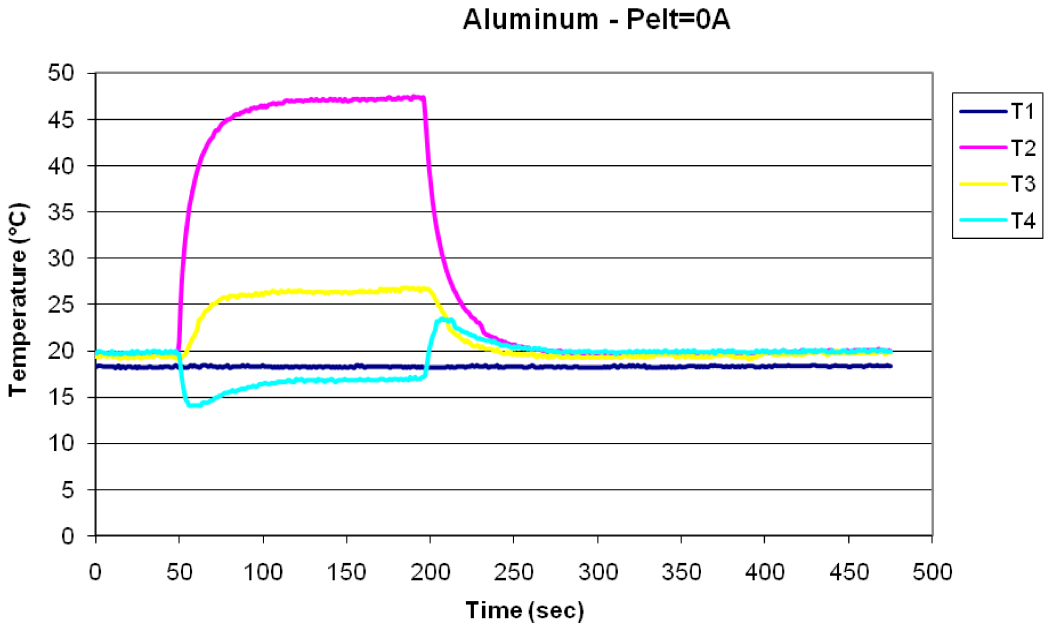

Figure 7.8: The aluminum heating and cooling curves at a Peltier cooling supply of 0A with the four thermocouples involved in the test.

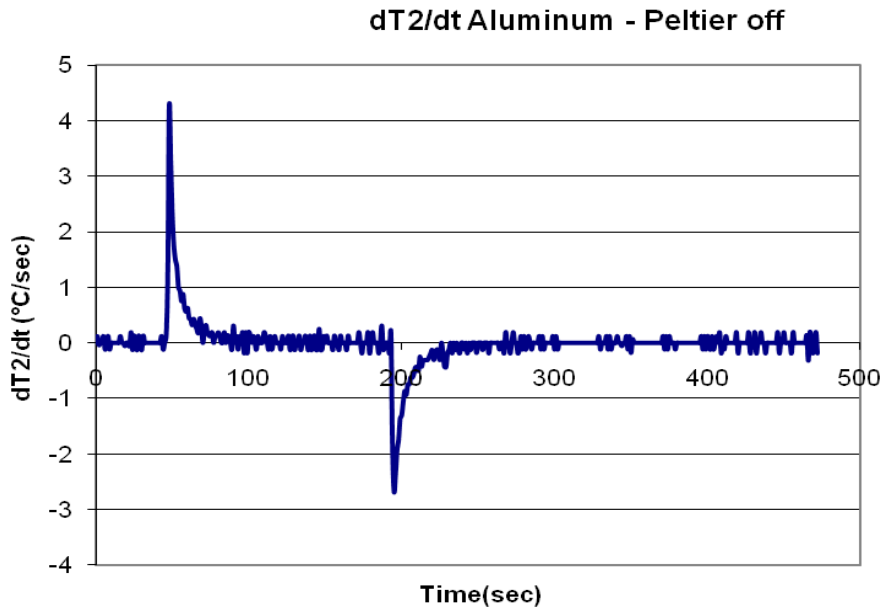

Figure 7.9: The aluminum T2derivative curve at a Peltier cooling supply of 0A.

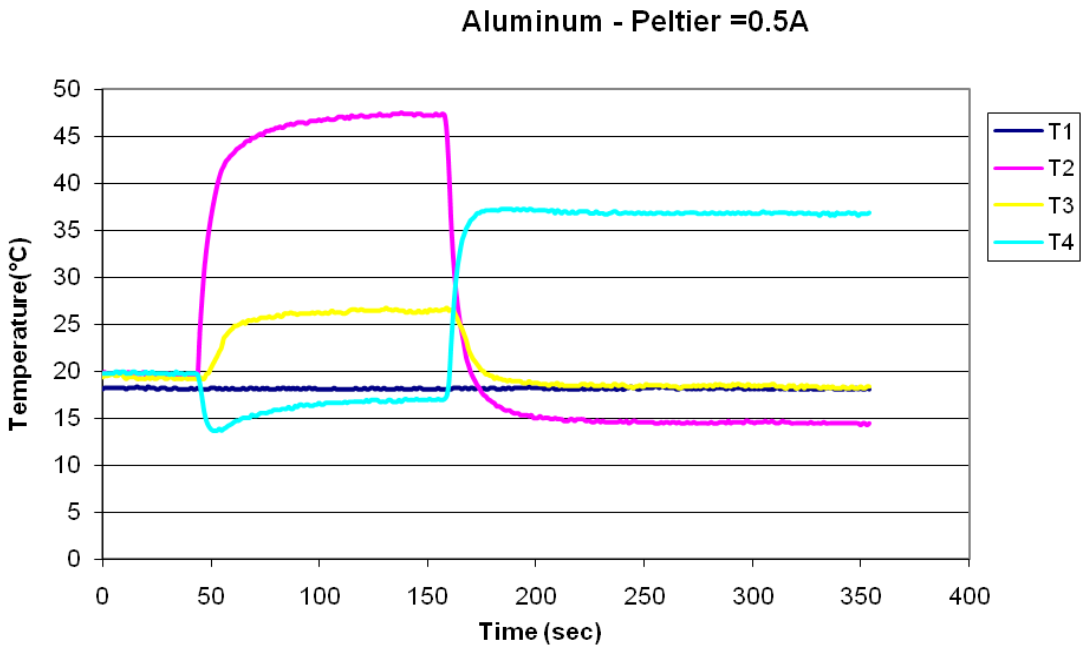

Figure 7.10: The aluminum heating and cooling curves at a Peltier cooling supply of 0.5 A with the four thermocouples involved in the test.

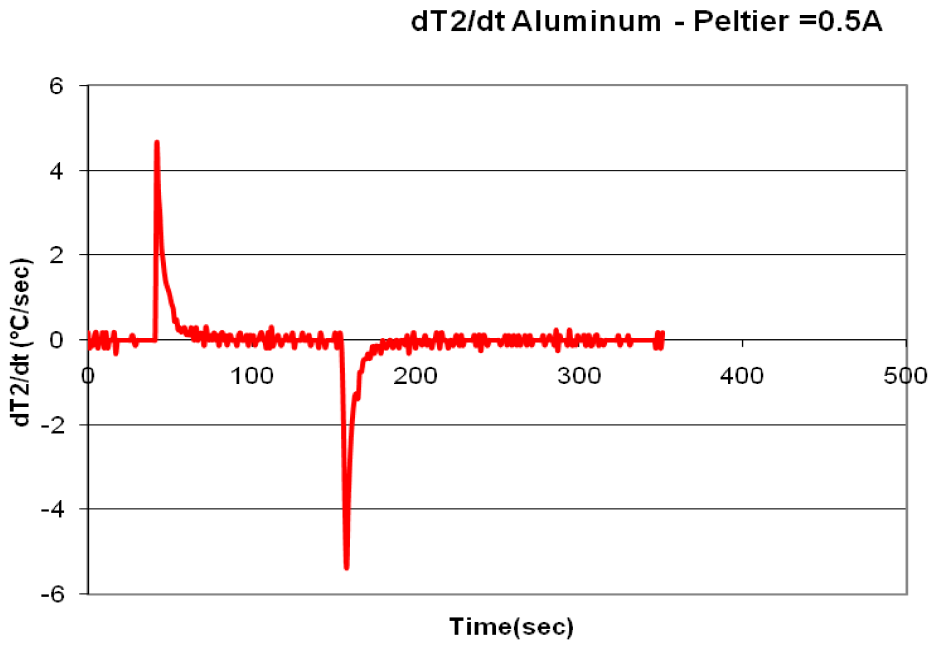

Figure 7.11: The aluminum T2derivative curve at a Peltier cooling supply of 0.5 A.

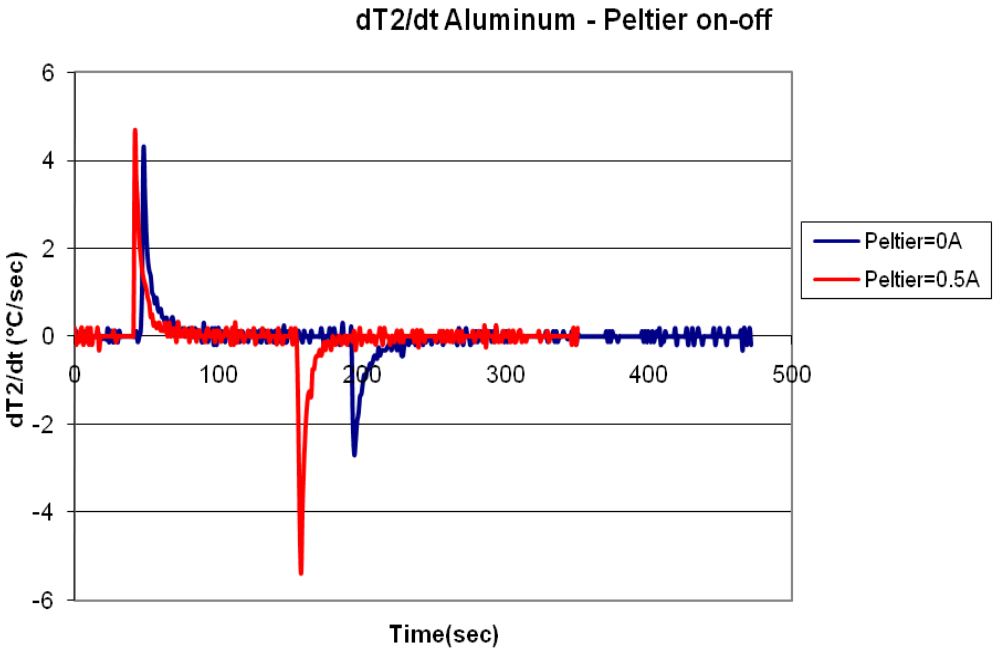

Figure 7.12: The aluminum T2derivative curves at a Peltier cooling supply of 0A and 0.5 A.

7.4 Experimental tests by using Peltier cell on S.M.A.

In this paragraph experimental tests on S.M.A. material sample have been presented.

In fact, as already done for the aluminum sample also in this test the same set-up composed of thermocouples, supply system, acquisition system and Peltier cell for heating and cooling function has been considered.

In this case an additional consideration have to be done because while for a conventional material as aluminum there is no phase change during heating and cooling process, for S.M.A. we have a phase change that is shown as a curve variation in the plot.

The S.M.A. thickness is 1 mm and the Peltier cell has a thickness of 4 mm as in the previous case.

The trend is the same used for the aluminum. In fact two test have been conducted in order to study the different behavior of the S.M.A. and to compare also these new results with the previous ones obtained for aluminum.

The test duration has been 800 sec in order to have a complete development of the phenomenon and the sample acquisition rate has been of 500 ms.

In figure 7.13 a view of the set-up for the S.M.A. sample is shown while in figure 7.14 and 7.15 the S.M.A. thickness is presented in comparison with a 1 euro money size.

As already done during the test with aluminum sample also for the S.M.A. sample two

tests have been conducted.

The first one has involved the Peltier cell only during the heating phase while during the cooling phase a current supply of 0 A has been provided.

The experiment on the S.M.A. has confirmed the trend already studied for aluminum test. In fact, in this case at 0 A in cooling phase the T2 temperature curve reaches the equilibrium condition at a temperature of 20°C in a total time of 150 sec (figure 7.16).

As in the previous case also T2 derivative calculation has been presented in figure 7.17 showing the rate of the process involved without Peltier cell cooling aid.

In the second experiment Peltier cell as cooling system at a current intensity of 0.5 A has been used showing the same behavior in terms of cooling time reduction already studied with aluminum material.

This confirms that the approach followed is correct. In fact a cooling time reduction has been presented (about 90 sec) and, in addition, in this second test the system composed of Peltier cell and S.M.A. reaches a temperature of 18°C under the equilibrium condition (20°C).

This results has confirmed that, when the Peltier cell is used as cooling system at a current intensity of 0.5 A (figure 7.18), the system is at a lower temperature with respect to the equilibrium one as it has been pointed out during the aluminum investigation.

This is confirmed also in figure 7.19 with the T2 derivative calculation.

Finally, aiming at defining the cooling rate advantage, a comparison between the two T2 derivative at 0 A and 0.5A is presented in figure 7.20, focusing attention on the evident descent rate during the cooling phase when Peltier cell is activated.

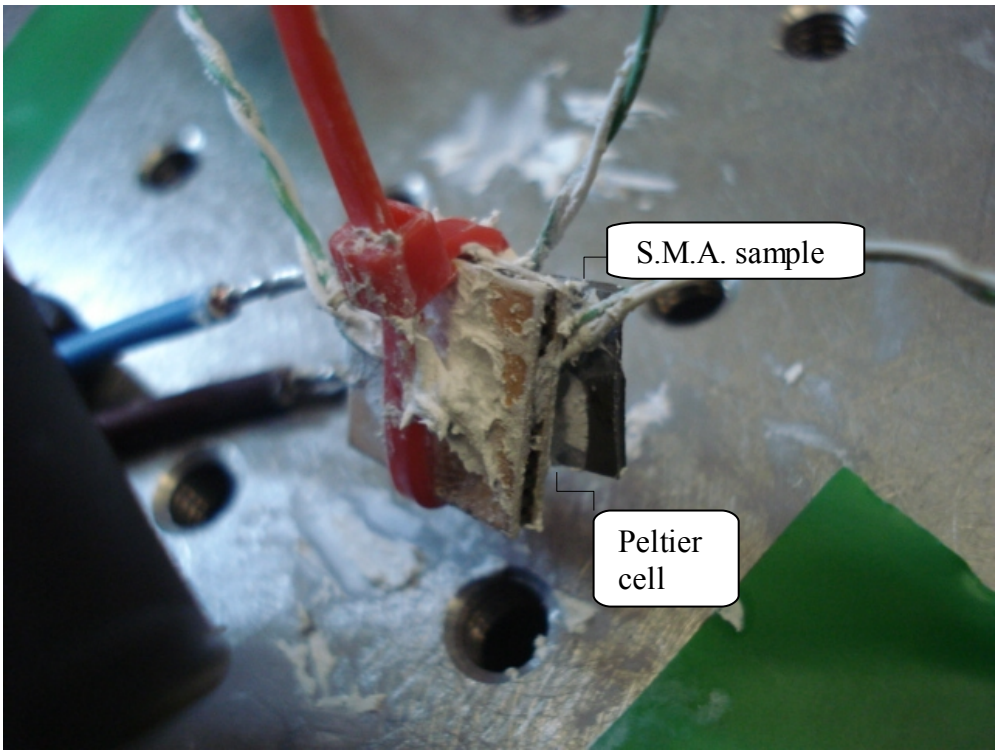

Figure 7.13: The set-up with S.M.A. material.

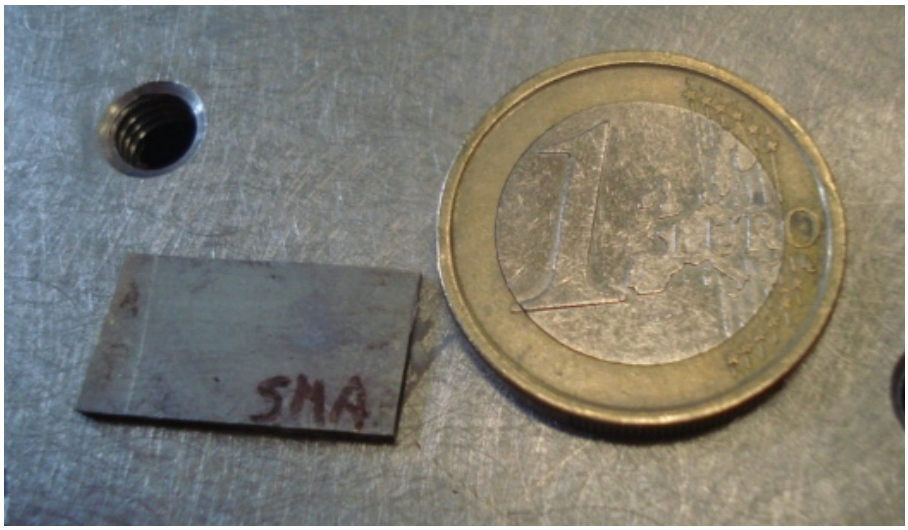

Figure 7.14: The S.M.A. sample with respect to a 1 euro money size.

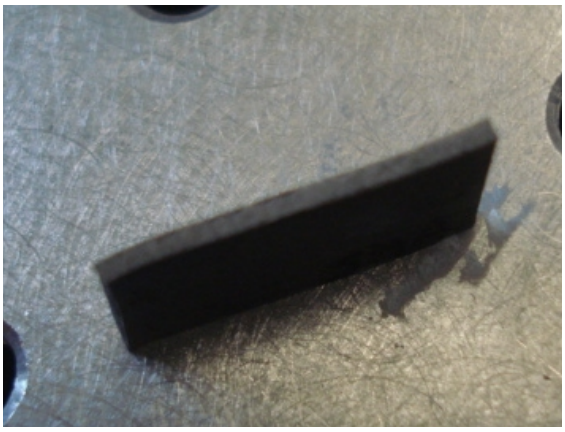

Figure 7.15: The S.M.A. thickness (1 mm).

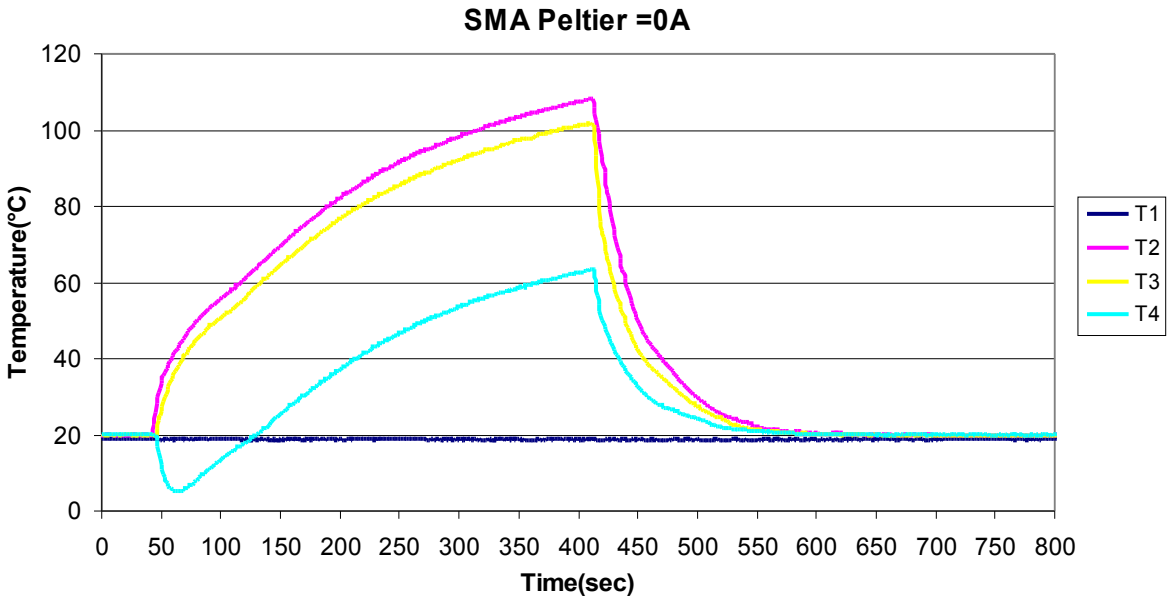

Figure 7.16: The S.M.A. heating and cooling curves at a Peltier cooling supply of 0A with the four thermocouples involved in the test.

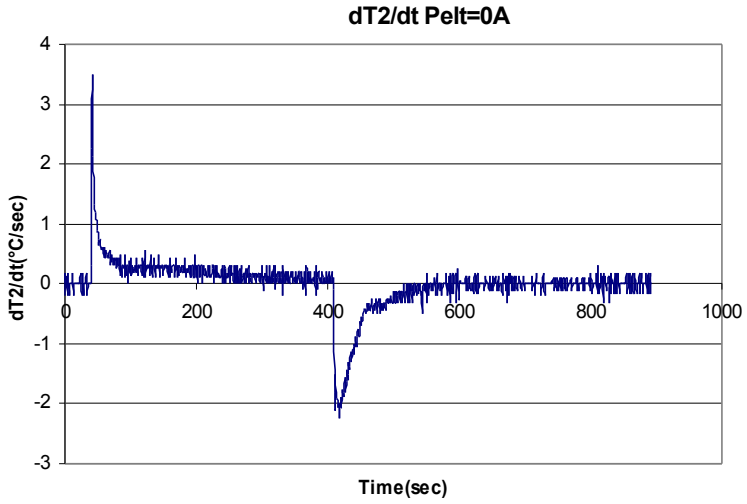

Figure 7.17: The S.M.A. T2 derivative curve at a Peltier cooling supply of 0A.

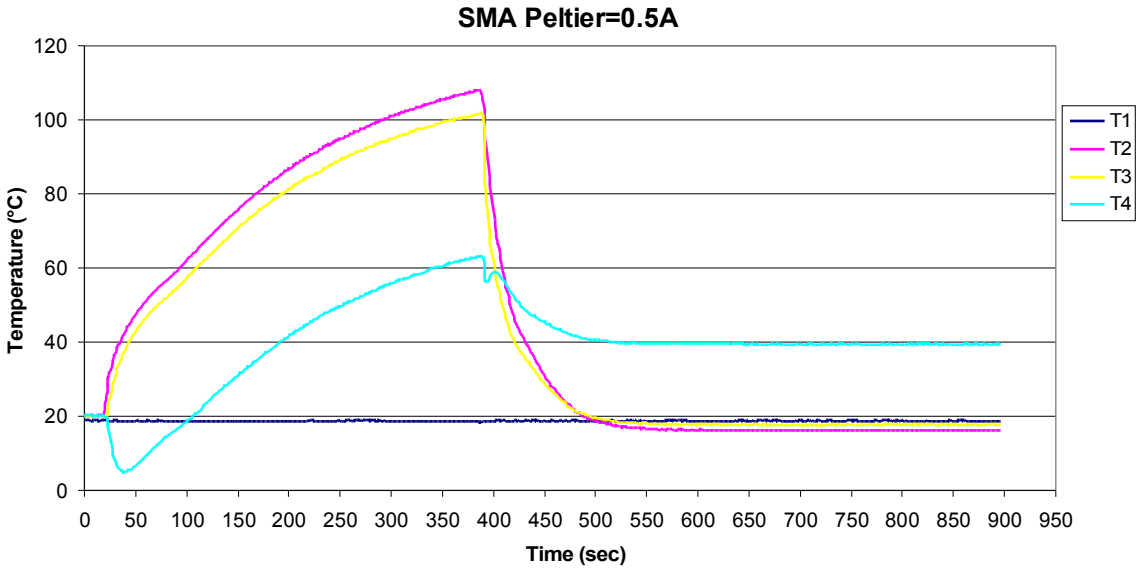

Figure 7.18: The S.M.A. heating and cooling curves at a Peltier cooling supply of 0.5 A with the four thermocouples involved in the test.

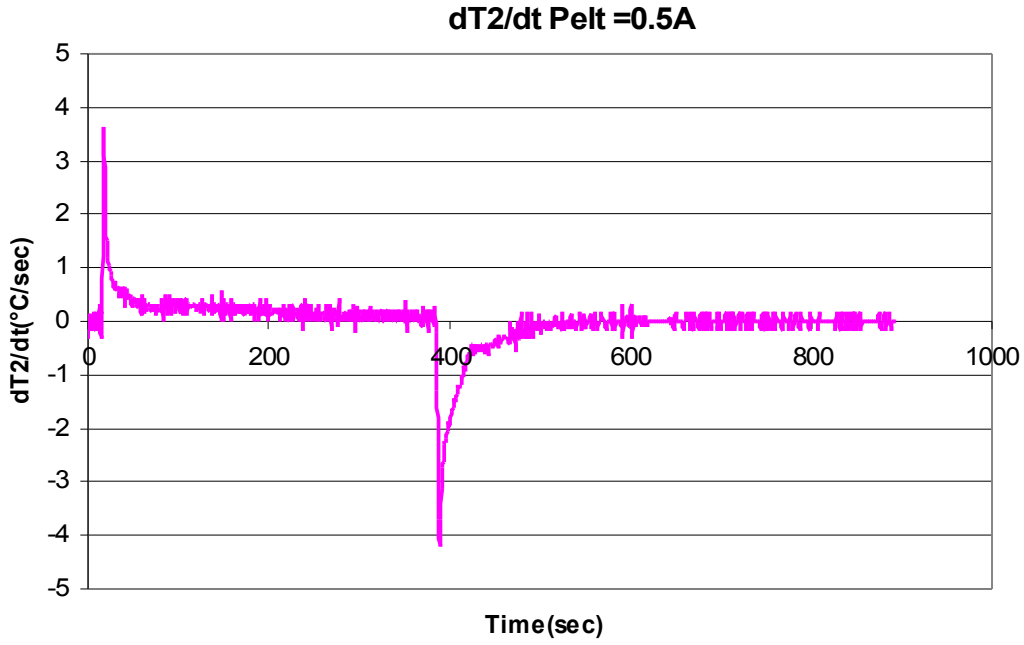

Figure 7.19: The S.M.A. T2 derivative curve at a Peltier cooling supply of 0.5A.

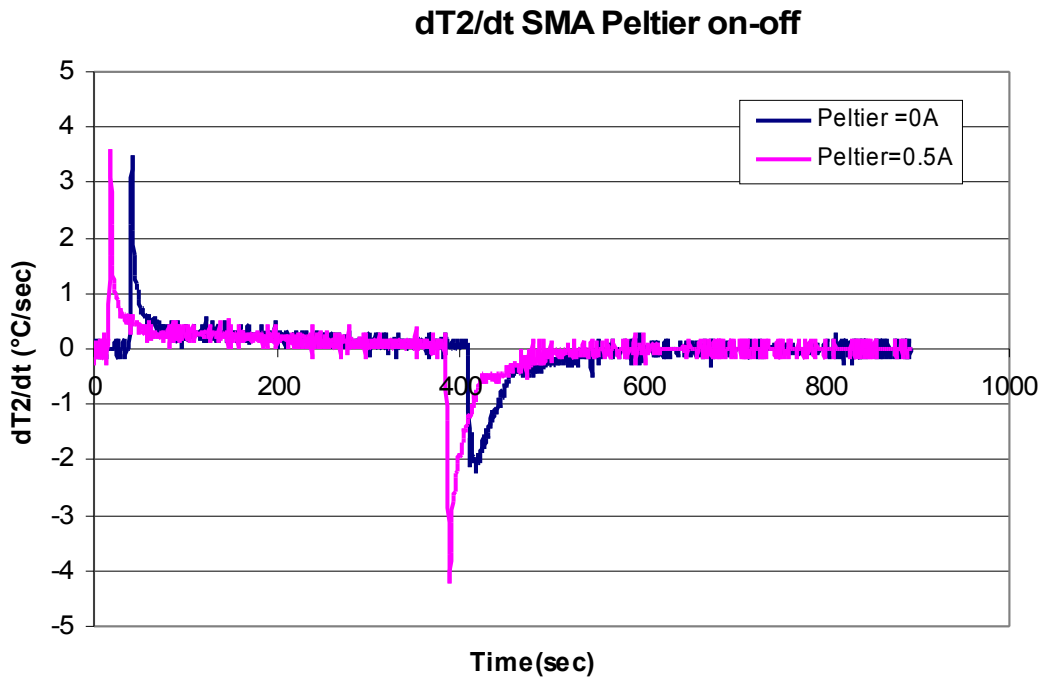

Figure 7.20: The S.M.A. T2 derivative curves at a Peltier cooling supply of 0A and 0.5 A.

7.5 S.M.A. system : numerical and experimental comparison

As final result also a comparison between numerical and experimental results have been presented in order to asses and validate the FE model already described in the chapter 6.

In the following plots only the curve related to the cooling time have been presented and have been compared.

As already done for the experimental test two comparison are here. The first one (figure 7.21 and 7.22) is at a current supply during the cooling phase of 0 A for the Peltier cell; while the second one (figure 7.23 and 7.24) is related to a Peltier cell current supply during the cooling phase of 0.5 A.

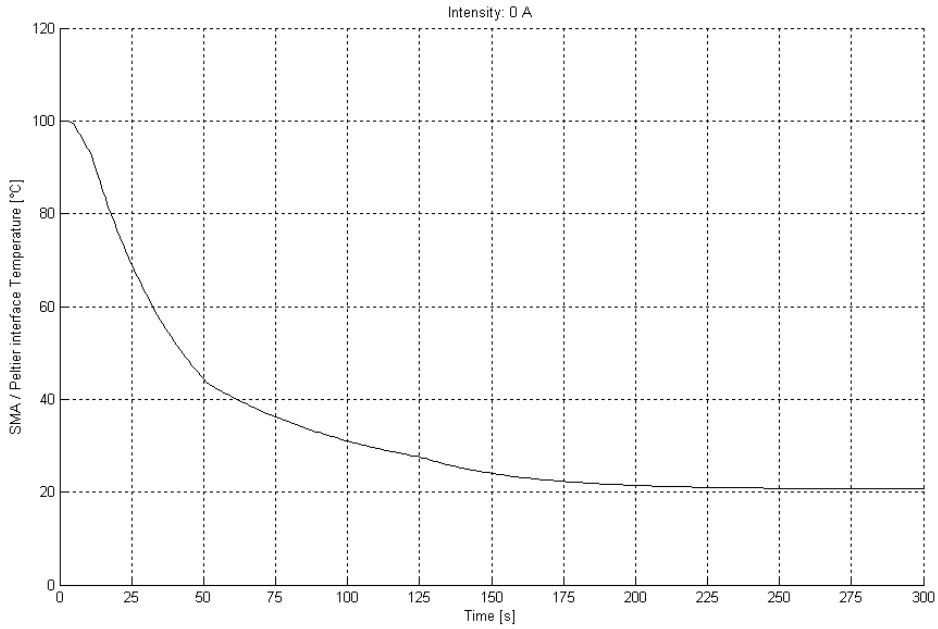

Figure 7.21: S.M.A. numerical curve at a Peltier cooling supply of 0A.

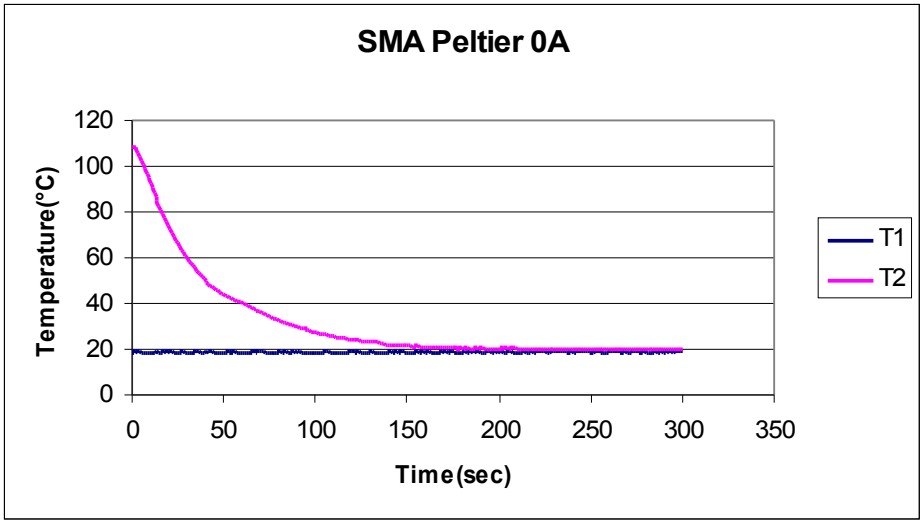

Figure 7.22: S.M.A. experimental curves at a Peltier cooling supply of 0A (blue curve is the reference temperature, red curve is the interface temperature).

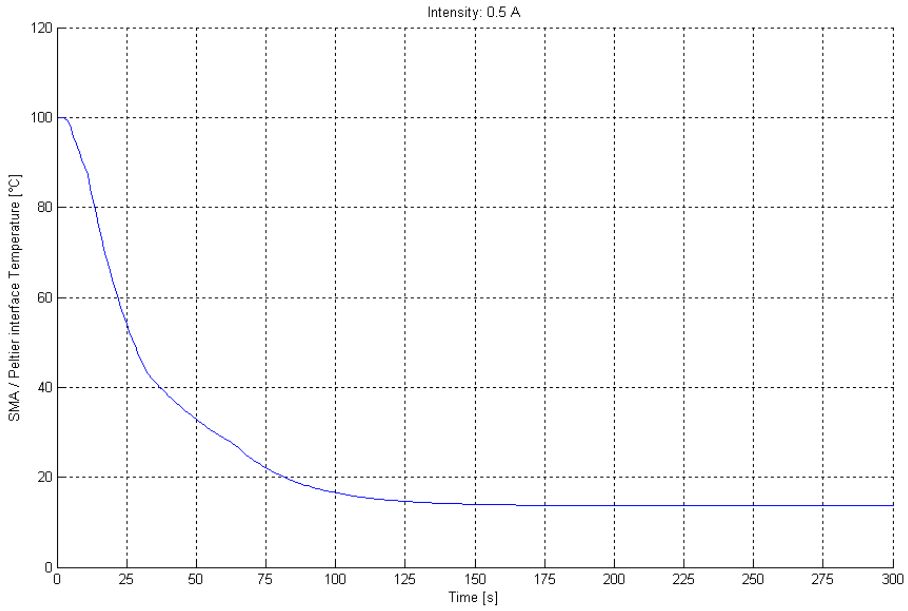

Figure 7.23: S.M.A. numerical curve at a Peltier cooling supply of 0.5 A.

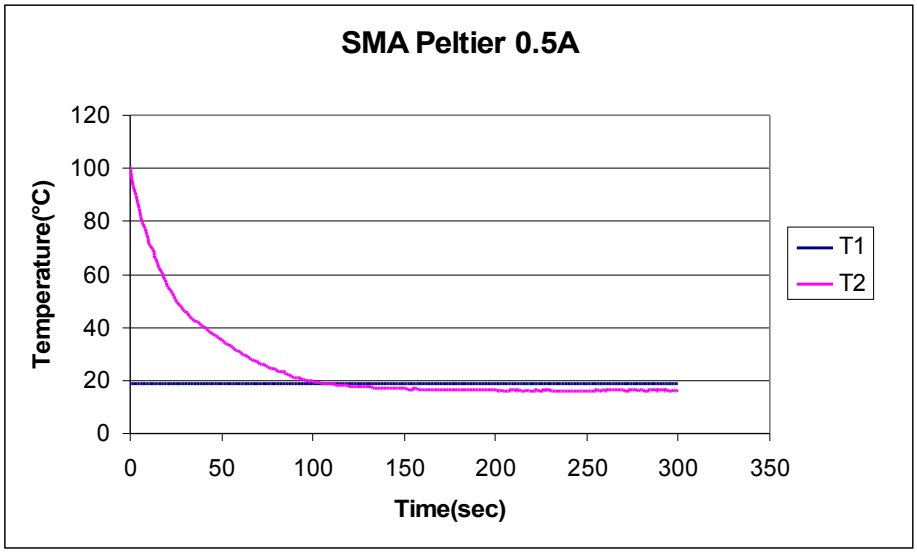

Figure 7.24: S.M.A. experimental curve at a Peltier cooling supply of 0.5 A (blue curve is the reference temperature, red curve is the interface temperature).

By these plots for numerical and experimental results for a current supply during the cooling phase of 0A and 0.5 A it is possible to underline that there is a complete overlapping for the curves found.

In fact, for a current supply of 0 A in cooling phase the total cooling time for reaching the equilibrium condition at 20°C is about 200 sec. (figure 7.21, 7.22) for numerical and

experimental results.

While during the cooling with a current supply of 0.5 A for the Peltier cell it is evident that there is a total cooling time reduction (about 90 sec.) evident in numerical and experimental results.

In addition as already stated when the cooling happens with a current supply of 0.5 A by using the Peltier cell cooling effect there is a lower temperature reached with respect to the equilibrium condition of 20 °C and this is again a relevant result in terms of cooling system advantage.

7.6 Conclusions about numerical and experimental investigation

In this chapter experimental investigations have been presented. The experiments have been conducted at the CIRA Smart Structures Laboratory in order to evaluate the effective advantage by using a Peltier cell as cooling system in a S.M.A. material.

At first, before starting with the experiments a previous set-up has been done, the supply and acquisition system, thermocouples and little fan have been described and also the Peltier cell features have been illustrated aiming at defining performance of all instrumentations involved.

In this context in order to have a clearer view of the soundness of the results obtained a previous analysis on a conventional material as aluminum has been presented.

In fact, initial investigations on aluminum sample have been conducted using the Peltier cell, during heating and cooling phase, with a relevant consumption reduction in terms of energy and systems involved for the test.

In fact, generally heating is achieved by means of Joule effect with a resistive system but with additional system and occupation.

For aluminum it is possible to note that when Peltier cell is used for cooling at a current supply of 0.5 A there is a real advantage in terms of time reduction with respect to the natural convection. In addition, in this case the temperature reached is also lower than the reference room temperature (20°C) and this confirms the soundness of the system designed. The same phenomenology has been verified also during the experimental test on S.M.A. material. In fact, even if for S.M.A. materials a transformation phase occurs during the Peltier cell cooling effect, at a current supply of 0.5 A, a total cooling time reduction has been observed and also the temperature reached has been lower than the equilibrium condition (20°C) as already noted for the aluminum sample.

This confirms that the phenomenology is comparable in these two different cases and it is also an evidence of the soundness of the designed configuration.

Finally, a numerical and experimental results comparison has been presented in order to assess and validate the methodology adopted during the FE approach confirming that there is a good relationship between numerical and experimental tests. As future development a dedicated cooling system for heat subtraction under the hot side of the Peltier cell has to be studied and used (f.i. a fluid circulation) but this is not object of the present work.

7.7 References

[1] web site:www.DeltaPowerSupplies.com

[2] web site: www.imcdataworks.com

[3] web site: www.marlowindustries.inc

[4] Ameduri S., Mennella F."Evaluation of actuating systems of morphing through increment of temperature: Peltier based and Joule based", 2005.

8.1 Conclusions and future developments

In this PhD thesis work an innovative cooling system for S.M.A. materials has been studied by using Peltier cell. In this context, in order to have a complete view of the solution to be adopted a previous investigation on phenomenological and physical problem has been dealt with.

In this work, after a preventive summary on activities (chapter 1) to be developed and an overview of the future implementation on next aircraft, a general description of S.M.A features has been shown (chapter 2).

Main characteristics of these innovative materials have been provided with particular reference to the SME effect and superelastic effect here deeply defined.

In this context in chapter 3 a panoramic view of wing morphing state of the art has been presented with reference to previous international project aiming at developing new solutions for adaptive wing approach in order to improve aircraft performances.

After that, also applications in different fields have been presented as space, mechanical, civil or surgery fields confirming a wider S.M.A. materials involvement apart from aeronautical field.

In the following of this work inside chapter 4 a Peltier cell description and operability has been presented showing advantages and disadvantages by using this system.

The main idea related to the application of a Pelier cell as system aiming at cooling down a S.M.A. tape has been assessed through an accurate physical investigation considering the problem and solving the differential equation applied to represent the system S.M.A.- Peltier cell (chapter 5).

Thermodynamical equation adaptation has been preferred in order to model the phenomenon and the interaction between S.M.A. and Peltier cell giving a qualitative result based on real convenience by using this cooling system.

According to the phenomenology described and after the analytic problem solution, a numerical investigation through a F.E.M. approach (chapter 6) has been developed modelling the system S.M.A.-Peltier cell and finding relevant results in terms of cooling time reduction.

A Matlab tool has been created able to extract the FEM results calculated by from Nastran code solver and then this tool is also able to provide a parametrization of results according to the intensity current supplied by the cell.

The tool developed has allowed a faster visualization of all results deriving from FE analysis In order to assess and correlate numerical results also an experimental investigation, inside chapter 7, has been carried out. The test phase has been conducted at the CIRA Smart Structure Laboratory as already defined in the previous chapter.

In this experimental phase, an heating-cooling investigation by using a Peltier cell on aluminium and S.M.A. materials has been conducted.

The innovation has been the use of the Peltier cell as heater and cooler system without additional system to heat the metal commonly used.

After the investigation on aluminium materials the same experiment has been conducted on S.M.A. material aim of this work confirming the main trend of heating and cooling behaviour showing a consistent improvement during heating and cooling phases when Peltier cell has been activated.

The experimental results, here presented, have confirmed numerical predictions before developed determining an energy consumption reduction because, by using the Peltier cell as heating and cooling system, no additional heating system (f.i. resistive system by Joule effect) have been involved during the test cutting down an additional external energy consumption.

Finally, a correlation between numerical and experimental results have been presented verifying the soundness of the proposed model.

It is clear that the main problem is related to the heat subtraction on the lower face of the Peltier cell and the system to be used in this application during the experimental phase has been a small fan able to cool the hot face of the cell.

In a future application a different system to cool the hot face of the cell could be developed even if this shall determine an additional energy consumption and other systems to be installed (for example a fluid refrigeration).

At the present state of the art a future development for the system composed of S.M.A.-Peltier cell will be installed under S.M.A. tape as actuator system for a flap deflection.

The involvement could be an installation of this innovative system on a flap actuator for a regional aircraft with an industrialization of the product.

This application is perfectly inserted inside an new optic of energy reduction reducing the traditional actuator systems generally installed on an aircraft.

Publications and scientific works

PAPER

PREDICTION OF SHAPE MEMORY ALLOY (S.M.A.) COOLING BY A PELTIER CELL

Michele Granito , Leonardo Lecce

Paper n. OT005 (6pp.).published on volume II "ASME/ATI/UIT - *International Conference on Thermal and Environmental Issues in Energy Systems"- ISBN 978-884672659-9* May 16-19, Sorrento (Na), Italy

PREDICTION OF SHAPE MEMORY ALLOY (S.M.A.) COOLING BY A PELTIER CELL

Michele Granito *, Leonardo Lecce °

* Dept. of Aerospace Engineering (DIAS), Univ. of Naples "Federico II", Via Claudio 21, Naples, Italy 80100
e-mail granito.michele@libero.it, (phone 081-7442274)
° Dept. of Aerospace Engineering (DIAS), Univ. of Naples "Federico II", Via Claudio 21, Naples, Italy 80100
e-mail leonardo@unina.it (phone 081-7683327)

ABSTRACT

Shape Memory Alloys (S.M.A.), due to their interesting and promising features in terms of transmittable forces and deformations, are well doing for themselves for several engineering applications: from aeronautics to civil field, from surgery to electronics and so on. Among the others, the morphing wing field is benefiting of S.M.A.: some airfoil geometrical features (f.i. camber, chord) and some wing characteristics (twist angle, swept, winglets) are, at the moment, object of investigations aiming at producing suitable, remarkable geometry variations thus achieving optimal configurations for different flight regimes.

One of the drawbacks of S.M.A. is the activation – deactivation time: being necessary a heat source, the thermal inertia of the material strongly penalizes working frequency range (< 1Hz). In this paper, the problem of making faster the cooling (i.e. the deactivation) of a S.M.A. ribbon, used for a morphing wing application, is dealt with.

A Peltier cell has been bonded on the lower face of a S.M.A. ribbon, being the upper face exposed to air. Required cooling time vs. Peltier cell supplied current has been estimated through an analytic approach, by assuming complete Austenite and Martensite concentration as initial and final states.

INTRODUCTION

Within the Smart Materials family, due to their promising performance in terms of transmittable forces and deformations, Shape Memory Alloys (S.M.A.) play a more and more fundamental role []. Several S.M.A. applications may be found in different engineering fields: aerospace, surgery, civil buildings and so on.

S.M.A. ability of recovering a pre-impressed shape (Shape Memory Effect) [2] and withstanding large deformations (Super Elastic Effect) [2-3] originates from the two possible crystal arrangements: Martensite and Austenite. The transformation from one

phase into the other one is governed by temperature and applied stress field; four different transformation temperatures, Austenite start and finish, A_s and A_f, Martensite start and finish, M_s and M_f, can be identified and strongly depend on material alloy type and concentration [3]. Moreover a linear increase of these values can be caused by a stress field application.

The possibility of improving aircraft performance, just changing the geometry of aerodynamic surfaces like wings, horizontal and vertical tails has been more and more taken into account in the last decades, as shown in the scheme of Figure 1.

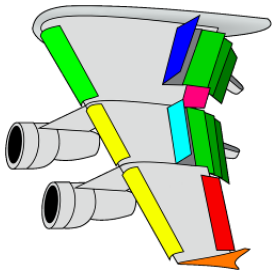

Figure1. Morphing applications since aeronautics origins.

A considerable incentive towards this direction has been given by the advent of above mentioned smart materials, generally guaranteeing compactness, cost and weight reduction, high integration level [4]. Among the others, a morphing application focusing on flap zone chamber control, based on S.M.A. ribbon integrated within the structure, has been carried out and a lab technology demonstrator has been built and tested. However, the intrinsic limit of S.M.A., that is the necessity of a heating and cooling for activation and deactivation, strongly penalized the frequency working range of the prototype, thus restricting tests to steady state.

While the activation time can be remarkably reduced by increasing the power supply, the deactivation cannot be made faster unless introducing a dedicated cooling system.

In the work at hand, the cooling effects due to a Peltier cell working at several regimes [5-6], bonded on a face of a S.M.A. ribbon in natural convection, has been considered.

Assuming a one-dimensional domain and uniform temperature distribution along S.M.A. thickness, starting from a complete Austenite phase, the cooling process has been described through an analytic approach; at first, it has been estimated the time required to arrive at M_s temperature [7] (beginning of Austenite into Martensite transformation); then, it has been

computed the temperature evolution during transition (up to reaching M_f).

A dedicated heat balance equation [8] has been written for the complete austenite interval and then solved, thus achieving temperature vs. time required relation. The same equation has been adapted for the case of phase transformation, by assuming as initial conditions the last ones given by the previous solution and taking into account of the arising concentration of Martensite. As S.M.A. material constitutive law, Liang and Rogers cosine model has been adopted and a piece wise approximation performed, thus preserving the linearity of the governing differential equation.

ACTUATOR AND COOLING SYSTEM DESCRIPTION

The actuator in charge of producing chamber variations of a wing of a regional aircraft is constituted by a S.M.A. ribbon.

The edges are suitably connected to elastic elements, parts of the rib structure and able to assure required rigidity against aerodynamic loads and necessary pre-stress within S.M.A.s for recovering operations.

In practice, heating by Joule effect the ribbons, Martensite into Austenite transformation is enforced thus achieving a contraction of the actuators and inducing a relative rotation of the different rib parts, linked each others by the elastic elements.

The activation is assured by a dedicated power supplier providing for an electrical current of 50 A at a voltage of 1V. By this power the activation in presence of 150MPa of pre-load within S.M.A. ribbons, is achieved in 65 s, temperature arising from room conditions to 100°C.

While it is thinkable to reduce this interval, either supplying greater power or cutting down activation temperature through an appropriate alloy dosage, the cooling is an open problem: the time required, 235 s in natural convection, represents a limitation of the system.

In order to accelerate the heat subtraction some solution can be adopted. Among the others, due to their integrability, Peltier cells are seen as promising components of a forced convection system. In the specific case, one face of the S.M.A. ribbon is directly exposed to the air, while the other one is in contact with a Peltier cell transferring, at several working regimes (current supply), the heat from the S.M.A. to the lower fluid layer. A scheme of this cooling system is depicted in Figure 2. The cell is mainly constituted by internal positive and negative junctions couples (named “P” and “N”), copper plates

(green) allowing for electron migration and two external ceramic insulation layers.

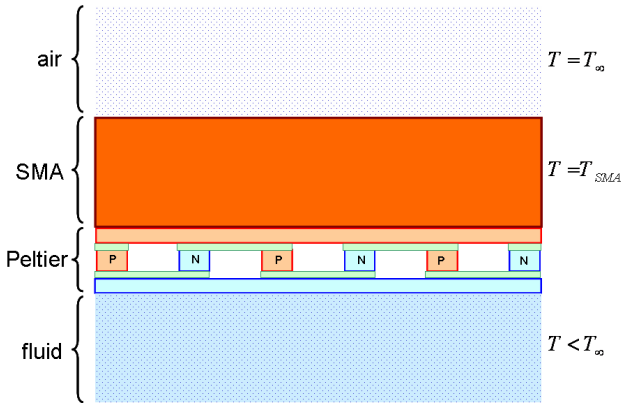

Figure2. Reference scheme S.M.A. – Peltier cells – air.

To make more effective this system, the temperature of the bottom fluid layer has been assumed lower than the top one ($T<T_\infty$). This corresponds to have a heat transfer system that allows the fluid circulation, thus further accelerating the cooling process. The main geometric and mechanical features of the system are summarized in table 1 and 2

Rectangular section (m)	1.0e-3
Area (m^2)	1.0e-6
Tape length (m)	13.0e-2

Table1. S.M.A. tape geometrical features

Austenite Young modulus (GPa)	40.18
Martensite Young modulus (GPa)	16.5
Austenite start, A_s, (°C)	47.3
Austenite finish, A_f, (°C)	58.9
Martensite start, M_s, (°C)	43.3
Martensite finish, M_f, (°C)	27.5

Table2. S.M.A. tape properties

Although the S.M.A. ribbon operates with an internal pre-load to assure its recovery when cooled, the effects on the transformation temperatures of the internal stress have been neglected. In the following paragraph, the simulation strategy adopted for predicting the time required for completely deactivating the S.M.A., has been described.

THE ANALYTICAL MODEL

In this article a theoretical model for S.M.A. tape cooling has presented. In order to reduce time cooling of the S.M.A. tape by means of a Peltier cell bonded on the bottom of one face of the ribbon an analytical model has been developed.

In table 3 thermodynamic characteristics are illustrated:

$c \left[\frac{J}{kg \cdot °K}\right]$	837
$k \left[\frac{J}{m \cdot s \cdot °K}\right]$	18
$\rho \left[\frac{kg}{m^3}\right]$	6500
$k_p \left[\frac{J}{m \cdot s \cdot °K}\right]$	148
$k_n \left[\frac{J}{m \cdot s \cdot °K}\right]$	59.9
$\bar{h} \left[\frac{J}{m^2 \cdot s \cdot °K}\right]$	11.63

Table 10. S.M.A. and Peltier thermodynamic parameters

The theoretical model is based on the two following assumption according to the thermodynamic phenomenology.

1 Biot number for SMA component is $6.0 \cdot 10^{-4}$ (Bi << 1)

2 Low thermal inertia of the Peltier cell

In this model, for the S.M.A., the internal thermal resistance has been considered negligible with respect to the external thermal resistance and so the temperature is practically uniform along the S.M.A. thickness.

In addition, there is a low thermal inertia for the Peltier cell and this hypothesis confirms that the cell, installed on the S.M.A. tape, has a negligible influence on the system thermal equilibrium.

The reference scheme adopted for this model is illustrated in Figure 2.

In Figure 2 along the S.M.A. lower face Peltier cells have been set but under the Peltier cells a fluid at a lower temperature has been considered, while above the S.M.A. only air has been foreseen.

In order to model the phenomenology, basing on such a scheme, the energy balance equation has been written.

At first, model analysis has been developed assuming Austenite as initial phase to compute the transformation time from Af to Ms. In the following, the first analytical model is presented. According to the energy balance equation for our purpose in presence of the initial Austenite phase we have the Eq. (1)

$$\left(c_{SMA}\cdot\rho_{SMA}\cdot L_{SMA}\cdot b_{SMA}\cdot t_{SMA}\right)\frac{dT_{SMA}}{dt}=\overline{h}\cdot(L\cdot b)\cdot(T_{\infty}-T_{SMA})+$$
$$-2\cdot a\cdot I\cdot T_{SMA}+R_{pelt}\cdot I^{2}+(k_{p}+k_{n})\cdot\left(\frac{L\cdot b}{t_{pelt}}\right)\cdot\left(T_{pelt-air}-T_{SMA}\right) \quad (1)$$

In the table 4 each terms in Eq. (1) is explained.

$a=\frac{1}{2}(a_{pm}+a_{nm})$	Averaged Seebeck coefficients (between positive and negative electrodes
$r=\frac{1}{2}(r_{p}+r_{n})$	Averaged semiconductor electrical resistivity
$R_{pelt}=r\cdot\frac{s}{A}$	Cell resistance
$\left(c_{SMA}\cdot\rho_{SMA}\cdot L_{SMA}\cdot b_{SMA}\cdot t_{SMA}\right)\frac{dT_{SMA}}{dt}$	S.M.A. Internal Energy variation
$\overline{h}\cdot(L\cdot b)\cdot(T_{\infty}-T_{SMA})$	S.M.A. tape output energy
$-2\cdot a\cdot I\cdot T_{SMA}$	Peltier cell output energy
$R_{pelt}\cdot I^{2}$	Joule effect (electric dissipation)
$(k_{p}+k_{n})\cdot\left(\frac{L\cdot b}{t_{pelt}}\right)\cdot\left(T_{pelt-air}-T_{SMA}\right)$	Fourier effect (thermal conduction between cell – S.M.A.)

Table 11. Energy balance terms for the analytical model

Eq. 1 has been formulated according to the first and second hypothesis (Bi <<1 in the system S.M.A. – Peltier cell and low thermal inertia of Peltier cell respectively).
But for the completely problem solution the Eq. (2) has been necessary.

$$T_{pelt}=T_{\infty} \quad (2)$$

Through Eq. (1), by assuming as final temperature the Martensite start value, Ms, the time, t_{M_S}, necessary to cool down the S.M.A. up to getting incipient transformation condition, has been estimated. In Eq. (3) the analytical equation solution and in table 5 the energy balance equation coefficients are presented.

$$t_{M_s} = -\frac{A_a}{B_a} \cdot \ln\left(\frac{C_a - B_a \cdot M_s}{C_a - B_a \cdot T_0}\right) \quad (3)$$

$A_a = (c_{SMA} \cdot \rho_{SMA} \cdot L_{SMA} \cdot b_{SMA} \cdot t_{SMA})$ $B_a = \bar{h}Lb + \left(\frac{k_p + k_n}{t_{pelt}}\right)(Lb) + 2aI$ $C_a = \bar{h}LbT_\infty + \left(\frac{k_p + k_n}{t_{pelt}}\right)(Lb)T_{pelt-air} + R_{pelt} \cdot I^2$	Equation (3) coefficients
$t = 0$ $T_{SMA} = T_0$	Initial conditions for equation (3)

Table 12. Energy balance equation condition and coefficient for initial transformation from Austenite to Martensite start.

After the austenite Eq. (3) solution for austenite phase, in order to compute the phase change occurring between Ms and Mf interval, according to our purpose, a new transformation equation has been written.

During the transformation phase from Ms to Mf , a new term in the energy balance equation has to be considered. So that, according to Liang and Rogers model, Martensite amount ξ produced has been computed.

The equations (4) and (5) describing the Martensite concentration during heating and cooling phases are the following

$$\xi = \frac{1-\xi_0}{2} \cdot \cos\left[\alpha_M\left(T - M_f\right) + b_M \cdot \sigma\right] + \frac{1+\xi_0}{2} \quad (4)$$

where $\alpha_M = \frac{\pi}{M_s - M_f}$ and b_M the slope coefficient of the dependence law of S.M.A. characteristic temperatures (As, Af, Ms, Mf) from the stress field but, in this case, the S.M.A. material has been assumed unloaded ($\sigma = 0$). To formulate an exact solution, Eq. (4) has been approximated through a piece wise function, equal to 1 for T ≤ M_f, equal to 0 for T ≥ M_s and linearly variable as

$$\xi = \left(\frac{M_s}{M_s - M_f} - \frac{T_{SMA}}{M_s - M_f}\right) \quad (5)$$

for T ∈ [Mf Ms,].

So that, from the Eq. (5), including the transformation phase, the energy balance equation

for the S.M.A. – Peltier cell system Eq. (1) becomes

$$\begin{aligned}&\left(c_{SMA}\cdot\rho_{SMA}\cdot L_{SMA}\cdot b_{SMA}\cdot t_{SMA}\right)\frac{dT_{SMA}}{dt}=\overline{h}\cdot(L\cdot b)\cdot(T_{\infty}-T_{SMA})+\\&-2\cdot a\cdot I\cdot T_{SMA}+R_{pelt}\cdot I^{2}+(k_p+k_n)\cdot\left(\frac{L\cdot b}{t_{pelt}}\right)\cdot\left(T_{pelt-air}-T_{SMA}\right)+\\&+\left(c_{SMA}\cdot\rho_{SMA}\cdot L_{SMA}\cdot b_{SMA}\cdot t_{SMA}\right)\frac{d\left(\xi\cdot T_{SMA}\right)}{dt}\end{aligned}\qquad\text{-6}$$

with $\left(c_{SMA}\cdot\rho_{SMA}\cdot L_{SMA}\cdot b_{SMA}\cdot t_{SMA}\right)\frac{d\left(\xi\cdot T_{SMA}\right)}{dt}$ the novel phase transformation term.

The solution of Eq. (6) is the time, t_{M_f} , computed according to the Martensite finish , Mf, temperature.

$$\begin{aligned}t_{M_f}&=\frac{A_t}{B_t}\cdot\ln\left(\frac{C_t\cdot M_f+D_t}{C_t\cdot M_s+D_t}\right)+\frac{B_t}{C_t}\left(M_f-M_s\right)+\\&-\left(\frac{B_tD_t}{C_t^{2}}\right)\ln\left(\frac{C_t\cdot M_f+D_t}{C_t\cdot M_s+D_t}\right)+t_{M_s}\end{aligned}\qquad(7)$$

with

$A_t=\left(c_{SMA}\cdot\rho_{SMA}\cdot L_{SMA}\cdot b_{SMA}\cdot t_{SMA}\right)\left[1-\frac{M_s}{M_s-M_f}\right]$ $B_t=\left(c_{SMA}\cdot\rho_{SMA}\cdot L_{SMA}\cdot b_{SMA}\cdot t_{SMA}\right)\left[\frac{2}{M_s-M_f}\right]T$ $C_t=\left(\overline{h}Lb+2aI+\left(\frac{k_p+k_n}{t_{pelt}}\right)(Lb)\right)T_{SMA}$ $D_t=R_{pelt}I^{2}+\left(\frac{k_p+k_n}{t_{pelt}}\right)(Lb)T_{pelt-air}$	Equation (7) coefficients
$t=t_{M_s}$ $T_{SMA}=M_s$	Initial conditions for equation (7)

Table 4. Energy balance equation condition and coefficient for initial transformation from Martensite start to Martensite finish.

From Eq. (7) total cooling time is presented. In this case, Eq. (7) provides the necessary

time to cool down the S.M.A. ribbon from the Austenite to Martensite phase, considering the transformation phase time from Ms to Mf temperature cooling time too.

The computed result has been obtained by considering the Peltier cell aid too during the modelling phase.

In these plots (Figure 3, 4, 5 and 6) predicted interval needed to pass from initial temperature (Austenite) to Martensite start, Ms, (blue curve) is presented, then, by this later value, calculating the transformation time by the Eq. (7), the Ms to Mf time interval has been computed (red curve), and finally, the total interval time from Austenite to Mf has been found as sum of the previous time (black curve).

These data have been plotted vs. current intensity within Peltier cell.

Such a way Peltier aid to S.M.A. cooling has been shown, remarking the advantages found by using this method adopted.

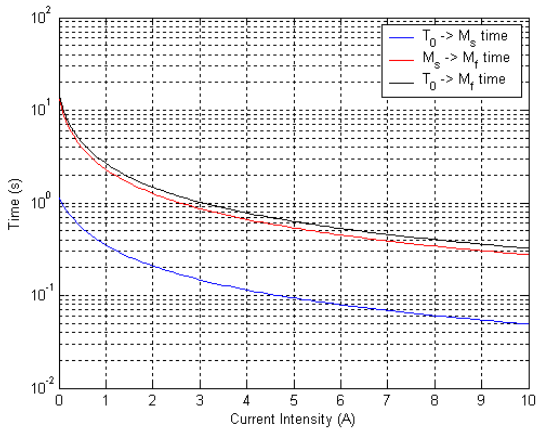

Figure 3. Time vs current intensity for S.M.A. tape cooling for $T_{pelt} = T_{\infty}$

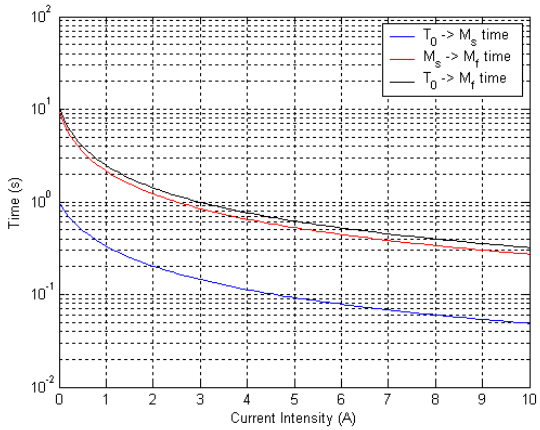

Figure 4. Time vs current intensity for S.M.A. tape cooling for $T_{pelt} = T_{\infty} - 10°C$

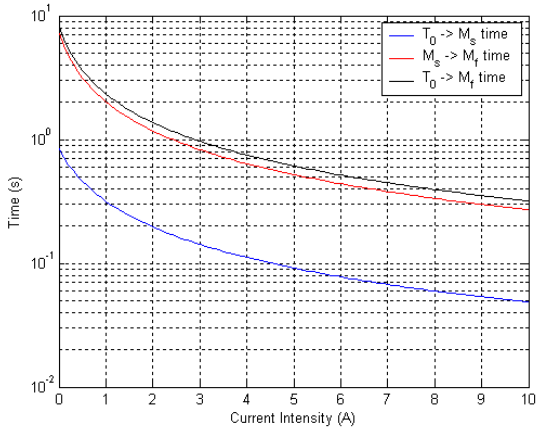

Figure 5. Time vs current intensity for S.M.A. tape cooling for $T_{pelt} = T_{\infty} - 20°C$

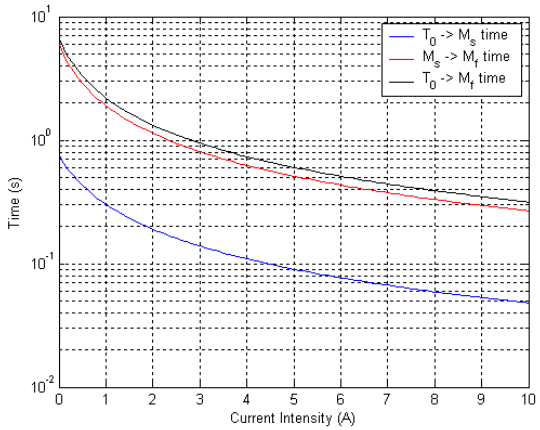

Figure 6. Time vs current intensity for S.M.A. tape cooling for $T_{pelt} = T_{\infty} - 30°C$

In these plots it is possible to choose a current intensity input, according to the supplied power by the Peltier cell, and, consequently, obtain the S.M.A. cooling time from Austenite to Martensite phase as reported above.

It results that for lower Tpelt temperature as in Figure 6 a sensible cooling time reduction is recordered.

So that, results here presented demonstrate a deep S.M.A. cooling time reduction by using the Peltier cell with respect to the natural convection.

For our purpose few seconds have to be enough to carry out flap deflection and this solution is compliant with this requirement.

CONCLUSIONS

In the present paper a possible solution to the S.M.A. structure cooling problem has been proposed. In particular, among other solutions the Peltier cell installation under the S.M.A. ribbon flap actuator has been preferred. Advantages in terms of energy consumption, weight reduction and system integrability has been assessed during the solution choice. So that, after a conceptual scheme presented and a brief system description of the architecture, an analytical procedure has been developed in order to verify a new S.M.A. cooling system by using a Peltier cell installed along the S.M.A. ribbon.

At first, Peltier cell as cooling system, has been preferred and then a differential equation system has been written according to the hypothesis related to a negligible S.M.A. thermal inertia and uniform temperature into the S.M.A. tape (Bi <<1).

By solving the differential equation system, cooling time from Austenite to Martensite finish phase has been computed; results have confirmed the soundness of the adopted solution by means of installation of Peltier cells along the S.M.A. tape, showing a sensible cooling time reduction with respect to a natural convection cooling system.

This proposed solution may be considered as the initial track to follow in order to satisfy a time cooling reduction in S.M.A. applications.

NOMENCLATURE

Symbol	Quantity	SI Unit
A	Surface area	m^2
A_f	Austenite finish temperature	$°C$
A_s	Austenite start temperature	$°C$
a	Seebeck coefficient	dimensionless
a_{nm}	Seebeck coefficient medium n-junction	dimensionless
a_{pm}	Seebeck coefficient medium p -junction	dimensionless
α_M	coefficient	dimensionless
b	Peltier cell width	dimensionless
b_M	Slope	dimensionless
b_{SMA}	SMA tape width	m
Bi	Biot number	dimensionless
c	Specific heat	$\frac{J}{kg \cdot °K}$
c_{SMA}	SMA specific heat	$\frac{J}{kg \cdot °K}$
k	Heat conductivity	$\frac{J}{m \cdot s \cdot °K}$
k_n	n-junction heat conductivity	$\frac{J}{m \cdot s \cdot °K}$

k_p	p-junction heat conductivity	$\frac{J}{m \cdot s \cdot °K}$
$\bar{h}$	Heat transfer coefficient	$\frac{J}{m^2 \cdot s \cdot °K}$
I	Current intensity	A
L	Peltier cell length	m
L_{SMA}	SMA tape length	m
M_f	Martensite finish temperature	$°C$
M_s	Martensite start temperature	$°C$
ξ	Martensite Volumetric fraction	%
ξ_0	Initial Martensite Volumetric fraction	%
r	resistivity	Ω
r_n	n-junction resistivity	Ω
r_p	p-junction resistivity	Ω
R_{pelt}	Peltier cell electrical resistance	Ω
ρ	Air Density	$\frac{kg}{m^3}$
ρ_{SMA}	SMA density	$\frac{kg}{m^3}$
σ	Stress load	MPa
s	Peltier transversal section	m
t_{SMA}	SMA tape tick	m
t_{pelt}	Peltier cell thick	m
t_{M_f}	Martensite finish time	sec
t_{M_s}	Martensite start time	sec
T	temperature	$°C$
T_{SMA}	SMA temperature	$°C$
T_{pelt}	Peltier cell temperature	$°C$
$T_{pelt-air}$	Air to Peltier cell temperature	$°C$
T_∞	Infinite temperature	$°C$

REFERENCES

[1] S. Ameduri, 2003, *Sistemi Integrati di Attuazione per il miglioramento delle prestazioni aerodinamiche di un profilo alare in campo transonico*, Philosophy Doctor's Thesis, Dept. Of Aerospace Engineering, University of Naples, Italy.

[2] C. Liang and C. A. Rogers, 1990 *One- Dimensional Thermomechanical Constitutive Relations For Shape Memory Material*, Journal of Intelligent Material Systems and Structures,1 (2), 207-234

[3] Tanaka K., 1986, *A Thermomechanical Sketch of Shape Memory Effect: One Dimensional Tensile Behaviour*, Res. Mech. 18(3), 251-263.

[4] S. Haidar, I. Isaac and T. Singleton *Thermoelectric Cooling Using Peltier cells in Cascade* Undergraduate laboratories, Dept. of Physics, University of Alberta, Edmonton, AB, T6G2G7.

[5] J. C. Contreras Vargas, MSc J. L. Diaz Rodriguez, Ph.D. A. P. Garcia, MSc. M. Figuerona *A Peltier Cells Research,* Universidad de Pamplona, Facultad de Ingegnerias y Arquitectura Ciutadela Universitaria, Pamplona, Notre de Santander, Colombia.

[6] R. Featherstone and Y. The, *Improving the Speed of Shape Memory Alloy Actuators by Fasten electrical Heating*, Dept. Systems Engineering Australian University Canberra, Australia.

[7] Srinivasan AV, Mc Farland DM, 2001, *Smart Structures:Analysis and Design,* Cambridge University, UK.

[8] F. Kreith, *Principles of Heat Trasfer* 3rd edition , chap. 4, translated by G. Alfano and V. Naso, Dept. of Thermodynamics and Energy, University of Naples, Italy.

PAPER

SHAPE MEMORY ALLOY (S.M.A.) COOLING ANALYSIS : NUMERICAL INVESTIGATION

Michele Granito

Paper RIP-4620- International Journal of Theoretical and Applied Mechanics (IJTAM) approved on 8/10/2010 (11pp.)

SHAPE MEMORY ALLOY (S.M.A.) COOLING ANALYSIS : NUMERICAL INVESTIGATION

Michele Granito

Dept. of Aerospace Engineering (DIAS), Univ. of Naples "Federico II", Via Claudio 21, Naples, Italy 80100 e-mail granito.michele@libero.it, (phone 081-7442274)

Abstract
Recently the development of new aeronautical structures and the implementation of innovative materials has been mandatory for succeeding in critical tasks in terms of weight, fuel consumption, aerodynamic efficiency, cost reduction and so on.
In fact, improvements in terms of aeroelastic behaviour, stability and manoeuvrability performance have been proved in the past, but now a new aircraft design concept is necessary and Shape Memory Alloy (S.M.A.) materials are taken into account for more and more aerospace applications.
S.M.A., are well doing for themselves for several engineering fields: from aeronautics to civils, from surgery to electronics and so on. Morphing wing field is benefiting of S.M.A.: some airfoil geometrical features (f.i. camber, chord) and some wing characteristics (twist angle, swept) are object of investigations aiming at producing suitable geometry variations achieving optimal configurations for different flight regimes.
In this paper a S.M.A. tape, used as actuator system for a flap deflection by activation and de-activation through heating and cooling, by assuming complete Austenite and Martensite concentration, as initial and final states, has been considered.
Drawback of S.M.A. is the activation – deactivation time: even if the activation phase of S.M.A. tape, by heating through Joule effect, is reasonably fast, the de-activation phase by cooling the system is actually an open problem for this type of materials.
In this work numerical results, for a prediction of S.M.A. cooling, achieved through a FE approach, are presented.

Keywords : S.M.A. , Austenite, Martensite, FE

Introduction

Traditional generation of aircraft is characterized by fixed airfoil geometry, optimized for a single or a few operational conditions of a typical mission profile.
This design approach leads a non complete exploitation of the aerodynamic performance, being the geometry not optimized for all flight condition [1]. The wing shape control, as proved by several numerical and experimental investigations [2-3], improves aerodynamic efficiency of a wing by assuring an optimal adaptive behaviour with respect to the external free stream conditions. Geometry modifications affect different parameters as local or global chamber [4-5], the wing span [6-7], the twist angle [8].
Within the Smart Materials family, due to their promising performance in terms of transmittable forces and deformations, Shape Memory Alloys (S.M.A.) play a more and more fundamental role. Several S.M.A. applications may be found in different engineering fields: aerospace, surgery, civil buildings and so on.
Chang & Read discovered S.M.A. in 1932 as a Cd-Au alloy, but only since 1962 when Buehler et alii observed the Shape Memory Effect for the Ni-Ti equi atomic alloy [9], they

have received increasingly more attention.
S.M.A. ability of recovering a pre-impressed shape (Shape Memory Effect) and withstanding large deformations (Super Elastic Effect) originates from the two possible crystal arrangements: Martensite and Austenite. The transformation from one phase into the other one is governed by temperature and applied stress field; four different transformation temperatures, Austenite start and finish, A_s and A_f, Martensite start and finish, M_s and M_f, can be identified and strongly depend on material alloy type and concentration . Moreover a linear increase of these values can be caused by a stress field application.
A considerable incentive towards this direction has been given by the advent of above mentioned smart materials, generally guaranteeing compactness, cost and weight reduction, high integration level. Among the others, a morphing application focusing on flap zone chamber control, based on S.M.A. ribbon integrated within the structure, has been carried out and a lab technology demonstrator has been built and tested. However, the intrinsic limit of S.M.A., that is the necessity of a heating and cooling for activation and deactivation, strongly penalized the frequency working range of the prototype, thus restricting tests to steady state.
While the activation time can be remarkably reduced by increasing the power supply, the deactivation cannot be made faster unless introducing a dedicated cooling system.
Assuming a one-dimensional domain and uniform temperature distribution along S.M.A. thickness, starting from a complete Austenite phase, the cooling process has been described through an analytic approach and then through a numerical simulation; at first, it has been estimated the time required to arrive at M_s temperature (beginning of Austenite into Martensite transformation); then, it has been computed the temperature evolution during transition (up to reaching M_f).
A dedicated heat balance equation has been written for the complete austenite interval and then solved, thus achieving temperature vs. time required relation. The same equation has been adapted for the case of phase transformation, by assuming as initial conditions the last ones given by the previous solution and taking into account of the arising concentration of Martensite. As S.M.A. material constitutive law, Liang and Rogers cosine model has been adopted and a piece wise approximation performed, thus preserving the linearity of the governing differential equation.

S.M.A.s Main Features And Simulation

S.M.A.s are metal alloys (commonly nickel-titanium, gold-cadmium, copper-zinc-aluminium) that exhibit both the unique characteristics of large recoverable strains and large induced internal forces under temperature change.
Aforementioned thermo-mechanical properties of S.M.A.s are due to a crystallographic phase transformation from a body centered cubic structure (Austenite / parent phase, present at high temperatures) to a face centred cubic structure (martensite / product phase, present at low temperatures), or vice versa.
These transformation can be induced by changes in the internal stress state: if the Austenite temperature is lower than the environmental temperature, the so called Superelestic Effect is shown, otherwise, the high residual strain may be recovered by a temperature change and the proper Shape Memory Effect takes place (Figure 1).

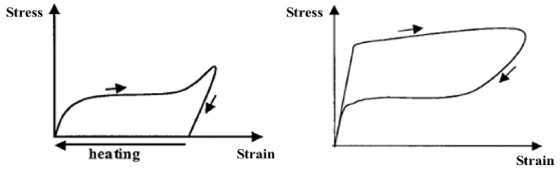

(a) Shape Memory Effect (b) Pseudoelasticity effect

Figure 1. Stress-Strain behaviour of S.M.A.s

In 1986, Tanaka, [10] presented a unified one dimensional stress induced martensitic phase transformation model.
His theory was based on the assumption that the thermomechanical phase transformation of the material is fully described by three state variables : strain, temperature and martensite (austenite) volume fraction (□) representing a measure of the phase evolution.
Tanaka developed the constitutive equation in the rate form:

(1)
$$(\sigma - \sigma_0) = E(\xi)(\varepsilon - \varepsilon_0) + \Theta(T - T_0) + \Omega(\xi - \xi_0)$$

where the subscript $_0$ represents the initial condition. As from this equation, the stress consists in three parts : mechanical, thermal and induced by phase transformation. The martensite fraction was assumed an exponential function of the applied stress and temperature.
In 1990, Liang and Rogers [11] developed a new phenomenological model base on the Tanaka's one: they adopted his constitutive equation but, for the phase kinetics, they assumed a simpler cosine relationship to describe the martensite fraction as a function of stress and temperature. They also assumed the material properties to be constant during the transformation.
The equation describing the martensite concentration during heating and cooling phases are:

(2)
$$\xi = \frac{\xi_M}{2} \cdot \cos\left[\alpha_A (T - A_s) + b_A \cdot \sigma\right] + \frac{\xi_M}{2}$$

(3)
$$\xi = \frac{1 - \xi_A}{2} \cdot \cos\left[\alpha_M (T - M_f) + b_M \cdot \sigma\right] + \frac{1 + \xi_A}{2}$$

where $\alpha_A = \frac{\pi}{A_f - A_s}$ and $\alpha_M = \frac{\pi}{M_f - M_s}$ are combinations of material constant A_f, A_s, M_f, M_s are material characteristic temperatures, respectively known as austenite final austenite start martensite final and martensite start.
They refer to phase transformations of the material and define when a particular crystal structures appears or the conversion is complete.
Two other combination of the material constants are $b_A = -\frac{\alpha_A}{C_A}$ and $b_M = -\frac{\alpha_M}{C_M}$, being C_A and C_M the slopes of the straight lines approximating the functions relating the four temperatures to the acting stress.
Finally, ξ_A and ξ_M are the martensite and austenite volume fractions in the alloy before heating and cooling, respectively.
For our purpose the cooling term has been considered during the analysis.

Actuator And Cooling System Description
The actuator in charge of producing chamber variations of a wing of a regional aircraft is constituted by a S.M.A. ribbon.
The edges are suitably connected to elastic elements, parts of the rib structure and able to assure required rigidity against aerodynamic loads and necessary pre-stress within S.M.A.s

for recovering operations.
In practice, heating by Joule effect the ribbons, Martensite into Austenite transformation is enforced thus achieving a contraction of the actuators and inducing a relative rotation of the different rib parts, linked each others by the elastic elements.
The activation is assured by a dedicated power supplier providing for an electrical current of $50A$ at a voltage of 1 V. By this power the activation in presence of $150MPa$ of pre-load within S.M.A. ribbons, is achieved in 65 s, temperature arising from room conditions to $100°C$. While it is thinkable to reduce this interval, either supplying greater power or cutting down activation temperature through an appropriate alloy dosage, the cooling is an open problem.
So, in this article a numerical simulation by a FE approach has been developed in order to predict the S.M.A. tape cooling time during the Austenite into Martensite transformation.

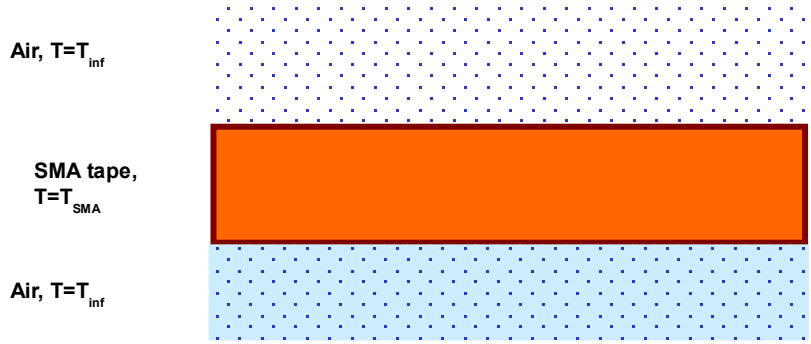

Figure 2. Reference scheme S.M.A. tape – air.

The main geometric and mechanical features of the system are summarized in table 1 and 2

Rectangular section (m)	1.0e-3
Area (m^2)	1.0e-6
Tape length (m)	13.0e-2

Table1. S.M.A. tape geometrical features

Austenite Young modulus (GPa)	40.18
Martensite Young modulus (GPa)	16.5
Austenite start, A_s, (°C)	47.3
Austenite finish, A_f, (°C)	58.9
Martensite start, M_s, (°C)	43.3
Martensite finish, M_f, (°C)	27.5

Table2. S.M.A. tape properties

Although the S.M.A. ribbon operates with an internal pre-load to assure its recovery when cooled, the effects on the transformation temperatures of the internal stress have been neglected. In the following paragraph, the simulation strategy adopted for predicting the time required for completely deactivating the S.M.A., has been described.

The Analytical Model

In this paragraph a theoretical model for S.M.A. tape cooling has been presented. In particular a numerical simulation by a FE approach has been developed in order to determine S.M.A. tape cooling time. In table 3 thermodynamic characteristics are illustrated:

c $\left[\frac{J}{kg\cdot°K}\right]$	837
k $\left[\frac{J}{m\cdot s\cdot°K}\right]$	18
ρ $\left[\frac{kg}{m^3}\right]$	6500
$\overline{h}$ $\left[\frac{J}{m^2\cdot s\cdot°K}\right]$	11.63

Table 3. S.M.A. and Peltier thermodynamic parameters

The theoretical model is based on the following assumption according to the thermodynamic phenomenology: Biot number for S.M.A. component is $6.0\cdot10^{-4}$ (Bi << 1). In addition in this model, for the S.M.A., the internal thermal resistance has been considered negligible with respect to the external thermal resistance and so the temperature is practically uniform along the S.M.A. thickness.
The reference scheme adopted for this model is illustrated in Figure 3.
In Figure 2 the S.M.A tape has been shown.
In order to model the phenomenology, basing on such a scheme, the energy balance equation has been written.
At first, model analysis has been developed assuming Austenite as initial phase to compute the transformation time from A_f to M_s. In the following, the first analytical model is presented. According to the energy balance equation for our purpose in presence of the initial Austenite phase we have the Eq. (4)

$$(c_{SMA}\cdot\rho_{SMA}\cdot L_{SMA}\cdot b_{SMA}\cdot t_{SMA})\frac{dT_{SMA}}{dt}=\overline{h}\cdot(L)\cdot(T_\infty-T_{SMA}) \quad (4)$$

In the table 4 each terms in Eq. (4) is explained and we find t_{M_s}.

$(c_{SMA}\cdot\rho_{SMA}\cdot L_{SMA}\cdot b_{SMA}\cdot t_{SMA})\frac{dT_{SMA}}{dt}$	S.M.A. Internal Energy variation
$\overline{h}\cdot(L)\cdot(T_\infty-T_{SMA})$	S.M.A. tape output energy

Table 4. Energy balance terms for the analytical model

$t=0$ $T_{SMA}=T_0$	Initial conditions for equation (4)

Table 5. Energy balance equation condition and coefficient for initial transformation

from Austenite to Martensite start.
During the transformation phase from M_s to M_f, a new term in the energy balance equation has to be considered. So that, according to Liang and Rogers model, Martensite amount ξ produced has been computed.
For the Martensite concentration during cooling phases Eq. (3) has been considered but in this case, assuming S.M.A. material unloaded ($\sigma = 0$). To formulate an exact solution, Eq. (3) has been approximated through a piece wise function, equal to 1 for T ≤ M_f, equal to 0 for T ≥ M_s and linearly variable as

(5) $$\xi = \left(\frac{M_s}{M_s - M_f} - \frac{T_{SMA}}{M_s - M_f} \right)$$

for T ∈ [M_f M_s,].
So that, from the Eq. (5), including the transformation phase, the energy balance equation for the S.M.A. – air system Eq. (4) becomes

(6) $$\begin{aligned} &(c_{SMA} \cdot \rho_{SMA} \cdot L_{SMA} \cdot b_{SMA} \cdot t_{SMA}) \frac{dT_{SMA}}{dt} = \overline{h} \cdot (L) \cdot (T_\infty - T_{SMA}) \\ &+ (c_{SMA} \cdot \rho_{SMA} \cdot L_{SMA} \cdot b_{SMA} \cdot t_{SMA}) \frac{d(\xi \cdot T_{SMA})}{dt} \end{aligned}$$

with $(c_{SMA} \cdot \rho_{SMA} \cdot L_{SMA} \cdot b_{SMA} \cdot t_{SMA}) \frac{d(\xi \cdot T_{SMA})}{dt}$ the novel phase transformation term, from solution t_{M_s}, we find the t_{M_f}.

with

$t = t_{M_s}$ $T_{SMA} = M_s$	Initial conditions for equation (6)

Table 6. Energy balance equation condition and coefficient for initial transformation from Martensite start to Martensite finish.

From this brief introduction to explain the problem to be solved a numerical investigation has been proposed.

S.M.A. Model : Numerical Investigation
The S.M.A. – air reference scheme (Fig.2) has been considered to introduce the numerical simulation. A Finite Element (FE) approach has been adopted to estimate the S.M.A. tape cooling time using as FE pre –post processor Femap 9.2 and the MSC\Nastran as solver code.
The FE model has been created according to the material properties of S.M.A. tape and considering a thermal convection between the tape and external air.
A thin S.M.A. layer has been modelled by means a CHEXA element with 8 nodes.
In order to solve the problem the boundary conditions on the two S.M.A. faces exposed to the air have been defined; in addition also material properties on the faces and the related boundary conditions surfaces with reference to the heat transfer, as in the present problem,

have been determined.
The heat transfer problem by using FE approach has been studied by means of a Transient Heat Transfer (SOL 159) because of the time dependent investigation.
The thermal distribution on the S.M.A. tape is uniform and is $100°C$ necessary for the alloy activation, but the reference temperature to be reached by the tape after the thermal exchange is $20°C$ that is the external air temperature considered during our analysis.
The model has been created considering the free convection for the two surfaces according to the heat transfer connection to a surface element for the heat exchange simulation.
In order to determine the rate of heat produced in the material, because of the heating of the tape for the flap deflection during the activation phase, a rate of heat power inside the FE model has been considered.
In this FE approach, for the thermal convection exchange between the tape and the air, a control node (n.99) at an appropriate distance with respect to the FE model dimension has been placed.
The control node is at a temperature of $20°C$.
Another problem to be considered during the simulation has been the transformation from A_f to M_s and from M_s to M_f modelled by means of a nonlinear approach.
By the FE simulation and analysis by means of transient heat transfer solution a thermal history has been considered.
The solution provided by the MSC\Nastran code has provided the thermal behaviour of the single node of the FE model.
In order to show the results, obtained by the numerical simulation, a tool in Matlab code has been developed.
This tool is able to plot the results of the all nodes of the FE model as shown in the Figure 3 where the green curve is the temperature of the reference node 99 constant at $20°C$ and the red curve is the thermal evolution of the S.M.A. surfaces during the thermal convection cooling down. It is evident (Fig.4) the two knees on the red curve depending on the transformation phase described from Austenite to Martensite.
The complete S.M.A. tape cooling time, t_{M_f} is $200s$ as final value.

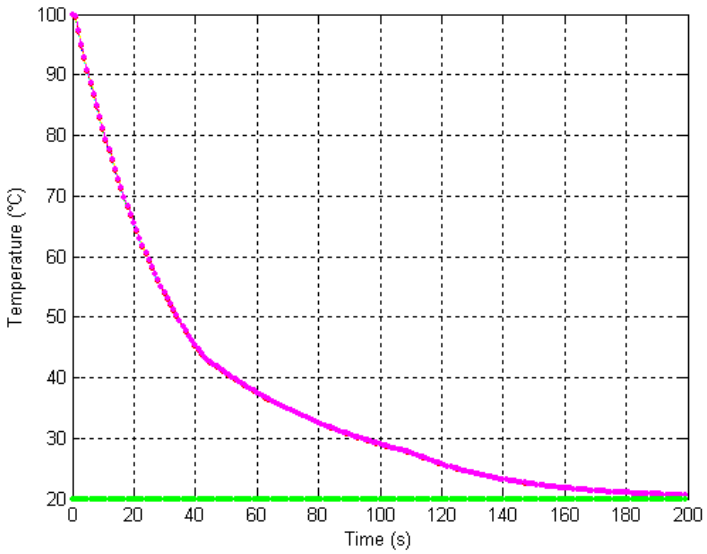

Figure 3. FE numerical simulation, Green curve : reference temperature, Red curve: S.M.A. cooling temperature

Conclusions

A novel approach has been adopted in this study by highly integrating the S.M.A.s' elements within the architecture for the flap deflection; this tape have both a structural and actuation role, working as actuators of the structure, whose integrity depends on S.M.A.s' structural capability of sustaining external loads.

In the present paper a possible solution to the S.M.A. structure cooling problem has been proposed. In particular, after a problem definition in terms of thermal convection equilibrium according to thermodynamic equation a FE approach has been followed.

In fact, even if the S.M.A. materials provide advantages in terms of energy consumption, weight reduction and system integrability in particular in aeronautical field, the cooling problem, during the de-activation phase, is actually under investigation. So that, after a conceptual scheme presented and a brief system description of the architecture, in order to explain the actuator system for the flap deflection, a numerical investigation has been presented.

At first, according to the hypothesis related to a negligible S.M.A. thermal inertia and uniform temperature into the S.M.A. tape (Bi <<1) a FE model has been created.

This approach for the thermal natural convection has been developed in order to predict the S.M.A. tape cool down during the de-activation phase. The actuator activation time, through heating by means of Joule effect in order to have the alloy transformation, from Martensite into Austenite phase, is negligible with respect to the cooling time, for the transformation from Austenite into Martensite, actually under investigation, so this article defines a study for the prediction of the cooling time necessary when the actuator is in thermal natural convection regime during the flap deflection.

This proposed study may be considered as the initial track to follow in order to satisfy a time cooling reduction in S.M.A. applications.

Nomenclature

Symbol	Quantity	SI Unit
A	Surface area	m^2
A_f	Austenite finish temperature	$°C$
A_s	Austenite start temperature	$°C$
a	Seebeck coefficient	dimensionless
a_{nm}	Seebeck coefficient medium n-junction	dimensionless
a_{pm}	Seebeck coefficient medium p -junction	dimensionless
α_M	coefficient	dimensionless
b	Peltier cell width	dimensionless
b_M	Slope	dimensionless
b_{SMA}	SMA tape width	m
Bi	Biot number	dimensionless
c	Specific heat	$\frac{J}{kg \cdot °K}$
c_{SMA}	SMA specific heat	$\frac{J}{kg \cdot °K}$
k	Heat conductivity	$\frac{J}{m \cdot s \cdot °K}$
k_n	n-junction heat conductivity	$\frac{J}{m \cdot s \cdot °K}$

k_p	p-junction heat conductivity	$\frac{J}{m \cdot s \cdot °K}$
$\bar{h}$	Heat transfer coefficient	$\frac{J}{m^2 \cdot s \cdot °K}$
I	Current intensity	A
L	Peltier cell length	m
L_{SMA}	SMA tape length	m
M_f	Martensite finish temperature	$°C$
M_s	Martensite start temperature	$°C$
ξ	Martensite Volumetric fraction	%
ξ_0	Initial Martensite Volumetric fraction	%
r	resistivity	Ω
r_n	n-junction resistivity	Ω
r_p	p-junction resistivity	Ω
R_{pelt}	Peltier cell electrical resistance	Ω
ρ	Air Density	$\frac{kg}{m^3}$
ρ_{SMA}	SMA density	$\frac{kg}{m^3}$
σ	Stress load	MPa
s	Peltier transversal section	m
t_{SMA}	SMA tape tick	m
t_{pelt}	Peltier cell thick	m
t_{M_f}	Martensite finish time	sec
t_{M_s}	Martensite start time	sec
T	temperature	$°C$
T_{SMA}	SMA temperature	$°C$
T_{pelt}	Peltier cell temperature	$°C$
$T_{pelt-air}$	Air to Peltier cell temperature	$°C$
T_∞	Infinite temperature	$°C$

References

[1] A.L. Martins and F.M. Catalano, "*Viscous Drag Optimization for a Transport Aircraft Mission Adaptive Wing*", 21st ICAS Congress, Melbourne, Australia Paper A98-31499 (1998).

[2] E. Stanewsky, "*Adaptive Wing and Flow Control Technology*", Progress in Aerospace Sciences, Elsevier Science Ltd., 37,pp. 583-667 (2001).

[3] J. Browman, B. Sanders, T. Weisshaar, "*Evaluating the Impact of Morphing Technologies on Aircraft Performance*", AIAA J. pp. 2002-1631 (2002)

[4] J. Spillman, "*The Use of Variable Chamber to Reduce Drag, Weight and Costs of Transport Aircraft* ", Aeronaut. J. 96, pp. 1-8 (1992).

[5] H.P. Monner, T. Bein, H. hanselka, E. Breitbach, "*Design Aspects of the Adaptive Wing – The Elastic Trailing Edge and Local Spoiler Bump*", Royal Aeronautical Society, Multidisciplinary Design and optimization, London, 1998.

[6] Gevers Aircraft Inc., "Multi-Purpose Aircraft", U.S. Patents No. 5,645,250 (1997).

[7] J. Blondeau and D. Pines, "*Pneumatic Morphing Aspect Ratio Wing*", 45th AIAA/ASME/ASCE/AHS/ASC Structures, Structural Dynamics and Materials Conference, Palm Springs, California, AIAA J. pp. 2004-1888 (2004).

[8] J. R. Wilson, "*Active Aeroelastic Wing: A New/Old Twist On Flight*", Aerospace America 40(99), pp. 34-37 (2002).

[9] W. J. Buehler, J. V. Gilfrich, R. C. Wiley, 1963, "*Effect of low-temperature phase changes on the mechanical properties of alloys near composition TiNi*", Journal of Applied Physics 34, p.1475 (1963).

[10] Tanaka K., 1986, *A Thermomechanical Sketch of Shape Memory Effect: One Dimensional Tensile Behaviour*, Res. Mech. 18(3), pp. 251-263.

[11] C. Liang and C. A. Rogers, 1990 *One- Dimensional Thermomechanical Constitutive Relations For Shape Memory Material*, Journal of Intelligent Material Systems and Structures,1 (2), pp. 207-234.

PAPER

Shape Memory Alloy (S.M.A.) Cooling Assessment by a Peltier Cell

Michele Granito , Leonardo Lecce

International Journal of Industrial Engineering and Technology (IJIERT) under submission (12 pp)

Shape Memory Alloy (S.M.A.) Cooling Assessment by a Peltier Cell

Michele Granito *, Leonardo Lecce °

* Dept. of Aerospace Engineering (DIAS), Univ. of Naples "Federico II", Via Claudio 21, Naples, Italy 80100 e-mail granito.michele@libero.it, (phone 081-7442274)
° Dept. of Aerospace Engineering (DIAS), Univ. of Naples "Federico II", Via Claudio 21, Naples, Italy 80100 e-mail leonardo@unina.it (phone 081-7683327)

Abstract
In a new aircraft design concept, due to fuel consumption reduction, low weight, low emission, morphing design approach by means of Shape Memory Alloys (S.M.A.) is an innovative alternative to traditional material applications.
S.M.A.s, and their promising features in terms of transmittable forces and deformations, are well doing for themselves in several engineering fields: from aeronautics to civils, from surgery to electronics and so on. Morphing wing field is benefiting of S.M.A.s: some airfoil geometrical features (f.i. camber, chord) and some wing characteristics (twist angle, swept) are object of investigations aiming at producing suitable geometry variations achieving optimal configurations for different flight regimes.
Drawback of S.M.A.s is the activation – deactivation time: being necessary an heat source, the thermal inertia of the material penalizes working frequency range (< 1Hz). In this paper, a faster cooling (i.e. the deactivation) of a S.M.A. ribbon, used for a morphing wing application, is dealt with.
A Peltier cell has been bonded on the lower face of a S.M.A. ribbon, being the upper face air exposed. Required cooling time vs. supplied current by Peltier cell has been estimated through an analytic approach, by assuming complete Austenite and Martensite concentration as initial and final states.

Keywords : S.M.A. , Austenite, Martensite, Peltier cell

Introduction

The possibility of controlling the geometry of aerodynamic surfaces (ailerons, flaps, horizontal and vertical tails, etc.) represents a challenging target that justifies the more and more research activities carried out on the morphing concept.
The aerodynamic surfaces of a typical aircraft are characterized by a fixed geometry and this design approach leads a non complete exploitation of the aerodynamic performance, being the geometry not optimized for all flight condition [1]. The wing shape control, as proved by several numerical and experimental investigations [2-3], improves aerodynamic efficiency of a wing by assuring an optimal adaptive behaviour with respect to the external free stream conditions. Geometry modifications affect different parameters as local or global chamber [4-5], the wing span [6-7], the twist angle [8].
Within the Smart Materials family, due to their promising performance in terms of transmittable forces and deformations, Shape Memory Alloys (S.M.A.) play a more and more fundamental role. Several S.M.A. applications may be found in different engineering fields: aerospace, surgery, civil buildings and so on.
S.M.A. were discovered in 1932 by Chang & Read as a Cd-Au alloy, but only since 1962 when Buehler et alii observed the Shape Memory Effect for the Ni-Ti equi atomic alloy [9], they have received increasingly more attention.

S.M.A. ability of recovering a pre-impressed shape (Shape Memory Effect) and withstanding large deformations (Super Elastic Effect) originates from the two possible crystal arrangements: Martensite and Austenite. The transformation from one phase into the other one is governed by temperature and applied stress field; four different transformation temperatures, Austenite start and finish, As and Af, Martensite start and finish, Ms and Mf, can be identified and strongly depend on material alloy type and concentration. Moreover a linear increase of these values can be caused by a stress field application.
A considerable incentive towards this direction has been given by the advent of above mentioned smart materials, generally guaranteeing compactness, cost and weight reduction, high integration level. Among the others, a morphing application focusing on flap zone chamber control, based on S.M.A. ribbon integrated within the structure, has been carried out and a lab technology demonstrator has been built and tested. However, the intrinsic limit of S.M.A., that is the necessity of a heating and cooling for activation and deactivation, strongly penalized the frequency working range of the prototype, thus restricting tests to steady state.
While the activation time can be remarkably reduced by increasing the power supply, the deactivation cannot be made faster unless introducing a dedicated cooling system.
In the work at hand, the cooling effects due to a Peltier cell working at several regimes [10], bonded on a face of a S.M.A. ribbon in natural convection, has been considered.
Assuming a one-dimensional domain and uniform temperature distribution along S.M.A. thickness, starting from a complete Austenite phase, the cooling process has been described through an analytic approach; at first, it has been estimated the time required to arrive at Ms temperature (beginning of Austenite into Martensite transformation); then, it has been computed the temperature evolution during transition (up to reaching Mf).
A dedicated heat balance equation has been written for the complete austenite interval and then solved, thus achieving temperature vs. time required relation. The same equation has been adapted for the case of phase transformation, by assuming as initial conditions the last ones given by the previous solution and taking into account of the arising concentration of Martensite. As S.M.A. material constitutive law, Liang and Rogers cosine model has been adopted and a piece wise approximation performed, thus preserving the linearity of the governing differential equation.

S.M.A.s main features and simulation

S.M.A.s are metal alloys (commonly nickel-titanium, gold-cadmium, copper-zinc-aluminium) that exhibit both the unique characteristics of large recoverable strains and large induced internal forces under temperature change. Aforementioned thermo-mechanical properties of S.M.A.s are due to a crystallographic phase transformation from a body centered cubic structure (Austenite / parent phase, present at high temperatures) to a face centred cubic structure (martensite / product phase, present at low temperatures), or vice versa. These transformation can be induced by changes in the internal stress state: if the Austenite temperature is lower than the environmental temperature, the so called Superelestic Effect is shown, otherwise, the high residual strain may be recovered by a temperature change and the proper Shape Memory Effect takes place (Figure 1).

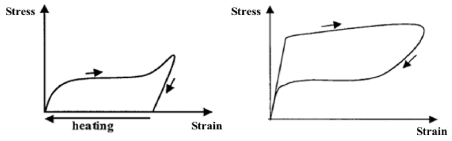

(a) Shape Memory Effect (b) Pseudoelasticity effect

Figure 1. Stress-Strain behaviour of S.M.A.s

In 1986, Tanaka, [11] presented a unified one dimensional stress induced martensitic phase transformation model.
His theory was based on the assumption that the thermomechanical phase transformation of the material is fully described by three state variables : strain, temperature and martensite (austenite) volume fraction (□) representing a measure of the phase evolution.
Tanaka developed the constitutive equation in the rate form:

$$(\sigma - \sigma_0) = E(\xi)(\varepsilon - \varepsilon_0) + \Theta(T - T_0) + \Omega(\xi - \xi_0) \qquad (1)$$

where the subscript 0 represents the initial condition. As from this equation, the stress consists in three parts : mechanical, thermal and induced by phase transformation. The martensite fraction was assumed as exponential function of the applied stress and temperature.
In 1990, Liang and Rogers [12] developed a new phenomenological model base on the Tanaka's one: they adopted his constitutive equation but, for the kinetic phase, they assumed a simpler cosine relationship to describe the martensite fraction as a function of stress and temperature. They also assumed the material properties to be constant during the transformation.
The equation describing the martensite concentration during heating and cooling phases are:

$$\xi = \frac{\xi_M}{2} \cdot \cos\left[\alpha_A (T - A_s) + b_A \cdot \sigma\right] + \frac{\xi_M}{2} \qquad (2)$$

$$\xi = \frac{1 - \xi_A}{2} \cdot \cos\left[\alpha_M (T - M_f) + b_M \cdot \sigma\right] + \frac{1 + \xi_A}{2} \qquad (3)$$

where $\alpha_A = \frac{\pi}{A_f - A_s}$ and $\alpha_M = \frac{\pi}{M_f - M_s}$ are combinations of material constant Af, As, Mf, Ms are material characteristic temperatures, respectively known as austenite final austenite start martensite final and martensite start.
They refer to phase transformations of the material and define when a particular crystal structures appears or the conversion is complete.
Two other combinations of the material constants are $b_A = -\frac{\alpha_A}{C_A}$ and $b_M = -\frac{\alpha_M}{C_M}$, being CA and CM the slopes of the straight lines approximating the functions relating the four temperatures to the acting stress.
Finally, ξ_A and ξ_M are the martensite and austenite volume fractions in the alloy before heating and cooling, respectively.
For our purpose the cooling term has been considered during the analysis.

Actuator and cooling system description
The actuator able to produce a wing chamber variations for a regional aircraft is composed

of a S.M.A. ribbon.
The edges are suitably connected to elastic elements, within the rib structure and able to assure the required stiffness against aerodynamic loads and adequate pre-stress within S.M.A.s in order to recover original conditions.
In practice, by heating ribbons through Joule effect, Martensite into Austenite transformation is obtained so achieving an actuator contraction and inducing a relative rotation of different rib, linked each others by elastic elements.
Activation by a dedicated power supplier providing an electrical current of 50 A at a voltage of 1V is assured. So, the actuator activation, within a range of 65 s is obtained.
In addition inside S.M.A. ribbons, a pre-load of 150 MPa is maintained, while the temperature from room conditions to 100 °C is reached.
While it is thinkable to reduce the activation range, either supplying greater power or cutting down activation temperature through an appropriate alloy dosage, cooling is an open problem: the time required, 235 s in natural convection, represents a limitation of the system.
In order to make the heat subtraction faster some solution can be adopted. Among the others, due to their integrability, Peltier cells are seen as promising components of a forced convection system. In the specific case, one face of the S.M.A. ribbon is directly air exposed , while the other one is in contact with a Peltier cell transferring, at several working regimes (current supply), heat from the S.M.A. to the lower fluid layer. A scheme of this cooling system in Figure 2 is presented. The cell is mainly composed of internal positive and negative junctions couples (named “P” and “N”), copper plates (green) allowing electron migration and two external ceramic insulation layers.

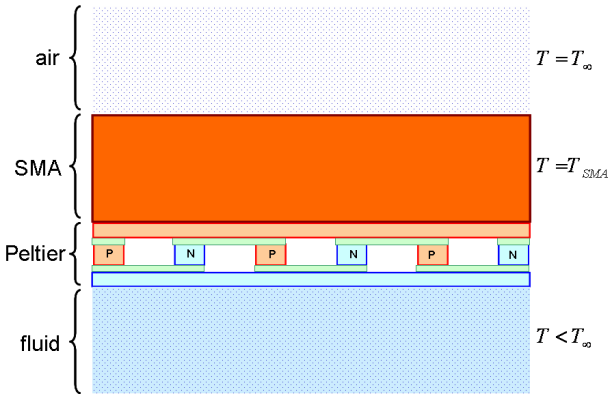

Figure 2. Reference scheme S.M.A. – Peltier cells – air.

In order to make more effective this system, the bottom fluid layer temperature lower than the top one (T<T∞) has been assumed. So, an heat transfer system allowing a fluid circulation, in order to have a faster cooling process, is obtained. Main geometric and mechanical features of the system are summarized in table 1 and 2

Rectangular section (m)	1.0e-3
Area (m2)	1.0e-6
Tape length (m)	13.0e-2

Table1. S.M.A. tape geometrical features

Austenite Young modulus (GPa)	40.18
Martensite Young modulus (GPa)	16.5
Austenite start, As, (°C)	47.3
Austenite finish, Af, (°C)	58.9
Martensite start, Ms, (°C)	43.3
Martensite finish, Mf, (°C)	27.5

Table2. S.M.A. tape properties

Although the S.M.A. ribbon has an internal pre-load assuring its recovery when cooled, the effects on the transformation temperatures of the internal stress have been neglected. In the following paragraph, the simulation strategy adopted for predicting the time required for completely S.M.A.deactivation, has been described.

The Analytical Model

In this article a theoretical model for S.M.A. tape cooling is presented. In order to reduce S.M.A. tape cooling time a Peltier cell bonded on the bottom of the ribbon lower face an analytical model has been developed. In table 3 thermodynamic characteristics are illustrated:

$c \left[\frac{J}{kg \cdot °K}\right]$	837
$k \left[\frac{J}{m \cdot s \cdot °K}\right]$	18
$\rho \left[\frac{kg}{m^3}\right]$	6500
$k_p \left[\frac{J}{m \cdot s \cdot °K}\right]$	148
$k_n \left[\frac{J}{m \cdot s \cdot °K}\right]$	59.9
$\overline{h} \left[\frac{J}{m^2 \cdot s \cdot °K}\right]$	11.63

Table 3. S.M.A. and Peltier thermodynamic parameters

The theoretical model is based on the two following assumption according to the thermodynamic phenomenology.

Biot number for SMA component is 6.0·10-4 (Bi << 1)

Low thermal inertia of the Peltier cell

In this model, for the S.M.A., the internal thermal resistance has been considered negligible with respect to the external thermal resistance and so the temperature is uniform along the S.M.A. thickness.

In addition, there is a low thermal inertia for the Peltier cell and this hypothesis confirms that the cell, installed on the S.M.A. tape, has a negligible influence on the system thermal equilibrium.

The reference scheme adopted for this model is illustrated in Figure 3.

In Figure 2 along the S.M.A. lower face Peltier cells have been set and under the Peltier cells a fluid at a lower temperature has been considered. The S.M.A. ribbon is air exposed.

In order to model the phenomenology, basing on this scheme, the energy balance equation has been written.

At first, model analysis has been developed assuming Austenite as initial phase to compute the transformation time from Af to Ms. In the following, the first analytical model is presented. According to the energy balance equation for our purpose only during initial Austenite phase we have the Eq. (4)

$$\left(c_{SMA}\cdot\rho_{SMA}\cdot L_{SMA}\cdot b_{SMA}\cdot t_{SMA}\right)\frac{dT_{SMA}}{dt}=\overline{h}\cdot(L\cdot b)\cdot(T_{\infty}-T_{SMA})-2\cdot a\cdot I\cdot T_{SMA}+R_{pelt}\cdot I^{2}+$$
$$+(k_{p}+k_{n})\cdot\left(\frac{L\cdot b}{t_{pelt}}\right)\cdot\left(T_{pelt-air}-T_{SMA}\right) \quad (4)$$

In the table 4 each terms in Eq. (4) is explained.

$a=\frac{1}{2}(a_{pm}+a_{nm})$	Averaged Seebeck coefficients (between positive and negative electrodes
$r=\frac{1}{2}(r_{p}+r_{n})$	Averaged semiconductor electrical resistivity
$R_{pelt}=r\cdot\frac{s}{A}$	Cell resistance
$\left(c_{SMA}\cdot\rho_{SMA}\cdot L_{SMA}\cdot b_{SMA}\cdot t_{SMA}\right)\frac{dT_{SMA}}{dt}$	S.M.A. Internal Energy variation
$\overline{h}\cdot(L\cdot b)\cdot(T_{\infty}-T_{SMA})$	S.M.A. tape output energy
$-2\cdot a\cdot I\cdot T_{SMA}$	Peltier cell output energy
$R_{pelt}\cdot I^{2}$	Joule effect (electric dissipation)
$(k_{p}+k_{n})\cdot\left(\frac{L\cdot b}{t_{pelt}}\right)\cdot\left(T_{pelt-air}-T_{SMA}\right)$	Fourier effect (thermal conduction between cell – S.M.A.)

Table 4. Energy balance terms for the analytical model

Eq. (4) according to the first and second hypothesis (Bi <<1 in the system S.M.A. – Peltier cell and low thermal inertia of Peltier cell respectively) has been provided.
But for the completely problem solution the Eq. (5) has been necessary.

$$T_{pelt} = T_{\infty} \qquad -5$$

Through Eq. (4), by assuming as final temperature the Martensite start value, Ms, the time, t_{M_S}, necessary to cool down the S.M.A. in order to reach initial transformation condition, has been estimated. In Eq. (6) the analytical equation solution and in table 5 the energy balance equation coefficients are presented.

$$t_{M_s} = -\frac{A_a}{B_a} \cdot \ln\left(\frac{C_a - B_a \cdot M_s}{C_a - B_a \cdot T_0}\right) \qquad (6)$$

$A_a = (c_{SMA} \cdot \rho_{SMA} \cdot L_{SMA} \cdot b_{SMA} \cdot t_{SMA})$ $B_a = \bar{h}Lb + \left(\frac{k_p + k_n}{t_{pelt}}\right)(Lb) + 2aI$ $C_a = \bar{h}LbT_{\infty} + \left(\frac{k_p + k_n}{t_{pelt}}\right)(Lb)T_{pelt-air} + R_{pelt} \cdot I^2$	Equation (6) coefficients
$t = 0$ $T_{SMA} = T_0$	Initial conditions for equation (6)

Table 5. Energy balance equation condition and coefficient for initial transformation from Austenite to Martensite start.

After the Eq. (6) solution for austenite phase, in order to compute the phase change occurring between Ms and Mf range, according to our purpose, a new transformation equation has been written.
During the transformation phase from Ms to Mf , a new term in the energy balance equation has to be considered. So that, according to Liang and Rogers model, Martensite amount ξ produced has been computed.
For the Martensite concentration during cooling phase Eq. (3) has been considered, assuming S.M.A. material unloaded ($\sigma = 0$). In order to have an exact solution, Eq. (3) has been approximated through a piece wise function, equal to 1 for T ≤ Mf, equal to 0 for T ≥ Ms and linearly variable as

$$\xi = \left(\frac{M_s}{M_s - M_f} - \frac{T_{SMA}}{M_s - M_f}\right) \qquad (7)$$

for T ∈ [Mf Ms,].

So that, from the Eq. (7), including the transformation phase, the energy balance equation for the S.M.A. – Peltier cell system Eq. (4) becomes

$$\left(c_{SMA}\cdot\rho_{SMA}\cdot L_{SMA}\cdot b_{SMA}\cdot t_{SMA}\right)\frac{dT_{SMA}}{dt}=\bar{h}\cdot(L\cdot b)\cdot(T_{\infty}-T_{SMA})-2\cdot a\cdot I\cdot T_{SMA}+R_{pelt}\cdot I^{2}+(k_p+k_n)\cdot\left(\frac{L\cdot b}{t_{pelt}}\right)\cdot\left(T_{pelt-air}-T_{SMA}\right)+$$
$$+\left(c_{SMA}\cdot\rho_{SMA}\cdot L_{SMA}\cdot b_{SMA}\cdot t_{SMA}\right)\frac{d\left(\xi\cdot T_{SMA}\right)}{dt} \qquad (8)$$

with $\left(c_{SMA}\cdot\rho_{SMA}\cdot L_{SMA}\cdot b_{SMA}\cdot t_{SMA}\right)\frac{d\left(\xi\cdot T_{SMA}\right)}{dt}$ the novel phase transformation term.

The solution of Eq. (8) is the time, t_{M_f} , computed according to the Martensite finish , Mf, temperature.

$$t_{M_f}=\frac{A_t}{B_t}\cdot\ln\left(\frac{C_t\cdot M_f+D_t}{C_t\cdot M_s+D_t}\right)+\frac{B_t}{C_t}\left(M_f-M_s\right)-\left(\frac{B_tD_t}{C_t^{2}}\right)\ln\left(\frac{C_t\cdot M_f+D_t}{C_t\cdot M_s+D_t}\right)+t_{M_s} \qquad (9)$$

with

$A_t=\left(c_{SMA}\cdot\rho_{SMA}\cdot L_{SMA}\cdot b_{SMA}\cdot t_{SMA}\right)\left[1-\frac{M_s}{M_s-M_f}\right]$ $B_t=\left(c_{SMA}\cdot\rho_{SMA}\cdot L_{SMA}\cdot b_{SMA}\cdot t_{SMA}\right)\left[\frac{2}{M_s-M_f}\right]T$ $C_t=\left(\bar{h}Lb+2aI+\left(\frac{k_p+k_n}{t_{pelt}}\right)(Lb)\right)T_{SMA}$ $D_t=R_{pelt}I^{2}+\left(\frac{k_p+k_n}{t_{pelt}}\right)(Lb)T_{pelt-air}$	Equation (9) coefficients
$t=t_{M_s}$ $T_{SMA}=M_s$	Initial conditions for equation (9)

Table 6. Energy balance equation condition and coefficient for initial transformation from Martensite start to Martensite finish.

From Eq. (9) total cooling time is presented. In this case, Eq. (9) provides necessary time to cool down the S.M.A. ribbon from the Austenite to Martensite phase, considering the transformation phase time from Ms to Mf temperature cooling time too.
During the modelling phase the computed result, also by considering the Peltier cell aid, has been obtained.
In these plots (Figure 3, 4, 5, and 6) predicted range required for the transformation from initial temperature (Austenite) to Martensite start, Ms, (blue curve) is presented, then, by

this later value, through the calculation of the transformation time by the Eq. (9), the Ms to Mf time range has been computed (red curve), and finally, the total interval as sum of the previous time (black curve)time from Austenite to Mf has been found.
These data have been plotted vs. current intensity within Peltier cell.
Such a way Peltier aid to S.M.A. cooling has been shown, remarking the advantages found by using this method adopted.

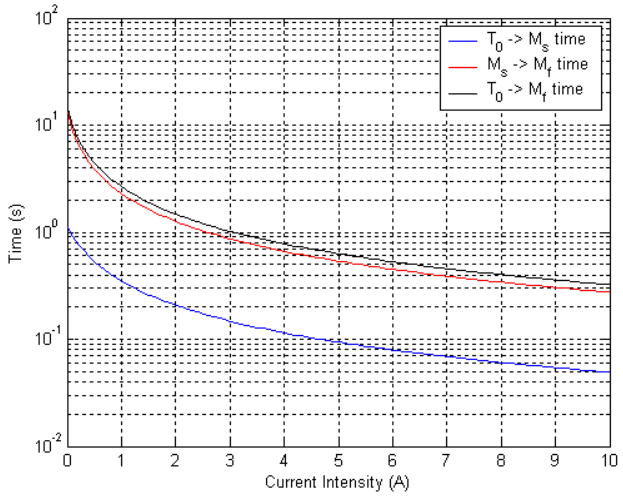

Figure 3. Time vs current intensity for S.M.A. tape cooling for $T_{pelt} = T_{\infty}$

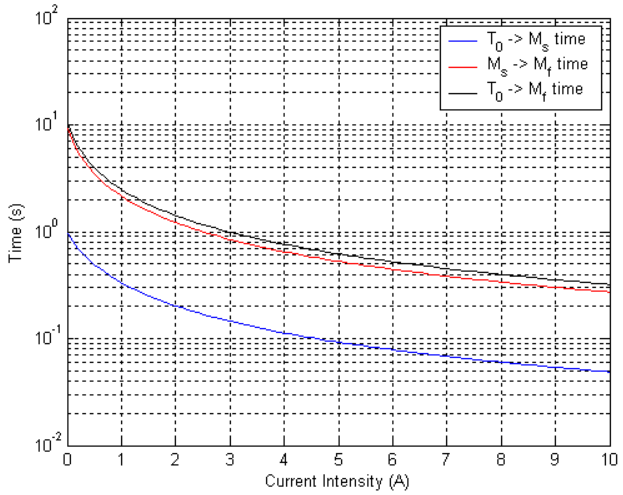

Figure 4. Time vs current intensity for S.M.A. tape cooling for $T_{pelt} = T_{\infty} - 10°C$

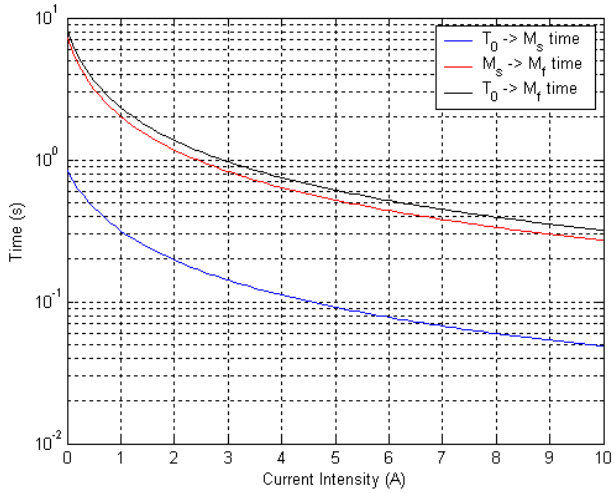

Figure 5. Time vs current intensity for S.M.A. tape cooling for $T_{pelt} = T_{\infty} - 20°C$

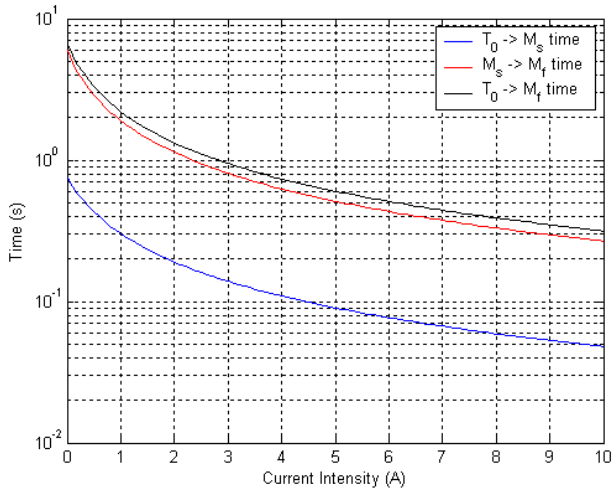

Figure 6. Time vs current intensity for S.M.A. tape cooling for $T_{pelt} = T_{\infty} - 30°C$

In these plots it is possible to choose a current intensity input, according to the supplied power by the Peltier cell, and, consequently, to obtain the S.M.A. cooling time from Austenite to Martensite phase as reported above.
It results that for lower Tpelt temperature as in Figure 6 a sensible cooling time reduction is recordered.
So that, results here presented demonstrate a deep S.M.A. cooling time reduction by using the Peltier cell with respect to the natural convection.
For our purpose few seconds have to be enough to carry out flap deflection and this solution is compliant with this requirement.

Conclusions

In the present paper a possible solution to the S.M.A. structure cooling problem has been proposed. In particular, among other solutions the Peltier cell installation under the S.M.A. ribbon flap actuator has been preferred. During the solution choice advantages in terms of energy consumption, weight reduction and system integrability have been assessed. So that, after a conceptual scheme presented and a brief system description of the architecture, an analytical procedure has been developed in order to verify a new S.M.A. cooling system by using a Peltier cell installed along the S.M.A. ribbon.

At first, Peltier cell as cooling system, has been preferred and then a differential equation system has been written according to the hypothesis related to a negligible S.M.A. thermal inertia and uniform temperature into the S.M.A. tape (Bi <<1).
By solving the differential equation system, cooling time from Austenite to Martensite finish phase has been computed; results have confirmed the soundness of the adopted solution by means of installation of Peltier cells along the S.M.A. tape, showing a sensible cooling time reduction with respect to a natural convection cooling system.
This proposed solution may be considered as the initial track to follow in order to satisfy a time cooling reduction in S.M.A. applications.

Nomenclature

Symbol	Quantity	SI Unit
A	Surface area	m^2
A_f	Austenite finish temperature	$°C$
A_s	Austenite start temperature	$°C$
a	Seebeck coefficient	dimensionless
a_{nm}	Seebeck coefficient medium n-junction	dimensionless
a_{pm}	Seebeck coefficient medium p -junction	dimensionless
α_M	coefficient	dimensionless
b	Peltier cell width	dimensionless
b_M	Slope	dimensionless
b_{SMA}	SMA tape width	m
Bi	Biot number	dimensionless
c	Specific heat	$\frac{J}{kg \cdot °K}$
c_{SMA}	SMA specific heat	$\frac{J}{kg \cdot °K}$
k	Heat conductivity	$\frac{J}{m \cdot s \cdot °K}$
k_n	n-junction heat conductivity	$\frac{J}{m \cdot s \cdot °K}$
k_p	p-junction heat conductivity	$\frac{J}{m \cdot s \cdot °K}$
$\bar{h}$	Heat transfer coefficient	$\frac{J}{m^2 \cdot s \cdot °K}$
I	Current intensity	A
L	Peltier cell length	m
L_{SMA}	SMA tape length	m
M_f	Martensite finish temperature	$°C$
M_s	Martensite start temperature	$°C$
ξ	Martensite Volumetric fraction	%
ξ_0	Initial Martensite Volumetric fraction	%
r	resistivity	Ω
r_n	n-junction resistivity	Ω
r_p	p-junction resistivity	Ω

R_{pelt}	Peltier cell electrical resistance	Ω
ρ	Air Density	$\frac{kg}{m^3}$
ρ_{SMA}	SMA density	$\frac{kg}{m^3}$
σ	Stress load	MPa
s	Peltier transversal section	m
t_{SMA}	SMA tape tick	m
t_{pelt}	Peltier cell thick	m
t_{M_f}	Martensite finish time	sec
t_{M_s}	Martensite start time	sec
T	temperature	$°C$
T_{SMA}	SMA temperature	$°C$
T_{pelt}	Peltier cell temperature	$°C$
$T_{pelt-air}$	Air to Peltier cell temperature	$°C$
T_{∞}	Infinite temperature	$°C$

References

[1] A.L. Martins and F.M. Catalano, "Viscous Drag Optimization for a Transport Aircraft Mission Adaptive Wing", 21st ICAS Congress, Melbourne, Australia Paper A98-31499 (1998).

[2] E. Stanewsky, "Adaptive Wing and Flow Control Technology", Progress in Aerospace Sciences, Elsevier Science Ltd., 37,583-667 (2001).

[3] J. Browman, B. Sanders, T. Weisshaar, "Evaluating the Impact of Morphing Technologies on Aircraft Performance", AIAA J. 2002-1631 (2002)

[4] J. Spillman, "The Use of Variable Chamber to Reduce Drag, Weight and Costs of Transport Aircraft ", Aeronaut. J. 96,1-8 (1992).

[5] H.P. Monner, T. Bein, H. hanselka, E. Breitbach, "Design Aspects of the Adaptive Wing – The Elastic Trailing Edge and Local Spoiler Bump", Royal Aeronautical Society, Multidisciplinary Design and optimization, London, 1998.

[6] Gevers Aircraft Inc., "Multi-Purpose Aircraft", U.S. Patents No. 5,645,250 (1997).

[7] J. Blondeau and D. Pines, "Pneumatic Morphing Aspect Ratio Wing", 45th AIAA/ASME/ASCE/AHS/ASC Structures, Structural Dynamics and Materials Conference, Palm Springs, California, AIAA J. 2004-1888 (2004).

[8] J. R. Wilson, "Active Aeroelastic Wing: A New/Old Twist On Flight", Aerospace America 40(99), 34-37 (2002).

[9] W. J. Buehler, J. V. Gilfrich, R. C. Wiley, 1963, "Effect of low-temperature phase changes on the mechanical properties of alloys near composition TiNi", Journal of Applied Physics 34, 1475 (1963).

[10]] J. C. Contreras Vargas, MSc J. L. Diaz Rodriguez, Ph.D. A. P. Garcia, MSc. M. Figuerona A Peltier Cells Research, Universidad de Pamplona, Facultad de Ingegnerias y Arquitectura Ciutadela Universitaria, Pamplona, Notre de Santander, Colombia (2008).

[11] Tanaka K., 1986, A Thermomechanical Sketch of Shape Memory Effect: One Dimensional Tensile Behaviour, Res. Mech. 18(3), 251-263.

[12] C. Liang and C. A. Rogers, 1990 One- Dimensional Thermomechanical Constitutive Relations For Shape Memory Material, Journal of Intelligent Material Systems and Structures,1 (2), 207-234.

PAPER

"SIX SIGMA" AIDED DESIGN OF A FUSELAGE COMPOSITE PANEL

M.Granito, B. Gambino, G, Iannuzzo, L.Lecce

Paper accepted on Journal of KOMPOZYTY on line publication IV issue ed. 2010 8pp.

"SIX SIGMA" AIDED DESIGN OF A FUSELAGE COMPOSITE PANEL

M.Granito(1), B. Gambino(2), G, Iannuzzo(2), L.Lecce(1)
(1)Dept. of Aerospace Engineering (DIAS) Univ. of Naples "Federico II", Via Claudio, 21, Naples, Italy, 80100, e-mail granito.michele@libero.it, (phone 081-7442274) leonardo@unina.it (phone 081-7683327)
(2)Alenia Aeronautica S.p.A. Viale dell'Aeronautca snc,POmiglianoD'arco, 80038 Naples, Italy, e-mail bgambino@alenia.it ,(phone 081-8872252) giannuzzo@alenia.it (phone 081-8872691)

ABSTRACT

Six Sigma Method (SSM) is included in the "Robust Design" context and allows to reduce the sensitivity to external factors during design and manufacturing phase and during the product lifecycle, too. Organisations like Sony, Honda, Lockeed Martin, Motorola, Toshiba proved to be interested in this method but, only in 1979, Motorola first took into account this method for industrial problems, with the aim of improving product quality and reducing manufacturing costs. 'Six Sigma' ability of meeting customer requirements (in terms of costs and quality) and its intrinsic property of identifying and quantifying design parameters influence on final product performance, makes such method a valid and powerful tool for designers.
In the paper at hand, a design evolution for a composite fuselage panel is presented applying SSM.
At first, basing on a Safety Margin optimized panel, the influence of the design parameters variation was estimated, assuming, as constraint, a deviation of the Safety Margin confined within ±5%. The most critical parameters resulted: the ply thickness, the material allowable strain, the lamina Young moduli along the main plane directions, the shear and Poisson modulus. By randomly varying these parameters, the FE models of novel panels, differing from the optimized one, were generated and, through the MSC\Nastran code, linear static and buckling investigations were performed. Predicted stress field and instability loads were used to compute the Safety Margin, thus achieving a normal distribution. Finally, allowed variation ranges of above mentioned parameters were found out, by verifying that the standard deviations fall within assigned Safety Margin range (i.e. within ±5%). The most critical parameter, both for the stress field generated and for the allowable instability load was the ply thickness, whose allowed excursion proved to be the narrowest one.

Keywords : Six Sigma, Composite, Margin of Safety, Mean value, Deviation Standard

INTRODUCTION

The new generation of aeronautical structures is characterized by light materials and high performance [1]. According to this trend, design efforts lead to use composite structure for envisaged weight and consumption cut down [2]. Due to their intrinsic nature, the investigations on buckling and strength behaviour of composites follows approaches generally different from traditional ones.[3]. In this scenario, criteria able to highlight and quantify design parameters influence on final product performance, play a fundamental role, allowing for compliance to customer requirements. Within the quality optimization field, many groups, like Sony, Honda, Lockeed Martin, Motorola, Toshiba were interested in the Six Sigma Method (SSM), belonging to "Robust Design" typology and relating the Safety Margin of a structural component to the variation of some design parameters; Six Sigma originated as a set of practices designed to improve manufacturing processes and eliminate defects, but its application was subsequently extended to other types of business processes as well [3] [4] [5]; in Six Sigma, a defect is defined as any process output that

does not meet customer specifications, or that could lead to create an output that does not meet the customer
specifications [6]. In a manufacturing context the method is able to focus the possibility of a process to meet the customer need but in a design context, as presented in this work, it means to verify if standard deviation, of each considered design parameter, fall within assigned Safety Margin range (i.e. within ±5%). In this context the SSM is a sound opportunity to solve the problem, so that this approach is included in a "Robust Design" concept to optimize structural parameters during a composite structural design improving the manufacturing process and reducing costs. So that, SSM in a composite design concept leads to show the variation range of each structural parameter to have a desiderate output as presented in this work.
To solve this problem it is common use to introduce a safety coefficient in structural design variable, but, from this point of view, a "Robust Design" leads to deterministic hypothesis connected to variations during a lifecycle as aging of material. This is connected to an increasing uncertainty and a probability of structural failure apart from an increasing manufacturing, repairing and maintenance costs. So that, it is important to know and foresee structural performances for an optimum design concept [7] [8] and this work focuses this aspect. Through a probabilistic approach, based on SSM, by MSC Nastran solver and MSC Patran pre-post processor, a strength and a buckling FEM analysis for a fuselage composite stiffened panel, composed of 2 frames and 3 stringers, have been conducted. During the design phase, target structural parameters, as necessary condition for the application of SSM, have been defined. With a random parameter variation (skin ply thickness th_{skin}, the allowable values ε_{all} , the lamina Young modulus E_{11} and E_{22}, the shear modulus G_{12} and Poisson modulus ν_{12}) , in a defined range, the normal distribution of Margin of Safety by strength analysis and eigenvalues found by buckling analysis, respectively, have been computed. In this way, the most critical design parameters have been determined and, on those ones, the SSM has been applied, determining reliability design requirements and information about design parameter "quality".
GEOMETRY DESCRIPTION AND MODELLING STRATEGY
The considered structure is a composite stiffened panel as in Figure 1 and about this one a strength and a buckling analysis have been conducted. In fact, for a weight saving purpose the added load capability before the ultimate strength of a composite panel is fundamental. A fuselage composite stiffened panel, by a FEM approach with real industrial requirements under Alenia Aeronautica S.p.A. property, has been designed.
The composite panel is a "stiffened" panel and it is composed of 3 omega profile (Figure 2) stringers with a reinforcing rule for the structure along the longer side, and of 2 frames along the shorter side in a perpendicular direction to the stringers. Panel dimensions are: 1270 mm x 674 mm and 0.184 mm thick.
After defining geometry a FEM modelling has been created using cquad4 elements composed of 4 nodes and widely used for this type of approach because of this type of element is able to support in plane forces, bending and shear loads while strain shear out of plane is not considered. So that, this model has a FEM meshing as follows: 20784 nodes and 20940 elements as shown in Figure 1. For our purpose, in order to compare main results, always the same element n. 16584, (Figure 3) between the 2 frames, has been considered. For this panel a composite material (CFRP) has been used composed of 13 plies with the following angular sequence : $45/-45/90/0/45/-45/0/-45/45/0/90/-45/45$ in degree with the following material property as in the Table 1.

th_{skin}	E_{11}	E_{22}	G_{12}	ε_{all}	
0.184 mm	**115000** N/mm^2	**7000** N/mm^2	**3200** N/mm^2	**3500** $\mu strain$	**0.3**

Table 1. Panel material property

A common fuselage panel is simultaneously loaded by distributed compressive load and also by shear load; so that the following panel has been loaded by a compressive load ($50N$) on the longer side and by a shear flux ($26.5N/mm$) on the shorter side. In order to have a static determinate structure, boundary conditions for the panel have been applied. On the longer front side in the FEM model (Figure 1) the left node has been hinged and the right node has been embedded while along the four sides of the panel simply supported nodes have been included. In the following, two analysis, strength and buckling, shall be presented.

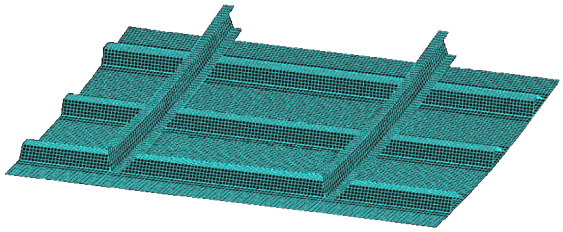

Figure 1. FEM meshing of the panel

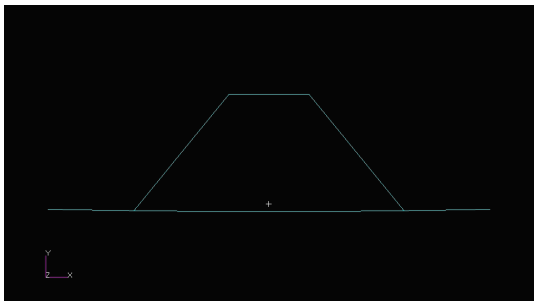

Figure 2. Omega profile stringer

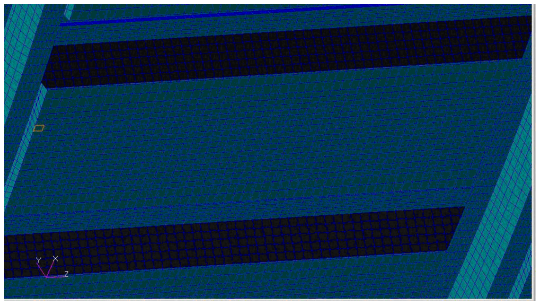

Figure 3. Node n.16584

STRENGTH ANALYSIS

At first, a strength analysis on the panel, using a FEM approach by a static linear analysis,

through the Nastran SOL 101, has been conducted. The design parameters of the panel for the strength analysis are in Table 2.

Mechanical parameters	Design parameters
$E_{11}\ (N/mm^2)$	115000
$E_{22}\ (N/mm^2)$	7000
$th_{skin}\ (mm)$	0.184
$\varepsilon_{all}\ (\mu strain)$	3500
$G_{12}\ (N/mm^2)$	3200
ν_{12}	0.3

Table 2. Panel design parameter for strength analysis

After this, the related Margin of Safety (MoS) have been evaluated for the element n. 16584 considering $MoS = 1.54$ as target value reference for the application of SSM.
In this analysis what is the influence of design parameters, in allowed variation range, on the MoS perturbation for a Robust Design, is the main purpose. So that, in order to apply the SSM, design parameters have been evaluated to determine which of these ones are critical for the MoS target value. In the Table 3 a defined variation range for each parameter is shown.

Mechanical parameters	Variation range
$E_{11}\ (N/mm^2)$	110000 - 12000
$E_{22}\ (N/mm^2)$	6000 - 8000
$th_{skin}\ (mm)$	0.175 – 0.187
$\varepsilon_{all}\ (\mu strain)$	3500 - 4100
$G_{12}\ (N/mm^2)$	2500 - 3900

Table 3. Panel design variation for strength analysis

According to a statistical approach in order to change randomly each of six parameters, by means of a numerical tool, a variation range has been defined. So that, 100 linear static analysis have been run for each parameter, so for 6 of these ones 600 SOL 101 analysis have been computed. This computational effort, according to the statistical approach, has been fundamental in order to have a more and more real result. The application of SSM is based on the requirement that standard deviation σ has to fall within $1/12$ of the requirement width as target Margin of Safety (MoS) for our purpose. Before applying the method the target value of $MoS = 1.54$, found for optimized panel, has been defined. From this target value upper and lower limits, respectively $1.54 + 5\%$ and $1.54 - 5\%$, according to this formula $\Delta = \frac{1.61 - 1.47}{1.54} = 0.1$, have been computed in order to verify the process capability in terms of bandwidth requirements. Standard deviation σ has to fall within $1/12$ of the requirement width, Δ □□, so finding the following reference value for the method application: $\sigma = \frac{\Delta}{12} = 0.008$. So that, a numerical tool has computed the MoS for

each of 100 random value related to six design parameters (in all 600 values); then the MoS mean value μ and standard deviation σ have been estimated, in order to check if the process is centred ($\mu = 1.54$) and is capable ($\sigma \leq 0.008$) so determining what design parameters are critical for a Robust Design concept, purpose of this work.
The tool, in Visual Basic language, selected the ply sequence and selected 100 values for the considered design parameters, automatically changes the values in the .bdf file and then generates other 100 .bdf files that can be analyzed by Nastran solver. By this procedure, for each of six parameters, in a more restricted range where the method is applicable, from 100 MoS values, the mean value μ, the standard deviation σ and normal distribution have been computed (Table 4).

Mechanical parameters	Variation range	Mean value (M.S.)	St. deviation	Six Sigma requirements
$E_{11}\ (N/mm^2)$	114500 - 115500	1.544	0.005685	yes
$E_{22}\ (N/mm^2)$	6500 - 7500	1.543	0.006765	yes
$th_{skin}\ (mm)$	**0.183 – 0.185**	**1.543**	**0.009574**	**no**
$\varepsilon_{all}\ (\mu strain)$	3790 - 3810	1.544	0.00492	yes
$G_{12}\ (N/mm^2)$	3000 - 3400	1.544	0.00747	yes

Table 4. Panel variation range and Six Sigma requirements for strength analysis

Only ν_{12} is always centred (mean value $\mu = 1.54$) and capable (standard deviation $\sigma = 0$) and so it does not influence the panel design.
By the analysis of results it is evident that E_{11}, E_{22} and G_{12} have a smooth influence on mean value μ and standard deviation σ so that, they are not too critical for the application of the SSM and for a Robust Design. On the other hand, ply th_{skin} results critical, in fact, for this parameter, even if the allowed variation range is very small and the process is centred (mean value $\mu = 1.54$), however, standard deviation value is not acceptable ($\sigma = 0.009574 > 0.008$) and so, the process may not be considered capable.
So that, during the design process, this parameter shall be relevant for the panel and, on that one, in a Robust Design design concept efforts shall be focused.

BUCKLING ANALYSIS

In order to determinate the instability behaviour, after the strength analysis, on the composite stiffened panel, a buckling analysis has been conducted, too. Buckling analysis is based on the Eigenvalues computation, through SOL 105 Nastran solution, for the panel area between the two frames as in Figure 3. So that, design

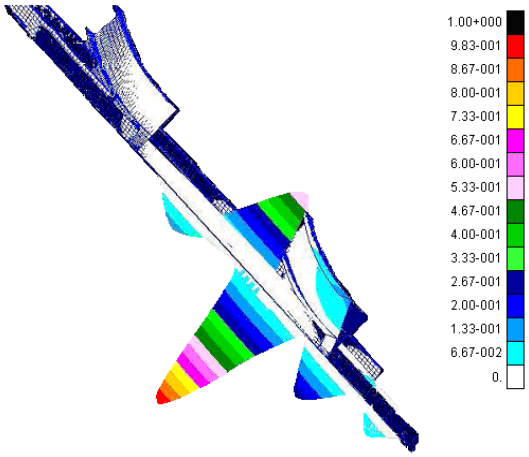

Figure 5: Buckling analysis for optimized panel (particular)

By buckling analysis ply th_{skin} is the most critical design parameter; E_{11} in a more restricted range is compliant to the requirements with a low standard deviation, as for G_{12} that in a restricted range respects the requirements with a standard deviation very low as shown in Table 5. For th_{skin}, even if in a small range $0.182-0.184mm$, through buckling analysis, a too high standard deviation value has been found. So that, for a composite stiffened panel design, during strength analysis and buckling analysis, this one is the most critical design parameter as presented during the investigation.

In a Robust Design concept, aim of this work, ply th_{skin} is the design parameter to be optimized to have a performance improvement.

CONCLUSIONS AND FURTHER STEPS

In this work a Six Sigma Method (SSM) application has been presented in a design approach.

SSM, in a Robust Design concept, leads to reduce the sensitivity to external factors during design and manufacturing phase and during the lifecycle, too. At first, while this method interested many groups (Motorola, Lockeed Martin etc.) to improve the product quality and to cut down manufacturing cost in order to meet the customer need, in a design concept, as presented in this paper, this method leads to estimate what are the most important design parameters and which of these ones are critical for the panel design. By knowing the critical design parameters a design improvement, weight reduction and cost cut down are possible before manufacturing phase.

The composite panel, under investigation, is a "stiffened" panel and it is composed of 3 omega profile stringers with a reinforcing rule for the structure along the longer side, and of 2 frames along the shorter side in a perpendicular direction to the stringer. In this paper two types of studies have been conducted on the panel: a strength analysis and a buckling analysis. The first analysis, by randomly varying design parameters, has shown that the ply thickness of the skin, th_{skin}, is the most important design parameter because it influences the method in terms of mean value and standard deviation and it does not respect the SSM requirements in terms of capability process. The target value for the method application is $MoS = 1.54$ for the optimized panel. Randomly varying parameters, by a numerical tool, MoS have been computed and for each design parameter has been verified if the standard

deviation value falls within assigned Margin of Safety (MoS) range (MoS±5%). With respect to other parameters during strength analysis (ply th_{skin}, E_{11}, G_{12}, ε_{all}, E_{22}, ν_{12}) ply th_{skin} is the critical parameter on the MoS and for this reason, on that one, efforts shall be focused. For the buckling analysis in terms of computed eigenvalue, according to the target value ($\lambda = 1.0182$), the critical parameter is still th_{skin}, in fact, even if in a restricted variation range, it does not fall within assigned range (λ ±5%). Results show what is the panel sensitivity and provide indications for a design improvement. For the two analysis (strength and buckling) ply th_{skin} has been critical for the design; from this point of view the result acceptability confirms the correct approach and this leads to further application of the method. A future application could deal with a study on a stiffened composite panel with a different lay up sequence to show different behaviour on a design parameter. Other studies could be interested to a post-buckling analysis or to a mixed load conditions on the panel.

BIBLIOGRAPHY

[1] Pecora R., Analisi della lamina ortotropa e teoria classica dei laminati, Italy (2006) 2-10.

[2] Davidson, B.D., Hu, H., and Schapery, R.A., An Analytical Crack Tip Element for Layered Elastic Structures, Journal of Applied Mechanics, (1995) 294-305.

[3] Kinloch, A.J., Wang, Y., Williams, J.G., and Yayla, P., The Mixed-Mode Delamination of Fibre Composite Materials, Composites Science and Technology (1993) 225-237.

[4] Davidson B.D., A Predictive Methodology for Delamination Growth in Laminated composites -Theoretical Development and preliminary experimental results Part I (1998) 1-3.

[5] Davidson B.D., A Predictive Methodology for Delamination Growth in Laminated composites Analysis- Applications and Accuracy Assessment (1998) 3-5.

[6] Radha Kismha and Dangayach, G.S., Six Sigma Implementation at an Auto Component Manufacturing Plant: A Case Study , International Journal of Six Sigma and Competitive Advantage, (2007). 282-302

[7] Lecce L., Metodo degli elementi finiti, Italy (2006) 10-15.

[8] Dickson J. N. and. Cole R.T, Design of Stiffened Composite Panels in the Post Buckling Range, USA (1978) 313-314.

Tools and numerical simulations

In this section a general overview of Matlab tools creared and related obtained simulations through Nastran code according to a Fem approach here are presented.

Matlab tools

Equationver2 tool

```
clc ;
close all;
clear all;
figure(1);
Iv=[0:.1:10];
for i=1:length(Iv)
   alfa_t=1;
   I=Iv(i);
   c_SMA=837;
   ro_SMA=6500;
   t_SMA=1e-3;
   L=1e-2;
   b=1e-2;
   h=11.63;
   T_inf=10+273;
   a=100e-3;
   t_pelt=4e-3;
   R_pelt=.0005*((0.46+0.46)/2)*t_pelt/(L*b*0.25);
   k_p=148/10;
   k_n=59.9/10;
   csi_0=0;
   Ms=43.3+273;
   Mf=27.5+273;
   As=47.3+273;
   Af=58.9+273;
   T_ini=Af+50;
   T_fin=Mf;
   T_Peltier_aria=T_inf;
   c_M=8e6;
   alfa_M=pi/(Ms-Mf);
   b_M=-alfa_M/c_M;
   tempo_0=0;
   Aa=c_SMA*ro_SMA*(t_SMA*L*b);
   Ba=h*L*b+(k_p+k_n)*(L*b)/t_pelt+2*a*I;
   Ca=h*L*b*T_inf+((k_p+k_n)*(L*b)/t_pelt)*T_Peltier_aria+R_pelt*I^2;
   tempo_Ms=-(Aa/Ba)*log((Ca-Ba*Ms)/(Ca-Ba*T_ini))+tempo_0;

   At=(ro_SMA*(t_SMA*L*b)*c_SMA)*(1-alfa_t*Ms/(Ms-Mf));
   Bt=(ro_SMA*(t_SMA*L*b)*c_SMA)*alfa_t*2/(Ms-Mf);
   Ct=-(h*L*b+(k_p+k_n)*(L*b)/t_pelt+2*a*I);
```

```
   Dt=((k_p+k_n)*(L*b)/t_pelt)*T_Peltier_aria+R_pelt*I^2;
            tempo_Mf=tempo_Ms+(At/Ct)*log((Dt+Ct*Mf)/(Dt+Ct*Ms))+(Bt/Ct)*(Mf-Ms)-
(Bt*Dt/Ct^2)*log((Dt+Ct*Mf)/(Dt+Ct*Ms));
   tempo_Msv(i)=tempo_Ms;
   tempo_Mfv(i)=tempo_Mf;
end
figure (1);
semilogy(Iv,tempo_Msv,'b',Iv,tempo_Mfv-tempo_Msv,'r',Iv,tempo_Mfv,'k');
legend('T_0 -> M_s time','M_s -> M_f time','T_0 -> M_f time ');
xlabel('Current Intensity (A)');
ylabel('Time (s)');
grid on;
```

cooling tool

```
clc ;
close all;
clear all;
figure(1);
Iv=[0:.1:10];
for i=1:length(Iv)
   alfa_t=1;
   I=Iv(i);
   c_SMA=837;
   ro_SMA=6500;
   t_SMA=1e-3;
   L=1e-2;
   b=1e-2;
   h=11.63;
   T_inf=10+273;
   a=100e-3;
   t_pelt=4e-3;
   R_pelt=.0005*((0.46+0.46)/2)*t_pelt/(L*b*0.25);
   k_p=148/10;
   k_n=59.9/10;
   csi_0=0;
   Ms=43.3+273;
   Mf=27.5+273;
   As=47.3+273;
   Af=58.9+273;
   T_ini=Af+50;
   T_fin=Mf;
   T_Peltier_aria=T_inf;
   c_M=8e6;
   alfa_M=pi/(Ms-Mf);
   b_M=-alfa_M/c_M;
   tempo_0=0;
   Aa=c_SMA*ro_SMA*(t_SMA*L*b);
   Ba=h*L*b+(k_p+k_n)*(L*b)/t_pelt+2*a*I;
   Ca=h*L*b*T_inf+((k_p+k_n)*(L*b)/t_pelt)*T_Peltier_aria+R_pelt*I^2;
```

```
    tempo_Ms=-(Aa/Ba)*log((Ca-Ba*Ms)/(Ca-Ba*T_ini))+tempo_0;

    At=(ro_SMA*(t_SMA*L*b)*c_SMA)*(1-alfa_t*Ms/(Ms-Mf));
    Bt=(ro_SMA*(t_SMA*L*b)*c_SMA)*alfa_t*2/(Ms-Mf);
    Ct=-(h*L*b+(k_p+k_n)*(L*b)/t_pelt+2*a*I);
    Dt=((k_p+k_n)*(L*b)/t_pelt)*T_Peltier_aria+R_pelt*I^2;
            tempo_Mf=tempo_Ms+(At/Ct)*log((Dt+Ct*Mf)/(Dt+Ct*Ms))+(Bt/Ct)*(Mf-Ms)-
(Bt*Dt/Ct^2)*log((Dt+Ct*Mf)/(Dt+Ct*Ms));
    tempo_Msv(i)=tempo_Ms;
    tempo_Mfv(i)=tempo_Mf;
end
figure (1);
semilogy(Iv,tempo_Msv,'b',Iv,tempo_Mfv-tempo_Msv,'r',Iv,tempo_Mfv,'k');
legend('T_0 -> M_s time','M_s -> M_f time','T_0 -> M_f time ');
xlabel('Current Intensity (A)');
ylabel('Time (s)');
grid on;
```

parameter tool

```
clc;
close all;
clear all;
I=100.0;
T_aria=20.0;
t_Pelt=4e-3;
a_Pelt=0.01;
b_Pelt=0.02;
t_SMA=1e-3;
k_SMA=18.0;
cp_SMA=837.0;
ro_SMA=6500;
h_SMA=110.63;
T_mart=27.5;
T_delta=15.8;
Q_lat=24.2e3;
k_Pelt=104.;
cp_Pelt=510.0;
ro_Pelt=3826.0;
h_Pelt=110.63;
h_Pelt_aT=300.00*I;
t=[0 50 100 500];
Pow_scale=[0 1 1 1];
power=9200;
T_all=100;
% scrivi geometria
fid_geo=fopen('geometria_n.dat','w');
    fprintf(fid_geo,'GRID,1,,0.0,0.0,0.0\n');
    fprintf(fid_geo,'GRID,2,,%8.5f,0.0,0.0\n',a_Pelt);
    fprintf(fid_geo,'GRID,3,,%8.5f,%8.5f,0.0\n',a_Pelt,b_Pelt);
```

```
    fprintf(fid_geo,'GRID,4,,0.0,%8.5f,0.0\n',b_Pelt);
    fprintf(fid_geo,'GRID,5,,0.0,0.0,%8.5f\n',t_Pelt);
    fprintf(fid_geo,'GRID,6,,%8.5f,0.0,%8.5f\n',a_Pelt,t_Pelt);
    fprintf(fid_geo,'GRID,7,,%8.5f,%8.5f,%8.5f\n',a_Pelt,b_Pelt,t_Pelt);
    fprintf(fid_geo,'GRID,8,,0.0,%8.5f,%8.5f\n',b_Pelt,t_Pelt);
    fprintf(fid_geo,'GRID,9,,0.0,0.0,%8.5f\n',t_Pelt+t_SMA);
    fprintf(fid_geo,'GRID,10,,%8.5f,0.0,%8.5f\n',a_Pelt,t_Pelt+t_SMA);
    fprintf(fid_geo,'GRID,11,,%8.5f,%8.5f,%8.5f\n',a_Pelt,b_Pelt,t_Pelt+t_SMA);
    fprintf(fid_geo,'GRID,12,,0.0,%8.5f,%8.5f\n',b_Pelt,t_Pelt+t_SMA);
    fprintf(fid_geo,'$ NODO FLUIDO SUPERIORE\n');
    fprintf(fid_geo,'GRID,99,,99.0,99.0,99.0\n');
    fprintf(fid_geo,'$ NODO FLUIDO INFERIORE\n');
    fprintf(fid_geo,'GRID,199,,99.0,99.0,-99.0\n');
    fprintf(fid_geo,'$ NODO RIFERIMENTO PELTIER\n');
    fprintf(fid_geo,'GRID,299,,99.0,-99.0,-99.0\n');
    fprintf(fid_geo,'$ hexa della cella di Peltier\n');
    fprintf(fid_geo,'CHEXA,1,6,1,2,3,4,5,6,+CHX1\n');
    fprintf(fid_geo,'+CHX1,7,8\n');
    fprintf(fid_geo,'$ hexa del nastro SMA\n');
    fprintf(fid_geo,'CHEXA,2,5,5,6,7,8,9,10,+CHX2\n');
    fprintf(fid_geo,'+CHX2,11,12\n');
fclose(fid_geo);
%
% scrivi materiali
fid_mat=fopen('materiali_n.dat','w');
    fprintf(fid_mat,'$ materiale SMA\n');
                                                fprintf(fid_mat,'MAT4,15,%8.3f,%8.3f,%8.2f,
%8.3f,,,0.0,+MAT4\n',k_SMA,cp_SMA,ro_SMA,h_SMA);
    fprintf(fid_mat,'+MAT4,%8.3f,%8.3f,%8.1f\n',T_mart,T_delta,Q_lat);
    fprintf(fid_mat,'$ materiale Peltier\n');
                                                fprintf(fid_mat,'MAT4,16,%8.3f,%8.3f,%8.2f,
%8.3f,,1.0,0.0\n',k_Pelt,cp_Pelt,ro_Pelt,h_Pelt);
    fprintf(fid_mat,'$ materiale Peltier per la sola simulazione di aT\n');
                                                fprintf(fid_mat,'MAT4,17,%8.3f,%8.3f,%8.2f,
%8.1f,,1.0,0.0\n',k_Pelt,cp_Pelt,ro_Pelt,h_Pelt_aT);
fclose(fid_mat);
%
% scrivi carico termico
fid_loa=fopen('carichi_n.dat','w');
    fprintf(fid_loa,'TLOAD1,200,300,,,400\n');
    fprintf(fid_loa,'TABLED1,400,,,,,,,,+TBD1\n');
                    fprintf(fid_loa,'+TBD1                %8.3f%8.3f%8.3f%8.3f%8.3f%8.3f%8.3f
%8.3f+TBD2\n',t(1),Pow_scale(1),t(2),Pow_scale(2),t(3),Pow_scale(3),t(4),Pow_scale(4));
    fprintf(fid_loa,'+TBD2,ENDT\n');
    fprintf(fid_loa,'QVOL        300%8.1f      8       1\n',power);
    fprintf(fid_loa,'SPC          10      99       %8.3f\n',T_aria);
    fprintf(fid_loa,'TEMP         20      99%8.3f     299     0.0\n',T_aria);
    fprintf(fid_loa,'TEMPD        20%8.3f\n',T_all);
fclose(fid_loa);
! C:\MSC.Software\MSC_Nastran\bin\nastran core.dat scr=yes old=no
```

```
fid_pch=fopen('core.pch');
k=0;
while (feof(fid_pch)==0)
   for i=1:7
      linea=fgetl(fid_pch);
      llinea=length(linea);
   end
   k=k+1;
   punto(k)=str2num(linea(12:24));
   for i=1:2000
      linea=fgetl(fid_pch);
      Temper(i,k)=str2num(linea(41:end));
   end
end
Tempo=linspace(0,1600,2000);
fclose(fid_pch);
hold on;
plot(Tempo,Temper(:,8));
```

parameter ver2new tool

```
clc;
close all;
clear all;
colore='kbrcmgy';
%Iv=[0.1 0.3 0.5 0.7 1 2 3];
Iv=[0 0.2 0.4 0.6 0.8 1 1.2 1.4 1.6 1.8 2.0 2.2 2.4 2.6 2.8 3.0];
for caso=1:length(Iv)
   fclose all;
   ! del core_par.pch
   ! del core_par.f06
   ! del GRID.dat
   ! del MAT.dat
   ! del carichi.dat
   ! del NOLIN.dat
   I=Iv(caso)
   T_aria=20.0;
   t_Pelt=4e-3;
   a_Pelt=0.01;
   b_Pelt=0.01;
   t_SMA=1e-3;
   k_SMA=18.0;
   cp_SMA=837.0;
   ro_SMA=6500;
   h_SMA=110.63;
   T_mart=27.5;
   T_delta=15.8;
   Q_lat=24.2e3;
   k_Pelt=104.;
   cp_Pelt=510.0;
```

```
ro_Pelt=3826.0;
h_Pelt=110.63;
aT=-I*0.01;
t=[0 3 100 500];
Pow_scale=[0 1 1 1];
power=920*1.0;
T_all=100;
Time_incr=0.1001;
nome_file='core_par.dat';
% scrittura geometria
fid_geo=fopen('GRID.dat','w');
fprintf(fid_geo,'GRID,1,,0.0,0.0,0.0\n');
fprintf(fid_geo,'GRID,2,,%8.5f,0.0,0.0\n',a_Pelt);
fprintf(fid_geo,'GRID,3,,%8.5f,%8.5f,0.0\n',a_Pelt,b_Pelt);
fprintf(fid_geo,'GRID,4,,0.0,%8.5f,0.0\n',b_Pelt);
fprintf(fid_geo,'GRID,5,,0.0,0.0,%8.5f\n',t_Pelt);
fprintf(fid_geo,'GRID,6,,%8.5f,0.0,%8.5f\n',a_Pelt,t_Pelt);
fprintf(fid_geo,'GRID,7,,%8.5f,%8.5f,%8.5f\n',a_Pelt,b_Pelt,t_Pelt);
fprintf(fid_geo,'GRID,8,,0.0,%8.5f,%8.5f\n',b_Pelt,t_Pelt);
fprintf(fid_geo,'GRID,9,,0.0,0.0,%8.5f\n',t_Pelt+t_SMA);
fprintf(fid_geo,'GRID,10,,%8.5f,0.0,%8.5f\n',a_Pelt,t_Pelt+t_SMA);
fprintf(fid_geo,'GRID,11,,%8.5f,%8.5f,%8.5f\n',a_Pelt,b_Pelt,t_Pelt+t_SMA);
fprintf(fid_geo,'GRID,12,,0.0,%8.5f,%8.5f\n',b_Pelt,t_Pelt+t_SMA);
fprintf(fid_geo,'$ NODO FLUIDO SUPERIORE\n');
fprintf(fid_geo,'GRID,99,,99.0,99.0,99.0\n');
fprintf(fid_geo,'$ NODO FLUIDO INFERIORE\n');
fprintf(fid_geo,'GRID,199,,99.0,99.0,-99.0\n');
fprintf(fid_geo,'$ NODO RIFERIMENTO PELTIER\n');
fprintf(fid_geo,'GRID,299,,99.0,-99.0,-99.0\n');
fprintf(fid_geo,'$ hexa della cella di Peltier\n');
fprintf(fid_geo,'CHEXA,1,6,1,2,3,4,5,6,+CHX1\n');
fprintf(fid_geo,'+CHX1,7,8\n');
fprintf(fid_geo,'$ hexa del nastro SMA\n');
fprintf(fid_geo,'CHEXA,2,5,5,6,7,8,9,10,+CHX2\n');
fprintf(fid_geo,'+CHX2,11,12\n');
fclose(fid_geo);
% fine srittura geometria

% scrivi materiali
fid_mat=fopen('MAT.dat','w');
fprintf(fid_mat,'$ materiale SMA\n');
                                        fprintf(fid_mat,'MAT4,15,%8.3f,%8.3f,%8.2f,
%8.3f,,1.0,0.0,+MAT4\n',k_SMA,cp_SMA,ro_SMA,h_SMA);
fprintf(fid_mat,'+MAT4,%8.3f,%8.3f,%8.1f\n',T_mart,T_delta,Q_lat);
fprintf(fid_mat,'$ materiale Peltier\n');
                                        fprintf(fid_mat,'MAT4,16,%8.3f,%8.3f,%8.2f,
%8.3f,,,0.0,0.0\n',k_Pelt,cp_Pelt,ro_Pelt,h_Pelt);
fclose(fid_mat);
% fine scrivi materiali
```

```
% scrivi carico termico
fid_loa=fopen('carichi.dat','w');
fprintf(fid_loa,'TLOAD1,200,300,,,400\n');
fprintf(fid_loa,'TABLED1,400,,,,,,,,+TBD1\n');
                fprintf(fid_loa,'+TBD1              %8.3f%8.3f%8.3f%8.3f%8.3f%8.3f%8.3f
%8.3f+TBD2\n',t(1),Pow_scale(1),t(2),Pow_scale(2),t(3),Pow_scale(3),t(4),Pow_scale(4));
fprintf(fid_loa,'+TBD2,ENDT\n');
fprintf(fid_loa,'QVOL        300%8.1f       8       1\n',power);
fprintf(fid_loa,'SPC          10      99       %8.3f\n',T_aria);
fprintf(fid_loa,'TEMP         20      99%8.3f     299     0.0\n',T_aria);
fprintf(fid_loa,'TEMPD        20%8.3f\n',T_all);
fclose(fid_loa);

% scrivi carico nonlineare(aT)
fid_NLI=fopen('NOLIN.dat','w');
fprintf(fid_NLI,'NOLIN1,333,5,1,%8.4f,5,1,444\n',aT);
fprintf(fid_NLI,'NOLIN1,333,6,1,%8.4f,6,1,444\n',aT);
fprintf(fid_NLI,'NOLIN1,333,7,1,%8.4f,7,1,444\n',aT);
fprintf(fid_NLI,'NOLIN1,333,8,1,%8.4f,8,1,444\n',aT);
fclose(fid_NLI);

%! C:\MSC.Software\MSC_Nastran\bin\nastran core_par.dat scr=yes old=no
!C:\MSC.Software\MSC.Nastran\bin\nastran core_par.dat scr=yes old=no
% lettura pch
fid_pch=fopen('core_par.pch','r');
for ii=1:7
   linea=fgetl(fid_pch);
end
ii=0;
while(feof(fid_pch)==0)
   linea=fgetl(fid_pch);
   llinea=length(linea);
   v=str2num(linea(11:end));
   ii=ii+1;
   tempo(ii)=v(1);
   temper(ii)=v(3);
end
fclose(fid_pch);
figure(1);
hold on;
if caso<=7
   plot(tempo, temper,colore(caso));
elseif caso>7 & caso<=14
   plot(tempo, temper,[colore(caso-7),'-.']);
elseif caso>14
   plot(tempo, temper,[colore(caso-14),'.']);
end
hold on;
xlabel('Time [s]');
ylabel('SMA / Peltier interface Temperature [°C]');
```

```
    grid on;
    axis([0 500 0 120])
end
%legend('0.1 A','0.3 A','0.5 A','0.7 A','1 A', '2 A', '3 A');

plot([tempo(1), tempo(end)],[T_mart, T_mart],'r');
plot([tempo(1), tempo(end)],[T_mart, T_mart]+T_delta,'r');
title('Intensity: 0 to 3 A');

file prova
clc;
close all;
clear all;
T = [125.3 55.17 38.05 30.00 25.35 23.40 22.17 20.10 19.70 18.75 17.97 17.23 16.67 16.45
15.7 15.0];
I = [0 0.2 0.4 0.6 0.8 1 1.2 1.4 1.6 1.8 2.0 2.2 2.4 2.6 2.8 3.0];
plot (I,T, 'r');
xlabel('Current Intensity (I)');
ylabel('Temperature °C');
legend ('sigma=0 Mpa')
grid on;

T = [71.85 38.15 27.85 22.75 19.60 17.58 17.56 16.75 16.15 16.05 15.55 13.37 12.77 12.55
12.50 12.40];
I = [0 0.2 0.4 0.6 0.8 1 1.2 1.4 1.6 1.8 2.0 2.2 2.4 2.6 2.8 3.0];
plot (I,T, 'r');
xlabel('Current Intensity (I)');
ylabel('Temperature °C');
legend ('sigma=150 Mpa')
grid on;

T = [176.04 70.92 53.35 41.30 34.30 29.75 26.47 24.09 23.63 23.18 22.18 21.18 20.75
20.23 19.53 19.4];
I = [0 0.2 0.4 0.6 0.8 1 1.2 1.4 1.6 1.8 2.0 2.2 2.4 2.6 2.8 3.0];
plot (I,T, 'r');
xlabel('Current Intensity (I)');
ylabel('Temperature °C');
legend ('sigma=0 Mpa, t_S_M_A=2mm')
grid on;

T = [98.70 53.0 38.0 30.4 26.8 22.7 20.5 19.0 18.3 17.7 17.65 17.15 16.68 16.60 16.5
16.0];
I = [0 0.2 0.4 0.6 0.8 1 1.2 1.4 1.6 1.8 2.0 2.2 2.4 2.6 2.8 3.0];
plot (I,T, 'r');
xlabel('Current Intensity (I)');
ylabel('Temperature °C');
legend ('sigma=150 Mpa, t_S_M_A=2mm')
grid on;
```

```
T = [100.35 48.21 34.07 27.13 23.11 20.40 19.63 18.55 18.53 17.73 17.05 16.40 15.98
15.09 14.60 14.50];
I = [0 0.2 0.4 0.6 0.8 1 1.2 1.4 1.6 1.8 2.0 2.2 2.4 2.6 2.8 3.0];
plot (I,T, 'r');
xlabel('Current Intensity (A)');
ylabel('Time (sec)');
legend ('sigma=50 Mpa, t_S_M_A=1mm')
grid on;

T = [63.96 34.78 28.83 21.18 18.43 16.63 16.11 15.28 14.33 13.03 12.47 12.10 12.00 11.75
11.50 11.00];
I = [0 0.2 0.4 0.6 0.8 1 1.2 1.4 1.6 1.8 2.0 2.2 2.4 2.6 2.8 3.0];
plot (I,T, 'r');
xlabel('Current Intensity (A)');
ylabel('Time (sec)');
legend ('sigma=200 Mpa, t_S_M_A=1mm')
grid on;

T = [84.71 43.00 30.93 24.94 21.30 19.03 18.58 17.63 17.31 16.94 16.25 15.52 14.67 13.97
13.50 13.40];
I = [0 0.2 0.4 0.6 0.8 1 1.2 1.4 1.6 1.8 2.0 2.2 2.4 2.6 2.8 3.0];
plot (I,T, 'r');
xlabel('Current Intensity (A)');
ylabel('Time (sec)');
legend ('sigma=100 Mpa, t_S_M_A=1mm')
grid on;

T = [117.10 60.22 42.38 33.60 28.31 24.91 22.31 20.47 19.56 19.07 18.80 18.11 17.95
17.52 17.20 16.90];
I = [0 0.2 0.4 0.6 0.8 1 1.2 1.4 1.6 1.8 2.0 2.2 2.4 2.6 2.8 3.0];
plot (I,T, 'r');
xlabel('Current Intensity (A)');
ylabel('Time (sec)');
legend ('sigma=100 Mpa, t_S_M_A=2mm')
grid on;

T = [139.70 68.20 47.22 37.07 31.05 27.07 24.20 22.11 20.75 20.43 19.89 19.15 19.08
18.43 17.95 17.50];
I = [0 0.2 0.4 0.6 0.8 1 1.2 1.4 1.6 1.8 2.0 2.2 2.4 2.6 2.8 3.0];
plot (I,T, 'r');
xlabel('Current Intensity (A)');
ylabel('Time (sec)');
legend ('sigma=50 Mpa, t_S_M_A=2mm')
grid on;

T = [87.40 48.12 34.88 28.09 24.04 21.24 19.28 17.90 17.67 17.05 16.72 16.06 15.81 15.50
14.70 14.05];
I = [0 0.2 0.4 0.6 0.8 1 1.2 1.4 1.6 1.8 2.0 2.2 2.4 2.6 2.8 3.0];
plot (I,T, 'r');
xlabel('Current Intensity (A)');
```

```
ylabel('Time (sec)');
legend ('sigma=200 Mpa, t_S_M_A=2mm')
grid on;

T = [83.06 47.05 34.26 28.08 24.09 23.03 21.30 20.03 19.40 19.31 18.40 17.70 17.08 16.50
16.18 15.30];
I = [0 0.2 0.4 0.6 0.8 1 1.2 1.4 1.6 1.8 2.0 2.2 2.4 2.6 2.8 3.0];
plot (I,T, 'r');
xlabel('Current Intensity (A)');
ylabel('Time (sec)');
legend ('sigma=0 Mpa, t_S_M_A=1mm, Tempext=10°C')
grid on;


T = [57.09 34.25 25.90 21.75 19.06 17.30 17.17 16.55 15.93 15.60 14.80 13.25 12.95 12.56
12.42 12.20];
I = [0 0.2 0.4 0.6 0.8 1 1.2 1.4 1.6 1.8 2.0 2.2 2.4 2.6 2.8 3.0];
plot (I,T, 'r');
xlabel('Current Intensity (A)');
ylabel('Time (sec)');
legend ('sigma=150 Mpa, t_S_M_A=1mm, Tempext=10°C')
grid on;
```

Nastran code

File pch core par

```
$TITLE   = EXAMPLE 7F1
$SUBTITLE=
$LABEL   =
$TEMPERATURE
$REAL OUTPUT
$SUBCASE ID =         1
$POINT ID =         8  IDENTIFIED BY TIME
TEMP*                 1               8    1.000000E+02
TEMP*                 2               8    9.929634E+01
TEMP*                 3               8    9.821316E+01
TEMP*                 4               8    9.657050E+01
TEMP*                 5               8    9.375535E+01
TEMP*                 6               8    8.395661E+01
TEMP*                 7               8    7.532965E+01
TEMP*                 8               8    6.756145E+01
TEMP*                 9               8    6.062932E+01
TEMP*                10               8    5.496104E+01
TEMP*                11               8    5.182650E+01
TEMP*                12               8    4.912154E+01
TEMP*                13               8    4.667651E+01
```

TEMP*	14	8	4.433031E+01
TEMP*	15	8	4.212275E+01
TEMP*	16	8	3.995329E+01
TEMP*	17	8	3.311872E+01
TEMP*	18	8	2.693613E+01
TEMP*	19	8	2.191257E+01
TEMP*	20	8	1.795211E+01
TEMP*	21	8	1.474195E+01
TEMP*	22	8	1.220111E+01
TEMP*	23	8	1.014836E+01
TEMP*	24	8	8.519314E+00
TEMP*	25	8	7.206080E+00
TEMP*	26	8	6.161981E+00
TEMP*	27	8	5.321633E+00
TEMP*	28	8	4.652583E+00
TEMP*	29	8	4.114751E+00
TEMP*	30	8	3.686086E+00
TEMP*	31	8	3.341830E+00
TEMP*	32	8	3.067240E+00
TEMP*	33	8	2.846818E+00
TEMP*	34	8	2.670946E+00
TEMP*	35	8	2.529820E+00
TEMP*	36	8	2.417175E+00
TEMP*	37	8	2.326818E+00
TEMP*	38	8	2.254670E+00
TEMP*	39	8	2.196818E+00
TEMP*	40	8	2.150609E+00
TEMP*	41	8	2.113567E+00
TEMP*	42	8	2.083972E+00
TEMP*	43	8	2.060254E+00
TEMP*	44	8	2.041300E+00
TEMP*	45	8	2.026114E+00
TEMP*	46	8	2.013975E+00
TEMP*	47	8	2.004250E+00
TEMP*	48	8	1.996476E+00
TEMP*	49	8	1.990250E+00
TEMP*	50	8	1.985271E+00
TEMP*	51	8	1.981284E+00
TEMP*	52	8	1.978095E+00
TEMP*	53	8	1.975542E+00
TEMP*	54	8	1.973500E+00
TEMP*	55	8	1.971865E+00
TEMP*	56	8	1.970558E+00
TEMP*	57	8	1.969511E+00
TEMP*	58	8	1.968673E+00
TEMP*	59	8	1.968003E+00
TEMP*	60	8	1.967467E+00
TEMP*	61	8	1.967038E+00
TEMP*	62	8	1.966694E+00
TEMP*	63	8	1.966419E+00

```
TEMP*           64          8   1.966199E+00
TEMP*           65          8   1.966023E+00

…

TEMP*         1996          8   1.965318E+00
TEMP*         1997          8   1.965318E+00
TEMP*         1998          8   1.965318E+00
TEMP*         1999          8   1.965318E+00
TEMP*         2000          8   1.965318E+00
```

Core par.dat

```
ID MSC-NASTRAN V68
SOL 159
DIAG 51
TIME 10
CEND
$
TITLE = EXAMPLE 7F1
ANALYSIS = HEAT
SET 1 =   0.0000,   0.8004,   1.6008,   2.4012,
          3.2016,   4.0020,   4.8024,   5.6028,
          6.4032,   7.2036,   8.0040,   8.8044,
          9.6048,  10.4052,  11.2056,  12.0060,
         12.8064,  13.6068,  14.4072,  15.2076,
         16.0080,  16.8084,  17.6088,  18.4092,
         19.2096,  20.0100,  20.8104,  21.6108,
         22.4112,  23.2116,  24.0120,  24.8124,
         25.6128,  26.4132,  27.2136,  28.0140,
         28.8144,  29.6148,  30.4152,  31.2156,
         32.0160,  32.8164,  33.6168,  34.4172,
         35.2176,  36.0180,  36.8184,  37.6188,
         38.4192,  39.2196,  40.0200,  40.8204,
         41.6208,  42.4212,  43.2216,  44.0220,
         44.8224,  45.6228,  46.4232,  47.2236,
         48.0240,  48.8244,  49.6248,  50.4252,
         51.2256,  52.0260,  52.8264,  53.6268,
         54.4272,  55.2276,  56.0280,  56.8284,
         57.6288,  58.4292,  59.2296,  60.0300,
         60.8304,  61.6308,  62.4312,  63.2316,
         64.0320,  64.8324,  65.6328,  66.4332,
         67.2336,  68.0340,  68.8344,  69.6348,
         70.4352,  71.2356,  72.0360,  72.8364,
         73.6368,  74.4372,  75.2376,  76.0380,
         76.8384,  77.6388,  78.4392,  79.2396,
         80.0400,  80.8404,  81.6408,  82.4412,
         83.2416,  84.0420,  84.8424,  85.6428,
         86.4432,  87.2436,  88.0440,  88.8444,
```

89.6448, 90.4452, 91.2456, 92.0460,
92.8464, 93.6468, 94.4472, 95.2476,
96.0480, 96.8484, 97.6488, 98.4492,
99.2496, 100.0500, 100.8504, 101.6508,
102.4512, 103.2516, 104.0520, 104.8524,
105.6528, 106.4532, 107.2536, 108.0540,
108.8544, 109.6548, 110.4552, 111.2556,
112.0560, 112.8564, 113.6568, 114.4572,
115.2576, 116.0580, 116.8584, 117.6588,
118.4592, 119.2596, 120.0600, 120.8604,
121.6608, 122.4612, 123.2616, 124.0620,
124.8624, 125.6628, 126.4632, 127.2636,
128.0640, 128.8644, 129.6648, 130.4652,
131.2656, 132.0660, 132.8664, 133.6668,
134.4672, 135.2676, 136.0680, 136.8684,
137.6688, 138.4692, 139.2696, 140.0700,
140.8704, 141.6708, 142.4712, 143.2716,
144.0720, 144.8724, 145.6728, 146.4732,
147.2736, 148.0740, 148.8744, 149.6748,
150.4752, 151.2756, 152.0760, 152.8764,
153.6768, 154.4772, 155.2776, 156.0780,
156.8784, 157.6788, 158.4792, 159.2796,
160.0800, 160.8804, 161.6808, 162.4812,
163.2816, 164.0820, 164.8824, 165.6828,
166.4832, 167.2836, 168.0840, 168.8844,
169.6848, 170.4852, 171.2856, 172.0860,
172.8864, 173.6868, 174.4872, 175.2876,
176.0880, 176.8884, 177.6888, 178.4892,
179.2896, 180.0900, 180.8904, 181.6908,
182.4912, 183.2916, 184.0920, 184.8924,
185.6928, 186.4932, 187.2936, 188.0940,
188.8944, 189.6948, 190.4952, 191.2956,
192.0960, 192.8964, 193.6968, 194.4972,
195.2976, 196.0980, 196.8984, 197.6988,
198.4992, 199.2996, 200.1001, 200.9005,
201.7009, 202.5013, 203.3017, 204.1021,
204.9025, 205.7029, 206.5033, 207.3037,
208.1041, 208.9045, 209.7049, 210.5053,
211.3057, 212.1061, 212.9065, 213.7069,
214.5073, 215.3077, 216.1081, 216.9085,
217.7089, 218.5093, 219.3097, 220.1101,
220.9105, 221.7109, 222.5113, 223.3117,
224.1121, 224.9125, 225.7129, 226.5133,
227.3137, 228.1141, 228.9145, 229.7149,
230.5153, 231.3157, 232.1161, 232.9165,
233.7169, 234.5173, 235.3177, 236.1181,
236.9185, 237.7189, 238.5193, 239.3197,
240.1201, 240.9205, 241.7209, 242.5213,
243.3217, 244.1221, 244.9225, 245.7229,
246.5233, 247.3237, 248.1241, 248.9245,

249.7249, 250.5253, 251.3257, 252.1261,
252.9265, 253.7269, 254.5273, 255.3277,
256.1281, 256.9285, 257.7289, 258.5293,
259.3297, 260.1301, 260.9305, 261.7309,
262.5313, 263.3317, 264.1321, 264.9325,
265.7329, 266.5333, 267.3337, 268.1341,
268.9345, 269.7349, 270.5353, 271.3357,
272.1361, 272.9365, 273.7369, 274.5373,
275.3377, 276.1381, 276.9385, 277.7389,
278.5393, 279.3397, 280.1401, 280.9405,
281.7409, 282.5413, 283.3417, 284.1421,
284.9425, 285.7429, 286.5433, 287.3437,
288.1441, 288.9445, 289.7449, 290.5453,
291.3457, 292.1461, 292.9465, 293.7469,
294.5473, 295.3477, 296.1481, 296.9485,
297.7489, 298.5493, 299.3497, 300.1501,
300.9505, 301.7509, 302.5513, 303.3517,
304.1521, 304.9525, 305.7529, 306.5533,
307.3537, 308.1541, 308.9545, 309.7549,
310.5553, 311.3557, 312.1561, 312.9565,
313.7569, 314.5573, 315.3577, 316.1581,
316.9585, 317.7589, 318.5593, 319.3597,
320.1601, 320.9605, 321.7609, 322.5613,
323.3617, 324.1621, 324.9625, 325.7629,
326.5633, 327.3637, 328.1641, 328.9645,
329.7649, 330.5653, 331.3657, 332.1661,
332.9665, 333.7669, 334.5673, 335.3677,
336.1681, 336.9685, 337.7689, 338.5693,
339.3697, 340.1701, 340.9705, 341.7709,
342.5713, 343.3717, 344.1721, 344.9725,
345.7729, 346.5733, 347.3737, 348.1741,
348.9745, 349.7749, 350.5753, 351.3757,
352.1761, 352.9765, 353.7769, 354.5773,
355.3777, 356.1781, 356.9785, 357.7789,
358.5793, 359.3797, 360.1801, 360.9805,
361.7809, 362.5813, 363.3817, 364.1821,
364.9825, 365.7829, 366.5833, 367.3837,
368.1841, 368.9845, 369.7849, 370.5853,
371.3857, 372.1861, 372.9865, 373.7869,
374.5873, 375.3877, 376.1881, 376.9885,
377.7889, 378.5893, 379.3897, 380.1901,
380.9905, 381.7909, 382.5913, 383.3917,
384.1921, 384.9925, 385.7929, 386.5933,
387.3937, 388.1941, 388.9945, 389.7949,
390.5953, 391.3957, 392.1961, 392.9965,
393.7969, 394.5973, 395.3977, 396.1981,
396.9985, 397.7989, 398.5993, 399.3997,
400.2001, 401.0005, 401.8009, 402.6013,
403.4017, 404.2021, 405.0025, 405.8029,
406.6033, 407.4037, 408.2041, 409.0045,

409.8049, 410.6053, 411.4057, 412.2061,
413.0065, 413.8069, 414.6073, 415.4077,
416.2081, 417.0085, 417.8089, 418.6093,
419.4097, 420.2101, 421.0105, 421.8109,
422.6113, 423.4117, 424.2121, 425.0125,
425.8129, 426.6133, 427.4137, 428.2141,
429.0145, 429.8149, 430.6153, 431.4157,
432.2161, 433.0165, 433.8169, 434.6173,
435.4177, 436.2181, 437.0185, 437.8189,
438.6193, 439.4197, 440.2201, 441.0205,
441.8209, 442.6213, 443.4217, 444.2221,
445.0225, 445.8229, 446.6233, 447.4237,
448.2241, 449.0245, 449.8249, 450.6253,
451.4257, 452.2261, 453.0265, 453.8269,
454.6273, 455.4277, 456.2281, 457.0285,
457.8289, 458.6293, 459.4297, 460.2301,
461.0305, 461.8309, 462.6313, 463.4317,
464.2321, 465.0325, 465.8329, 466.6333,
467.4337, 468.2341, 469.0345, 469.8349,
470.6353, 471.4357, 472.2361, 473.0365,
473.8369, 474.6373, 475.4377, 476.2381,
477.0385, 477.8389, 478.6393, 479.4397,
480.2401, 481.0405, 481.8409, 482.6413,
483.4417, 484.2421, 485.0425, 485.8429,
486.6433, 487.4437, 488.2441, 489.0445,
489.8449, 490.6453, 491.4457, 492.2461,
493.0465, 493.8469, 494.6473, 495.4477,
496.2481, 497.0485, 497.8489, 498.6493,
499.4497, 500.2501, 501.0505, 501.8509,
502.6513, 503.4517, 504.2521, 505.0525,
505.8529, 506.6533, 507.4537, 508.2541,
509.0545, 509.8549, 510.6553, 511.4557,
512.2561, 513.0565, 513.8569, 514.6573,
515.4577, 516.2581, 517.0585, 517.8589,
518.6593, 519.4597, 520.2601, 521.0605,
521.8609, 522.6613, 523.4617, 524.2621,
525.0625, 525.8629, 526.6633, 527.4637,
528.2641, 529.0645, 529.8649, 530.6653,
531.4657, 532.2661, 533.0665, 533.8669,
534.6673, 535.4677, 536.2681, 537.0685,
537.8689, 538.6693, 539.4697, 540.2701,
541.0705, 541.8709, 542.6713, 543.4717,
544.2721, 545.0725, 545.8729, 546.6733,
547.4737, 548.2741, 549.0745, 549.8749,
550.6753, 551.4757, 552.2761, 553.0765,
553.8769, 554.6773, 555.4777, 556.2781,
557.0785, 557.8789, 558.6793, 559.4797,
560.2801, 561.0805, 561.8809, 562.6813,
563.4817, 564.2821, 565.0825, 565.8829,
566.6833, 567.4837, 568.2841, 569.0845,

569.8849, 570.6853, 571.4857, 572.2861,
573.0865, 573.8869, 574.6873, 575.4877,
576.2881, 577.0885, 577.8889, 578.6893,
579.4897, 580.2901, 581.0905, 581.8909,
582.6913, 583.4917, 584.2921, 585.0925,
585.8929, 586.6933, 587.4937, 588.2941,
589.0945, 589.8949, 590.6953, 591.4957,
592.2961, 593.0965, 593.8969, 594.6973,
595.4977, 596.2981, 597.0985, 597.8989,
598.6993, 599.4997, 600.3002, 601.1006,
601.9010, 602.7014, 603.5018, 604.3022,
605.1026, 605.9030, 606.7034, 607.5038,
608.3042, 609.1046, 609.9050, 610.7054,
611.5058, 612.3062, 613.1066, 613.9070,
614.7074, 615.5078, 616.3082, 617.1086,
617.9090, 618.7094, 619.5098, 620.3102,
621.1106, 621.9110, 622.7114, 623.5118,
624.3122, 625.1126, 625.9130, 626.7134,
627.5138, 628.3142, 629.1146, 629.9150,
630.7154, 631.5158, 632.3162, 633.1166,
633.9170, 634.7174, 635.5178, 636.3182,
637.1186, 637.9190, 638.7194, 639.5198,
640.3202, 641.1206, 641.9210, 642.7214,
643.5218, 644.3222, 645.1226, 645.9230,
646.7234, 647.5238, 648.3242, 649.1246,
649.9250, 650.7254, 651.5258, 652.3262,
653.1266, 653.9270, 654.7274, 655.5278,
656.3282, 657.1286, 657.9290, 658.7294,
659.5298, 660.3302, 661.1306, 661.9310,
662.7314, 663.5318, 664.3322, 665.1326,
665.9330, 666.7334, 667.5338, 668.3342,
669.1346, 669.9350, 670.7354, 671.5358,
672.3362, 673.1366, 673.9370, 674.7374,
675.5378, 676.3382, 677.1386, 677.9390,
678.7394, 679.5398, 680.3402, 681.1406,
681.9410, 682.7414, 683.5418, 684.3422,
685.1426, 685.9430, 686.7434, 687.5438,
688.3442, 689.1446, 689.9450, 690.7454,
691.5458, 692.3462, 693.1466, 693.9470,
694.7474, 695.5478, 696.3482, 697.1486,
697.9490, 698.7494, 699.5498, 700.3502,
701.1506, 701.9510, 702.7514, 703.5518,
704.3522, 705.1526, 705.9530, 706.7534,
707.5538, 708.3542, 709.1546, 709.9550,
710.7554, 711.5558, 712.3562, 713.1566,
713.9570, 714.7574, 715.5578, 716.3582,
717.1586, 717.9590, 718.7594, 719.5598,
720.3602, 721.1606, 721.9610, 722.7614,
723.5618, 724.3622, 725.1626, 725.9630,
726.7634, 727.5638, 728.3642, 729.1646,

729.9650, 730.7654, 731.5658, 732.3662,
733.1666, 733.9670, 734.7674, 735.5678,
736.3682, 737.1686, 737.9690, 738.7694,
739.5698, 740.3702, 741.1706, 741.9710,
742.7714, 743.5718, 744.3722, 745.1726,
745.9730, 746.7734, 747.5738, 748.3742,
749.1746, 749.9750, 750.7754, 751.5758,
752.3762, 753.1766, 753.9770, 754.7774,
755.5778, 756.3782, 757.1786, 757.9790,
758.7794, 759.5798, 760.3802, 761.1806,
761.9810, 762.7814, 763.5818, 764.3822,
765.1826, 765.9830, 766.7834, 767.5838,
768.3842, 769.1846, 769.9850, 770.7854,
771.5858, 772.3862, 773.1866, 773.9870,
774.7874, 775.5878, 776.3882, 777.1886,
777.9890, 778.7894, 779.5898, 780.3902,
781.1906, 781.9910, 782.7914, 783.5918,
784.3922, 785.1926, 785.9930, 786.7934,
787.5938, 788.3942, 789.1946, 789.9950,
790.7954, 791.5958, 792.3962, 793.1966,
793.9970, 794.7974, 795.5978, 796.3982,
797.1986, 797.9990, 798.7994, 799.5998,
800.4002, 801.2006, 802.0010, 802.8014,
803.6018, 804.4022, 805.2026, 806.0030,
806.8034, 807.6038, 808.4042, 809.2046,
810.0050, 810.8054, 811.6058, 812.4062,
813.2066, 814.0070, 814.8074, 815.6078,
816.4082, 817.2086, 818.0090, 818.8094,
819.6098, 820.4102, 821.2106, 822.0110,
822.8114, 823.6118, 824.4122, 825.2126,
826.0130, 826.8134, 827.6138, 828.4142,
829.2146, 830.0150, 830.8154, 831.6158,
832.4162, 833.2166, 834.0170, 834.8174,
835.6178, 836.4182, 837.2186, 838.0190,
838.8194, 839.6198, 840.4202, 841.2206,
842.0210, 842.8214, 843.6218, 844.4222,
845.2226, 846.0230, 846.8234, 847.6238,
848.4242, 849.2246, 850.0250, 850.8254,
851.6258, 852.4262, 853.2266, 854.0270,
854.8274, 855.6278, 856.4282, 857.2286,
858.0290, 858.8294, 859.6298, 860.4302,
861.2306, 862.0310, 862.8314, 863.6318,
864.4322, 865.2326, 866.0330, 866.8334,
867.6338, 868.4342, 869.2346, 870.0350,
870.8354, 871.6358, 872.4362, 873.2366,
874.0370, 874.8374, 875.6378, 876.4382,
877.2386, 878.0390, 878.8394, 879.6398,
880.4402, 881.2406, 882.0410, 882.8414,
883.6418, 884.4422, 885.2426, 886.0430,
886.8434, 887.6438, 888.4442, 889.2446,

890.0450, 890.8454, 891.6458, 892.4462,
893.2466, 894.0470, 894.8474, 895.6478,
896.4482, 897.2486, 898.0490, 898.8494,
899.6498, 900.4502, 901.2506, 902.0510,
902.8514, 903.6518, 904.4522, 905.2526,
906.0530, 906.8534, 907.6538, 908.4542,
909.2546, 910.0550, 910.8554, 911.6558,
912.4562, 913.2566, 914.0570, 914.8574,
915.6578, 916.4582, 917.2586, 918.0590,
918.8594, 919.6598, 920.4602, 921.2606,
922.0610, 922.8614, 923.6618, 924.4622,
925.2626, 926.0630, 926.8634, 927.6638,
928.4642, 929.2646, 930.0650, 930.8654,
931.6658, 932.4662, 933.2666, 934.0670,
934.8674, 935.6678, 936.4682, 937.2686,
938.0690, 938.8694, 939.6698, 940.4702,
941.2706, 942.0710, 942.8714, 943.6718,
944.4722, 945.2726, 946.0730, 946.8734,
947.6738, 948.4742, 949.2746, 950.0750,
950.8754, 951.6758, 952.4762, 953.2766,
954.0770, 954.8774, 955.6778, 956.4782,
957.2786, 958.0790, 958.8794, 959.6798,
960.4802, 961.2806, 962.0810, 962.8814,
963.6818, 964.4822, 965.2826, 966.0830,
966.8834, 967.6838, 968.4842, 969.2846,
970.0850, 970.8854, 971.6858, 972.4862,
973.2866, 974.0870, 974.8874, 975.6878,
976.4882, 977.2886, 978.0890, 978.8894,
979.6898, 980.4902, 981.2906, 982.0910,
982.8914, 983.6918, 984.4922, 985.2926,
986.0930, 986.8934, 987.6938, 988.4942,
989.2946, 990.0950, 990.8954, 991.6958,
992.4962, 993.2966, 994.0970, 994.8974,
995.6978, 996.4982, 997.2986, 998.0990,
998.8994, 999.6998, 1000.5003, 1001.3007,
1002.1011, 1002.9015, 1003.7019, 1004.5023,
1005.3027, 1006.1031, 1006.9035, 1007.7039,
1008.5043, 1009.3047, 1010.1051, 1010.9055,
1011.7059, 1012.5063, 1013.3067, 1014.1071,
1014.9075, 1015.7079, 1016.5083, 1017.3087,
1018.1091, 1018.9095, 1019.7099, 1020.5103,
1021.3107, 1022.1111, 1022.9115, 1023.7119,
1024.5123, 1025.3127, 1026.1131, 1026.9135,
1027.7139, 1028.5143, 1029.3147, 1030.1151,
1030.9155, 1031.7159, 1032.5163, 1033.3167,
1034.1171, 1034.9175, 1035.7179, 1036.5183,
1037.3187, 1038.1191, 1038.9195, 1039.7199,
1040.5203, 1041.3207, 1042.1211, 1042.9215,
1043.7219, 1044.5223, 1045.3227, 1046.1231,
1046.9235, 1047.7239, 1048.5243, 1049.3247,

1050.1251, 1050.9255, 1051.7259, 1052.5263,
1053.3267, 1054.1271, 1054.9275, 1055.7279,
1056.5283, 1057.3287, 1058.1291, 1058.9295,
1059.7299, 1060.5303, 1061.3307, 1062.1311,
1062.9315, 1063.7319, 1064.5323, 1065.3327,
1066.1331, 1066.9335, 1067.7339, 1068.5343,
1069.3347, 1070.1351, 1070.9355, 1071.7359,
1072.5363, 1073.3367, 1074.1371, 1074.9375,
1075.7379, 1076.5383, 1077.3387, 1078.1391,
1078.9395, 1079.7399, 1080.5403, 1081.3407,
1082.1411, 1082.9415, 1083.7419, 1084.5423,
1085.3427, 1086.1431, 1086.9435, 1087.7439,
1088.5443, 1089.3447, 1090.1451, 1090.9455,
1091.7459, 1092.5463, 1093.3467, 1094.1471,
1094.9475, 1095.7479, 1096.5483, 1097.3487,
1098.1491, 1098.9495, 1099.7499, 1100.5503,
1101.3507, 1102.1511, 1102.9515, 1103.7519,
1104.5523, 1105.3527, 1106.1531, 1106.9535,
1107.7539, 1108.5543, 1109.3547, 1110.1551,
1110.9555, 1111.7559, 1112.5563, 1113.3567,
1114.1571, 1114.9575, 1115.7579, 1116.5583,
1117.3587, 1118.1591, 1118.9595, 1119.7599,
1120.5603, 1121.3607, 1122.1611, 1122.9615,
1123.7619, 1124.5623, 1125.3627, 1126.1631,
1126.9635, 1127.7639, 1128.5643, 1129.3647,
1130.1651, 1130.9655, 1131.7659, 1132.5663,
1133.3667, 1134.1671, 1134.9675, 1135.7679,
1136.5683, 1137.3687, 1138.1691, 1138.9695,
1139.7699, 1140.5703, 1141.3707, 1142.1711,
1142.9715, 1143.7719, 1144.5723, 1145.3727,
1146.1731, 1146.9735, 1147.7739, 1148.5743,
1149.3747, 1150.1751, 1150.9755, 1151.7759,
1152.5763, 1153.3767, 1154.1771, 1154.9775,
1155.7779, 1156.5783, 1157.3787, 1158.1791,
1158.9795, 1159.7799, 1160.5803, 1161.3807,
1162.1811, 1162.9815, 1163.7819, 1164.5823,
1165.3827, 1166.1831, 1166.9835, 1167.7839,
1168.5843, 1169.3847, 1170.1851, 1170.9855,
1171.7859, 1172.5863, 1173.3867, 1174.1871,
1174.9875, 1175.7879, 1176.5883, 1177.3887,
1178.1891, 1178.9895, 1179.7899, 1180.5903,
1181.3907, 1182.1911, 1182.9915, 1183.7919,
1184.5923, 1185.3927, 1186.1931, 1186.9935,
1187.7939, 1188.5943, 1189.3947, 1190.1951,
1190.9955, 1191.7959, 1192.5963, 1193.3967,
1194.1971, 1194.9975, 1195.7979, 1196.5983,
1197.3987, 1198.1991, 1198.9995, 1199.7999,
1200.6003, 1201.4007, 1202.2011, 1203.0015,
1203.8019, 1204.6023, 1205.4027, 1206.2031,
1207.0035, 1207.8039, 1208.6043, 1209.4047,

1210.2051, 1211.0055, 1211.8059, 1212.6063,
1213.4067, 1214.2071, 1215.0075, 1215.8079,
1216.6083, 1217.4087, 1218.2091, 1219.0095,
1219.8099, 1220.6103, 1221.4107, 1222.2111,
1223.0115, 1223.8119, 1224.6123, 1225.4127,
1226.2131, 1227.0135, 1227.8139, 1228.6143,
1229.4147, 1230.2151, 1231.0155, 1231.8159,
1232.6163, 1233.4167, 1234.2171, 1235.0175,
1235.8179, 1236.6183, 1237.4187, 1238.2191,
1239.0195, 1239.8199, 1240.6203, 1241.4207,
1242.2211, 1243.0215, 1243.8219, 1244.6223,
1245.4227, 1246.2231, 1247.0235, 1247.8239,
1248.6243, 1249.4247, 1250.2251, 1251.0255,
1251.8259, 1252.6263, 1253.4267, 1254.2271,
1255.0275, 1255.8279, 1256.6283, 1257.4287,
1258.2291, 1259.0295, 1259.8299, 1260.6303,
1261.4307, 1262.2311, 1263.0315, 1263.8319,
1264.6323, 1265.4327, 1266.2331, 1267.0335,
1267.8339, 1268.6343, 1269.4347, 1270.2351,
1271.0355, 1271.8359, 1272.6363, 1273.4367,
1274.2371, 1275.0375, 1275.8379, 1276.6383,
1277.4387, 1278.2391, 1279.0395, 1279.8399,
1280.6403, 1281.4407, 1282.2411, 1283.0415,
1283.8419, 1284.6423, 1285.4427, 1286.2431,
1287.0435, 1287.8439, 1288.6443, 1289.4447,
1290.2451, 1291.0455, 1291.8459, 1292.6463,
1293.4467, 1294.2471, 1295.0475, 1295.8479,
1296.6483, 1297.4487, 1298.2491, 1299.0495,
1299.8499, 1300.6503, 1301.4507, 1302.2511,
1303.0515, 1303.8519, 1304.6523, 1305.4527,
1306.2531, 1307.0535, 1307.8539, 1308.6543,
1309.4547, 1310.2551, 1311.0555, 1311.8559,
1312.6563, 1313.4567, 1314.2571, 1315.0575,
1315.8579, 1316.6583, 1317.4587, 1318.2591,
1319.0595, 1319.8599, 1320.6603, 1321.4607,
1322.2611, 1323.0615, 1323.8619, 1324.6623,
1325.4627, 1326.2631, 1327.0635, 1327.8639,
1328.6643, 1329.4647, 1330.2651, 1331.0655,
1331.8659, 1332.6663, 1333.4667, 1334.2671,
1335.0675, 1335.8679, 1336.6683, 1337.4687,
1338.2691, 1339.0695, 1339.8699, 1340.6703,
1341.4707, 1342.2711, 1343.0715, 1343.8719,
1344.6723, 1345.4727, 1346.2731, 1347.0735,
1347.8739, 1348.6743, 1349.4747, 1350.2751,
1351.0755, 1351.8759, 1352.6763, 1353.4767,
1354.2771, 1355.0775, 1355.8779, 1356.6783,
1357.4787, 1358.2791, 1359.0795, 1359.8799,
1360.6803, 1361.4807, 1362.2811, 1363.0815,
1363.8819, 1364.6823, 1365.4827, 1366.2831,
1367.0835, 1367.8839, 1368.6843, 1369.4847,

1370.2851, 1371.0855, 1371.8859, 1372.6863,
1373.4867, 1374.2871, 1375.0875, 1375.8879,
1376.6883, 1377.4887, 1378.2891, 1379.0895,
1379.8899, 1380.6903, 1381.4907, 1382.2911,
1383.0915, 1383.8919, 1384.6923, 1385.4927,
1386.2931, 1387.0935, 1387.8939, 1388.6943,
1389.4947, 1390.2951, 1391.0955, 1391.8959,
1392.6963, 1393.4967, 1394.2971, 1395.0975,
1395.8979, 1396.6983, 1397.4987, 1398.2991,
1399.0995, 1399.8999, 1400.7004, 1401.5008,
1402.3012, 1403.1016, 1403.9020, 1404.7024,
1405.5028, 1406.3032, 1407.1036, 1407.9040,
1408.7044, 1409.5048, 1410.3052, 1411.1056,
1411.9060, 1412.7064, 1413.5068, 1414.3072,
1415.1076, 1415.9080, 1416.7084, 1417.5088,
1418.3092, 1419.1096, 1419.9100, 1420.7104,
1421.5108, 1422.3112, 1423.1116, 1423.9120,
1424.7124, 1425.5128, 1426.3132, 1427.1136,
1427.9140, 1428.7144, 1429.5148, 1430.3152,
1431.1156, 1431.9160, 1432.7164, 1433.5168,
1434.3172, 1435.1176, 1435.9180, 1436.7184,
1437.5188, 1438.3192, 1439.1196, 1439.9200,
1440.7204, 1441.5208, 1442.3212, 1443.1216,
1443.9220, 1444.7224, 1445.5228, 1446.3232,
1447.1236, 1447.9240, 1448.7244, 1449.5248,
1450.3252, 1451.1256, 1451.9260, 1452.7264,
1453.5268, 1454.3272, 1455.1276, 1455.9280,
1456.7284, 1457.5288, 1458.3292, 1459.1296,
1459.9300, 1460.7304, 1461.5308, 1462.3312,
1463.1316, 1463.9320, 1464.7324, 1465.5328,
1466.3332, 1467.1336, 1467.9340, 1468.7344,
1469.5348, 1470.3352, 1471.1356, 1471.9360,
1472.7364, 1473.5368, 1474.3372, 1475.1376,
1475.9380, 1476.7384, 1477.5388, 1478.3392,
1479.1396, 1479.9400, 1480.7404, 1481.5408,
1482.3412, 1483.1416, 1483.9420, 1484.7424,
1485.5428, 1486.3432, 1487.1436, 1487.9440,
1488.7444, 1489.5448, 1490.3452, 1491.1456,
1491.9460, 1492.7464, 1493.5468, 1494.3472,
1495.1476, 1495.9480, 1496.7484, 1497.5488,
1498.3492, 1499.1496, 1499.9500, 1500.7504,
1501.5508, 1502.3512, 1503.1516, 1503.9520,
1504.7524, 1505.5528, 1506.3532, 1507.1536,
1507.9540, 1508.7544, 1509.5548, 1510.3552,
1511.1556, 1511.9560, 1512.7564, 1513.5568,
1514.3572, 1515.1576, 1515.9580, 1516.7584,
1517.5588, 1518.3592, 1519.1596, 1519.9600,
1520.7604, 1521.5608, 1522.3612, 1523.1616,
1523.9620, 1524.7624, 1525.5628, 1526.3632,
1527.1636, 1527.9640, 1528.7644, 1529.5648,

```
        1530.3652, 1531.1656, 1531.9660, 1532.7664,
        1533.5668, 1534.3672, 1535.1676, 1535.9680,
        1536.7684, 1537.5688, 1538.3692, 1539.1696,
        1539.9700, 1540.7704, 1541.5708, 1542.3712,
        1543.1716, 1543.9720, 1544.7724, 1545.5728,
        1546.3732, 1547.1736, 1547.9740, 1548.7744,
        1549.5748, 1550.3752, 1551.1756, 1551.9760,
        1552.7764, 1553.5768, 1554.3772, 1555.1776,
        1555.9780, 1556.7784, 1557.5788, 1558.3792,
        1559.1796, 1559.9800, 1560.7804, 1561.5808,
        1562.3812, 1563.1816, 1563.9820, 1564.7824,
        1565.5828, 1566.3832, 1567.1836, 1567.9840,
        1568.7844, 1569.5848, 1570.3852, 1571.1856,
        1571.9860, 1572.7864, 1573.5868, 1574.3872,
        1575.1876, 1575.9880, 1576.7884, 1577.5888,
        1578.3892, 1579.1896, 1579.9900, 1580.7904,
        1581.5908, 1582.3912, 1583.1916, 1583.9920,
        1584.7924, 1585.5928, 1586.3932, 1587.1936,
        1587.9940, 1588.7944, 1589.5948, 1590.3952,
        1591.1956, 1591.9960, 1592.7964, 1593.5968,
        1594.3972, 1595.1976, 1595.9980, 1596.7984,
        1597.5988, 1598.3992, 1599.1996, 1600.0000
THERMAL (SORT2,PUNCH)= ALL
FLUX = ALL
ENTHALPY = ALL
SPCF = ALL
OLOAD = ALL
OTIME = 1
SPC = 10
IC = 20
DLOAD = 200
TSTEPNL = 100
OUTPUT(XYPLOT)
XTITLE = TIME, SECONDS
YTITLE = TEMPERATURE DEGREES CELSIUS
TCURVE = TEMPERATURE VS. TIME
XYPLOT TEMP/1(T1)
BEGIN BULK
PARAM,NDAMP,0.1
$TSTEPNL,100,980,5.0,1,,,,,+TSTP
$+TSTP,0.001
TSTEPNL,100,150000,0.01,,,,,,+TSTP
+TSTP,0.001
INCLUDE 'geometria_n.dat'
$
$ proprietà SMA
PSOLID,5,15
$ proprietà Peltier
PSOLID,6,16
$
```

```
INCLUDE 'materiali_n.dat'
$
$ FACCIA INFERIORE PELTIER
CHBDYE,10,1,1
$ FACCIA SUPERIORE SMA
CHBDYE,20,2,2
$ FACCIA SUPERIORE PELTIER
CHBDYE,30,1,2
$
$ CONVEZIONE PELTIER - ARIA
CONV,10,45,,,99
$ CONVEZIONE SMA - ARIA
CONV,20,35,,,99
$ SOTTRAZIONE PELTIER DA FACCIA SUPERIORE
CONV,30,55,,,299
$ EMISSIONE PELTIER DA FACCIA INFERIORE
CONV,30,65,,,299
```

Geometry

```
GRID,1,,0.0,0.0,0.0
GRID,2,, 0.01000,0.0,0.0
GRID,3,, 0.01000, 0.01000,0.0
GRID,4,,0.0, 0.01000,0.0
GRID,5,,0.0,0.0, 0.00400
GRID,6,, 0.01000,0.0, 0.00400
GRID,7,, 0.01000, 0.01000, 0.00400
GRID,8,,0.0, 0.01000, 0.00400
GRID,9,,0.0,0.0, 0.00600
GRID,10,, 0.01000,0.0, 0.00600
GRID,11,, 0.01000, 0.01000, 0.00600
GRID,12,,0.0, 0.01000, 0.00600
$ NODO FLUIDO SUPERIORE
GRID,99,,99.0,99.0,99.0
$ NODO FLUIDO INFERIORE
GRID,199,,99.0,99.0,-99.0
$ NODO RIFERIMENTO PELTIER
GRID,299,,99.0,-99.0,-99.0
$ hexa della cella di Peltier
CHEXA,1,6,1,2,3,4,5,6,+CHX1
+CHX1,7,8
$ hexa del nastro SMA
CHEXA,2,5,5,6,7,8,9,10,+CHX2
+CHX2,11,12
```

Material

```
$ materiale SMA
```

MAT4,15, 18.000, 837.000, 6500.00, 110.630,,1.0,0.0,+MAT4
+MAT4, 40.500, 15.800, 24200.0
$ materiale Peltier
MAT4,16, 104.000, 510.000, 3826.00, 110.630,,,0.0,0.0

Nonlin

NOLIN1,333,5,1, -0.0300,5,1,444
NOLIN1,333,6,1, -0.0300,6,1,444
NOLIN1,333,7,1, -0.0300,7,1,444
NOLIN1,333,8,1, -0.0300,8,1,444